②

A Final Report to

THREE-DIMENSIONAL UNSTEADY SEPARATION AT LOW REYNOLDS NUMBERS

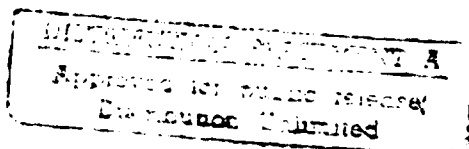N000014-86-K-0066

AD-A225 167

Submitted to

DR. BRUCE WELLS

(RE 1421:pjt)
Office of Naval Research
Resident Representative
University of New Mexico
Bandelier Hall West
Albuquerque, N.M. 87131

July 1990

Submitted by

HELEN L. REED

Department of Mechanical and Aerospace Engineering
College of Engineering and Applied Science
Arizona State University
Tempe, AZ 85287-6106

90 06 06 054

ABSTRACT

The work covered under this Contract included two numerical efforts and one companion experimental effort.

One of the numerical efforts generated a procedure to analyze the boundary layer on airfoils experiencing unsteady flight conditions and to predict the changes in the performance characteristics during off-design. The method predicts the flow in the boundary-layer region near the separation bubble using the incompressible Navier-Stokes equations with boundary conditions from inviscid and laminar boundary-layer solutions. The rate at which the separation bubble develops and decays is of primary interest in this study. Unsteady surface-pressure-coefficient distributions and velocity profiles are presented. The work includes application of this techniq to two state-of-the art airfoils, the ASM-LRN-010 (Pfenninger et al. 1988 "Design of Low Reynolds Number Airfoils-11" *AIAA-88-3766*) and Wortmann FX63-137 airfoil sections with chord Reynolds numbers of 250,000 and 500,000 and operating under light dynamic-stall conditions (Reed & Toppel 1990 "Low Reynolds Number Airfoils Under Gusting Conditions" in preparation).

The second numerical effort and the experimental effort involved the study of three-dimensional unsteady separation under low-Reynolds-number conditions. The test geometry consisted of a channel with a suction patch on the opposite wall. Contributions from the numerical effort include a novel, robust adaptive-grid technique for incompressible flow (Shen & Reed 1990a "Shepard's Interpolation for Solution-Adaptive Methods" submitted to *Journal of Computational Physics*; Shen & Reed 1990b "Solution-Adaptive Methods for Incompressible Navier-Stokes Equations" in preparation) as well as insight into the temporal development of unsteady separation (Shen & Reed 1990c "Three-Dimensional Separation at Low Reynolds Numbers" in preparation). Additional contributions from the experiments include a database for comparison with theory and computations (Henk, Reynolds, & Reed 1990 "Unsteady, Three-Dimensional Separation Experiments" in preparation).

TABLE OF CONTENTS

1. INTRODUCTION

In this Final Report, Part 2 contains a list of related experience and accomplishments. Part 3 presents results from completed experimental work (Stanford University - W.C. Reynolds and H.L. Reed), Part 4 from completed unsteady 2-D computational work (Arizona State University - H.L. Reed), and Part 5 from completed unsteady 3-D computational work (Arizona State University - H.L. Reed).

2. RELATED EXPERIENCE AND TECHNICAL ACCOMPLISHMENTS

In the past, 3 students were supervised, 11 publications were written, and 6 talks and lectures were given.

Publications

1. "Shepard's Interpolation for Solution-Adaptive Methods," C.-Y. Shen and H.L. Reed, submitted to *Journal of Computational Physics*, 1990.

2. "Solution-Adaptive Methods for Incompressible Navier-Stokes Equations," C.-Y. Shen and H.L. Reed, in preparation, 1990.

3. "Three-Dimensional Separation at Low Reynolds Numbers," C.-Y. Shen and H.L. Reed, in preparation, 1990.

4. "Low Reynolds Number Airfoils Under Gusting Conditions," H.L. Reed and B.A. Toppel, in preparation, 1990.

5. "Unsteady, Three-Dimensional Separation Experiments," R.W. Henk, W.C. Reynolds, and H.L. Reed, in preparation, 1990.

6. "Unsteady Separation at Low Reynolds Numbers," H.L. Reed, Low Reynolds Number Aerodynamics Conference, Notre Dame, June 5-7, 1989; in *Lecture Notes in Engineering*, Springer-Verlag, New York, to be published.

7. "Experiments on an Unsteady, Three-Dimensional Separation," R.W. Henk, W.C. Reynolds, and H.L. Reed, in *Proceedings of the Second AFOSR Workshop on Unsteady Separated Flows*, USAF, CO, July 28-29, 1987.

8. "Unsteady Separation at Low Reynolds Numbers," H.L. Reed, *ASME Forum on Unsteady Separation*, Cincinnati, June 1987.

9. "Fluids Engineering Workshop Unsteady-Flow Subgroup Final Report," H.L. Reed et al. (Prepared and edited: H.L. Reed), NSF Workshop, Savannah (Sept. 1986), Dec. 1986.

10. "An Analysis of Unsteady, Two-Dimensional Separation Bubbles," H.L. Reed and L.K. Pauley, in Proceedings of the *Royal Aeronautical Society Conference on Aerodynamics at Low Reynolds Numbers*, London UK, Oct. 15-18, 1986.

11. "Report of Computational Group," H.L. Reed, in *Transition in Turbines,* NASA CP 2386, NASA Lewis Research Center, May 1984.

Presentations

1. "Unsteady Separation at Low Reynolds Numbers," H.L. Reed, Low Reynolds Number Aerodynamics Conference, Notre Dame, June 5-7, 1989; in *Lecture Notes in Engineering,* Springer-Verlag, New York, to be published.

2. "Structure of an Unsteady, Three-Dimensional Separation," R. Henk, W. Reynolds, and H. Reed, Bull. Amer. Phys. Soc., Vol. 32, No. 10, p. 2050, Nov. 1987.

3. "Experiments on an Unsteady, Three-Dimensional Separation," R.W. Henk, W.C. Reynolds, and H.L. Reed, in *Proceedings of the Second AFOSR Workshop on Unsteady Separated Flows,* USAF, CO, July 28-29, 1987.

4. "Unsteady Separation at Low Reynolds Numbers," H.L. Reed, *ASME Forum on Unsteady Separation,* Cincinnati, June 1987.

5. "The Future of Unsteady-Flow Research," H.L. Reed et al., NSF Workshop on Engineering Fluid Mechanics-Future Directions in Fluid Mechanics, Winter Annual Meeting of ASME, Dec. 7-12, 1986, Anaheim.

6. "An Analysis of Unsteady, Two-Dimensional Separation Bubbles," H.L. Reed and L.K. Pauley, in Proceedings of the *Royal Aeronautical Society Conference on Aerodynamics at Low Reynolds Numbers,* London UK, Oct. 15-18, 1986.

Ph.D. Students

R. Henk, "Fundamental Studies of Three-Dimensional Unsteady Separation at Low Reynolds Numbers," Stanford, completed Spring 1990.

C.Y. Shen, "Numerical Simulation of Three-Dimensional Unsteady Separation at Low Reynolds Numbers," expected Fall 1990.

MS Students

B. Toppel, "Numerical Simulation of Two-Dimensional Unsteady Separation at Low Reynolds Numbers," expected Fall 1990.

The basic accomplishments that are described in these publications can be outlined as follows:

1. Consistent definition of unsteady and/or 3-D separation established.

2. Full Navier Stokes, spatial-simulation numerics developed for both 2-D and 3-D.

3. 2-D and 3-D adaptive-grid schemes developed for flat plate for full, unsteady, *incompressible* Navier Stokes.

4. 2-D and 3-D unsteady, vortex-lattice code developed to solve inviscid flow

over an airfoil. This was established for the farfield boundary condition for the boundary-layer code and the Navier-Stokes simulation.

5. 2-D boundary-layer code developed including leading edge and curvature. This was established for the upstream boundary condition for the simulation.

6. Established platform for unsteady-separation studies for unswept wings at 50,000-500,000 chord Reynolds numbers.

7. Companion experiments on unsteady, 3-D, low-Reynolds-number separation finished at Stanford.

PART 3. COMPLETED COMPANION EXPERIMENTAL WORK (STANFORD UNIVERSITY WITH W. C. REYNOLDS)

This section begins with a literature review, then proposes a consistent definition for separation, and finally describes the experimental results in a water channel at Stanford University. Because of the time constraints to complete this final report, Part 3 is a draft of the PhD dissertation of Roy Henk at Stanford, working under the direction of W.C. Reynolds and H.L. Reed.

This section will ultimately appear as part of the Stanford report; however, it is included here as well because money was budgeted in the Arizona State University side of the grant for H.L. Reed to travel at least once a month to Stanford to advise the PhD student Roy Henk.

Chapter 1

Introduction

1.1 Background

When the boundary layer on a solid surface encounters an adverse pressure gradient, the shear layer may depart from the surface in what is commonly referred to as flow separation. In flows of technological nature, *e.g.* turbomachinery and airfoils, flow separation (hereafter separation) often has devastating consequences. Separation inhibits heat transfer, increases the drag of vehicles, stalls turbines, and causes aircraft to lose lift.

For engineers, flow separation has historically been a problem of peculiar difficulty because conventional boundary-layer calculations break down at the point of separation. For many years research concentrated on stationary, two-dimensional separation. This work led to a generally agreed upon model for separation and the ability to calculate beyond the point of separation.

More recently, interest has shifted to separation in the nonstationary and three-dimensional flow regimes. Most practical flows in nature and technology are both three-dimensional and time-varying. The model for stationary, two-dimensional separation has been found by many researchers to be inadequate for describing three-dimensional and/or nonstationary separation.

Some advantages can result from a greater understanding of unsteady separa-tion, for instance dynamic enhancement of lift (Carr, McAlister and McCroskey, 1977). Maxworthy (1981) and Saharon and Luttges (1987) report that those flying creatures which can hover, *e.g.* hummingbirds, bees, and other insects, manipulate unsteady, three-dimensional separation in order to remain aloft and to maneuver.

Some questions that need to be answered are: How long does separation take to develop? What determines the size or extent of separation? Through what

stages does the flow structure pass on the way to fully developed separation? How long does each stage persist? How does separation decay? How does turbulence come into play in a separation of a laminar boundary layer? And finally, is there a precise definition for *separation* in the global nonstationary, three-dimensional context?

Consequently, there is a need for comprehensive, fundamental examination of carefully controlled, unsteady, three-dimensional separations. This investigation is part of a program intended to meet this need.

1.2 Objective and Overview

The objective of the present experimental program at Stanford has been to characterize the time development and decay pressure-driven, unsteady, three-dimensional, laminar separation. In particular, interest focused on the structure and time-scaling of flow separation.

In order to achieve this objective, an existing water tunnel that was originally designed for the study of unsteady, two-dimensional boundary layers was modified to allow imposition of a controlled, time-dependent, three-dimensional, freestream velocity field on a laminar boundary layer. The facility was largely rebuilt for this work and special, fast-acting, flow-control valves were developed.

The experiment studied the response of a laminar boundary layer on a flat plate to the sudden imposition of a local, three-dimensional deceleration in the freestream flow, which resulted in a pressure-driven separation of the boundary layer. The developing flow structure was studied with a combination of visual and quantitative measurements. The relaxation to a zero pressure-gradient boundary layer upon sudden return to a uniform freestream velocity was also investigated.

The separation structure that was generated in this investigation is similar to flow separations that have been identified in a variety of situations; Bippes (1987) gives several examples. Though the global geometries of these situations may

differ, the local features of separation are the same. Hence, flow separation can be thought of as a "module" within a larger flowfield which can be isolated for study.

The most important observation in this investigation was that the three-dimensional separation contains an unstable free-shear layer which sheds vortices much like a conventional, two-dimensional mixing layer. The Strouhal number of the shedding frequency f was found to be

$$St = \frac{f \cdot \theta_0}{U_0} \quad ,$$

where U_0 is the upstream velocity and θ_0 is the momentum thickness of the approaching boundary layer. The Strouhal number was independent of the strength of the adverse freestream-velocity gradient.

The companion numerical simulation of Pauley, *et al.* (1988) provides extensive detail of the flow filed, pressure, and vorticity for one of the test cases reported herein. The experiment complements the simulation primarily by providing a relatively rapid scan of the separation structure over a wide parameter space. Together, these studies have enhanced understanding of nonstationary, three-dimensional separation. Insights from these programs should assist the modeling of these complex flowfields which are observed throughout nature and technology.

Chapter 2

Background and Literature

2.1 Overview and some definitions

This chapter will review literature pertinent to unsteady and three-dimensional separation. Highlights of new analytical tools and theories that have already been developed for this field will be discussed.

It is important to note that the very definition of separation has been under dispute. Consequently, terminology used among researchers has often become confused. Differing definitions, however, can usually be resolved because various authors have merely emphasized identical phenomena to differing degrees.

For the sake of preciseness, a few frequently used terms will now be defined. "Stationary" will be used to refer to fixed initial and boundary conditions. "Non-stationary" will be used for time-variable initial and/or boundary conditions. "Steady" means that the local flowfield does not vary with time. "Unsteady" will primarily refer to organized unsteadiness in the flowfield which may arise from inherent instabilities under stationary conditions or may be a response to nonstationary conditions. "Quasi-steady" refers to an unsteady flowfield that has lost all phase coherence. "Fluctuating" is a catchall for random unsteadiness and or other effects which were not identified as organized unsteadiness. A "saddle point" is a special point where the wall shear-stress vector field (or equivalently the limiting streamlines at the wall) has the topology shown in figure 2.1. These and ensuing definitions are collected in the glossary, appendix A.

The definition of "separation" or "separation region" used here is a flow structure that consists of a separation line and a separation wake. A "separation line", also shown in figure 2.1, is the line that passes through a saddle point on a solid surface. There must be a point, therefore, where $\bar{\tau}_w = 0$ (or $C_f = 0$) for

separation to exist. In order to distinguish from attachment, flow near the saddle point moves away from the wall. Sluggish fluid downstream of a separation line will be called a "separation wake."

There are several attractive features of this definition. The saddle point has a precise mathematical definition. The reference frame is the surface of the solid body. The definition is valid for stationary and nonstationary flow. This definition for separation is strongly akin to the one held by Prandtl.

When Prandtl (1905) first identified flow separation, he described several different phenomena that all occurred at the same point:

> For our application, however, the most important consequence of this investigation is that in certain cases *the flow detaches from the wall* at a spot completely determined by the boundary conditions. This fluid layer displaces itself into the freestream, which is set into rotation through the friction of the wall causing a complete rearrangement of the motion, and there plays the same roll as the Helmholtz separation layer [1].

Prandtl [2] later refined the definition of separation to

$$\frac{\partial u}{\partial y} = 0 \qquad (\text{for} \quad y = 0) \quad , \tag{2.1}$$

where he selected the zero shear-stress condition as the key phenomenon.

During the following seven or so decades, most separation research emphasized stationary, two-dimensional flows. It was repeatedly noted that the vortical shear layer broke away from the surface and that reversed flow began at the separation point. Furthermore, the boundary-layer equations, so useful for engineering calculations and design, became singular at this point. Unfortunately, the zero shear-stress definition of separation became encumbered with the associated phenomena of shear-layer breakaway, reversed flow, and computational instability.

---

[1] "Das für die Anwendung wichtigste Ergebnis dieser Untersuchungen ist aber das, daß sich in bestimmten Fällen an einer durch die äußeren Bedingungen vollständig gegeben Stelle *der Flüssigkeitsstrom von der Wand Ablöst*. Es scheibt sich also eine Flüssigkeitsschicht, die durch die Reibung an der Wand in Rotation versetzt ist, in the freie Flüssigkeit hinaus und spielt dort, eine völlige Umgestaltung der Bewegung bewirkend, dieselbe Rolle wie die Helmholtzchen Trennungsschichten." (English translation by R. W. Henk and P. J.-D. Juvet)

[2] Literature regarding flow separation universally attributes this definition to Prandtl. For example, see Prandtl and Tietjens (1934) pp. 63f.

Accordingly, a concept of separation from stationary, two-dimensional flow that encompassed all these phenomena became the norm.

The concept for stationary, two-dimensional separation was found inadequate to address all the phenomena when either three-dimensionality or unsteadiness was added. For these cases, the phenomena of (1) zero shear stress on the surface, (2) reversed flow, and (3) shear-layer breakaway, may occur independently or not at all. Consequently, a variety of definitions have been proposed to make up for the deficiencies in the concept of a stationary, two-dimensional separation. A dispute over various definitions has arisen and has not been fully resolved to date. The controversy can be avoided altogether by dealing with each phenomena individually. Returning to the fundamentals, the working definition above is found consistent for all cases of stationary and nonstationary, two- and three-dimensional laminar flows. Simpson (1989) defines turbulent detachment similarly. We have come full circle.

Since the field of nonstationary, three-dimensional separation is fairly new, most of the literature reviewed has been assembled by isolating the two adjectives, "nonstationary" and "three-dimensional." So, after briefly touching on stationary, two-dimensional separation, this chapter will move on to nonstationary, 2-D separation, and conclude with stationary and nonstationary, three-dimensional separation.

A review of the literature indicates that...

• Three-dimensionality arises in two-dimensional separations;

• Unsteadiness is inextricably intertwined with three-dimensional flow;

• Organized unsteadiness is observed in practically all separated flows, even in "stationary" two-dimensional cases. Marginal separation at low adverse pressure gradients may be truly steady;

• Inherent unsteadiness and three-dimensionality requires careful interpretation of visualized flows;

- Topology has been a valuable mathematical tool for classifying stationary three-dimensional flows and distinguishing flow zones. It has also proved useful for ensuring accurate reconstruction of flow phenomena from flow visualization;

- Global flow conditions in wind/water tunnels such as blockage and wall constraints greatly affect separation studies and should be considered in design;

- Momentum thickness of the boundary layer, up to separation, is one of the most important flow parameters; For the remainder of this chapter, we will look at each related field in more depth.

2.2 Stationary, Two-dimensional Separation

The study of stationary, two-dimensional separation has provided a healthy database and well-established model, figure 2.2. Reviews and compendia of stationary, two-dimensional separation abound (*e.g.* Williams, 1977 and Simpson, 1989). Williams dealt primarily with laminar separation and reviewed computational techniques that which bypass the singularity of the boundary-layer equations, thereby permitting calculations into the separated zone. These techniques are valid only for "small" separation zones, *i.e.* zones of a size of the boundary-layer thickness. Simpson dealt primarily with turbulent separation under stationary and nonstationary conditions.

Kline (1959) reviewed and significantly extended the then current understanding of "stall", that is "any backflow at a wall whether small of large, transient or steady." He focused primarily on internal flows, *i.e.* diffusers, and through the results of flow visualization was able to distinguish "four major types of stall flow patterns", each of which included steady and unsteady elements. He also formulated a qualitative parameter which enabled engineers to interpret and predict the qualitative behavior of stall. He indicated that the presence of the extra wall in internal flows resulted in a larger diversity of stall patterns than were observed for external flows.

Sandborn and Kline (1961) later introduced flow models for the inception of boundary-layer stall that correlated the data better and increased understanding of internal and external stall. They proposed a useful set of definitions on the detachment state near the wall. These definitions are based on fraction of time that the flow moves downstream. Such distinctions are important for turbulent separation because under adverse pressure gradients the layer of fluid nearest the wall contains locally reversed flow long before detachment. "Detachment" was defined as the point where the time-averaged, wall shear stress, $\bar{\tau}_w$, equals zero. Kline, Bardina, and Strawn (1983) later developed a single-variable correlation for detachment of laminar and turbulent boundary layers.

Gaster (1966) noted two types of stationary, two-dimensional separation for external flows. He gathered results from several investigations of stationary, two-dimensional separation and added his own to develop a criterion for which a "long" bubble "bursts" into a "short" bubble. What differentiated a long bubble from a short bubble is that a short-bubble separation reattached to the surface whereas a long bubble formed a large wake. Another distinguishing feature between long and short bubbles was the comparative impact on an airfoil's pressure distribution. Long bubbles accompanied airfoil stall and loss of lift. A short bubble, however, had little effect on the overall pressure distribution; its sole consequence often was to act as a fluidic trip to turbulence.

Gaster's observations were based on the velocities measured with a hotwire. For example, he noticed that when the hotwire was positioned in the recovery portion of the separation, unsteadiness appeared in oscilloscope traces. Traces in the recovery region of short bubbles exhibited "low-frequency character" of "high harmonic content," that is quasi-sinusoidal behavior. Gaster attributed this to "the growth of instability waves in the attached boundary layer," but does not identify the instability. Long bubbles traces showed steady behavior with intermittent turbulence.

Gaster also identified the momentum thickness as a primary parameter for research in flow separation. The momentum thickness varies slowly as the boundary

8

layer separates. For the "bursting" criterion, Gaster found a unique relationship between the momentum-thickness Reynolds number, Re_θ, and a non-dimensionalized pressure gradient formed from the results of potential flow analysis and the experimentally determined momentum thickness, θ, at the point of separation.

Pauley, Moin, and Reynolds (1988, 1990) add, through direct numerical simulation, considerable new insight into the physics which dissociate Gaster's long bubbles from short bubbles. Long bubbles were confirmed to be steady. They found, however, that the mechanism that shortens the separation bubble is an oscillatory roll-up and shedding of spanwise vorticity from the detached shear layer. They then refined Gaster's criterion and compared their results with his to show that the onset of shedding, *i.e.* the "bursting" of a long bubble to a short one, occurs at

$$P_{max} = \frac{\theta_{sep}^2}{\nu} \left(\frac{du_i}{dx} \right)_{max} \approx -0.24 \quad .$$

In addition, they made the following conclusions:

o The application of stationary, inlet, boundary conditions with strong adverse-pressure gradient produced a separation with periodic shedding.

o The propagation velocity of the shed spanwise vortex was approximately 60% of the local freestream velocity, U_∞, downstream of separation.

o Spanwise vortices shed at a constant frequency which was independent of the pressure gradient applied. For all cases, the characteristic Strouhal number was

$$St_\theta = \frac{f \cdot \theta_{sep}}{U_{sep}} = 0.00686 \pm 0.6\% \quad ,$$

which is consistent with the results of linear stability theory.

Winkelmann and Barlow (1981) found that stationary, "two-dimensional" separations on airfoils set at an angle of attack were truly three-dimensional. They found this true independent of the airfoil's aspect ratio. Visualization of the separated flow used the surface oil-film technique. They looked at both leading-edge and trailing-edge separation bubbles. The "two-dimensional" leading-edge separation exhibited small three-dimensional eddies. The trailing-edge separation bubble

9

was found to be a single three-dimensional structure for low-aspect-ratio airfoils and multiples of the same structure for high-aspect ratio airfoils. Hot-wire measurements in the wake of the airfoil agreed with their characterizations of the trailing-edge separation bubble.

Kiya and Sasaki (1983) thoroughly documented the velocity and press re signatures of a stationary turbulent separation bubble. They observed that coherent "large-scale vortices shed downstream from the separation bubble at a characteristic frequency of $0.6U_\infty/x_R$, where x_R is the time-mean length of the separation bubble." The factor $0.6U_\infty$ is suggestive of the convection velocity of structures. They found even larger-scale unsteadiness at a frequency of $0.2U_\infty/x_R$. Two-point correlations and autocorrelations enabled the size and convection speeds of shed vortices to be quantified.

Liebeck and Blackwelder (1987) report on the performance of a LA2573A airfoil operating at a low Reynolds number and document the separation bubble at an angle of attack, $\alpha = 8°$ and $Re_c = 0.23 \times 10^6$. A peak frequency in the detached shear layer occurred at $3.7kHz$. For the sake of comparison with the results of this experiment, a few approximations will be made. Given that the chord length is $0.15m$, the freestream velocity can be estimated to be $U_\infty \approx 23m/s$. From a plot, the boundary layer upstream of the separation appears to have $\delta_{99} \approx 0.6mm$. Now the Strouhal number can be estimated

$$St_\theta = \frac{\theta \cdot f}{U_\infty} \approx \frac{\delta_{99}}{8} \frac{f}{U_\infty} \approx 0.01 \quad .$$

This value compares well with the results of the present investigation.

This section has shown that many two-dimensional separations are unsteady, even under stationary conditions. A model for steady, two-dimensional separation arose from taking a time-averaged perspective of unsteady phenomena subjected to stationary boundary conditions. The next section will report on research where a two-dimensional boundary layer is separating under nonstationary boundary conditions, which is often confusingly classified as "unsteady separation."

10

2.3 Nonstationary, Two-Dimensional Separation

Dynamic stall of pitching helicopter blades and of turbomachinery has been a large motivating force behind investigations of nonstationary, two-dimensional separation. Stall has been approached from two perspectives: (1) from the laboratory perspective as an oscillating airfoil in a uniform freestream, and (2) from the vehicle's perspective as a nonstationary freestream over the body. This section concentrates on literature from the second perspective—theoretical and experimental, respectively—with a brief digression with regards to the debate that has arisen over the definition of nonstationary separation.

Watson (1958) and Stuart (1955) performed some early theoretical work on boundary-layer responses to a time-varying freestream. The work is an extension of Stokes first and second problems of a nonstationary plate. Watson, for instance, found phase-leads and lags in the boundary layer that have been verified experimentally, *e.g.* Brereton and Reynolds (1987). The works by Watson and Stuart, however, did not specifically cover nonstationary, separated flows.

As mentioned above, there is little agreement over the definition of separation when it is growing or traveling. It has been documented by many sources that the point of zero shear stress does not coincide with the location of boundary-layer breakaway during nonstationary conditions. Reviews by Sears (1956) and Riley (1975) approached the nonstationary separation problem from a theoretical framework and drew opposing conclusions. Sears has found more supporters for his side. The present focus of attention in this dispute is the MRS definition of separation, which will be elaborated on shortly.

This dispute can be resolved by recognizing the importance of each phenomenon through simple, precise definitions. The debate is simply over semantics and could have been avoided altogether by dropping the term "separation" and by dealing individually with the phenomena: zero shear stress, reversed flow, and shear-layer breakaway. Our working definition for separation does not negate the validity of any research based on other definitions.

11

The list below describes each phenomenon individually:

- "Zero shear stress" occurs on a surface when the gradient of tangential velocities, u and w, normal to the surface simultaneously equal zero, that is $\partial u/\partial y = \partial w/\partial y = 0$. This is also denoted $\bar{\tau}_w = 0$. In this chapter, "zero shear stress" is typically equated with a "saddle point".

- "Reversed flow" occurs when a velocity vector has a component opposite to the freestream direction.

- "Breakaway" occurs when the transport of vorticity away from the wall shifts from a diffusion process to convection. This phenomena corresponds to large v-velocities which invalidate the boundary-layer equations. For the sake of consistency, articles reviewed below will adopt the above terminology instead of the respective author's except when quoting directly or when the context is clear.

The MRS Condition. Moore (1957), Rott (1956), and Sears (1956) independently contended that the zero shear-stress criterion was inadequate for identifying separation and that breakaway equals separation. For example, Moore predicted reversed flow without displacement of the outer freestream flow. Sears stated

> ... that "separation" is presumed to mean the breaking away of the boundary layer from the surface, invalidating the boundary-layer approximations, and that (by analogy with the stationary case) this will be caused by wake fluid thrusting itself under the boundary layer and deflecting it away. Thus the appearance of a dividing streamline (trajectory) between wake fluid and boundary-layer fluid would be a necessary feature of separation, and this surely can have meaning only when viewed from the moving frame of reference. Certainly the local, instantaneous vanishing wall shear has no such significance.

Thus the MRS condition was proposed as an improved mathematical definition for separation (breakaway), namely that

$$u = 0, \qquad \partial u/\partial y = 0 \tag{2.2}$$

at some point within the boundary layer in a reference frame moving with the separation. The unsteady separation can travel upstream or downstream, as shown in figure 2.3.

12

The MRS condition abandoned a wall-fixed reference frame. Two conceptual problems resulted. The first was that $u = 0$ criterion is defined for a reference frame translating with the separation, usually at some nonzero velocity with respect to the surface. In other words, since the MRS separation velocity was not known à priori, the definition appeared circular and arbitrary. The second was that since a surface was not required, the flow could conceivably separate from nothing.

Riley (1975) discouraged unqualified acceptance of the MRS definition "which is based on the conviction that the boundary-layer equations become singular in all cases of separation." He supported his argument with cases which contradict this conviction.

The analysis by Van Dommelen and Shen (1982) resolved the first conceptual problem (arbitrariness) of the MRS condition by adopting a Lagrangian viewpoint for unsteady separation. Having focused on the ejection of vortical boundary-layer fluid into the irrotational freestream, they found that the location of this phenomenon coincided with the MRS definition.

Having adopted a different phenomenon for the definition of separation, the working definition clashes with the MRS condition on several points. Consider the "upstream-moving" and "downstream-moving separations", according to the MRS perspective, shown in figure 2.3. The first disagreement concerns the location of the separation for the upstream-moving case. Whereas the working definition identifies separation at the saddle point on the surface, the MRS condition puts the "separation point" somewhere out in the flow at "breakaway." Secondly, the working definition refuses to denote a downstream-moving MRS separation as "separation" because there is no point of zero shear stress on the wall.

In summary, the MRS condition focuses on the phenomenon of ejection of the vortical boundary layer into the outer freestream, which has been labeled "breakaway." Its primary contribution has been to define a velocity for a traveling separation. The MRS condition recently gained a firm mathematical basis but remains almost impossible to identify in practice. Nevertheless, the MRS condition is

presently the most popular definition among investigators of nonstationary separation. Their choice of the ejection phenomena is important to separation research. How experimentalists have approached the MRS condition will be discussed in the next section.

2.3.1 Experiments on Nonstationary Separation   Most

experiments regarding nonstationary two-dimensional separation rely entirely on flow visualization. The reviews by McCroskey (1977) and Telionis (1979) cover scant quantitative experimental results. In addition to reviewing the literature on forced nonstationary separation, Reynolds and Carr (1985) introduce the discrete vortex model and a simple control-volume analysis. The agreement that they find with experiment is remarkable for such a simple model.

Smith and Kline (1971) visualize and quantify some of the unsteady aspects of the transitory stall regime of two-dimensional diffusers. Although they visually observed the flow patterns that correspond to both upstream- and downstream-moving "MRS separations" during the development and "wash-out" of transitory stall, they did not quantify the velocity at which the separation moved.

Flow visualization about an oscillating airfoil by Carr, *et al.* (1977) clearly differentiated between reversed flow and shear-layer breakaway. As the airfoil began to pitch up, flow along the top surface reversed but the streamlines remained parallel to the surface, appearing attached. Shortly thereafter, still during pitch-up, the boundary-layer vorticity lifted from the surface generating a dynamic-stall vortex at the leading edge. The dynamic-stall vortex would shed and be replaced by smaller vortices which passed through in the wake on the lifting surface. As the airfoil pitched down, the stalled wake was released.

Koromilas and Telionis (1980) studied nonstationary separation by subjecting the flow in a water channel to an impulsive, adverse pressure gradient. They applied three methods of forcing unsteadiness: by changing the mean flow, by a flap on the test surface, and by deforming the test surface. In each case they reported both upstream- and downstream-moving MRS separations.

Many problems must be addressed thoroughly in assessing the results of this experiment. Their nonstationary velocity profiles are generated from flow-visualization pictures. All three cases the initial conditions of the boundary layer and the inlet flow were nonstationary, the first case intentionally so, but also the second and third cases because tunnel blockage changed with the forcing. They had difficulty identifying the downstream-moving MRS separations they had reported and could not quantify them. This is due to their dependence on quantifying velocities from flow visualization by hand before the advent of digital particle-tracking velocimetry.

They reported that the developing separation experienced large-scale unsteadiness. This occurred at a time approximately L_x/U_0, where L_x is the distance from the leading edge. Due to the blockage problem mentioned above, an alternative explanation can be offered for the onset of unsteadiness in the separation that had already developed.

The alternative explanation follows. The sudden change in inlet velocity, whether by intent (case 1) or by blockage (cases 2 and 3) causes an impulse vortex to form at the leading edge. This impulse vortex convects downstream with the freestream. Consequently, the vortex would be expected to arrive at one unit of convective time, i.e. at time L_x/U_∞. This point was overlooked in their analysis. The present experiment required specific measures in order to avoid the same problem.

Their conclusions include the following:

o An upstream-moving MRS separation is preceded by a thin layer of reversed flow. A shear-stress sensor would therefore be incapable of properly identifying an nonstationary separation.

o For mild pressure gradients, the point of zero shear stress and the MRS separation region can be easily confused.

o After an impulsive increase of the adverse pressure gradient, the separation initially erupts to disturb the potential flow up to three times the subsequent steady-state separation wake. The explosive disturbances evolve into vortical

15

wakes before becoming steady-state. This is the probable cause [3] for the hysteresis and overshoots observed on oscillating airfoils.

o The averaged location of breakaway is not affected by the amplitude of oscillation, but responds to changes in the frequency. Their averaged breakaway location moved downstream with oscillation.

o It was not possible for them to observe or measure the speed of propagation of breakaway. Sears (1956), Sears and Telionis (1971), Williams (1977) and Shen (1978) made predictions which agreed qualitatively but could not be verified quantitatively. A thin layer of reversed flow precedes a violent wake region which corresponded to substantial pressure disturbances.

o They could conceive of no means to experimentally predict nonstationary breakaway.

Didden and Ho (1985) investigated the flow due to a strong vortex traveling close to a wall. The traveling vortex was created as a vortex ring on an axisymmetrical jet which then impinged on a flat plate. The traveling vortex induced a moving, hence unsteady, separation wake by which they were the first to validate a downstream-moving MRS separation. they had quantified a nonstationary, separating flow field more extensively than previous investigations, which had relied more on flow visualization than measurement probes.

They considered several key velocities in their flow to discover if any satisfies the MRS condition, since the MRS reference frame is not known *à priori*. They found the convection velocity of the separation, identified by zero shear stress, to be $0.4U_0$. The convection velocity of peak displacement thickness was also $0.4U_0$. The primary vortex moved at $0.61U_0$, the secondary one at $0.73U_0$. Thus they concluded that the velocity at which the largest displacement thickness traveled was the "MRS velocity." Note that U_0 is the exit velocity of the original jet, so presumably it is also the maximum velocity in the time-averaged boundary layer after impinging on the plate. They concluded that the nonstationary adverse

---

[3] The alternative explanation offered above primarily contradicts the analysis by Koromilas and Telionis that lead to this conclusion.

pressure gradient induced by the primary vortex was the mechanism that led to unsteady breakaway.

In a theoretical investigation akin to the above experiment by Didden and Ho, Walker (1978) looked at a boundary layer induced by a traveling vortex. Choosing a reference moving with the vortex, he observed a recirculation zone at the wall. The traveling vortex was highly unstable.

Houdeville, Bonnet, and Cousteix (1989) investigated the leading-edge separation bubble on an oscillating flat plate with a sharp leading edge. They found that the mean extent of the separation bubble was 30% of the chord. Phase effects were very important. The flow was dominated by convection effects with a convection velocity on the order of $0.4U_0$, where U_0 is measured at the tunnel inlet. This held for integral thicknesses, external velocity and for $\langle u'^2 \rangle$.

Chandrasekhara and Carr (1989) used flow visualization to study dynamic stall on an oscillating airfoil at various Mach numbers. By differentiating measurements made from pictures, they noted that the dynamic-stall vortex convected with a speed 0.3 times the freestream velocity.

Simpson (1989) reviewed turbulent, boundary-layer separation for a large variety of flow conditions, stationary and nonstationary. He extends the stationary, separating, turbulent, boundary-layer definitions of Sandborn and Kline (1961) to nonstationary free-stream flows. He found that the point of "detachment", where the time-averaged $\bar{\tau}_w = 0$, coincided with the point of "transitory detachment", where instantaneous backflow occurs 50% of the time. Such coincidence need not be universal, a possible exception being backward-facing steps.

In the light of the present review, Simpson's review nicely extends the working definition of separation to stationary, turbulent detachment if a zone of separation is admitted as well as a point or line of separation.

To conclude this section, it should also be noted that a variety of schemes have attempted to control separated flows, including dynamic stall. Most efforts have used devices that introduce three-dimensionality or other means to bring detached

vorticity back to the surface, *e.g.* Humphreys and Reynolds (1988) and the review by Gad-el-Hak (1989).

In summary, this section has touched on research where a two-dimensional boundary layer is separating under nonstationary boundary conditions. For such cases, the phenomena of zero shear stress, reversed flow, and breakaway typically do not coincide. Consequently a debate has arisen over the appropriate definition. The prevailing view of the day holds to the MRS condition, which equates breakaway with separation. Nevertheless, the definition of separation adopted for this paper remains valid for separation under nonstationary conditions. The case for the saddle-point (zero-shear stress) definition will be strengthened in the following sections which introduce new factors that research in three-dimensional separation has brought to light.

2.4 Stationary, Three-dimensional Separation

Investigations of three-dimensional separation have primarily focused on theoretical analysis and flow visualization. Several researchers have attempted to establish a concise classification of the infinite variety of three-dimensional flows, including separation. Ensuing attempts to distinguish three-dimensional separation from other three-dimensional flows have been controversial. Reviews by Tobak and Peake (1982) and Perry and Chong (1987) cover these developments in detail; this section summarizes the main developments.

Maskell (1955) inaugurated the classification of three-dimensional flows by introducing the concept of "limiting streamlines." Limiting streamlines coincide with surface shear-stress patterns, and can be visualized by surface flow techniques, for example oil-film, ablation, and so forth. Limiting streamlines have also been called "surface streamlines" and "skin-friction lines" in later literature. Throughout this chapter, the terminology "skin-friction pattern" or "skin-friction lines" is preferred over either of the "streamline" terms because the no-slip condition at the surface precludes true streamlines.

18

Flow visualization work at ONERA, especially that of Werlé (1962), the review by Peake and Tobak (1980), and Bippes (1987) each offer a glimpse of the rich variety of skin-friction patterns. These sources illustrate beautiful and recurrent patterns from numerous experiments in stationary flow, *e.g.* figures 2.4 and 2.5, which have stimulated intense interest among theoreticians.

Lighthill (1963) laid the foundation for theoretical analysis of three-dimensional separation. In this landmark paper, Lighthill took surface shear-stress patterns, *i.e.* skin-friction lines, that were being observed and mapped them onto a phase plane, a technique which is familiar to the field of differential equations. All types of singular points, which are fundamental to the phase plane, appeared: saddle points, nodes, foci, and their degenerate forms.

Conceptually, the points can be described as follows. A "singular point," see figure 2.1, is a point where the wall shear stress, $\bar{\tau}_w$, equals zero. A singular point can either be a "node" or a "saddle point". A "node" is common to an infinite number of skin-friction lines; if the skin-friction lines spiral into the node then it is called a "focus". A "saddle point" is common to only two skin-friction lines. "Ordinary points," which cover the rest of the surface, posses only a single skin-friction line. Lighthill mathematically defined a saddle point and a node according to the Jacobian of the shear-stress vector.

With a map of the singular points, a three-dimensional flowfield could then be classified according to the number and arrangement of these singular points. Subsequent theoreticians have extended Lighthill's analysis primarily by the application of topological principles to the phase plane.

Hunt, Abell, Peterka, & Woo (1978) extended Lighthill's phase-plane analysis by applying principles from topology. They provide guidelines for discerning between physically realizable and impossible characterizations of flow about a three-dimensional surface. Their topological analysis derives the following important result which governs real flows on a simply-connected surface, namely that singular points

satisfy the equation...

$$\sum nodes + \sum foci - \sum saddles = 2. \tag{2.3}$$

Contours of a flow must satisfy this equation. If a schematic of a flow is drawn which violates this equation, the schematic is in error [4]. The analysis can be extended for multiply-connected/complex surfaces. For such extensions however, minor modifications to equation (2.3) are required.

Due to the work of Lighthill (1963) and Hunt, *et al.* (1978), there has been widespread aggreement among the research community over the interpretation and use of singular points in surface skin-friction patterns. In contrast, there has been a vigorous debate over how to deal with cases of streamline convergence without a saddle point, such as shown in figure 2.6. The present review has adopted the term "isolated line of convergence" or "LOC" for this type of flow. Topologically speaking, there are only ordinary points in the neighborhood of a LOC. Wang (1974), one of the early researchers to discuss this type of flow pattern, had suggested the term "open separation."

Legendre (1982) discusses the regular or catastrophic evolution of three-dimensional separation. He reiterates his strict definition for separation, specifically that a "line of separation ... has no local property. Its only characteristic is to pass through a saddle point (Legendre, 1956)." He states an uncertainty about applying his definition to unsteady flow. The working definition adopted for this paper is simply an extension of Legendre's to unsteady flows.

The informative review by Tobak and Peake (1982) adds finer distinctions to the field of stationary, three-dimensional separation. They designate the term "global separation" for cases when a saddle point is present, such as figure 2.5, and "local separation" for cases of an isolated line of convergence without a saddle point.

In order to capture the global flowfield, Tobak and Peake extend phase-plane analysis to "steady dividing surfaces", *i.e.* a mathematical surface in the flow where

---

[4] An well-regarded example from the literature will be given shortly. The example appears reasonable but nevertheless violates equation 2.3.

the normal velocity component is zero. They recognized that the problem with steady dividing surfaces is that the unsteady structures which are always present in three-dimensional separated flows are ignored. They offer their definitions strictly for steady flows, otherwise the working definition would be a subset of theirs.

Hornung and Perry (1984) set out to standardize classification of three-dimensional separations. Before detailing the classification scheme, they define three-dimensional separation, stationary or nonstationary, based on the strength of the local convergence of near-wall streamlines. They call a LOC a "negative bifurcations," see figure 2.7, which they may call a "separation" if the convergence is strong enough. Note that a "negative bifurcation" does not contain a saddle point. They propose the concept of a "degree of separation" based on a "strength of streamline convergence". Lacking an appropriate length scale, they also acknowledge the difficulty of determining the strength of convergence. The remainder of the article details a useful classification scheme which identifies clusters of singular points that frequently occur.

It is important to carefully interpret schematics such as figure 2.7. The problem is that although figure 2.7 makes the converging skin-friction lines appear to coalesce, the lines can only asymptote otherwise a nonexistent type of singular point is required on the line of convergence. No planar singular point exists that has three inflows, one from the LOC and one from each side of the LOC, and only one outflow, to the next point on the LOC. If lines truly coalesced, the "line of convergence" would contain an infinite number of such singular points which furthermore violates equation (2.3). Thus this figure gives an example of how the topological analysis represented by equation (2.3) can contradict what appears to be a reasonable interpretation of near-wall flow.

Perry.and Hornung (1984), a companion to the above article, describes a classification scheme for the global, three-dimensional, separated flowfield. This scheme centers on vortex skeletons which can map out the global flowfield under stationary conditions. One example, the owl-face of the first kind, is shown in figure 2.8. This type of separation is characterized by a saddle point a little upstream of two foci

21

with a second saddle point yet further downstream. By this classification scheme, Bippes (1987) observed an owl-face of the first kind on an axisymmetrical body and on an airfoil at angle of attack, see figure 2.5. Moreover, the trailing-edge separation observed on a stalled airfoil by Winkelmann and Barlow (1980) is an owl-face of the first kind. Incidentally, the same separation structure is observed on the flat plate for the experiment described in this dissertation. It is important to note that a multitude of separation structures other than an owl-face of the first kind have been observed for stalled airfoils and for axisymmetrical bodies at angle of attack.

Chapman (1986) also proposes a classification scheme by combining the topological rules with collections of singular points. He renames a LOC a "crossflow-type separation", because "there is a change of the topology of the velocity field in the crossflow plane." The topology of the skin-friction lines in "crossflow-type separation" has not changed, however, because there are only ordinary points in the immediate neighborhood of the body surface due to the absence of singular points.

Principal evidence for "crossflow-type separation" arises on an axisymmetrical body at small angle of attack at supersonic speeds; figure 2.6 shows one example at Mach 2.4. These conditions require careful interpretation of the flowfield. Models of the flow in the literature have indicated that a pair of streamwise vortices arise from the LOC, although flow visualization didn't suggest attachment of the vortices to the surface. Furthermore, flow downstream of the LOC has actually accelerated while upstream flow approaching the LOC has decelerated. The higher velocity of downstream fluid is evidenced by the angle between downstream skin-friction lines and the LOC being considerably shallower than the angle between upstream lines and the LOC; on both sides, the momentum normal to the LOC must be identical. With the exception that some vortical fluid near the LOC is carried away from the wall into the freestream, such a flowfield contradicts most concepts of separation.

The review by Perry and Chong (1987) covers all types of three-dimensional flows with transient coherent structures, including separated flows. The review is quite interesting, but most of their proposed approaches for analysis are found to

encounter acute obstacles. The disadvantage "of using instantaneous streamline patterns is the sensitivity of such patterns" to the velocity of the reference frame chosen by the observer. Thus they propose vorticity, because it is invariant, as more appropriate for analyses of instantaneous streamlines. A major problem that then arises is the inaccuracy, and almost complete absence, of experimental vorticity measurements.

Ünal (1988) introduces the nomenclature from the field of dynamics in order to narrowly define singular points. The nature of a singular point is classified as index 1 if only one streamline leaves the singular point, or as index 2 if a stream surface leaves the point. He claims to resolve "once and for all" the controversy regarding "local" or "open" separations, which have no saddle point. Without a saddle point, there is "...no separated stream surface; hence no separation."

To sum up, classification schemes for three-dimensional flows are caught in a debate. The primary issue is whether or not to consider an isolated lines of convergence as "separation." To understand the controversy, consider again the "negative bifurcation" at a LOC as shown in figure 2.7 (Hornung and Perry, 1984). Vortical boundary-layer fluid is carried into the outer, potential flow. There is, however, no point of zero shear stress nor any region of reversed flow as there was in figure 2.8. Shall a LOC be called a separation? Our working definition, Lighthill (1963), and Legendre (1956, 1982), and Ünal (1988) unequivocally answer "No!", because there is no saddle point. There is not even a singular point. On the other hand, Chapman (1986) and others claim that such flows are indeed separation. Tobak and Peake (1982) would call this is a local separation. Hornung and Perry (1984) would determine if streamline convergence is strong enough before deciding.

An incidental observation from this section must be made to clarify terminology. In fluid mechanical parlance it is almost impossible to say the word "separation" without following it by the word "bubble." If we take the word "bubble" to refer to a closed surface across which there is no transfer of fluid particles, then three-dimensional separations are practically never bubbles. This is not apparent at

first. For example, Maskell (1953) envisioned closed 3-D bubbles and Moore (1957) suggested that a 3-D separation may be identified "by the existence of a bubble of fluid in the boundary not exchanging fluid with its surrounding." Tobak and Peake (1982), among others, showed that stationary, three-dimensional separations do not have a re-attachment line that closes with the separation line; topological rules prohibit it. Instead, a three-dimensional separation region must constantly exchange fluid with the outer flow. It appears that the only practical case where a three-dimensional separation would close into a bubble is by capping a cavity flow at low Reynolds numbers.

Since three-dimensional separations do not close into a bubble, the detached shear layer experiences instabilities which cause unsteadiness, as Prandtl (1905) had originally noted. This can happen by the shear layer rolling up and shedding or by vortex meander and break down.

Through a review of the literature pertaining to stationary, three-dimensional separation, this section has introduced new elements that arise with the extra space dimension. For instance, the two-dimensional line of zero shear stress collapses to a singular point. Tools from phase-plane analysis and topology have been useful for theoretical investigation of 3-D separation and aid the evaluation of surface flow models. The thrust of the debate regarding the definition for three-dimensional separation has been whether or not to call the mere convergence of surface streamline separation. The working definition of separation, adopted from Legendre (1956, 1982), avoids the inconsistencies and ambiguities of designating an "isolated line of convergence" as "separation". The next section supports this extension of Legendre's definition to nonstationary flows as well.

2.5 Nonstationary, three-dimensional separation

Although certain aspects of nonstationary, three-dimensional separation have been investigated for some time, extensive quantification and analysis of the velocity flowfield has begun fairly recently. Most earlier work focused on flow visu-

alization or the measurement of the applied aerodynamic forces and moments of pitching, three-dimensional bodies.

Some recent examples of work on a pitching bodies will be mentioned briefly. Robinson, *et al.* (1986) use flow visualization to track the motion of leading-edge and trailing edge vortices that have shed during dynamic stall. The works of Wood, Lee, and Roberts (1988) and Roberts and Wood (1989) describe how these vortices can be controlled by tangential leading-edge blowing. Through small changes in the surface boundary conditions through tangential leading-edge blowing, a significant degree of dynamic control is available for maneuvering an aircraft after stall.

Hui (1988) uses the continuity equation to construct a mathematical framework for steady and unsteady, compressible or incompressible, three-dimensional separation. The continuity equation determines flow topology, whereas the momentum equation only determines magnitude of flow velocities. Most importantly, instantaneous stream surfaces from a three-dimensional, unsteady flow can be topologically analyzed as if the flow were steady.

Pauley, Moin, and Reynolds (1988) perform a comprehensive quantitative investigation through direct numerical simulation (DNS) for one case of nonstationary, three-dimensional separation. This case mirrors the geometry and flow conditions of the base case for this experiment. Only a few conclusions will be listed here. A more thorough comparison between the DNS and the experiment will be made in chapter 6.

For three-dimensional separation:

o When a three-dimensional adverse pressure gradient was applied to a two-dimensional boundary layer on a flat plate, the separation structure passed through several topologies before becoming an "owl-face of the first kind."

o The detached shear layer became unstable and periodic shedding of shear-layer vorticity occurred.

o At the release of the adverse pressure gradient the near wall velocity becomes positive. A free shear layer persisted further downstream but began to shed at a higher frequency.

o Velocity profiles indicated that the flow first adjusts near the wall to a change in pressure gradient. Other aspects of this work were described in section 2.2.

They obtained a convincing definition for breakaway that applies to two- and three-dimensional flows. Van Dommelen and Cowley (1990) extensively develop the Lagrangian approach for describing the ejection of vortical boundary-layer fluid from the wall (breakaway). Their approach establishes a concrete mathematical foundation for for a time-dependent, three-dimensional MRS condition, thereby providing the best definition [5] of the mathematical singularity at breakaway. Having determined that the momentum equations are completely regular in the Lagrangian coordinate system, the singularity is shown to appear in the continuity equation. Van Dommelen (1990) applied the theory to the case of an impulsively-spun sphere. Lagrangian computations were able to proceed while Eulerian computations broke down at breakaway.

Van Dommelen and Cowley described the physics of breakaway as follows: "These singularities occur when a fluid particle becomes compressed in one direction parallel to the boundary [wall]" which forces the fluid particle "out of the boundary layer in the form of a detached vorticity layer. A common feature of all the singularities is that the typical lengthscale in the direction of compression is $O(|\delta t|^{-\frac{3}{2}})$." By their definition, the local displacement thickness of the boundary layer must also become infinite. As a final comment, it would be helpful to combine this analysis with that of Hui (1988) since both rely on the continuity equation, albeit in the search of different separation phenomena.

2.6 Summary

---

[5] The definition will not be given here because the results of this experiment are not cast according to the Langrangian description. Several pages of new nomenclature and equations are required.

A definition for laminar "separation" that applies to two- and three-dimensional, stationary and nonstationary separation has been proposed. The working definition of "separation" is a region that includes a "separation line" and a "separation wake." A "separation line" is a surface skin-friction line that passes through a saddle point. There must be a point, therefore, where $\bar{\tau}_w = 0$ (or $C_f = 0$) for separation to exist. The reference frame for this definition is the surface of the solid body. Sluggish fluid downstream of the separation line is called the "separation wake". This definition for separation is akin to the one held by Prandtl.

Several alternate definitions for separation have been proposed to offset the inadequacies of the standard definition of stationary, two-dimensional separation. The standard definition had associated the zero shear-stress condition with boundary-layer breakaway, reverse flow, and computational instability. It is possible, however, to find exceptions to practically every definition for separation by considering nonstationary or three-dimensional effects. This paper's definition is valid for steady and unsteady, two- and three-dimensional cases.

The debate over the definition of unsteady separation concerns whether or not to focus on zero shear stress or on the MRS condition. The highly-touted MRS condition identifies the breakaway of the vortical shear layer from the wall into the freestream rather than the zero shear-stress condition.

The debate over the definition three-dimensional separation concerns whether or not to denote the mere convergence of surface skin-friction lines as "separation." The position of this paper is that a saddle point is required for separation, whether steady or unsteady, two- or three-dimensional. This view accords with or is an extension to the views of Legendre (1956, 1982), Lighthill (1963), Ünal (1988) and Hui (1988). Several reasons are forwarded for rejecting the idea that convergent streamlines constitute separation.

The working definition can be easily amended to include stationary, turbulent separation if we admit to a zone of separation rather than a point or line of separation.

The following conclusions can be highlighted:

- Most separations are unsteady and three-dimensional.

- The momentum thickness, θ, is significant for scaling separation.

- Phase-plane analysis and topological rules are useful for the investigation of three-dimensional flows. Since practically any measurement and correlation is new to the fledgling field of unsteady, three-dimensional flow separation, this experiment and its companion direct numerical simulation by Pauley, *et al.* (1988) are able to make a substantial contribution.

Chapter 3

Facility

The Stanford, Unsteady Boundary Layer, Research Water Tunnel is particularly-well suited for careful investigations of unsteady boundary layers under known initial and boundary conditions. With this tunnel, stationary or nonstationary, two- and three-dimensional freestream flows can be generated to perturb a two-dimensional laminar or turbulent boundary layer. Dynamic control of the freestream and acquisition of data proceed under computer control.

This chapter describes the water tunnel and other experimental tools. Special features of this facility enabled the present experimental investigation on unsteady, three-dimensional separation. Some of the features were inherited from previous research. In addition, many enhancements were made through redesign of the test section and computer-control of the flow.

3.1 The Facility

The experimental facility, figure 3.1, is a closed-circuit water tunnel. Flow follows a circuit from the overhead tank, through the test section, and into the sump, from which the water is pumped back to the overhead tank. More specifically, a weir in the overhead tank maintains the pressure head for the flow. The flow from the overhead tank is turned into the axial direction of the tunnel. Honeycomb, three screens, and acceleration through a nozzle attenuate flow turbulence to provide a relatively low turbulence freestream to the test section. An array of valves control the freestream velocity, $U_\infty(x,t)$, along the test section by withdrawing fluid through the control wall opposite the test surface. Pipes and hose conduct flow from the valves to the sump.

In the test section, the test boundary layer grows on a flat plate. The boundary layer develops under a stationary, uniform freestream velocity until it reaches

the nonstationary portion of the test section. At this point, the boundary layer encounters (1) a stationary, uniform freestream velocity, (2) a stationary, decelerating freestream, or (3) a computer-controlled, nonstationary freestream waveform. The growth of the boundary layer and its response to the imposed conditions is investigated by two-component velocity measurements.

Flow ranges. The primary flow parameters for this facility are the inlet velocity, U_0, and the freestream velocity gradient. The inlet velocity can span the range 0.1 to 0.73m/s. The freestream velocity can be reduced up to 0.3m/s over each streamwise segment, of 0.15m axial extent. The maximum freestream velocity gradient can be made significantly higher than $0.3/0.15 = 2s^{-1}$ by tailoring suction through the control wall.

A broad range of chord Reynolds numbers is available. The working length of the test surfaces extends from 0.5 to 2.6m. The water is typically maintained at 17° for a kinematic viscosity of $1.081 \times 10^{-6}m^2/s$. Thus the chord Reynolds number, Re_c, can range from 5×10^4 to 2×10^6.

Control of inlet flow. Upstream of the inlet to the test section, flow is turned several times. Figure 3.1 shows two 90° turns in the overhead tank and one before the nozzle. Each time this chapter refers to "turning the flow", flow is turned by an "oblique flow header" with a "free-discharge exit condition" through honeycomb. Crawford (1977) has shown that the exit flow is most uniform when the aspect ratio of exit area to inlet area, $AR \approx 3$. Exit uniformity degrades for $AR \leq 2$ or $AR \geq 4$. The AR of the oblique flow header just upstream of the nozzle is 3.0; consequently a relatively uniform freestream entered the nozzle.

Before the flow enters the test section, it is carefully conditioned to attenuate turbulence. The flow passes through a 1.0m by 1.0m by 0.15m thick piece of 9.5mm cell honeycomb and three taut screens of 22 mesh stainless steel at 69.7% porosity. A 20:1 contraction ratio in the nozzle accelerates the flow from a cross section of 1.0m by 1.0m into a cross section of 0.35m by 0.15m for entry into the

test section. At this point, the RMS level of streamwise velocity fluctuations is $\sqrt{u_1'^2}/U_0 \leq 0.6\%$, which is the minimum that the measurement system can resolve.

Quality Control. Some subsystems, not shown, operate continuously to ensure the quality of the flow during the acquisition of extended datasets. A temperature-control system maintains the water temperature at the desired set point $\pm 0.1°C$. Entrained air bubbles are removed by a de-aeration system.

3.2 Tunnel Design and Modifications

The original channel, described by Jayaraman, *et al.* (1982) and Brereton, *et al.* (1987), was extensively modified for these experiments. The modified facility is shown in figure 3.1. The new modular test section features interchangeable test surfaces, windows, and valves. Computer control of the freestream flow is performed by an array of custom-designed Revolving-Disc gate valves (RD-valve), such as the one shown in figure 3.2.

A team of three research assistants was responsible for the present modifications. The principal author is primarily responsible for design of the test section, the RD-valves, and most modules that plug into the test section. He also replaced the temperature control system which, incidentally, reduced electrical noise in the laboratory. W. W. Humphreys streamlined the plumbing system and the flow path through the constant-head reservoir. He also designed the turbulent test surfaces and a sump tank with increased capacity and durability. A. B. Carlson designed the custom hardware and software for valve control and data acquisition. Subsequent sections describe the facility in detail.

3.2.1 Test Section

The new test section measures $3.66m$ along the streamwise direction, $0.36m$ across the span, and $0.13m$ from the test surface to the control wall. Glass and acrylic on the top, sides, and at the end of the test section provide substantial optical access for flow visualization and LDA measurements.

The backbone of the test section is a stainless steel framework. The stainless steel bars are sealed at the joints by Boatlife® boat caulk for a durable, corrosion resistant, and leak resistant framework. Four cross-flanges span the top to furnish lateral reinforcement and a sealing surface for test surface modules. The two side walls are each composed of eight interlocking side frames. Twenty-four cross-girders span the bottom of the test section, dividing it into twenty-four stations. Stainless steel plates cover two stations to support the frame structure. Remaining stations provide access for control valves. An end frame terminates the downstream side of the framework.

Plug-in modules on each side of the framework enclose the test section and maintain a smooth surface in the axial direction for on the top, side, and bottom walls. Three drop-in test surfaces, tailored for individual experiments, fit into the top of the test section. Continuity between the test surfaces is brought about by inserts that fit under the cross-flanges. The first cross-flange also supports the leading-edge module and the bypass-bleed assembly. An acrylic window sets into each side frame to provide optical access. At the joint between side frames, a bleed manifold removes part of the side-wall boundary layer. Drain plates line the inside of the control wall. An array of manual and RD-valves are attached to the outside of the control wall.

Leading edge. Just upstream of the test surface is a module supporting the leading edge, figure 3.3. A fresh boundary layer is started on the leading edge for laminar and turbulent experiments.

The critical feature the stainless-steel leading edge is its shape: a half-elliptical nose with a major to minor axis ratio of 16:1. The half-ellipse imposes a marginally favorable pressure gradient on the new laminar boundary layer and inhibits the formation of an unpredictable leading-edge separation bubble. At a length of $50.8\,mm$ from the tip, the elliptical curve tangents with a flat surface. This piece was fabricated on a N-C mill and its surface hand-polished to 400 grit.

At the junction between the leading edge and the test surface, figure 3.4, there is a 0.15mm slot for the injection of dye during flow visualization. The edge of the slot forms a backward-facing step of $h < 0.3mm$ with respect to the test surface.

Several factors were considered in the placement of the leading edge. Two reasons for selecting a backward-facing step were:

1. to avoid a forward-facing step which would generate larger perturbations on the laminar boundary layer than the backward-facing step, and

2. to diminish boundary-layer perturbations from dye injection during flow visualization. Consequently a laminar two-dimensional free-shear layer formed at this junction but it also reattached before transition could occur.

Bypass bleed.   Also shown in figure 3.4 is the bypass bleed. The bypass was designed to uniformly extract flow at the inlet to the test section. Hexcel® honeycomb and contractions direct bypass fluid to four manually adjusted valves. Valves are trimmed to give uniform flow across the span. Mass flow rate through the bypass is set such that the stagnation point is on the lower (test surface) side of the leading edge. With the stagnation point at this location, a fresh, laminar boundary layer is generated on the test surface.

Bubble wire / Trip.   Near the leading edge, a mobile wire was installed for the dual purposes of hydrogen-bubble flow visualization and boundary-layer trip. The wire is a crimped piece of 0.13mm diameter stainless steel wire. When energized, dense streams of hydrogen bubbles emit from the crimped wire. The wire can be rotated forward to visualize flow around the leading edge. The wire can also be rotated until it contacts the test surface at a streamwise location of 0.128m. At this location the wire trips the boundary layer for turbulent boundary-layer experiments.

Test surfaces.   Drop-in test surfaces form the top wall of the test section. Together they extend to a 3.0m chord for flat-plate boundary-layer experiments, but individually these are tailored for specific experiments.

33

The laminar boundary-layer test surface, $1.37\,m$ long, is a $19\,mm$ thick sheet of float glass encased in a stainless steel frame. Float glass was chosen to optimize flow visualization. The significantly higher value of Young's modulus for glass meant that structural-support ribs that hinder optical access through acrylic surfaces were unnecessary. Since mechanical access was not needed through the test surface, the brittleness of glass was not a factor.

Downstream test surfaces were fabricated out of $19\,mm$ thick acrylic stiffened by spanwise ribs every $0.23\,m$. The turbulent test surface, $1.37\,m$ long, has two smaller ports for specialized test surfaces. These ports enable rapid change of test configurations. To date these ports have been used for an array of vortex generators, a dye slot, and a heat transfer surface. The exit-section test surface supports a $13\,mm$ float-glass plate at a $15°$ angle to the axis of the tunnel. This glass plate, required for the uniform deflection of flow to the exit valves, also permits optical access upstream through the end of the tunnel.

Optical access through all test surfaces enhanced flow visualization. It also enabled measurement of the spanwise velocity component by passing the LDA beams through the surfaces.

Control wall is perforated for tailoring the freestream. The control wall is parallel to the test surface and $0.13\,m$ away from it. This wall is partitioned into twenty-four $0.15\,m$ intervals along the streamwise direction. A PVC plate is fastened in place over each one of these intervals to provide a reasonably smooth surface for the boundary layer on the control wall.

Flow is bled through the control wall to remove its boundary layer and to locally control the freestream velocity gradient. Each plate is perforated according to the type of freestream control required. For example, at a location where the freestream gradient is nominally zero and stationary, the plate contains two staggered, spanwise rows of $3.2\,mm$ diameter holes for a total open area of $890\,mm^2$, figure $3.5a$. The majority of plates are of this type 1 design. Type 2 plates, figure $3.5b$, are used at locations where a strong streamwise, freestream-velocity is to be imposed.

Each type 2 plate is perforated with nine staggered rows of $6.4\,mm$ holes for a total open area of $21000\,mm^2$. Fluid is withdrawn uniformly across the span through plates of type 1 and 2. Type 2 plates are used to generate a nominally 2-D separation. This experiment used a type 3 plate, which contains a single, centered hole $38.1\,mm$ square. The singular hole concentrates outflow through the control wall in order to impose the local streamwise and spanwise pressure gradients necessary to generate a three-dimensional separation on the test surface.

Flow passing through a plate enters a valve manifold, which smoothly directs the flow to a control valve. For type 1 plates, flow passes through a manual valve into the air purge/drain down system and then into the sump tank. For type 2 and 3 plates, a computer-controlled valve regulates the flow and sends it through a downcomer directly into the sump tank.

Dynamic control of flow. Manual or computer-controlled valves, figure 3.6, control the amount of flow bled through the control wall during stationary and nonstationary flow conditions. Near the exhaust of each valve is a fixed reference pressure of 0 gage which assures consistent operation of the valve. For the computer-controlled valves, 0 gage pressure is set at the orifice. For manual valves, 0 gage occurs $0.3\,m$ downstream from the valve at the junction with the air-purge/drain-down system. Computer-controlled valves will be described more fully in section 3.3.

Side frames and windows. Eight stainless-steel side frames provide the structural support for each side of the tunnel. Each side frame is $0.46\,m$ long and $0.24\,m$ deep. Adjoining frames interlock to form a slot for side-wall bleed. Precision craftsmanship of the side frames ensured that the cross-sectional area of the tunnel deviates at most by $\pm0.07\%$ between $0.46\,m$ sections. A row of windows set into side frames of the test section to form a smooth surface for the side-wall boundary layer.

Side windows, of $25\,mm$ acrylic, provide abundant optical access for two-component velocity measurements and flow visualization. Each window has an unobstructed optical area of $0.39\,m$ long by $0.17\,m$ deep. Since the unobstructed area

extends past the edges of the test-surface and control-wall planes, near-wall measurements by the LDA are possible. The joint between frames causes a 64mm optical obstruction in the streamwise direction.

Side windows are fastened around their perimeter to the side frames. Since side windows are sealed to frames via O-rings, ide windows furnish the quickest access to the interior of the tunnel for cleaning or for exchanging other modules.

Side wall bleeds. At the joint between sections, a side-wall bleed slot removes the inner layer of the side-wall boundary layer. The 0.25mm wide slot extends over the 0.15m depth of the tunnel, intersecting both test-surface and control-wall planes, in order to affect the entire side-wall boundary layer. Bleed flow turns 45° as it enters the slot. The slot is canted 45° with respect to the tunnel axis and the slot edges are rounded to inhibit separation of the side-wall boundary layer at the slot inlet. Bleed flow passes into a small manifold where it is uniformly turned toward a regulating valve, which governs the mass flowrate through the side bleed.

3.2.2 Special Subsystems for quality control

Three subsystems gave control over the quality of the flow. These maintained the integrity of experimental results by compensating for environmental changes and for corruption of the working fluid.

Temperature control. A dedicated water chiller and temperature controller tightly held the temperature of tunnel water at 17.0±0.1°C throughout these experiments. There are several reasons for chilling the water. The first is to fix fluid properties, such as viscosity and density, during extended phase-averaged profiles. Secondly, the growth of algae was inhibited. Thirdly, the entire facility leaks far less at lower temperatures.

Failure of the former temperature control system required that a new temperature controller and water chiller be installed. The replacement chiller is a 5 ton Carrier® 38EH060 Compressor with a 09WQ060 Heat Exchanger. It more closely matches our standard load than the former 10 ton Trane® unit. The temperature

controller, Omega® CN 9000, senses the temperature in the tunnel exit section via a RTD thermistor. The temperature controller operates in PID mode for more intelligent control than the former thermostat. When the target temperature is reached, the controller switches a solenoid valve to direct 50% of the fluid from the heat exchanger through a bypass loop, decreasing the thermal load on the compressor.

Air-purge/Drain-down system. This system serves two purposes, one to expedite data-readiness of the tunnel and the second for quality control of all data runs. As air purge, the system forces air trapped in low-velocity, opposite- and side-wall boundary-layer control assemblies into the test section where it can easily be removed. The entire test section can then be free of air bubbles within two hours. As drain down, the pipe provides an outlet for fluid withdrawn through control- and side-wall assemblies. The system sets atmospheric pressure at the exit for these assemblies. Atmospheric pressure is set in the pipe by venting one of the ports to the atmosphere. The pipe conveys exhaust fluid directly to the sump.

De-aeration. Water returning to the sump is violently and effectively aerated at the air/water interface. In order to prevent microbubbles at the test surface, it is necessary to continually remove air and dissolved air from the water. To do this, flow (about $4 gpm$) is bled from the pipe that feeds the overhead tank. The water cavitates at a venturi and the bubbles accumulate in a centrifugal separator held at $25 inHg$ vacuum. At the bottom of the settling chamber a pipe removes the de-aerated water. A pump boosts the fluid pressure and returns it to the pipe which feeds the main and chiller pump.

3.3 Valve design and control

A custom valve was designed for accurate control of the transient pressure gradient. The design was mandated after a fruitless search for a computer-controllable, fast-response, large-flowrate water valve. The resulting product is a revolving-disc gate valve (RD-valve) as shown in figure 3.2. The primary design feature is a

slotted stainless-steel sprocket that revolves atop a slotted Delrin® bearing/seal. Open area of the valve corresponds to the overlap of these respective slots. The principle is similar to that of Kraft® grated-cheese containers.

3.3.1 Valve Specifications

Valve specifications are:

- a maximum pressure drop, ΔP, of approximately $3psi$ or $1/5atm$.

- a variable-capacity flowrate up to $240gpm$.

- fast dynamic response in order to follow waveforms as demanding as square waves at frequencies of up to $10Hz$.

- precise position control for computer-generated waveforms.

- leak tight when fully closed is desirable but not essential.

- durability for tens of thousands of repetitions during datasets that extend for weeks.

- one dimension that does not exceed $0.15m$ so that it can fit in neighboring streamwise stations along the control wall.

- reasonable cost, since several valves were needed at one time.

3.3.2 Description of the revolving-disc valve   The RD-valve,

shown in figure 3.7 minus its housing, measures $18in$ spanning the tunnel $\times$ $5.75in$ for each streamwise segment $\times$ $10in$ high. The low-pressure-drop specification meant that a durable valve housing could be fabricated from plastic instead of metal. The RD-valve weighs about $25lb$ so it can be reasonably handled by a single graduate student during installation or repair; the brawn of two students is preferred. Fabrication of these custom valves cost about $1000; the cost of the drive system doubled the cost to a total of $2000.

Valve capacity at low pressure drop. The RD-valve exists in two versions, one for coarse variation of the flow and one for finer variation. The only difference between the versions is the area of the slot cut through the $4in$ revolving sprocket (hereafter

"disc"). The requirement of a large flowrate at a low pressure drop necessitated a large open area of the valve orifice in the coarse version. The coarse RD-valve disc has a slot area of $4.64in^2 = 0.00300m^2$. The fine RD-valve disc has a slot area of $1.29in^2 = 0.000833m^2$.

Two types of valve coefficients will be given for the revolving-disk valve: the discharge coefficient C_d, which is familiar to mechanical engineering academics; and the valve coefficient C_v, which is familiar to valve manufacturers.

The discharge coefficient is defined by the equation $C_d(\alpha) = \dot{Q}_{actual}/\dot{Q}_{ideal}$. The numerator is determined experimentally. Figure 3.8 shows the volume flowrate for coarse and fine RD-valves versus open angle. Both valves show a linear $\dot{Q}_{actual}(\alpha)$. The denominator is given by the formula $\dot{Q}_{ideal}(\alpha) = A(\alpha)\sqrt{\Delta P/\rho}$. Since $A(\alpha)$ is also linear, C_d is simply the ratio of the slopes. Thus $C_d = 0.80$ for the coarse valve and $C_d = 0.83$ for the fine valve. These values for C_d values are within the range typical for orifices.

The valve coefficient is defined by the equation $C_v = \dot{Q}\sqrt{S.G./\Delta P}$ and has units $[gpm/psi^{1/2}]$. The coarse valve has a maximum $C_v = 550$ and the fine valve a maximum $C_v = 160$. For the sake of comparison, a generic $4in$ valve has $C_v \sim 200$.

Computer control. The open position of an RD-valve is set by computer control to any one of 256 increments between closed and full open. Valve position is varied over time to create waveforms of suction for control of the freestream velocity gradient. Sine, triangle, and square waveforms are preprogrammed with interactive adjustment of the amplitude, offset, phase delay, and period of the waveform. Arbitrary waveforms can also be programmed.

In the hybrid control scheme, a dedicated IBM® PC delivered open-loop position commands to closed-loop analog control systems at each valve. A Scientific Solutions, Inc.® Lab Tender board provided communication between PC and the custom analog control box. The computer monitored the status of all valves through this board. The analog control loop determined valve position *via* a rotary,

39

variable-displacement transducer and used this information to close the loop. The result was a wide-bandwidth (fast) control system that gave precise position control necessary for repeatable datasets. Power is only required to change valve position; no power is required to hold a fixed valve position. Circuitry and software to drive the valves were designed by A. B. Carlson, a fellow graduate student. Further details of the flexible hardware/software interface are given by Carlson (1990).

Fast-response. A fast dynamic response meant that the number of moving parts in the valve should be kept to a minimum and that the analog control system must possess substantial power. The valve had only four moving parts: the slotted stainless-steel disc, the drive sprocket, one belt and a pump seal. Motion of the sprockets and pump seal was rotary. Except for the zero-backlash belt, each moving part was symmetrical about its axis of rotation to reduce vibration.

The analog control system contained three main components. High torques were provided by printed-circuit motors by PMI Motors®, of Kollmorgen Corp., model number U12M4H. These flat *dc motors* can sustain continuous torques of 220*oz-in*, and pulse torques of 2300*oz-in*. A Sorensen® DCR 40-125A Power Supply empowered the motors. Rotary variable-displacement transducers (RVDT), model 23330, by Pickering and Co.®, sensed shaft position for analog feedback.

The valve was tested under load. It responded without distortion to waveforms as severe as a 40*Hz* square wave, full closed to full open.

There was one commercial valve that had the same response time and capacity as the RD-valve. It is manufactured by the Digital Valve Company®. This valve, however, was over-designed, oversized, and overpriced for this application—it would handle pressure drops of 300*psi*, weighed one ton, and cost $50K.

Benefits of Linearity. By design the open area of the valve, A, was a linear function of open angle, α. If the RD-valve had a discharge capacity that was not a linear function of the open angle, waveform corrections could have been implemented in software. Since the valve discharge coefficient, C_d, was constant, no software correction was required.

40

3.4 Velocity Measurement Systems

Two Laser Doppler Anemometer (LDA) systems operated concurrently during data acquisition. One LDA was stationed at the entrance to the test section to measure the inlet velocity . Downstream, the second LDA measured the velocity field of the separated flow.

Dantek HeNe LDA. A one-color, one-component, $5mW$ HeNe LDA system operating in forward-scatter, tracking mode was used to set and monitor the inlet freestream velocity. The laser, transmitting optics, and receiving optics were all affixed to a custom yoke which rested on the tunnel frame. The ₋DA and yoke assembly had no provision for automatic traversing, but could be positioned manually anywhere along the tunnel.

TSI two-color LDA. A special LDA built up chiefly from TSI components was used to make simultaneous u- and v-velocity measurements. The beam from a $4W$ Lexel model 95 Argon-ion laser was folded through the LDA breadboard. A dichroic color separator split the beam into green and blue beams. The blue beam ($488nm$), or reserve for the w-component, was discarded. The green beam ($514.5nm$) was split into three beams: a $40MHz$ Bragg-shifted beam for the u-component, a $38MHz$ Bragg-shifted beam for the v-component, and a nonshifted reference beam. A TSI 9186A mixer supplied the Bragg signal for the u-component. An IntraAction ME-42 light-modulator signal processor drove an IntraAction AOM-40T acousto-optic light modulator for the $38MHz$ v-component Bragg shift. Beams were Bragg-shifted in order that reversed flow can be measured; two shift frequencies were chosen in order that the two velocity signals could be distinguished in later processing. The beams passed through a beam expanded so that the beam waists would narrow when focused. Transmitting optics folded the expanded beams towards the test section and a $480mm$ lens focused the beams into a LDA measuring volume.

Light scattered from the LDA measuring volume was picked up in forward-scattering mode by the receiving optics. A $200\mu m$ pinhole in the field-stop system

blocked out extraneous light signals. A color separator split the remaining light; green carried the signals for u- and v-components; blue was ignored because it had been set aside for the w-component. Finally a photomultiplier (PMT) converted the light signal to a electrical signal for further processing.

The electrical signal was then processed as follows. The output from the PMT was delivered to two TSI 9186A downmixers. One of the downmixers subtracted off $40MHz$ with a $200kHz$ offset to give the downmixed u-signal. The other downmixer subtracted off $38MHz$ with a $200kHz$ offset to give the downmixed v-signal. Each downmixed signal was processed by a band-pass filter with cutoffs at $50kHz$ and $600kHz$ before entering its respective TSI 1090 tracker. Of most importance was the removal of an extraneous $2MHz$ signal which resulted from the interaction of the $38MHz$ Bragg shift for the v-channel with the $40MHz$ Bragg shift for the u-channel. Each tracker converted the frequency of the processed signal into a DC voltage. An A/D converter performed the final signal processing for the data-acquisition system.

The TSI LDA is mounted on a traverse that permits movement of the measuring volume in all spatial directions. Motion normal to the test surface, the y-direction, is automated for velocity surveys, which can continue for days without intervention. Receiving optics tracked the LDA measuring volume by traversing the y-direction concurrently with the transmitting optics. The whole LDA system moved together during manual traverses in the x- and z-directions. Detailed descriptions of the LDA and traverse system for two-color, two- and three-component velocity measurements are given by Brereton & Reynolds (1986) and Humphreys & Reynolds (1988). Humphreys & Reynolds (1988) also gives a helpful and detailed procedure for selecting the pinhole size of the field-stop system.

Although Humphreys configured this LDA for measurement of all three velocity components, the w-component was not measured for two reasons:

1. most nonstationary, phase-averaged data was acquired on the centerline of the tunnel where w is negligible, and

2. substantial time is invested in realigning three-component optics whenever the LDA is manually traversed. Documentation of the three-dimensional flowfield required frequent manual traverses. The procedure for setting up the LDA and its accompanying signal-processing equipment is described in detail in Appendix B.

3.5 Computer-controlled data acquisition and processing

A dedicated $10\,MHz$ AST® Premium 286 personal computer controlled data acquisition and y-traverses of the two-component LDA. Output signals from the two trackers were brought into two channels of the A/D converter. A Scientific Solutions, Inc.® Lab Master board, model TM-40-PGH, provided programmable-gain A/D processing. When triggered, the two channels were sampled sequentially within a period of 50 microseconds rather than simultaneously *via* sample/hold.

Two trigger lines between acquisition PC and the valve-control PC maintained *synchronization between the two computers during data acquisition*. The *valve*-control PC triggered one line to give the zero-phase reference. It also triggered the second line at every phase to maintain phase-synchronization.

Further details of the data-acquisition subsystem are given by Carlson (1990). Menu-driven software for both data acquisition and valve control, originally written by A.B. Carlson, was enhanced by the principal author.

For this experiment sample size varied depending on the manner that data was processed. Time-averages were derived from 20,000 samples collected at $200\,Hz$. Phase-averages, partitioned into 512 distinct phases, were derived from 200 realizations (or cycles). Nonaveraged data was collected for post-processing of power spectra and also for validating the convergence of velocity averages. When phase-averaging 200 cycles, phase-mean velocities $\langle u \rangle$ and $\langle v \rangle$ converged to within 2%, while double-product terms converged to within 15%.

3.6 Summary

The Stanford, Unsteady Boundary Layer, Research Water Tunnel has many special features which suit it for quality nonstationary boundary-layer experiments. It's capabilities have been improved through redesign and replacement of the test section and computer-controlled valves. This chapter has described the facility and other experimental tools used for this investigation in unsteady, three-dimensional separation. The next chapter will discuss the mathematical tools used for the reduction and analysis of data collected.

Details of the documentation of this facility will be given in chapter 5.

Chapter 4

Equations and Approximations

This chapter describes the mathematical tools—equations, approximations, and methods—that guide the analysis of data acquired. In section 4.1, the techniques of time- and phase-averaging will be discussed. The following section examines the stationary flowfield for the geometry and boundary conditions of this experiment by potential-flow analysis. Finally, section 4.3 validates integral parameters for the boundary layer during the adverse flow conditions that produced separation. New definitions for integral parameters that rely on the potential-flow analysis are proposed. Chapters 5 and 6 will present integral parameters for time- and phase-averaged u-velocity profiles that were calculated according to these new definitions.

4.1 Velocity decompositions

Since it is not possible to measure the entire three-dimensional flowfield simultaneously, averaging techniques must be implemented for the acquisition and analysis of data.

For steady initial and boundary conditions, standard practice decomposes the velocity measurement into a time-averaged mean and an instantaneous fluctuating component

$$u = U + u'. \tag{4.1}$$

For forced unsteady flow, an appropriate averaging technique follows the phase- or ensemble-averaging derivations developed by Hussain and Reynolds (1970). For example, in cases of periodic forcing of flow about a mean, there is the triple decomposition

$$u = U + \tilde{u} + u'. \tag{4.2}$$

The new term $\tilde{u}$ is the deviation from the time-mean velocity at each phase. Many repetitions of the forced waveform cycle are required to establish representative values at each phase. Phase- or ensemble-averaging supplies $U + \tilde{u} = \langle u \rangle$ and u' directly. The u' term, however, assimilates cycle-to-cycle variations as well as instantaneous fluctuations. In practice, the U term is derived from a average of the ensemble averages and then subtracted out to obtain $\tilde{u}$ at each phase. Brereton and Reynolds (1987) give an extensive derivation of the equations resulting from the triple decomposition.

For this experiment the forcing is a long-period square wave which forces the flow to alternate between two states: one at zero pressure gradient, the other at a fixed, adverse freestream-velocity gradient. Thus, the time-averaged mean, U, loses usefulness altogether. Instead a double decomposition

$$u = \langle u \rangle + u', \tag{4.3}$$

where $\langle u \rangle$ denotes phase-mean velocity, is most appropriate. As in the triple decomposition, instantaneous fluctuations and cycle-to-cycle variations are both absorbed in u' terms.

For this experiment, time-averages were formed from accumulations of 20,000 samples. Phase-averages were formed from 200 realizations, where the cycle of each realization was partitioned into 512 distinct phases.

4.2 Potential-Flow Analysis

Potential-flow analysis provides a useful estimate of the irrotational freestream flowfield that results from the geometry of this experiment and the velocity gradient generated at the control wall. The freestream is found to be a three-dimensional velocity field $U_{pot} = G(x, y, z, U_0, S)$, rather than be a uniform velocity.

Potential-flow estimates were constructed by analyzing a simplified flow without walls and then by reflecting images to generate walls. First, analytic functions were found for for the u-, v-, and w-velocity components due to a finite-area square sink

embedded in a uniform velocity flow of infinite extent. Then, symmetrical sets of image flowfields were reflected until the relative velocity correction was less than $10^{-4} U_0$. Up to several thousand images were required to adequately resolve the test-surface and side walls of the tunnel. Details of this analysis are given in appendix C. An example of the estimated pressure-field $C_p(x, z)$ on the test surface is shown in figure 4.1 for the base case flow.

The utility of the potential-flow analysis was extended by finding a function that locally fits the velocity field. In appendix C it is shown that on the centerline, the polynomial $g(y) = C_0 + C_2 \cdot y^2$ fits U_{pot} to within 1%, where C_0 and C_2 are functions of (x, U_0, S).

The most significant problem limiting a potential-flow analysis is that blockage due to boundary-layers has been neglected. Separated boundary layers cause even greater blockage. For most of the flow cases investigated in this experiment, blockage apparently did not cause significant error. Figure 4.2 confirms the excellent fit of $g(y)$ to the outer six points of a velocity profile of the separated flow.

4.3 Integral representations of boundary layers

Integral parameters give a general view of the local boundary layer and provide good comparison with other research. The displacement thickness δ^*, a statement of the steady-flow, mass-conservation equation, marks an equivalent displacement of the potential freestream flow. The momentum thickness θ is often used for the correlation of data.

Standard definitions for the integral parameters assume a uniform velocity field at velocity U_∞ some finite distance normal to the test surface. The standard equations of displacement thickness δ^*, and momentum thickness, θ, are:

Displacement thickness

$$\delta^*(x, t) = \int_0^\infty \left(1 - \frac{\langle u \rangle}{U_\infty}\right) dy \tag{4.3}$$

47

Momentum thickness

$$\theta(x,t) = \int_0^\infty \frac{\langle u \rangle}{U_\infty} \left(1 - \frac{\langle u \rangle}{U_\infty}\right) dy \quad . \tag{4.4}$$

The shape factor is derived from the above parameters, $H = \delta^*/\theta$, and commonly indicates the health or robustness of the boundary layer. In many circumstances, a "healthy" or "robust" boundary layer has a low H indicating one that is not separated nor is prone to separate: for laminar boundary layers, $H_{sep} \approx 3.7$; for turbulent boundary layers, H_{sep} ranges from 1.8 to 2.4 (Cebeci and Bradshaw, 1977). A related parameter

$$h = \frac{H-1}{H} = \frac{\delta^* - \theta}{\delta^*} \quad , \tag{4.5}$$

developed by Kline, *et al.* (1983), correlates unsteady turbulent detachment well. This parameter also avoids such degeneracies as H becoming infinite.

4.3.1 Redefining integral parameters

In section 4.2 it was shown that the freestream velocity field $U_{pot} = g(x, y, z, U_0, S)$ was three-dimensional instead of uniform. Consequently, there is no uniform reference velocity to substitute into the standard integral equations listed above. It became necessary to revise the definitions of the integral parameters in terms of U_{pot}. New equations for integral parameters were derived by (1) returning to the principles used to obtain the original equations for a uniform velocity field, and (2) applying these principles to the potential velocity field. Spalart (1990) proposed a set of definitions for integral parameters based on vorticity. His definitions are conceptually superior to the definitions proposed here but impractical for experiments, since experimental vorticity estimates are error-prone.

Definitions for integral parameters are complicated by skewing of boundary layers in three-dimensional flow. This complication has been avoided altogether by confining analysis to the centerline of the channel where the w-velocity component is negligible. The defining equations are simplified further by the use of the polynomial $g(y) = C_0 + C_2 y^2$ for the potential velocity profile.

New equations for the integral parameters are:

Displacement thickness

$$C_0\delta^* + \frac{C_2}{3}\delta^{*3} = \int_0^\infty \Big(g - \langle u \rangle\Big)dy \tag{4.6}$$

Momentum thickness

$$C_0^2\theta + \frac{2C_0C_2}{3}\theta^3 + \frac{C_2^2}{5}\theta^5 = \int_0^\infty \langle u \rangle\Big(g - \langle u \rangle\Big)dy \tag{4.7}$$

The cubic and quintic equations were easily solved using a classic root-finding routine. Rules that selected the answer from all the roots found are:

1. δ^* and θ must real valued.

2. $0 < \delta^* < 2\delta_{99}$, and   (4.8)

3. $|\theta| < \delta^*$.

4.3.2 Search for the upper limit

The main impediment to integrating experimental boundary-layer data is determining a satisfactory upper limit, *i.e.* the interface between the viscous boundary layer and the potential freestream; the lower limit is the wall. For this experiment, the problem is further complicated due to the three-dimensional U_{pot}. Incidentally, this search corresponds to finding the border between the Middle and Upper decks as discussed by Smith, *et al.* (1981).

Three candidate algorithms were considered for determining the edge of the boundary layer:

1. Fit outer datapoints of the averaged profile to the analytical potential-flow profile. When an inner datapoint differs markedly from the analytical profile, mark the edge of the profile. Interpolate y's to find y_{99} at $u = 0.99 U_{pot}$.

2. Set $y_\infty = y$ at the U_{max} of the velocity profile.

   At least three problems surfaced with the second approach: (a) Error analysis has shown a relative error of $0.02 \cdot U_0$ in the u-velocity. Consequently the maximum velocity can arbitrarily appear anywhere from the edge of the boundary

layer to the outer edge of the sampling domain for even zero pressure-gradient cases. These outer datapoints are spaced at large Δy's which made large contributions to Simpson's rule integration. The momentum thickness could vary as much as 10% depending on which outer point was selected. (b) When suction is imposed, there is always a question as to which datapoint best represents U_∞. For velocity profiles upstream of the suction port, the velocity u increases monotonically with y. For velocity profiles downstream of the suction port, strong spanwise vortices induce peak velocities within the boundary layer and not necessarily at its edge. (c) The edge of the boundary layer may not coincide exactly with one of the datapoints.

3. Fit the whole profile to one of the standard boundary-layer approximation formulas. This approach was abandoned because the standard formulas apply to steady, two-dimensional boundary layers and do not attempt to model the separated zone. Figure 4.2 displays the displacement-thickness areas to be integrated as identified by algorithms (1) and (2). The irrotational freestream profile is given by the curve $g(y)$ which divides the light and dark gray regions. Clearly, algorithm (1) detects the departure of the boundary layer from the freestream profile better than algorithm (2). Figure 4.3 shows how algorithms (1) and (2) compare for the calculation of θ over time at a point within the developing separation, ($x = $ LP:1, $z = 0$, flow Case 10).

The two algorithms also generate different estimates for U_∞. The estimate for U_∞ from algorithm (1) is the coefficient C_0. From algorithm (2) $U_\infty = U_{max}$. Figure 4.4 shows the estimates of U_∞ by these two schemes. It is interesting to compare the estimates during the zero pressure-gradient conditions, *i.e.* from $t = $ -4s to 0s. Algorithm (1) determines $U_\infty = 0.2156 m/s \pm 0.0006$ whereas algorithm (2) determines $U_{max} = 0.2170 \pm 0.0011$.

Algorithm (1) was chosen and used exclusively for integrating boundary layers in this report. The upper limit for the integrals in equations 4.6 and 4.7 is now $y = \delta_{99}$ instead of $y \to \infty$. For the sake of reference, Table 4.1 presents integral

parameters for the Blasius, zero pressure-gradient, velocity profile for both upper limits.

4.3.3 Search for the lower limit

The lower limit for the integral parameters is the test-surface wall. The location of the wall had to be estimated *via* an offset y_{wall}, however, because the zero reference on the LDA traverse mechanism did not correspond to the true location of the wall.

Determining y_{wall} was a three step process. The first step entailed the initial positioning of the LDA measuring volume during run time. The LDA measuring volume was traversed towards the wall until it upon the wall, at which point the LDA tracker would saturate. The measuring volume was then traversed $75 \times 10^{-6} m$ away from the wall and the traverse reference point reset to zero. The second step was the acquisition of a 40-point velocity profile for one of the U_0 at zero pressure-gradient conditions. For the third step, a series of linear regressions would then be made from the near-wall datapoints and the smallest y_{wall} that satisfied $0 \leq y_{wall} \leq 75 \times 10^{-6} m$ would be selected.

A linear regression was found to be the optimal fit for the experimental, near-wall datapoints of a laminar, zero pressure-gradient, boundary-layer profile, $U(y)$. A polynomial expansion of the Blasius, self-similar differential equation for the profile gives the formula $p(y) = Cy - (C^2/48)y^4 + \ldots \approx U(y)$. The linear term is more significant (according to theory) and more robust (according to experience) than the higher-order terms.

4.4 Summary

This chapter has spelled out the mathematical techniques and approximations that have been used for the acquisition and analysis of data for this investigation. The first section described the techniques of time- and phase-averaging data. The second section showed that a potential-flow analysis adequately approximated the

freestream flow during adverse velocity-gradient conditions. The final section proposed an set of equations that redefine the integral boundary-layer parameters and justified the methods used to determine the upper and lower limits.

Chapter 5

Experimental Plan

This chapter describes the experimental plan that guided the acquisition of data. Section 5.1 specifies the parameter space and cases chosen for investigation, the measurement stations, and the scales for non-dimensionalization of results. Section 5.2 validates the tunnel flow for stationary, uniform freestream velocity conditions, for stationary, adverse velocity-gradient conditions, and finally for non-stationary conditions. Section 5.3 presents some observations of the time-averaged, stationary, three-dimensional separation and examines, in particular, the growth of the integral parameters.

5.1 Parameter space, measurement stations, and scales

This experimental study focused on three-dimensional flow separation at low Reynolds numbers, where $210 < Re_\theta < 290$ near the separation point. The corresponding chord Reynolds numbers, Re_c, ranged from 7×10^4 to 1.3×10^5. Several parameters had to be chosen in order to narrow the scope of this investigation while sampling a broad parameter space.

One of the key features of this investigation is that a constant inlet velocity was chosen in order to keep initial and boundary conditions well-defined. This investigation, therefore, was able to avoid the complications due to time variations of the leading-edge vorticity that plague much research in unsteady boundary-layer flow.

5.1.1 Flow cases

The parameters that were varied were the inlet flow velocity, U_0, and the freestream velocity gradient, $U_\infty(x, z, t)$, via suction through the control wall. Four inlet velocities, U_0 were chosen and held constant during stationary and nonstationary

cases. The upstream conditions for each of the U_0 are listed in table 5.1a. The values for inlet flowrate in table 5.1a are derived by multiplying the inlet velocity by the cross-sectional area. The values for $\theta_{0P.G}$ and Re_θ are derived from a fit of laminar, zero pressure-gradient theory to 32 velocity profiles listed in table 5.2. The velocity profiles were collected for all four U_0 at several streamwise stations, LP:ப.

Flexibility of the tunnel design offered many options for regulating the free-stream velocity gradient *via* suction through the control wall. The shape of the suction port and the suction flowrate had to be selected. A type-3 plate was installed on the control wall to tailor suction so that a three-dimensional separation could be generated on the test surface (see heading *Control wall...* in subsection 3.2.1). The upstream edge of the square port in the plate was positioned at $x = 0.613m$.

The waveform of the suction strength governs the time-behavior of the suction flowrate. Computer control of the RD-valves guaranteed repeatable suction through the plate. The shape, period, and amplitude S of the suction waveform could all be varied. A square-wave shape was chosen in order to distinguish between the fast and slow responses of the boundary layer to a suddenly-imposed freestream gradient. The square wave had a total period of 20.48s: 10.24s with the suction 'off' to allow a two-dimensional Blasius boundary layer to establish itself on the test surface, and 10.24s with the suction 'on' to complete the evolution to a quasi-steady, three-dimensional separation. Preliminary tests had shown that this period was of adequate but not excessive duration for the chosen U_0.

Table 5.1b lists the six suction strengths, S, that were chosen in addition to a 'no suction,' uniform freestream condition. Case numbers for each U_0 and S are given for later reference. The volume flowrates for each S are obtained from the valve calibration given in section 3.3.2. Suction waveforms during nonstationary conditions are shown in figure 5.1. During stationary, adverse freestream-gradient conditions the suction S is maintained at the volume flowrate for "valve open." In

addition, table 5.1 *b* shows the relation of *S* to percentage of the inlet flow given in table 5.1 *a* and to pressure-gradient estimates from potential-flow analysis.

All (U_0, S) cases were investigated during stationary conditions. Time-averaged velocity profiles were collected along the centerline for all cases. Velocity histories of nonaveraged data were also collected in order to identify non phase-locked phenomena.

The **Base Case** 10, was selected for phase-averaged profiles along the centerline. Case 10 also corresponds to the single case investigated by the direct numerical simulation of Pauley, *et al.* (1988). For this case, the DNS was able to generate a comprehensive dataset unachievable in this experiment. The strength of the experiment over the DNS, however, was that the experiment covered a larger parameter space albeit less thoroughly.

5.1.2 Measurement stations

Seven streamwise stations along the tunnel centerline were chosen for the acquisition of most data. These stations are shown with relation to the tunnel ς metry and Case 10, quasi-steady, separation structure in figure 5.2. Six of these stations correspond to the coordinates where Pauley, *et al.* (1988) reported results and are labeled LP:⊔ accordingly. The sixth station, LP:3 is approximately the location of the mean reattachment node of the Case 10, quasi-steady separation. Measurements at the seventh station LP:4 reveal effects downstream of this node. Phase-averaged velocity profiles at these stations were composed of 28 *y*-points and 512 phases, at $0.04s$ intervals, for dense data in the *y*-spatial and time dimensions.

5.1.3 Selection of Scales

In order to apply the results of this experiment to real world technical flows, the results need to be non-dimensionalized appropriately. Scales for velocity, length, and time were needed. The velocity scale is the upstream velocity U_0. Two length scales were chosen:

1. the *y*-depth of the channel, *H*, because it provides direct comparison with Pauley, *et al.* (1988).

2. the momentum thickness, $\theta_{0P.G.}$ at uniform freestream (approximately zero pressure gradient) conditions. There is one exception where the displacement thickness, $\delta^*_{0P.G.}$ is used, but this is essentially equivalent to length scale (2) multiplied by 2.6.

The momentum thickness, θ, is a particularly apt length scale for separated flows. It is a robust length parameter because it is nearly constant near the point of separation. Furthermore, most integral-approximation methods for boundary layers rely on the momentum thickness.

Three time scales are used:

1. $t_H = H/U_0$,

2. $t_\theta = \theta_{0P.G.}/U_0$, and

3. $T_c = L_S/U_0$. The first two time scales are derived from the ratio of U_0 to each length scale. The third, the convective time, T_c, is defined to be the period of time required for the freestream to travel the length of the separation, L_S. Time-averaged data suggested that for the base case 10, $L_S \approx 0.17 \pm 0.02 m$ from the separation saddle point to the mean reattachment node, so that $T_c \approx 0.8s$. Since $H = 0.129m$, the scale t_H is approximately $3/4 T_c$.

5.2 Facility Validation

Stationary inlet and boundary conditions in the facility are documented from time-averaged velocity measurements. Inlet and boundary conditions during non-stationary forcing are documented from non-averaged and phase-averaged velocity measurements.

5.2.1 Stationary, uniform freestream

The uniform-velocity freestream (essentially zero pressure gradient) was set and confirmed through streamwise velocity profiles collected as the LDA was traversed along the tunnel axis (x-direction). To achieve streamwise uniformity, the inlet velocity $U_0 = 0.214 m/s$ for case 1Z, was selected and the manual control-wall

valves trimmed until the velocity at all streamwise stations fell within $\pm 0.02 U_0$. For the other inlet-velocity cases, a RD-valve at the exit was repositioned to change U_0, but the remaining control-wall valves were not adjusted. Figure 5.3 shows the development of freestream velocity along the centerline for the different inlet-velocity cases. For each case, table 5.3 confirms that freestream velocity is uniform within $\pm 2\%$, which is the error bound for u-velocity.

A second, independent method verified streamwise uniformity for the case 1Z. Forty-point velocity profiles were collected along the centerline and integral boundary-layer parameters computed. The growth of integral boundary-layer parameters were compared against laminar theory, table 5.2 and figure 5.4. The momentum thickness of the Blasius boundary layer grows in the test section at the rate predicted by theory, within $\pm 12\%$, given a virtual leading edge, $X_{le} = -0.2m$.

A negative value for X_{le} implies that the boundary-layer is more developed than would normally be expected for the x-chord location. The negative value was anticipated due to the backward-facing step at the junction between the leading-edge assembly and the test surface. The two-dimensional separation bubble which formed at this junction accelerated the growth of the laminar boundary-layer thicknesses. Consequently, slightly amplified values for integral parameters were calculated for boundary-layer profiles downstream.

The LDA was traversed in the spanwise direction to confirm the spanwise uniformity of the freestream. A plot of the streamwise u-velocity across the span, figure 5.5a, shows that the freestream velocity is uniform within $\pm 0.02 U_0$. Spanwise profiles within the boundary layer, figure 5.5a, also reveal a waviness which result from upstream conditions characteristic to this facility. The waviness was tenacious and repeatable. Several attempts were made to alter the spanwise waviness by cleaning the honeycomb and the screens, but to no avail.

Boundary-layer profiles were collected at different points across the span to confirm spanwise uniformity. The integral parameters of these profiles were evaluated also verified that the momentum thickness of the incoming test boundary layer was uniform to within $\pm ???\%$.

No attempt was made to validate pressure-gradient conditions by pressure measurements. Pressures were not measured chiefly because static pressures cannot be resolved satisfactorily at such low flow velocities. Appendix B gives additional reasons for avoiding the measurement of pressure in this facility.

5.2.2 Stationary, adverse freestream-velocity gradients

Figure 5.5b shows three spanwise profiles of u-velocity during adverse velocity-gradient conditions. For one of the profiles the LDA measuring volume traversed across the freestream. The measuring volume passed through the quiescent part of the separation structure for the other two profiles. The freestream is uniform across the span to within $\pm 0.02 U_0$. Velocities inside the separation are symmetrical about the centerline.

Potential-flow analysis exposes a conspicuous consistency figure throughout the parameter space, (U_0, S), see table 5.1b. Although the maximum, streamwise pressure gradient, $\partial C_p / \partial x$, varies threefold across the parameter space, the ratio of the maximum spanwise to maximum streamwise pressure gradient falls in the range of 9.1% to 10.6%. The spanwise pressure gradient accelerates the freestream flow towards the center of the span.

5.2.3 Validation of the nonstationary freestream

Effects of the nonstationary forcing of the freestream were confined to tunnel flow downstream of measurement station LP:A. Figure 5.6 shows the u-velocity freestream response $vs.$ time at three streamwise locations along the centerline of the tunnel. Freestream flow remained uniform and constant at station LP:A. Hence, significant influence of the nonstationary, adverse pressure gradient was confined to downstream of $x \approx 0.55m$. A distinct square wave is measured at stations LP:D and LP:4. Figure 4.4 shows that at the intermediate station LP:1, the freestream waveform takes noticeably non-square waveform. Figures 5.7 graphically depicts of the freestream gradient $vs.$ time at all centerline measurement stations to give a view of the time-varying freestream gradient.

5.3 Stationary, three-dimensional separation

Stationary, three-dimensional separation was investigated by flow visualization and by time-averaged sampling for all cases listed in table 5.1b. The literature commonly refers to such a time-averaged perspective of flow separation subject to stationary conditions as "steady" separation. Flow visualization revealed that the structure of the separation generated in this tunnel was an Owl-face of the first kind, according to the classification scheme proposed by Perry and Hornung (1984).

Flow visualization also revealed two distinctly unsteady features of the steady separation structure. The most noticeable feature was the periodic roll-up and shedding of vorticity from the detached shear layer. The period of the oscillation during roll-up, roughly $0.7T_c$, will be discussed and quantified more exactly in section 6.3. The second feature was a slowly varying asymmetry of the separated structure. Recall that Perry and Hornung (1984) asserted that symmetrical structures were unstable in three-dimensional separation. This investigation noted that a nearly symmetrical Owl-face structure would typically persist for about 50 T_c after forming before becoming noticeably asymmetrical. The asymmetrical separation would flop from side-to-side with a highly irregular period, sometimes dwelling for several minutes on a side. A definitive period for flopping was never established.

Due to the inherent unsteadiness, time-averaged velocity profiles of the stationary, 3-D separation were collected carefully. The duration of each time-average, $100s$ (or about 130 T_c), was chosen in order to average out greater than 150 periodic-shedding events, but was admittedly inadequate to cancel out effects of asymmetrical unsteadiness. This duration was a compromise made in order to avoid waste of laboratory run time while keeping errors below 5%.

5.3.1 Integral parameters for "steady" separation
Integral parameters were calculated from centerline, velocity profiles for all velocity and suction cases. Figure 5.8 shows boundary-layer growth for the stationary base-case 10. Table 5.4 lists integral and derivative boundary-layer parameters for all

cases of upstream velocity and suction. The table shows the streamwise growth of integral parameters case by case.

Qualitatively, the table of integral parameters indicates that the centerline of a time-averaged, three-dimensional separation can be divided into 5 zones. Zone 1, upstream of separation, sees a small increase in the displacement and momentum thicknesses. In zone 2, the quiescent region of the separation, the displacement thickness increases monotonically with x-location whereas the momentum thickness remains uniform. Near zone 3, where the shear layer begins to roll up, the momentum thickness decreases suddenly to near zero. Shedding of vorticity is most distinguishable at zone 4; correspondingly there is a dramatic increase in momentum thickness with x, while the displacement thickness hardly increases. Zone 5 and further downstream undergoes a decrease in the displacement thickness and momentum thickness as the shear layer re-establishes itself into a turbulent boundary layer.

5.4 Summary

This chapter has described the experimental plan for this investigation. Nineteen adverse velocity-gradient cases in addition to four uniform velocity cases compose the parameter space. A square-wave forcing dissociates fast responses of the boundary layer from slow responses. Upstream flow was held constant during nonstationary as well as stationary tunnel conditions.

Data acquisition focused primarily on flow near the centerline of the tunnel and consequently the centerline of the separation structure. Time-averaged and raw, non-averaged velocity data of the u- and v-components were collected during stationary boundary conditions. Streamwise and spanwise uniformity of the tunnel flow were validated for uniform flow conditions. Spanwise symmetry of tunnel flow was also shown for one adverse velocity-gradient case.

The growth of integral boundary-layer parameters along the centerline of the "steady", 3-D separation was presented. The displacement thickness grows monotonically until downstream of the separation structure. The momentum thickness, however, demonstrates much a more varied growth pattern depending on the zone of the separation. The momentum thickness remained unchanged through the quiescent zone of the separation, decreased significantly as the boundary layer approached the shedding zone, and then grew dramatically until a turbulent boundary layer was re-established.

Chapter 6

Unsteady, Three-dimensional Separation

6.1 Introduc.ion

This chapter presents the observations and analysis of the phase-averaged and non-averaged velocity fields that were acquired in the course of this investigation. Section 6.2 looks at the history of separation development for the base case 10 through phase-averaged velocity profiles in a variety of formats to identify the stages of development. Section 6.3 presents the single most significant contribution from this investigation: that a Strouhal number collapses the frequency of the periodic shedding of vorticity across the parameter space. Section 6.4 identifies the stages of separation decay. Section 6.6 reveals some interesting behavior from the analysis of instantaneous boundary-layer integral parameters. Section 6.5 draws some comparisons and contrasts with the results of Pauley, et al. (1988). Finally, section 6.7 documents a classic, downstream-moving "MRS separation," which has been long sought by proponents of the MRS condition.

Several basic observations were made from the experiment. When an adverse freestream-velocity gradient was impulsively applied and sustained, a three-dimensional separation evolved through four stages until it reached a quasi-steady state. The quasi-steady state flowfield embodied a complex, unsteady, vortical structure known as an Owl-face of the first kind, cf. figure 6.1 with figures 2.5 and 2.8. Vorticity shed periodically from the detached shear layer. When the adverse-pressure gradient was impulsively released, the separation decayed through four stages until a two-dimensional, zero pressure-gradient profile was re-established.

This chapter describes the history of a developing and decaying separation for the base case 10 primarily along the centerline of the separation structure. The phase-averaged velocity database collected in the course of this experiment has been essential for discerning ι .. zones of the structure and the stages of separation

evolution. The presence or absence of particular events during the development and decay of separation are used to distinguish the various zones of the separation structure.

Figure 6.2, a schematic of the quasi-steady separation structure, is useful for the ensuing discussion of the history of separation at various zones. Zone I experiences quiescent, forward, laminar flow at all times. Zone II predominantly experiences quiescent laminar flow, but flow becomes reversed during application of the adverse freestream-velocity gradient and the shear layer detaches from the surface. Zone III sees strongly reversed flow during the first two stages of separation development, which becomes transitory, reversed flow with transition during the latter two stages. Zone IV experiences forward, turbulent flow during the latter two stages of separation development. Zone V is outside the principal separation structure. Fresh fluid from zone V continually feeds into Zones II and III, which make up the separation wake. Measurement stations, with respect to tunnel geometry and the three-dimensional separation, were shown in figure 5.2.

To aid analysis, time- and phase-averaged results have been be shown in a variety of formats. All plots were made using linear joins rather than with cubic fits, except where otherwise noted. This choice was made because cubic spine plots, although attractively smooth, hid the true resolution of data and occasionally added spurious wiggles. A linear join, in contrast, exposed how well or poorly data was resolved in space and time. When time constitutes one axis of a plot, a non-dimensionalized $t^* = t/t_H \approx (4/3)t/T_c$ is used. For the base case 10, $t^* = t \cdot 1.66s^{-1}$.

6.2 Separation development

When the adverse freestream-velocity gradient was impulsively applied and sustained, the developing three-dimensional separation evolved through four distinct stages:

1. the sudden inviscid response,

2. breakaway of the shear layer,

63

3. initiation of large-scale unsteadiness, and finally

4. the quasi-steady state. The duration of each stage can be seen in a plot of the velocity histories at various measurement stations along the centerline, figures 6.3a-d. For example, figure 6.3a shows that at LP:1, the sudden inviscid response lasts from $t^* = 0$ until approximately $t^* = 0.53$; breakaway of the shear layer lasts from $t^* = 0.53$ until approximately $t^* = 7.5$; initiation of large-scale unsteadiness lasts from $t^* = 7.5$ until approximately $t^* = 11$; and quasi-steady state begins at about $t^* = 11$. In the following paragraphs, *important features of each stage will be described more thoroughly.*

Sudden inviscid response (Stage 1). Flow through the entire tunnel responded suddenly when suction was impulsively applied. During this stage, near-wall fluid responded first and reversed flow was detected. The remainder of the tunnel flow rapidly adjusted to the new boundary conditions. The flowfield at the end of this stage can be modeled by taking the base case of a Blasius boundary layer and superimposing the potential flow correction, with an allowance made for no slip at the wall. Since there is reversed flow, a zero shear-stress point must appear and therefore, according to the working definition, separation exists.

Although there is reversed flow at the wall during this stage, significant v-velocities near the wall have not yet appeared. By all appearances the wall-bounded shear layer is still attached. This is the reason that MRS proponents were unwilling to designate the term "separation" for this transient condition. Significant v-velocities will appear during the the breakaway of the shear layer in the next stage.

Breakaway of shear layer (Stage 2). Since the tunnel flow has now matched the new newly-imposed adverse-pressure gradient *via* the sudden inviscid response, the subsequent breakaway of the shear layer from the surface is part of the viscous response. For example, figure 6.3a shows that this stage begins at approximately $t^* = 0.53$ and lasts until $t^* \approx 7.5$ at station LP:1.

The process that takes place during this stage is the displacement of the wall-bounded shear layer at zone II away from the surface as fluid from zones III and IV is convected underneath the shear layer. The fluid sandwiched by the shear layer and the test surface is the separation wake. Figures 6.4a-c show the translation of the shear layer through instantaneous, phase-averaged velocity profiles at several phases; experimental results are shown alongside the results of Pauley, $et\ al.$ (1988). Figures 6.5a-c and 6.6a-c, which display the evolution of the phase-mean $\langle u \rangle$- and $\langle v \rangle$-velocity profiles, show the smooth departure of the shear layer away from the surface for $0.53 < t^* < 7.5$.

Throughout this stage of development, the entire flow is remarkably quiescent. Figures 6.7a-c, 6.8a-c, and 6.9u-c, which display the evolution of the phase-fluctuating $\langle u'u' \rangle$-, $\langle v'v' \rangle$-, and $\langle u'v' \rangle$-profiles, show practically zero fluctuations (at the level of instrument noise) for $t^* < 7.5$. Note: At stations LP:B and LP:D, the double-product profiles were practically zero throughout the period of the waveform, which confirms that zones I and 2 contained quiescent laminar flow.

Inception of large-scale unsteadiness (Stage 3).   At the onset of large-scale unsteadiness, the detached shear layer rolls up and sheds in a dramatic and vigorous fashion, signaling the next stage of separation development. This stage is visible in figures 6.3a-e by the large velocity oscillations during the time period $7.5 < t^* < 11$. The first second and third cycles of this unsteadiness at LP:1, figure 6.3a, dwarf all other cycles.

The passage of spanwise vortices that have shed from the shear layer are responsible for the large-scale unsteadiness. Note that the $\langle u \rangle$-velocity oscillations of near-wall datapoints, $i.e.$ $y/H < 0.040$, are approximately 180° out-of-phase with those of outer datapoints, signaling the passage of spanwise vortices. Furthermore, the $\langle v \rangle$-velocity oscillations are approximately 90° or 270° out-of-phase with $\langle u \rangle$-velocity oscillations; compare figure 6.3e with figure 6.3b. Vector plots of the two velocity components at two measurement stations and two instances in time, figures 6.10a-b, show fluid being thrust out from the wall and towards the wall,

65

respectively. The corresponding $\langle u \rangle$-velocity profiles, also shown in figures 6.10a-b, can become quite corrugated and reveal steep velocity gradients.

This stage begins when the shear-layer instability catches up with the viscous response of stage 2. The phase-mean velocity profiles, figures 6.5b-f and 6.6b-f, alter dramatically and undergo vigorous oscillations during this stage. Concurrently, the double-product $\langle u'u' \rangle$-, $\langle v'v' \rangle$-, and $\langle u'v' \rangle$-profiles, figures 6.7a-c, 6.8a-c, and 6.9a-c, change explosively. By $t^* \approx 11$, large-scale unsteadiness in figures 6.5b-f and 6.6b-f appears to settle down.

Arrival at quasi-steady state (Stage 4). Quasi-steady state arrives at $t^* \approx 11$ and lasts until the end of the cycle, when the adverse freestream-velocity gradient is impulsively released. During this stage, phase-mean $\langle u \rangle$- and $\langle v \rangle$-velocity profiles, shown in figures 6.5a-f and 6.6a-f, each exhibit an almost unchanging profile over time.

A comparison can be made between the quasi-steady state attained during the forced, nonstationary conditions and the time-averaged, "steady," three-dimensional separation shown in figure 5.8. Figure 6.11 shows velocity profiles along the centerline of the tunnel during the quasi-steady state of the nonstationary separation. Each of the velocity profiles in this figure is pseudo-"time-averaged" or "phase-smoothed" by averaging twenty consecutive, phase-mean profiles during $15.8 < t^* \leq 16.7$. The integral boundary-layer parameters, also shown on both plots, also compare well.

The plot of phase-averaged data, figure 6.11, shows a separation that is slightly larger and smoother than the time-averaged plot. The most probable reason is the inherent unsteadiness of the separation structure that is suppressed by nonstationary forcing (for the phase-averaged results) causes irregularities in the time-averaged results. For example, stationary boundary conditions during the collection of time-averaged profiles permitted a slow asymmetric meander of the separation about the centerline. Such behavior was expected since the symmetrical structure

is topologically unstable (Tobak and Peake, 1982). Evidence from flow visualization confirmed that the separation was unsteady and would waver spanwise about the xy-centerplane of symmetry for a stationary adverse freestream-velocity gradient. In contrast, nonstationary forcing used while phase-averaging released the adverse freestream-velocity gradient before the same slow meander became significant.

Although the phase-mean profiles in figures 6.5c-f and 6.6c-f appear steady during quasi-steady state, they conceal a perpetual unsteadiness in the steady-state structure of three-dimensional separation. Unsteadiness was principally characterized by continual periodic shedding of the detached shear layer. An in-depth look at the double-product profiles will shed a little more light on this unsteadiness.

Effects of periodic shedding on the structure of separation. Details of how the unsteadiness affects the structure of separation during quasi-steady state are better understood by considering profile histories of double-product terms. Double-product profiles indicate that in the quiescent zone II, the detached shear layer gently flaps normal to the wall. Further downstream in zone III, the flapping shear layer rolls up into locally spanwise vortices. These vortices shed and pass downstream, vigorously agitating flow near the wall.

To verify that the detached shear layer flaps at LP:1, consider figure 6.7a. After $t^* \approx 11$, the broad $\langle u'u' \rangle$-profile at LP:1 has collapsed to a narrow peak. The narrow peak could be indicative of flapping of the shear layer in the y-direction, of regular vortex roll-up, or of some other unsteady phenomenon. The relative flatness of $\langle v'v' \rangle$- and $\langle u'v' \rangle$-profile plots (figures 6.8a and 6.9a, respectively) convince us of the first explanation. For example, were vortex roll-up the dominant mechanism at LP:1, then the $\langle v'v' \rangle$-profiles should show a peak similar to $\langle u'u' \rangle$ during the quasi-steady state. Instead, flapping of the shear layer at this location resulted in the observed peak in $\langle u'u' \rangle$-profiles and in flat $\langle v'v' \rangle$- and $\langle u'v' \rangle$-profiles.

In contrast, at the downstream location LP:2, the broad peak in the $\langle u'u' \rangle$-profile persists throughout the quasi-steady state. This broad peak also appears

in $\langle v'v' \rangle$ and $\langle u'v' \rangle$ profiles. The consistent peak throughout the double product profiles confirms that at this streamwise location, vigorous activity in the x- and y-directions trades high-velocity fluid in the outer flow with low-velocity fluid that was near the wall. In other words, spanwise vortices pass through streamwise location LP:2. Results from flow visualization had also suggested that the flapping shear layer near LP:1 began to roll up and shed well-defined vortices through LP:2. Since the shed vortices appeared to thrust fluid up into the quiescent zone II, there is probably feedback between the flapping shear layer and the shed vortices.

The technique of phase-averaging this forced, nonstationary flow obscured some of the observable flow physics, such as the periodic shedding mentioned above. This problem was most troublesome for non phase-locked time responses. Section will show that the acceleration of shed vorticity during separation decay was also obscured. Unsteady behavior at these stages in the evolution of separation were studied and quantified *via* non-averaged data collected during stationary conditions or *via* single realizations of the nonstationary event.

6.3 Strouhal number of shed vorticity

One of the salient features of three-dimensional separation is the inherent unsteadiness of the free shear layer. The instability of the free shear layer caused vorticity to roll-up and shed at a characteristic frequency during quasi-steady state. Details of this process were gleaned through the analysis of non-averaged data.

The frequency of shedding was determined for each $U_0 - Suction$ case in the parameter space. Stationary adverse freestream-velocity gradient conditions were set in order to obtain an adequate number of samples to confidently resolve the shedding frequency. A power-spectra algorithm (Press, *et al.*, 1988), implemented an overlapping Parzen window to obtain the smallest error from the fixed number of sampled data points, during the post-processing of non-averaged data.

The Strouhal number of the shedding frequency f was defined

$$St = \frac{f \cdot \theta_0}{U_0} \quad ,$$

68

where U_0 is the upstream velocity and θ_0 is the corresponding momentum thickness during uniform, freestream-velocity gradient conditions. The Strouhal number $St = 0.011 \pm 0.001$ collapses all cases in the parameter space for which a dominant frequency was detected. Figure 6.12a indicates that for a single upstream velocity, U_0, the Strouhal number of shedding frequency, $St = 0.011 \pm 0.001$, is independent of the freestream velocity gradient for cases 00 to 04. Figure 6.12b shows that $St = 0.011 \pm 0.001$ also holds for cases 10 to 14. Figure 6.12c confirms $St = 0.011 \pm 0.001$ for cases 20 to 24. For case 34, $St \approx 0.0116$.

Cases 05, 15, and 25 did not demonstrate a dominant frequency. This indicates that incipient shedding of vorticity from the separated shear layer occurred at the adverse freestream-velocity gradient which corresponds to 7% suction through the port in the control wall, see table 5.1. Incipient shedding may coincide with incipient separation for these laminar cases because of the strong tie between unsteadiness and three-dimensional separation indicated in the literature.

The value for St from the experiment contrasts with the value $St = 0.0143$ reported by Pauley, et al. (1988). Communication with the authors indicated that the DNS value was derived manually from the two oscillations shown in figure 6.13a (figure 4.23a of their report). The most likely source for the difference from the experiment is that two oscillations from the computation do not constitute an adequate sample. Furthermore, although these two oscillations may appear definitive and regular, the subsequent oscillation differs markedly. Had a FFT been used to determine the shedding frequency from the two DNS oscillations, the finest frequency interval is about $0.5 Hz$ which corresponds to a Strouhal number resolution of ± 0.002. In contrast, experimental results were obtained using a FFT Power Spectrum from N oscillations, where $160 < N < 650$, such that the frequency resolution was $0.1 Hz$.

6.4 Separation decay

When the adverse freestream-velocity gradient was impulsively released, the separation decayed through four stages:

1. the sudden inviscid response,

2. return of vorticity back to the surface,

3. amplification of shed vorticity,

4. the zero pressure-gradient, Blasius boundary layer. Stage 3 occurred concurrently with stage 2, but primarily affected only zone III. The separation decayed more rapidly than it had developed.

The duration of each stage can be seen in a plot of the velocity history at station LP:2, figure 6.14. For example, the sudden inviscid response lasts from $t^* = 0$ until approximately $t^* = 0.53$; return of vorticity to the surface lasts from $t^* = 0.53$ until approximately $t^* = 10$; acceleration of shed vorticity lasts from $t^* = 0.53$ until approximately $t^* = 5$; and zero pressure-gradient conditions are restored at about $t^* = 10$. In the following paragraphs, important features of each stage will be described more thoroughly.

Sudden inviscid response (Stage 1). Flow through the entire tunnel responded suddenly when suction was impulsively released. Reversed flow at the surface disappeared soon after release of the adverse pressure gradient, that is, within $t^* < 0.27$. The remainder of the tunnel flow rapidly adjusted to the new boundary conditions.

According to the working definition the separation technically vanished when the saddle point (zero shear stress) disappeared during the first stage. The remnant of separation wake experienced the later three stages. In contrast to our definition, the MRS definition maintains that the separation instantly became a downstream-moving separation. In any case, subsequent stages of the decay of three-dimensional separation will be described and quantified.

Return of vorticity back to the surface (Stage 2). Under the new boundary conditions, the separation wake, which displaces the shear layer from the surface, can

not be sustained at its fixed location. Figure 6.15 shows the phase-averaged veloc-ity profiles during this stage of separation decay. The vorticity of the shear layer returns to the surface as the remnant of the separation wake is accelerated and convected downstream.

At first, diffusion of vorticity was thought to be the dominating physics during this stage of decay. Tests were therefore made to establish if this were true. Two reasons indicate that the diffusion of vorticity, although present, was not the most significant factor. The first reason arises from an analysis by Watson (1958) that is akin to Stokes first problem: the suddenly accelerated plate. His analysis suggests a time scale, $t_{Watson} = \delta_{99}^2/16\nu$, for the influence of the new boundary conditions to reach the edge of the boundary layer. This time scale exceeds the time ob-served for the Blasius profile to be completely restored by a factor of at least four. The second reason, discovered by a simple analysis, is easily shown heuristically. Consider again figure 6.15. The maximum velocity gradient, $\partial u/\partial y$, is essentially constant during this stage. Had diffusion of vorticity been the dominant process, the gradient $\partial u/\partial y$ should have diminished.

Instead, the separation wake is pushed downstream and the vorticity pushed towards the surface by a slightly favorable pressure gradient [6] that also accelerates the freestream. Acceleration of the freestream to a velocity greater than U_0 during this stage can be seen in figure 6.16. The source of the slight acceleration of the freestream is the blockage caused by the lingering presence of the separation wake.

Concurrent with the return of vorticity back to the surface, but downstream in zone III, a much more vigorous process occurred.

Acceleration/amplification of shed vortices (Stage 3). By the end of stage 1, shear layer vorticity that had begun to roll up now finds itself embedded in a noticeably faster flowfield. The velocity of the local freestream flow, U_∞, first exceeds U_0 and then settles down it, in accordance with the blockage-induced acceleration that was mentioned in the concurrent stage 2. The shed vortices, therefore, accelerate

---

[6] The effect is analogous to shooting a watermelon seed by squeezing it between your fingers.

and amplify as they are convected over the separation wake. The new frequency at which shed vortices pass downstream measuring stations is related to the quasi-steady state shedding frequency by approximately the ratio U_0/U_{ss}, where U_{ss} is the local U_∞ during quasi-steady state. It appeared that four or five vortices were passed during this stage.

This whole process was obscured by phase-averaging the velocity data in figure 6.14 because the passage of these vortices is not phase-locked with the impulsive release of suction. This process is most easily identified in plots of non-averaged raw data of single realizations as in figure 6.17.

Return to a Blasius boundary layer (Stage 4). The Blasius boundary layer is completely re-established by $t^* > 10$.

6.5 Comparison with Direct Numerical Simulation

The simple geometry and known initial conditions and boundary conditions in this experiment facilitated comparison with a direct numerical simulation (DNS). Thus as a companion to this experiment, Pauley, *et al.* (1988) undertook a computational study of the developing and decaying three-dimensional separation for conditions largely the same as base case 10. Since the DNS generated far more comprehensive quantitative results for this case, Pauley, *et al.* (1988) ought to be referred to for details of the global velocity and pressure fields.

A few differences between the experiment and the DNS need to be mentioned. First, it is important to remember that the experimental results are phase-averaged whereas the DNS results come from a single realization. Secondly, the DNS boundary conditions for the sides of the tunnel were set as follows: no-slip conditions on the test surface, periodic conditions on the side walls, and slip conditions on the control wall; the experiment had no-slip conditions everywhere.

Finally, in the experiment the adverse freestream-velocity gradient was also sustained for 40% longer than it was in the DNS. There are three reasons for this. First, since results from the DNS arrived first and it appeared that the separation

was fully developed by $t^* = 12$, it was hard to justify spending any more CRAY® time on the DNS. Secondly, in order to determine when the experimental separation was fully developed, several cycle periods were examined; from this examination a period of "suction on" for $t^* = 17$ was selected as adequate for an unchanging quasi-steady state. Thirdly, a period of "suction off" for $t^* = 17$ was selected because the Blasius boundary layer could re-establish itself throughout the test section at this period and because symmetrical waveforms were preprogrammed in the valve controller.

Figures 6.4, 6.15, and 6.13 present the results of the experiment alongside those of Pauley, *et al.* (1988). Figures 6.4 *a-c* and 6.15 *a-b* show the results on the experiment alongside those of the DNS during the second stage of separation development and decay, respectively. There appears to be excellent agreement between both investigations during these stages. Figures 6.13 *a-b* show a plot from the DNS alongside a version of figure 6.3 *a* that has been re-scaled for direct comparison. Although the results agree well for the time periods for $t^* < 7.5$ and for $t^* > 10$, they differ significantly during the intervening stage of large-scale unsteadiness. The difference may be due to the influence of side-wall boundary layers in the experiment; the DNS instead used periodic boundary conditions on the side walls.

Finally, to recap the result from section 6.3, the experiment found that the shedding frequency for stationary three-dimensional separation satisfied $St = (f \cdot \theta_0)/U_0 \approx 0.011 \pm 0.001$ across the parameter space for which shedding was detected. This value contrasts with the value of $St = 0.0143$ reported by Pauley, *et al.* (1988).

6.6 Integral Parameters in the unsteady, separated boundary layer

Figures 6.18 and 6.19 show the histories of the instantaneous integral parameters for the developing separation. Likewise figures 6.20 and 6.21 show the histories of the instantaneous integral parameters for the decaying separation. These histories have been normalized to the local value for the phase-averaged, uniform-freestream,

velocity profile. No comparison of integral boundary-layer parameters was made with the DNS results because none were reported by Pauley, *et al.* (1988).

Instantaneous values of boundary-layer integral parameters exhibited some unusual behavior during development of the three-dimensional separation. For example, the displacement thickness δ^*, shown in figure 6.18, grew dramatically and at times exceeded the δ_{99} thickness of the boundary layer. In addition, the momentum thickness θ, shown in figure 6.19, became negative at times. The associated estimates of the local U_∞ are shown in figure 6.22. Corresponding to the zero crossings of the momentum thickness, the shape factor, H, became infinite and changed sign, yielding not very useful information. Instead, the more useful relation $h = (H - 1)/H$, given in equation 4.5, is plotted *vs.* δ^*/δ_{99} in figure 6.23. Figure 6.23 shows that the time variation of h deviates erratically from the correlations during stage 3 of separation development at LP:1.

The key to the explanation of these unusual occurrences is a strong upwash of reversed flow inside the boundary layer; a local, downstream-moving, spanwise vortex is one possible culprit. The upwash creates a steep velocity gradient in the boundary layer (*e.g.* figure 6.10*b*): between the steep gradient and the wall flow is reversed, *i.e.* $\langle u \rangle < 0$; outside of the steep gradient, flow is nearly at the freestream value (and may even exceed $\langle U_\infty \rangle$. This combination can easily be shown to result in $\theta < 0$ and $\delta^* > \delta_{99}$.

Although uncommon, these results are not new. Simpson (1985) had reported negative momentum thicknesses in a nonstationary turbulent separation.

Integral parameters for the decaying separation, figures 6.20 and 6.21, exhibited much milder behavior which may be due to the absence of phase-locked unsteadiness.

6.7 The decay of separation and the MRS condition

Recall that due to the sudden absence of reverse flow after stage 1 of separation decay, the saddle point disappears and separation vanishes according to the

working definition. The remnant of sluggish fluid that constituted the separation wake now evolves into a velocity profile which indisputably matches the classical rendering of a downstream-moving "MRS separation" shown in figure 2.3. The velocity of the MRS separation increases from 0 to $0.2U_0$ in the interval from the release of the adverse pressure gradient until $t^* \approx 3$.

Few downstream-moving "MRS separations" have been documented besides this one. Smith and Kline (1971) visualized such a flow in a diffuser undergoing transitory stall. Didden and Ho (1985) documented an interesting relative in the flow associated with a wall-jet vortex.

6.8 Summary

This chapter has described this investigation's observations and analysis into forced, nonstationary, three-dimensional separation. Flow conditions for the base case 10 (see section 5.1) have been examined most thoroughly. Freestream velocity-gradient conditions were changed impulsively in order to distinguish between fast and slow responses of the boundary layer. The developing separation undergoes four stages as it evolves into a quasi-steady state separation. The quasi-steady state separation is characterized by inherent unsteadiness, primarily arising from periodic shedding of the detached shear layer. The frequency of shedding across the parameter space collapsed to a Strouhal number, $St = 0.011$. Integral boundary-layer parameters exhibited unusual behavior during separation development. Specific conclusions are listed in the next and final chapter.

Results from this experiment largely agree with the results of the companion direct numerical simulation by Pauley, *et al.* (1988). Certain differences may be due to slightly different boundary conditions between the investigations. Both efforts have been are early efforts at documenting and quantifying the unsteady flowfield of a nonstationary, three-dimensional separation. Together, these studies have enhanced understanding of nonstationary, three-dimensional separation. Insights

from these programs should assist the modeling of these complex flowfields which are observed throughout nature and technology.

Chapter 7

Conclusions

This experimental study has made several contributions to the fledgling field of unsteady, three-dimensional flow separation. In general, its primary contribution has been to broaden our understanding of the *time behavior* of these flows.

Specific accomplishments:

- The rig has been successfully modified for the study of simple and complex, steady and unsteady, two- and three-dimensional flows. The durability, optical access, modularity, and flexibility of the test section were all improved. The facility successfully survived the 7.0 Loma Priete quake at 5:04p.m. on 17 October 1989.

- Inexpensive, compact, fast, high-capacity valves were designed for computer-control of stationary and nonstationary freestream velocity fields. Linearity of the valve's characteristics facilitated implementation of desired waveforms for freestream forcing.

- A **definition** for laminar separation that applies to two- and three-dimensional, stationary and nonstationary separation has been proposed. The definition of "separation" or "separation region" is a flow structure that consists of a separation line and a separation wake. A "separation line", shown in figure 2.1, is the line that passes through a saddle point on a solid surface. Therefore, there must be a point where $\tau_w = 0$ (or $C_f = 0$) for separation to exist. In order to distinguish from attachment, flow near the saddle point moves away from the wall. The reference frame for this definition is the surface of the solid body. Sluggish fluid downstream of a separation line is a "separation wake".

Conclusions:

1. The above definition of "separation", akin to the original description by Prandtl, is consistent for stationary and nonstationary, two- and three-dimensional separated flows. This definition is closely aligned with Legendre's and is not far removed from Tobak and Peake's. This definition can be easily amended to include stationary, turbulent separation. Controver sies that have arisen over alternative definitions presented in the literature have been resolved because various authors have merely emphasized identical phenomena to differing degrees.

2. When an adverse pressure gradient was impulsively applied and sustained, a three-dimensional separation developed until it reached a quasi-steady state. This separated flowfield embodies a complex, unsteady, vortical structure known as an owl-face of the first kind. When the adverse pressure gradient was impulsively released, the separation decayed until a two-dimensional, zero pressure-gradient profile was restored.

3. The evolution of a three-dimensional separation as it developed or decayed could be divided into four stages. Some zones of the flow structure experienced all of the stages as the separation evolved under impulsively-imposed adverse pressure-gradient conditions.

4. The four stages during separation development are: (i) the sudden inviscid response, (ii) breakaway of the shear layer, (iii) inception of large-scale unsteadiness, and finally (iv) the quasi-steady state. For base case conditions, a quasi-steady separation will have been established by $t^* > 7.5$.

5. The Strouhal number for shedding of vorticity from the quasi-steady owl-face structure is given by the formula, $St = f \cdot \theta_0/U_0 = 0.011 \pm 0.001$. This conflicts with the conclusions of Pauley, et al. (1988).

6. Distinctive frequencies for vorticity shed from 3-D separation were detected for suction strengths down to about 7%. This is considerably less than the value of 12% for 2-D separation as determined by Pauley, et al. (1988).

7. The four stages of separation decay are: (*i*) the sudden inviscid response, (*ii*) return of vorticity back to the surface, concurrent with (*iii*) amplification of shed vorticity, and (*iv*) the Blasius boundary layer. According to our definition the separation technically vanished when the point of zero shear stress disappeared during the first stage. Only the unsteady zone of the separation wake experienced stage (*iii*). The separation wake decayed more rapidly than the separation had developed.

8. The decay of the separation wake is equivalent to a "downstream-moving separation" as defined by proponents of the MRS condition. Taking the view of the MRS condition, separation decay is the process in which sluggish fluid within the separation is continually sheared until a Blasius profile is attained.

9. This experiment documented a classic, downstream-moving MRS separation profile and its associated velocity. The MRS velocity of the downstream-moving separation increased from 0 to $0.2U_0$ during the interval $0 \le t^* < 2$ of separation decay.

10. Calculations of integral boundary-layer parameters were reasonably redefined and calculated by asymptotic matching of the potential flow velocity profiles with experimental data. It was observed at certain instances in the developing separation that the displacement thickness, δ^*, could exceed δ_{99} and that the momentum thickness, θ, could become negative. Such behavior for the instantaneous values of displacement and momentum thicknesses are justifiable and have been discussed in the literature.

11. Phase-averaging of the velocity fields of forced, unsteady flows causes some of the observable physics to be obscured. This problem was most troublesome for non phase-locked time responses. Consequently, during the stage of quasi-steady separation, there was the appearance of steady separation, and during separation decay the acceleration of shed vorticity was concealed. Unsteady behavior at these stages in the evolution of separation were quantified *via* non-averaged data collected from single realizations of the nonstationary event.

12. This experiment underscores the conclusions that inviscid and convective time scales dominate the separation process for this experiment. The importance of convective terms has been inferred from several papers in the literature.

13. The size of the separation was observed but not quantified. As suction increased, the spanwise extent of separation increased. The length of the shear layer from separation to roll-up appeared to remain constant.

Suggestions for future research:

• Develop a flow visualization technique to determine spanwise extent/size of separation at different flow conditions.

• Repeat the experiment for different geometries of suction holes. Broaden range of flow parameters, especially Re_θ. Study multiple structures, like those seen by Winkelmann.

• Determine a pressure-gradient criterion for (i) incipient three-dimensional separation and for (ii) the onset of shedding. Check if $P_{max} = -0.24$ for the onset of shedding.

• Collect histograms of non phase-averaged data to evaluate velocity behavior within the separated zone.

• Extract more information from the DNS by Pauley, et $al.$ (1988). There is considerable interest regarding the contours of v_{max} and of integral parameters for comparison with van Dommelen and Cowley (1990). The comprehensive results from the DNS may verify or invalidate the assertions by van Dommelen and Cowley.

• Investigate if the growth of separation and the ejection of vorticity away from the wall corresponds to the bursting process of a turbulent boundary layer.

• Examine tools from control-theory system identification to assess whether these can be implemented to describe the time-behavior of separation.

Appendix A

Glossary

Boundary-layer profile refers to a collection of velocities obtained by traversing the LDA measuring volume only in the y-direction (normal).

Breakaway of a wall-bounded shear layer requires a significant component of velocity normal to the surface. Advocates of the MRS condition contend that breakaway equals separation and that the MRS condition identifies breakaway. Of these, Van Dommelen and Cowley (1990) have convincingly identified the singularity at breakaway.

One **convective time**, T_c, is the period of time required for the freestream flow to travel the length of the separation, L_S.

Direct Numerical Simulation (DNS) solves the time-dependent, three-dimensional, Navier-Stokes equations without the imposition of a model. The comprehensive, quantitative results generated by DNS show the evolution of all significant scales of motion.

Double-product terms for time-averaged data (see "fluctuating") are equal to the variances of instantaneous velocity fluctuations about the time-mean value: $\overline{u'u'}$ is the variance of the mean u-velocity; $\overline{u'u'}$ is the variance of v, and $\overline{u'v'}$ is the cross-variance. For phase-averaged data (see "phase-fluctuation") the **double-product** terms, $\langle u'u' \rangle$, $\langle v'v' \rangle$, and $\langle u'v' \rangle$, assimilate cycle-to-cycle variations as well as instantaneous fluctuations.

The **displacement thickness**, δ^*, is an integral boundary-layer parameter related to the steady-flow, mass-conservation equation. It marks an equivalent displacement of the potential freestream flow from a surface. The standard and modified equations for δ^* are given in section 4.3.

Fluctuating is a catchall for random unsteadiness and or other effects which were not identified as organized unsteadiness.

A focus, figure 2.1, is a node where the skin-friction lines spiral into or away from the node. A "saddle point" is common to only two skin-friction lines.

An isolated line of convergence (LOC) is used to describe a pattern of skin-friction lines, such as in figure 2.6, which converge to an asymptote without the presence of a singular point. This pattern does not fit the working definition of separation, which requires the presence of a saddle point.

Local Separation is the term for an "isolated line of convergence" used by some researchers, *e.g.* Tobak and Peake (1982).

The **momentum thickness**, θ, is an integral boundary-layer parameter often used for the correlation of data. It is an important element of the steady-flow, *momentum-integral* equation of von Kármán (see Schlichting, 1979).

MRS separation refers to the definition of separation according to the proponents of the MRS condition. This term is equivalent to "breakaway," which is the preferred for the sake of consistency in this paper.

Negative bifurcation is the terminology used by Hornung and Perry (1984) to describe an "isolated line of convergence." Their schematic is shown in figure 2.7. The term connotes that multiple lines become one. Topologically, this term is misleading because converging skin-friction lines can only asymptote to the LOC.

A node, figure 2.1, is singular point common to an infinite number of skin-friction lines.

Nonstationary will be used for time-variable initial and/or boundary conditions.

Open Separation is the term for an "isolated line of convergence" used by some researchers, *e.g.* Wang (1974).

Quasi-steady refers to an unsteady flowfield that has lost all phase coherence.

Ordinary points have a nonzero wall shear stress and posses only a single skin-friction line. All points which are not singular are ordinary points.

The **phase-fluctuations** (double product terms) $\langle uu \rangle$, $\langle vv \rangle$, and $\langle uv \rangle$ are the two variances and the cross-variance corresponding to the "phase-mean" velocities.

The **phase-mean** velocities $\langle u \rangle$ and $\langle v \rangle$ are computed at each phase of the forced waveform cycle by averaging many realizations of said cycle. Phase-averages were accumulated from 200 realizations, where the cycle of each realization was partitioned into 512 distinct phases.

Reversed flow occurs when a velocity vector has a component that opposes the freestream velocity direction.

Revolving-Disc valve (RD-valve) is the type of computer-controlled valve that was custom-designed for the Water Tunnel Facility. The characteristics and operation of this valve is described in detail in section 3.3.

A saddle point is a singular point where the wall shear-stress vector field (or equivalently the limiting streamlines at the wall) has the topology shown in figure 2.1.

Separation is the flow structure consisting of a separation line and a separation wake.

A laminar separation line is the line that passes through a saddle point. Therefore, there must be a point where $\bar{\tau}_w = 0$ (or $C_f = 0$) for separation to exist.

A separation wake is the sluggish fluid downstream of a separation line.

A singular point is a point where the wall shear stress, $\bar{\tau}_w$, equals zero. A singular point can either be a "node" or a "saddle point", see figure 2.1.

Spanwise profile refers to a collection of velocities obtained by traversing the LDA measuring volume only in the z-direction. Actually the y-direction was traversed slightly during spanwise traverses. For these experiments, the LDA beams approached the test surface at an angle of about $0.9°$. The LDA approach angle was set to enable measurements very close to the surface. Consequently, if

83

the measuring volume penetrated the boundary layer during a spanwise profile, velocity corrections needed to be made.

Stationary will be used to refer to fixed initial and boundary conditions.

Steady means that the local flowfield does not vary with time.

Streamwise velocity profile refers to a collection of velocities obtained by traversing the LDA measuring volume only in the x-direction. Since slight traverses in both the y- and z-directions accompanied streamwise traverses, only measurements of the freestream velocity were taken.

Two-dimensional (2-D) refers to flow that is two-dimensional in the mean so that there are two non-zero velocity components that vary in only two spatial coordinates. The main examples covered in this literature review deal with flat plates or high aspect-ratio airfoils where end effects are neglected. Another example is axisymmetrical flows. Literature indicates that many presumed "two-dimensional" separated flows were truly three-dimensional in the mean.

Three-dimensional (3-D) refers to a flowfield that can be represented by not less than three non-zero velocity components that vary in three spatial coordinates.

Unsteady will primarily refer to organized unsteadiness in the flowfield which may arise from inherent instabilities under stationary conditions or may be a response to nonstationary conditions.

Velocity-gradient conditions is the term used instead of pressure gradient conditions because the freestream velocity-gradient is controlled via suction through the control wall. The pressure gradient is not controlled at all, although it is modified by the freestream velocity gradient.

Velocity profile is identical to "boundary-layer profile" when not modified by "spanwise" or "streamwise."

Appendix B

Experimental Procedure

The procedures that will be described in this appendix were developed to streamline changeover between the various experiments performed in the unsteady-flow water tunnel. These procedures generally either exploit the advantages or attempt to circumvent the problems associated with using water as the flow medium.

The two pre-eminent strengths of water facilities are (1) the assortment of flow visualization techniques available to the experimentalist, and (2) the water is usually contaminated enough to not require seeding for LDA velocity measurement. Before discussing flow visualization techniques used in this facility—the second strength needs no further comment—this appendix will discuss procedures common to the setup and everyday operation of the Stanford unsteady boundary-layer research water tunnel.

B.1 Selecting and Setting flow conditions/parameters

The Unsteady-Flow Boundary-layer Water Tunnel has been designed for careful control of initial and boundary conditions experienced by the flow. The bypass-bleed, side-wall, and opposite-wall boundary layer bleeds mentioned in chapter 3 control initial and boundary conditions. In addition, special subsystems for temperature control and de-aerationb help control global flow conditions. This appendix details techniques for setting each of these subsystems.

Temperature control. The dedicated water chiller and temperature controller confined held the temperature of tunnel water to $\pm 0.1^\circ C$ throughout all experiments.

Failure of the former temperature-control system required that a new temperature controller and water chiller be installed. The replacement chiller was a 5

ton Carrier® 3SEH060 Compressor with a 09WQ060 Heat Exchanger. This system more closely matched our standard load than the former 10 ton Trane® unit. A hot-gas bypass system, added to the system, unloaded the chiller as demand decreased.

The temperature controller, Omega® CN 9000, sensed the temperature in the tunnel exit section via a RTD thermistor. The temperature controller operated in PID mode for more intelligent control than the former thermostat. Detailed instructions for setting the temperature controller are given in its manual. When the thermal load decreased, the controller would switch a solenoid valve to divert 50% or more of the fluid from the heat exchanger through a bypass loop. Since the hot-gas bypass has a long time constant, the chiller accomodated changes smoothly; it did not deliver surges of over-cooled water or cause electrical power surges.

Air purge/Drain down system. This system served two purposes, one to expedite data-readiness of the tunnel and the second for quality control of all data runs. As air purge, the system could force air trapped in low-velocity, opposite- and side-wall boundary-layer control assemblies into the test section where it could be easily removed. The entire test section would then be free of air bubbles within two hours. As drain down, the system would set the exit pressure for the same opposite- and side-wall assemblies. The pipe provided an outlet for fluid withdrawn through these assemblies. The pressure was set by one of the ports which vented to atmospheric pressure. The pipe conveyed exhaust fluid directly to the sump. Caution: close the vent before using this system to purge air.

Setting the streamwise freestream-velocity gradient. Adjustment of the streamwise freestream-velocity gradient of the water tunnel operating at stationary conditions was first task in the setting of initial and boundary conditions for this experiment. For the purpose of setting a streamwise uniform freestream velocity, a target velocity was chosen. Opposite-wall valves were then adjusted to match this velocity within ±1% as the LDA, measuring the potential core, was traversed upstream.

The upstream direction is preferred because opposite-wall valves affected the upstream velocity considerably more than the downstream velocity. This can be understood if we consider opening a valve halfway down the test section. Gage pressure downstream, which is the driving force determining flowrate through a fixed valve, increases little. The flow entering the test section, however, sees a different open area and increases flow upstream of the valve accordingly. Direct pressure measurements were not used for adjusting the pressure gradient as will be explained below.

Test surfaces were not designed for implementation of pressure taps. One reason for choosing not to measure pressures directly was to maintain the optical and structural integrity of the glass test surface, which was comprised the first $1.0m$ of test-surface chord. But even acrylic test surfaces were not installed with pressure taps. The reason was that velocity resolution of the LDA is 15 times better than the resolution of available pressure probes. At the low flowrates used in this channel the difference between static and dynamic pressures were on the order of 0.01 inches of water. Using available pressure probes the finest velocity resolution would have been $\pm0.035m/s$ or 14%. This made standard pressure taps or a scanivalve system inaccurate as well as impratical for setting the stationary freestream-velocity gradient.

Setting flow at the test-section leading edge. On the leading edge a fresh boundary layer is started for laminar and turbulent experiments. The quality of the test boundary layer is set by adjusting flow through the bypass bleed. The bypass was designed to uniformly extract flow across the span of the channel. Flow wedges and honeycomb direct bypass fluid to four manually adjusted valves, which are trimmed to give uniform flow across the span.

Mass flow rate through the bypass is set such that the stagnation point is just on the lower (test surface) side of the leading edge. This is detected by visualization of the test surface boundary layer. Mass flow rate should not be significantly more than this. The procedure for setting the mass flow rate is as follows. (Recall that

Roy W. Henk   7/16/90 9:14am

a $0.15mm$ dye slot is formed at the junction of the leading edge and the first test surface.)

1. Open all valves an equivalent amount to match flowrates;

2. Pass dye at a very slowly through the dye slot. There are three possibilities for behavior of the dye emitting from the slot.

o If a smooth sheet of dye covers the test surface until $x_{chord} \sim 0.5m$, the bypass is open just right or perhaps too much. Explanation: a stagnation point (line) is resident on the test surface at the leading edge.

o If hairpins of dye are visible, dye flowrate is too high.

o If turbulent spots are visible as dye leaves the slot, the bypass flowrate is too low. Explanation: a separation on the test surface is resident at the leading edge.

3. The stagnation line can be crudely checked by hydrogen-bubble visualization if the inlet flowrate is less than $0.2m/s$. Swing the hydrogen-bubble wire/trip ahead of the leading edge and power it up safely.

Setting nonstationary waveforms. The magnitude of the six waveforms at the test RD-valve were initially chosen according to the appearance of separation during flow visualization. The magnitude of waveform 0.Wav, which exerted the maximum suction, was chosen to keep spanwise extent of the separation from exceeding 1/3 of the tunnel width, W. The magnitude of waveform 5.Wav, which exerted the minimum suction, appeared to correspond to incipient separation. The magnitudes of intermediate waveforms were chosen at equal intervals between 0.Wav and 5.Wav.

Complementary waveforms at the exit RD-valve were chosen to maintain a stationary freestream velocity at the inlet. The magnitude and the phase delay of the complementary waveform could be specified. A phase delay of $180°$ performed best for each of the waveforms. The magnitude of the selected test and complementary waveforms are given in table C.1. Power spectra of the Dantek LDA tracker output

confirmed that the inlet flow was stationary during forced, nonstationary conditions. For each case, the power spectra of u-velocity was flat (essentially white noise) for frequencies below $20Hz$ and tapered off for higher frequencies.

Setting side-wall bleeds. A small regulating valve controls the flowrate for each side-wall bleed. The flowrate is set based on flow visualization and measurement. The amount of flow withdrawn through the side-wall bleeds was not significant enough to affect streamwise freestream-velocity gradient. Side-wall bleeds could, however, considerably alter the spanwise freestream-velocity gradient. Flow vizualization revealed that the test-surface boundary layer was severely distorted in the spanwise direction when flowrate through the side-wall bleeds was too high. Side-wall bleeds were then adjusted to cause streaks to remain parallel with the side walls and set equal to one another.

B.2 Calibration and Operation of Electronics/Instruments

Instruments were calibrated regularly and calibration values were used during real-time data acquisition. The manner in which we forced the typical two-color, two-component LDA system to supply three components demanded a special procedure for calibration of each component. The goal was an offset voltage and velocity/voltage slope for each individual channel which the computer could convert to real velocities.

The u-component was probed by green beams with a $40MHz$ shift and processed by a tracker. Thus the standard procedure described below could be used for calibration. The v-component was probed by green beams with a $38MHz$ shift and processed by a tracker. The consequences of this nonstandard shift will also be described below. The w-component was probed by blue beams with a $40MHz$ shift and processed by a counter.

Standard Calibration Procedure. The calibration of voltage offsets remained the same for all channels regardless of the Bragg frequency shift. First the signal to

89

the Bragg cell is fed into the photo detector port on the front of the downmixer. The signal is downmixed by $200kHz$, the standard setting for this facility, and then passed to the tracker or counter which converts the frequency into a nominally-DC voltage. An A/D converts and delivers this signal to the computer. Thus we obtain the offset voltage corresponding to a velocity of $0m/s$.

Determination of the velocity/voltage slope required as an intermediate step the determination of the frequency/voltage slope. For the $40MHz$ lines, the slope was found by recording the tracker's output voltage as the frequency of the downmixed signal changed. A linear regression through the frequency/voltage data determines the slope.

Variations on a Calibration Procedure. As was mentioned before $38MHz$ Bragg shifting applied to the v signal prevented us from solely using the standard procedure. Why was $38MHz$ shifting necessary? The compact optical configuration developed by Humphreys (1988) put both u and v signals on green beams which required electronic separation after the green photomultiplier. The $2MHz$ frequency difference accomplished the electronic separation. The advantage of this optical configuration was that it assured the coincidence of the measuring volumes for all three components through the use of a common pinhole in the field-stop system. see notebook on 14 July 88.

The downmixer referenced to the $38MHz$ line does not deliver calibrated downmixed frequencies since we are operating it off-design. The voltage offset is calibrated according the the procedure in the previous subsection. But the slope is calibrated only for the tracker and A/D in this channel. This is done by sending a downmixed signal out of the u-downmixer into the v-tracker and then following the procedure above. Thus the $38MHz$ mixer only participates in calibration during determination of the voltage offset, and not for slope.

Although the w-component was not measured for this study, the procedure for its calibration can be quickly dispatched for the sake of reference. By reciprocating

the A/D output from the counter, the u-component could be calibrated exactly like a tracker. Reciprocation took place in the software.

B.3 Flow visualization

Of the assortment of flow visualization techniques available to water flow experiments, three have been used in this facility: hydrogen bubbles, injection of food dye, and laser-induced fluorescence.

Hydrogen bubble. Hydrogen-bubble visualization was used during qualification of the facility rather than for presentation quality imaging. The range of flow velocities typically run in this tunnel, from 0.15 to $8m/s$, is too fast for quality hydrogen-bubble images.

On~ hydrogen-bubble wire has been quasi-permanently installed near the leading ed$_{\iota}$ of the test surface. The other electrode is one of the brass valves nearby; these valves set the stationary streamwise freestream-velocity gradient. The wire was $0.13mm$ stainless steel that was crimped every $3mm$. This is the same type of bubble wire that was used by McAlister of Ames (I think the reference is Carr, *et al.* 1977). Crimping causes the bubbles to detach in dense streams rather than a simple sheet.

The wires permanent status is a consequence of the dual usage it has served. Hydrogen-bubble visualization was initially used for visual confirmation of the leading-edge stagnation point. The wire doubles as a turbulence trip when it is swung to contact the test surface near the tail of the leading-edge assembly.

Food dye. Food dye has been the technique most used in this tunnel. Every type of slot that connects the test section has been used at one time or another for the injection of food dye. By this means the boundary layers on the test surface and along the side walls have been visualized. For instance, dye was injected through the side-wall bleed to visualize the side-wall boundary layers during times when the prevailing freestream-velocity gradient was zero and when it was adverse. The

evolution of the three-dimensional separation on the test surface was visualized extensively for all cases of U_0 and suction S. Food dye visualizations were recorded on VHS videotape, $35mm$ color slide film and black-and-white print film.

Laser-induced fluorescence (LIF). Fluoroscene dye was also used in conjunction of laser-light sheets to visualize cross-sections of the separated-flow structure. The effect is dramatic as the dye turns to a bright yellow-green in a dark background. Cross-sections of the xz-plan view and the xy-cut were visualized for the base case during separation development and decay. LIF visualizations were recorded on $35mm$ color slide film, $35mm$ black-and-white print film, and $16mm$ black-and-white and color movie film.

Appendix C

Data Acquisition and Analysis

C.1 Types of data acquisition

raw data.

C.1.1 time-averaged

profile.

streamwise.

spanwise.

C.1.2 phase-averaged

Phase-averaging is essential for the experiment because the global flow-field for each cycle is highly sensitive to the initial conditions. Small variations in the initial boundary layer at the instant the adverse freestream-velocity gradient was imposed would be amplified in the separation structure. The roll-up of the first 5 or so spanwise vortices from the separated shear layer were strongly phase-locked, but subsequent vortices were less phase-locked which gave the appearance of a quasi-steady separation. Individual realizations of separation development, shedding, and decay were never identically repeatable. Since the whole flowfield was not swept instantaneously, but sampled point-by-point, phase-averaging was essential.

Due to the extended times over which phase-averaged profiles were sampled, in Resultant time delays show up in It is not the global structure that is so sensitive, but the time-delays in the unsteady structure. A period of duration greater than $20s$ did not guarantee better convergence of phase-averaged profiles, but more

samples per average converge at about 200 samples. This is demonstrated in figure C.1.

The primary resistance to convergence arose from the periodic roll-up and shedding of the separated shear layer. Small delays in the release of shed vortices brought large variances in later phases and consequently delayed convergence. Surprisingly, the phases that required most samples for convergence were those immediately after release of the adverse freestream-velocity gradient. This behavior was resolved by investigation of non-averaged velocity histories. Consider phases greater than 8 seconds after imposition of the adverse freestream-velocity gradient through 2 seconds after its release. A non-averaged velocity history compared to a phase-averaged velocity history shows that large velocity fluctuations from vortex shedding are the dominating physics during these phases. These fluctuations disappear as phase-averaging converges.

Smoothing. Neither phase-averaged data nor raw data has been smoothed artificially.

Warning against phase-smoothing. *Phase-smoothing data can be deceptive. I highly discourage its usage.* Phase smoothing as reported by Humphreys (1988) needs to be carefully reconsidered. The method when applied to time-mean values is innocucus enough, though interpolation is not a necessarily a conservative (check???) technique. The method when applied to double and triple products is quite erroneous. This can be quickly shown by considering the definition of the simple double product $\langle u_i u_j \rangle$. The value was obtained from the subtraction of ensemble sums $\sum u_i$, $\sum u_j$ and $\sum u_i u_j$, according to the formula

$$\langle u_i u_j \rangle = \frac{n(\sum u_i \sum u_j) - \sum u_i u_j}{n}.$$

In order to properly smooth this $\langle u_i u_j \rangle$ across several phases, the formula above needs to be inverted to back out original sums, the sums then applied to the larger time interval, and finally the above formula re-evaluated.

A related difficulty is that different y-locations in the profile did not see the same cycle-to-cycle variations. I admit that I am being persuaded to phase smooth even as I write at least for the purpose of presenting good integral parameter plots. Rather than resort to phase-smoothing another possibility is to time-average phase-averaged results and to compare resultant profiles and their integral results with time-averaged profiles in a stationary separation. It is instructive to openly discuss the difficulties rather than hide them.

C.2 Types of analysis

A wide assortment of programs were written to analyze raw, time-averaged and phase-averaged data that were collected during this experiment. Programs were written to fit linear and nonlinear functions, perform spectra analyses, interpolate, integrate, and just rearrange the data in a clear format. Most of these programs depended heavily on functions described in *Numerical Recipes in C* by Press, *et al.* (1988).

From Raw Data

Power spectra. Raw data, i.e. unaveraged, from individual channels were stored for processing by a power spectra program. Segments of a data record have a Parzen window applied and are averaged for minimum variance per data point. Most power spectra analyzed have been for cases of stationary, adverse freestream-velocity gradients wherein continuous data records were collected. For estimates of peak frequencies during unteady flow, apparent cycles were counted and then divided by elapsed time.

Number of samples needed for averaging.

Integral boundary-layer parameters.

Time-development, shedding frequency. time traces

   Time-responses were measured from both phase-averaged and raw data.

Comparison of phase-averaged results with raw data. Phase-averaging both reveals and hides some significant features of unsteady separation as is seen by comparing figures 6.14 and 6.17. Information that is lost includes the magnitude of velocity oscillations 6 seconds after imposition of the adverse freestream-velocity gradient in (a), and the amplified oscillations immediately after restoration of a uniform freestream velocity in (b).

C.3 Potential-flow analysis

The potential flow analysis follows a two step process. First, take a very simplified geometry containing suction through a square hole in a flat plat with a uniform freestream. Then generate the complete geometry by imaging the results of the simplified analysis about specified planes. Imaging thereby generates the rectangular cross-section of the test section.

The simplified geometry. Consider the potential flow of a uniform stream affected by a continuous distribution of sinks from $(x : x_1 < x < x_2, z : z_1 < z < z_2)$.

The potential at point P due to a source at S is

$$\Phi = -\frac{q}{4\pi}\frac{1}{|\vec{r} - \vec{s}|} \quad ,$$

where $q = [volume \ / \ time]$ disappearing per sink. Let $-|s|$, a constant be sink strength per unit area, where $|s|$ is two times local suction speed since there are two sides to a sink.

At $x = \xi, z = \eta$, consider an element $d\xi d\eta$ of the distribution. Then the potential at field point $P(x, y, z)$ due to elementary source $-|s|d\xi d\eta$ in a uniform stream at velocity U is

$$\Phi(x,y,z) = Ux + \frac{|s|}{4\pi}\int_{x_1}^{x_2}\int_{z_1}^{z_2}\frac{d\xi d\eta}{\sqrt{(x-\xi)^2 + y^2 + (z-\eta)^2}} \quad ,$$

which can be differentiated to obtain the velocities $u = \partial\Phi/\partial x$, $v = \partial\Phi/\partial y$, and $w = \partial\Phi/\partial z$.

96

The resulting equations for u and w are easily integrated twice to obtain

$$u = U - \frac{|s|}{4\pi} \left\{ \ln \left| (z_2 - z) + \sqrt{(x - x_2)^2 + y^2 + (z - z_2)^2} \right| \right.$$

$$- \ln \left| (z_1 - z) + \sqrt{(x - x_2)^2 + y^2 + (z - z_1)^2} \right|$$

$$- \ln \left| (z_2 - z) + \sqrt{(x - x_1)^2 + y^2 + (z - z_2)^2} \right|$$

$$\left. + \ln \left| (z_1 - z) + \sqrt{(x - x_1)^2 + y^2 + (z - z_2)^1} \right| \right\} \quad (Three.0)$$

and

$$w = -\frac{|s|}{4\pi} \left\{ \ln \left| (x_2 - x) + \sqrt{(x - x_2)^2 + y^2 + (z - z_2)^2} \right| \right.$$

$$- \ln \left| (x_1 - x) + \sqrt{(x - x_1)^2 + y^2 + (z - z_2)^2} \right|$$

$$- \ln \left| (x_2 - x) + \sqrt{(x - x_2)^2 + y^2 + (z - z_1)^2} \right|$$

$$\left. + \ln \left| (x_1 - x) + \sqrt{(x - x_1)^2 + y^2 + (z - z_2)^1} \right| \right\} \quad .$$

The equation for v is easily integrated once. For the second integration, however, we need the identity...

$$\int \frac{dx}{(mx^2 + n)\sqrt{ax^2 + b}} = \frac{1}{\sqrt{n(bm - an)}} \tan^{-1} \frac{x\sqrt{bm - an}}{\sqrt{n(ax^2 + b)}} \quad \text{for } bm - an > 0$$

$$= \frac{x}{n\sqrt{ax^2 + b}} \quad \text{for } an = bm.$$

For completeness, two more identities ought to be considered but these arise only for $y^2 = 0$, which is at the suction wall. Since I am not interested in the flow exactly at the suction wall and consequently will not be evaluating any integrals

there, I will not list the two extra cases even though they are simple. After the second integration, v is given by...

$$v = -\frac{|s|y}{4\pi}\left\{\frac{(z_2 - z)}{y|z - z_2|}\left[\tan^{-1}\frac{(x_2 - x)|z - z_2|}{\sqrt{y^2[(x_2 - x)^2 + y^2 + (z - z_2)^2]}}\right.\right.$$

$$\left.- \tan^{-1}\frac{(x_1 - x)|z - z_2|}{\sqrt{y^2[(x_1 - x)^2 + y^2 + (z - z_2)^2]}}\right]$$

$$-\frac{(z_1 - z)}{y|z - z_1|}\left[\tan^{-1}\frac{(x_2 - x)|z - z_1|}{\sqrt{y^2[(x_2 - x)^2 + y^2 + (z - z_1)^2]}}\right.$$

$$\left.\left.- \tan^{-1}\frac{(x_1 - x)|z - z_1|}{\sqrt{y^2[(x_1 - x)^2 + y^2 + (z - z_1)^2]}}\right]\right\} \quad.$$

When either of the factors $(z_2 - z)$ or the $(z_1 - z)$ equals zero, then the whole quantity $\left[\,...\,\right]$ that it multiplies must be identically zero.

The complete geometry. $U_{pot}(x, y, z, U_0, S)$ for the complete geometry, a rectangular cross-section of height H and span W, was estimated by the standard procedure of images. In this procedure, the influence of images using the above analytic formulas functions are summed as necessary, up to several thousand images, in order to generate the walls of the tunnel geometry. Iterations proceded automatically until the iterative correction to the velocity magnitude was less than 10^{-5}.

The resulting velocity field $U_{pot}(x, y, z, U_0, S)$ for the three velocity components is not represented by such a simple (or complex) collection of functions as those listed above. Instead, it is now just a collection of numbers. The usefulness of the resulting field was increased by finding a polynomial fit to the field when the variables (x, z, U_0, S) were fixed.

C.3.1 Polynomial fit to the potential flowfield

The following analysis will concern itself only with flow along the centerline, in order to avoid complications from skewing of the boundary layer, and only with the streamwise velocity, $u_{pot}(x, y, z = 0)$. We seek a fit $g(y) = u_{pot}$. Fix $x = a$. Let

$y = H - \tilde{y}$ so that the equations are referenced to the test surface by $\tilde{y}$ instead of the control (suction) surface by y. The procedure of images sums up equation C.0 many times over, so that g can be reckoned from the individual terms as

$$g(y) = \sum_{n} \left[k_{1n} - k_{2n} \ln \left| k_{3n} + \sqrt{k_{4n}^2 + (\tilde{y} - H + k_{5n})^2} \right| \right] \quad .$$

An involved set of gross simplifications reduced this equation to

$$g(y) = k_{6n} + k_{7n} \ln \left| 1 + \tilde{y}^2 \right| \quad .$$

Finally, the expansion $\ln|1 + x| = x - \frac{1}{2}x^2 + \frac{1}{3}x^3 - \frac{1}{4}x^4 + \dots$ gives to first order

$$g(y)\Big|_{x=a} = C_0 + C_2 \cdot \tilde{y}^2 \qquad (Three.1)$$

as a possible polynomial fit. Figure shows that such a simple polynomial fit $g(y)$ for a fixed (x, z, U_0, S) adequately fits u_{pot} to within ?????% at each point.

C.4 New equations for integral parameters

Now that the potential velocity profile was approximated by the function $g(y) = C_0 + C_2 y^2$, algorithm (1) furnishes new equations for the integral parameters. Outer points of each velocity profile, whether time- or phase-averaged, were compared with this function. By interpolating to determine where the potential and experimental profiles matched within 1%, δ_{99} was found and designated as the edge of the boundary layer. The new equations for the integral parameters are...

Displacement thickness

$$C_0 \delta^* + \frac{C_2}{3} \delta^{*3} = \int_0^{\delta_{99}} (g - u)\, dy \qquad (C.2)$$

Momentum thickness

$$C_0^2 \theta + \frac{2C_0 C_2}{3} \theta^3 + \frac{C_2^2}{5} \theta^5 = \int_0^{\delta_{99}} u\, (g - u)\, dy \qquad (C.3)$$

99

The cubic and quintic equations were easily solved using a classic root-finding routine. Rules that selected the answer from all the roots found are...

1. δ^* and θ must real valued.

2. $0 < \delta^* < 2\delta_{99}$, and $\qquad\qquad\qquad\qquad\qquad$ (3.4)

3. $|\theta| < \delta^*$.

Appendix D

Error Analysis

Careful analysis of errors establishes the bounds within which numerical simulations and future experiments can be expected to duplicate these experimental results. In this appendix, we will state error bounds for the experimental results and for derived quantities and analysis. Error bounds differ entirely from the bounds of the experimental domain which were described earlier in section 5.1.

For this analysis we will apply two methods for determining error bounds:

1. The method set forth by Kline and McClintock (1953) gives bounds for worst-case errors. This method considers each source of error to be linearly independent of the others. Consequently the total error is the square root of the sum of individual errors squared. This is akin to the magnitude of a n-space vector for n linearly-independent errors. The chosen confidence level for this analysis is 95% or 20:1 odds.

2. A modification to method (1) which describes likely error bounds based on duplicate measurements under identical conditions. This method, based on experiment repeatability, substitutes some arbitrarily-estimated error bounds with observed error bounds. Sources of error are classified according to the categories set forth by Moffat (1988). The two categories are *bias* and *random* errors. *Bias* errors are fixed and can be due to calibration errors, probe alignment problems, *etc.* Slowly-varying effects like signal drift will also be assigned to bias errors. *Random* errors are analyzed according to stochastic methodology and assumed sample distributions.

A summary of the error analysis is given in table D.1. The following sections will describe how these values were obtained.

D.1 Bias errors

Primary contributions to bias errors arise from valve positioning errors, calibration of the LDA intersection angles, cross-contamination of velocity signals, and instrument system errors. Each of these will be discussed individually.

Valve-positioning errors.   Error in positioning is ±1 increment from the input valve position.

Calibration of LDA intersection angles.   An error in the calibration slope affects the fluctuating quantities in a similar manner, except that each must be treated as a product term. That is

$$\frac{\Delta(u'u')}{\Delta\text{slope}} = 2u'\frac{\Delta u'}{\Delta\text{slope}}. \tag{C.1}$$

Cross-contamination of velocity signals.   Primary contributions to cross-contamination of velocity signals arises from the following two reasons: (1) LDA fringes are not perfectly orthogonal to each other, (2) LDA fringes are not perfectly aligned with the channel axes.

Throughout data acquisition beams were oriented to minimize contribution from the u-component into the v-velocity component. This was accomplished by rotating the transmitting optics until the time-averaged v-profile was flat near the wall for zero pressure-gradient conditions. The finest adjustment that can be expected is $0.5°$ which suggests an error of $±0.009 \cdot u$.

Flatness of the v-profile was the condition of choice for two reasons: (1) errors in the zero-velocity voltage offset prohibited setting v identically equal to zero near the wall; and (2) for all intents and purposes the zero pressure-gradient v-profile is flat throughout. For example, table D.1 indicates that the error bounds for the v-component is ?????. The analytical solution to the Blasius laminar boundary layer, however, gives a maximum v-velocity of $\approx 6 \times 10^{-4} m/s \approx 0.003 \cdot U_\infty$. Thus the zero pressure-gradient v-profile is flat within the error bounds for v.

The approach angle required for measuring near the wall caused a w-contribution to the v-velocity component. The nonshifted reference beam approached the wall

102

at an angle of $0.0156 radians$. From table D.2, the v-fringes were generated at an angle of $0.0488 radians$ with respect to the reference beam. Thus the w-component contribution to v was $0.0644 \cdot w$. Since the majority of data acquired was along the centerline of the channel, the contribution from the w-component is small but not identically zero due to the separation asymmetry mentioned in chapter 5.

The u-component also received a w-contribution on the order of $-0.0462 \cdot w$, from table D.2, since the nonshifted reference beam cut across the span of the channel. As in the previous paragraph, the contribution of the w-component is small but not identically zero.

Instrument system errors. TSI estimates system errors for the entire tracker system to be 0.4% of full scale range. For this experiment, full scale covered $0 - 5\,Volts$ for the frequencies $0 - 500\,kHz$. This corresponds to $0.02\,Volts$ or about $0.011\,m/s$ uncertainty on u and v. This worst-case estimate is more than three times larger than the total estimated uncertainty for u and v given in table D.1. The reason for this discrepancy follows the second method of determining error bounds and is given in the following paragraph.

An independent estimate of portions of instrument system bias error was determined by comparing system calibrations made throughout the data-acquisition process. Table D.2 shows the average calibration for voltage offset and for velocity-voltage slope. In addition, this table gives the range over which calibration values varied about the average. The second estimate for system error in u is then given by the formula $(0.554 \cdot 0.0074)[\Delta Volts_{max} + (2.001 \cdot 0.0012)]$. Since $\Delta Volts_{max}$ for u is $< 0.8\,Volts$, the system error in u is $< 0.0033\,m/s$. The corresponding estimate for v-system error is $< 0.0006\,m/s$.

D.2 Random errors

Primary contributors to random errors include electronic noise, quantization errors by the A/D converter. Each of these will be discussed below.

Sources for error in the integral parameters will be thoroughly discussed.

Chapter 4 described various definitions for the integral parameters. For the zero pressure-gradient boundary layer, discrepancies between the definitions are generally less than 5%. The largest source of error for the displacement thickness arises from errors in estimating the location of the wall. Discrepancies in the displacement-thickness integral for differing wall-estimates can be up to 30%, varying linearly with the estimate.

For steady, applied suction (adverse pressure-gradient cases), discrepancies between integral parameters for the definitions are often 40% or more. In unsteady flow cases, it is better to describe absolute discrepancies since zero-crossings cause ratios to hit infinity.

D.4 Summary

Problems. It is interesting that in figure 6.11, the quasi-steady velocity profile showed a weakly positive (forward) flow near the wall, while at LP:2 the flow near the wall was distinctly reverse. I tested the calibration to determine if a faulty calibration could explain this peculiarity. A new calibration did not change the sign of the velocity. It should be noted, however, that the uncertainty analysis of $\langle u \rangle$-velocity would allow for a zero or negative velocity. The effect was repeatable because time-averaged profiles and an independent phase-averaged profile confirmed these results. The best explanation is that since the quiescent owl-face structure is sustained by inflow through the sides, a mean stagnation point can be observed upstream of LP:1 resulting in forward flow there. At the location LP:2, however averaged profiles are dominated by shed vortices forcing the near-wall flow in the reverse direction.

Bibliography

BIPPES, H. 1987 'Experimental investigation of topological structures in three-dimensional separated flow.' *Boundary-Layer Separation. Proceedings of the IUTAM Symposium London, August 26-28, 1986*, eds. F. T. Smith & S. N. Brown, Springer-Verlag Berlin. pp. 379-381.

BOERSEN, S. 1975 'Reynolds number effects on pressure and normal force distributions along conically pointed circular cylinders at Mach of 2.3.' NLR TR 75124U, Sept 1975.

BOGDONOFF, S. M. 1987 'Observation of three-dimensional "separation" in shock wave turbulent boundary-layer interactions.' *Boundary-Layer Separation. Proceedings of the IUTAM Symposium London, August 26-28, 1986*, eds. F. T. Smith & S. N. Brown, Springer-Verlag Berlin. pp. 37-55.

BRERETON, G. J. & REYNOLDS, W. C. 1987 'Experimental study of the fluid mechanics of unsteady turbulent boundary layers.' Ph.D. Thesis: Report No. TF-29. Stanford University, Dept. of Mech. Engineering: Thermosciences Division.

CARR, L. W., MCALISTER, K. W. & MCCROSKEY, W. J. 1977 'Analysis of the development of dynamic stall based on oscillating airfoil experiments.' NASA TN D8382.

CARR, L. W. & CEBECI, T. 1985 'Boundary layers on oscillating airfoils.' *3rd Symposium on Numerical and Physical Aspects of Aerodynamic Flows*, Long Beach, CA, Jan. 21-24.

CEBECI, T. & BRADSHAW, P. 1977 *Momentum Transfer in Boundary Layers*, McGraw Hill Book Co., New York.

CHANDRASEKHARA, M. & CARR, L. W. 1989 'Flow visualization studies of the Mach number effects on the dynamic stall of an oscillating airfoil.' AIAA Paper 89-0023.

CHAPMAN, G. T. 1986 'Topological classification of flow separation on three-dimensional bodies.' AIAA Paper 86-0485.

CHONG, M. S., PERRY, A. E. & CANTWELL, B. J. 1988 'A general classification of three-dimensional flow patterns.' Stanford University Dept. of Aero. and Astro. Report 572.

CRAWFORD, M. E. 1977 'Oblique flow headers for heat exchangers with a free discharge exit condition.' Stanford University, Dept. of Mechanical Engineering: Report prepared for Rocketdyne Division of Rockwell International, April 1977.

DESPARD, R. A. & MILLER, J. A. 1971 'Separation in oscillating laminar boundary-layer flows.' *Journal of Fluid Mechanics* 47, part 1, pp. 21-31.

DIDDEN, N. & HO, C. M. 1985 'Unsteady separation in a boundary layer produced by an impinging jet.' *Journal of Fluid Mechanics* 160, pp. 235-256.

EICHELBRENNER, E. A. 1973 'Three-dimensional boundary layers.' *Annual Review of Fluid Mechanics.* 5:339-360.

GAD-EL-HAK, M. 1989 'The art and science of flow control.' *Lecture Notes in Engineering: Frontiers in Experimental Fluid Mechanics*, ed. M. Gad-el-Hak, Springer-Verlag Berlin. pp. 211-290.

GADD, G. E., JONES, C. W., & WATSON, E. J. 1963 'Approximate methods of solution.' *Laminar Boundary Layers*, ed. L. Rosenhead, VI, 26:329-331. Oxford University Press.

GASTER, M. 1966 'The structure and behavior of laminar separation bubbles.' AGARD CP-4, 813-854.

GOLDSTEIN, S. 'On laminar boundary-layer flow near a position of separation.' *Quarterly Journal Mech. Appl. Math.* 1:43-69.

HO, C. M. 1983 'An alternative look at the unsteady separation phenomenon.' *Recent Advances in Aerodynamics*, ed. A. Krothapalli & C. A. Smith, Springer. pp. 165-178.

HONAMI, S. & JOHNSTON, J. P. 1980 'A new definition of integral thickness for boundary layer flow over longitudinally-curved surfaces.' Internal Report IL-26. Stanford University Mechanical Engineering Department.

HOUDEVILLE, R., BONNET, J. L., & COUSTEIX, J. 1989 'Experimental study of a flat plate oscillrting in pitch.' *Proceedings of the Seventh Symposium on Turbulent Shear Flows.* 1, pp. 11.3.1-6.

HORNUNG, H. & PERRY, A. E. 1984 'Some aspects of three-dimensional separation, Part I: Streamsurface bifurcations.' *Zeitschrift für Flugwissenschaften und Weltraumforschung.* 8, Heft 2:77-87.

HORTON, H. P. 1968 'Laminar separation bubbles in two- and three-dimensional incompressible separated flow.' Ph.D. Thesis, University of London.

HUI, W. H. 1988 'Unsteady three-dimensional flow separation.' University of Waterloo, Dept. Applied Mathematics. Final Report, Contract NAGW-575 BASIC.

HUMPHREYS, W. W. & REYNOLDS, W. C. 1988 'An experimental study of the effect of streamwise vortices on unsteady turbulent boundary-layer separation.' Ph.D. Thesis: Report No. TF-42. Stanford University, Dept. of Mech. Engineering: Thermosciences Division.

HUNT, J. C. R., ABELL, C. J., PETERKA, J. A. & WOO, H. 1978 'Kinematical studies of the flows around free or surface-mounted obstacles; applying topology to flow visualization.' *Journal of Fluid Mechanics* 86, pp. 179-200.

HUSSAIN, A. K. M. F. & REYNOLDS, W. C. 1970 'The mechanics of an organized unsteady wave in turbulent shear flow.' *Journal of Fluid Mechanics* 241, pp. 241.

JAYARAMAN, R., PARIKH, P. & REYNOLDS, W. C. 1982 'An experimental study of the dynamics of an unsteady turbulent boundary layer.' Stanford University Dept. of Mech. Engineering: Thermosciences Division. Report No. TF-18.

KIYA, M. & SASAKI, K. 1983 'Structure of a turbulent separation bubble.' *Journal of Fluid Mechanics* **137**, pp. 83-113.

KIYA, M. 1987 'Structure of flow in leading-edge separation bubbles.' *Boundary-Layer Separation. Proceedings of the IUTAM Symposium London, August 26-28, 1986,* eds. F. T. Smith & S. N. Brown, Springer-Verlag Berlin. pp. 57-71.

KLINE, S. J. & McCLINTOCK, F. A. 1953 'Describing uncertainties in single-sample experiments.' *Mechanical Engineering* **75**, 3.

KLINE, S. J. 1959 'On the nature of stall.' *Journal of Basic Engineering: Transactions of the ASME—Series D* **81**, pp. 305-320.

KLINE, S. J., BARDINA, J. G., & STRAWN, R. C. 1983 'Correlation of the detachment of two-dimensional turbulent boundary layers.' *AIAA Journal* **21**, No. 1: 68-73.

KOROMILAS, C. A. & TELIONIS, D. P. 1980 'Unsteady laminar separation: an experimental study.' *J. Fluid Mech.* **97**, part 2, pp. 347-384.

LEGENDRE, R. 1956 'Séparation de l'écoulement laminaire tridimensionnel.' *La Recherche Aéronautique* **54**: 3-8.

LEGENDRE, R. 1982 'Regular or catastrophic evolution of steady flows depending on parameters.' *La Recherche Aérospatial* 1982-4:41-49.

LIEBECK, R. & BLACKWELDER, R. 1987 'Low Reynolds Number—Separation Bubble.' Final Technical Report N00014-84-K-0500, ONR Scientific Officer: S. Lekoudis.

LIGHTHILL, M. J. 1963 'Attachment and separation in three-dimensional flows.' *Laminar Boundary Layers,* ed. L. Rosenhead, II, 2.6:72-82. Oxford University Press.

MASKELL, E. C. 1955 'Flow separation in three dimensions.' R.A.E. Report No: Aero. 2565.

MATHIOULAKIS, D. S. & TELIONIS, D. P. 1987 'Velocity and vorticity distributions in periodic separating laminar flow.' *Journal of Fluid Mechanics* **184**: 303-333.

MAXWORTHY T. 1981 'The fluid dynamics of insect flight.' *Annual Review of Fluid Mechanics* **13**, pp. 329-350.

MCCROSKEY, W. J. 1977 'Some current research in unsteady fluid dynamics.' *Journal of Fluids Engineering* **99**: 8-38.

MCCROSKEY, W. J. 1981 'The phenomenon of dynamic stall' NASA TM-81264, March.

MOFFAT, R. J. 1985 'Describing the uncertainties in experimental results.' *Experimental Thermal and Fluid Science*, 1, 3, Elsevier Science Publishing Co., Inc., New York.

MOORE, F. K. 1957 'On the separation of the unsteady laminar boundary layer.' in Boundary Layer Research, Proceedings of a Symposium of the International Union of Theoretical and Applied Mechanics, edited by H. Görtler, Freiburg, Germany, pp. 296-311.

NELSON, C. F., KOGA, D. K., & EATON, J. K. 1990 'Unsteady, separated flow behind an oscillating, two-dimensional spoiler.' *AIAA Journal* **28**, No. 5: 845-852.

NETER, J., WASSERMAN, W. & KUTNER, M. 1985 *Applied Linear Statistical Models.* Irwin, Homewood, Illinois.

PAULEY, L. L., MOIN, P. & REYNOLDS, W. C. 1988 'A numerical study of unsteady laminar boundary-layer separation.' Ph.D. Thesis: Report No. TF-34. Stanford University, Dept. of Mech. Engineering: Thermosciences Division.

PAULEY, L. L., MOIN, P. & REYNOLDS, W. C. 1990 'The structure of two-dimensional separation.' to appear in *Journal of Fluid Mechanics*.

PEAKE, D. J. & TOBAK, M. 1980 'Three-dimensional interactions and vortical flows with emphasis on high speeds.' AGARD AG-252.

PERRY, A. E. & HORNUNG, H. 1984 'Some aspects of three-dimensional separation, Part II: Vortex skeletons.' *Zeitschrift für Flugwissenschaften und Weltraumforschung.* **8**, Heft 2:155-160.

PERRY, A. E. & CHONG, M. S. 1987 'A description of eddying motions and flow patterns using critical point concepts.' *Annual Review of Fluid Mechanics* **19**, pp. 125-155.

PRANDTL, L. 1905 'Über Flüssigkeitsbewegegung bei sehr kleiner Reibung.' In *Proc. III Intl. Math. Congr., Heidelberg, pp. 484-491.*

PRANDTL, L. & TIETJENS, O. G. 1934 *Applied Hydro- and Aeromechanics*, trans. J. P. Den Hartog. Dover Publications, Inc.

PRESS, W. H., FLANNERY, B. P., TEUKOLSKY, S. A., & VETTERLING, W. T. 1988 *Numerical Recipes in C*, Cambridge University Press, Cambridge.

REYNOLDS, W. C. & CARR, L. W. 1985 'Review of unsteady, driven, separated flows.' AIAA Paper 85-0527.

RILEY, N. 1975 'Unsteady laminar boundary layers.' *SIAM Review* **17**, pp. 274-297.

RICE, JOHN A. 1988 *Mathematical Statistics and Data Analysis.* Wadsworth & Brooks/Cole, Pacific Grove, California.

ROBERTS, L. & WOOD, N. J. 1989 'Control of vortex aerodynamics at high angles of attack.' AGARD FDP 65 Symposium on Aerodynamics of Combat Aircraft Controls and of Ground Effects.

ROBINSON, M., HELIN, H., GILLIAM, F., RUSSELL, J., & WALKER, J. 1986 'Visualization of three-dimensional forced unsteady separated flow.' AIAA Paper 86-1066.

ROTT, N. 1956 'Unsteady viscous flow in the vacinity of a stagnation point.' *Quarterly Appl. Maths* **13**, pp. 444-451.

ROTT, N. 1964 'On the separation problem in unsteady flow.' in *Theory of Laminar Flows* (ed. F.K. Moore). Princeton University Press.

RUSSELL, J. M. & LANDAHL, M. T. 1984 'The evolution of a flat eddy near a wall in an inviscid shear flow.' *Physics of Fluids* **27** (3), pp. 557-570.

SAHARON, D. & LUTTGES, M. 1987 'Three-dimensional flow produced by a pitching-plunging model dragonfly wing.' AIAA Paper 87-0121.

SANDBORN, V. A. & KLINE, S. J. 1961 'Flow models in boundary-layer stall inception.' *Journal of Basic Engineering: Transactions of the ASME—Series D*, **83**, pp. 317-327.

SANDBORN, V. A. & LIU, C. Y. 1968 *Journal of Fluid Mechanics* **32**: 293-304.

SANDBORN, V. A. 1969 'Characteristics of boundary layers at separation and reattachment.' *Res. Memo.* no. 14 College of Engineering, Colorado State University.

SCHLICHTING, H. 1979 *Boundary-Layer Theory*, 7th ed. Trans. J. Kestin. New York: McGraw-Hill Book Company.

SEARS, W. R. 1956 'Some recent developments in airfoil theory.' *Journal of Aeronautical Science* **23**, pp. 490-499.

?SEARS, W. R. & TELIONIS, D. P. 1971 In *Recent Research of Unsteady Boundary Layers* (ed. E.A. Eichelbrenner), vol. 1, p. 404. Laval University.

?SEARS, W. R. & TELIONIS, D. P. 1975 'Boundary-layer separation in unsteady flow.' *SIAM J. Appl. Math* **28**, pp. 215-235.

SHEN, S.-F. 1978 'Unsteady separation according to the boundary-layer equation.' *Advances in Applied Mechanics* **18**, 177-220.

SIMPSON, R. L. 1989 'Turbulent boundary-layer separation.' *Annual Review of Fluid Mechanics.* **21**:205-234.

SMITH, C. R., JR. & KLINE, S. J. 1971 'An experimental investigation of the transitory stall regime in two-dimensional diffusers including the effects of periodically disturbed inlet conditions.' Report No. PD-15. Stanford University, Dept. of Mech. Engineering: Thermosciences Division.

SMITH, F. T., BRIGHTON, P. W. M., JACKSON, P. S., & HUNT, J. C. R. 1981 'On boundary-layer flow past two-dimensional obstacles.' *Journal of Fluid Mechanics* **113**: 123-152.

SMITH, F. T. 1984 'Theoretical aspects of steady and unsteady laminar separation.' AIAA-84-1582.

SMITH, F. T. 1986 *Annual Review of Fluid Mechanics* **18**: 197-220.

SOBEY, I. J. 1982 'Oscillatory flows at intermediate Strouhal numbers in asymmetric channels.' *Journal of Fluid Mechanics* **125**: 359-373.

STUART, J. T. 1955 'A solution of the Navier-Stokes and energy equations illustrating the response of skin friction and temperature of an infinite plate thermometer to fluctuations in the stream velocity.' *Proc. R. Soc. Lond.* **231**, pp. 116-130.

TAYLOR, E. S. 1967 'Some problems of recognizing and defining separation of the skewed boundary layer.' *Fluid Mechanics of Internal Flow*, ed. G. Sovran, Elseveir Publishing Company. pp. 320-332.

TELIONIS, D. P. 1979 'Review — Unsteady boundary layers, separated and attached.' *Journal of Fluids Engineering* **101**: 29-43.

TOBAK, M. & PEAKE, D. J. 1982 'Topology of three-dimensional separated flows.' *Annual Review of Fluid Mechanics* **14**: 61-85.

ÜNAL, A. 1988 'Three-dimensional singular points in aerodynamics' NASA TM-100045, USAAVSCOM TM TR-87-A-14.

VAN DOMMELEN, L. L. & SHEN, S.-F. 1982 'The genesis of separation.' *Proc. Symp. Num. Phys. Aspects Aerod. Flows*, Springer-Verlag. pp. 293-311.

VAN DOMMELEN, L. L. & COWLEY, S. J. 1990 'On the Lagrangian description of unsteady boundary-layer separation. Part I. General theory.' *Journal of Fluid Mechanics* **210**: 593-626.

VAN DOMMELEN, L. L. 1990 'On the Lagrangian description of unsteady boundary-layer separation. Part II. The spinning sphere.' *Journal of Fluid Mechanics* **210**: 627-645.

WALKER, J. D. A. 1978 'The boundary layer due to a rectilinear vortex.' *Proceedings of the Royal Society of London* A 359: 167-188.

WANG, K. C. 1974 'Boundary layer over a blunt body at high incidence with an open type of separation.' *Proceedings of the Royal Society of London* A 340: 33-35.

WATSON, J. 1958 'A solution of the Navier-Stokes equations illustrating the response of a laminar boundary layer to a given change in the external stream velocity.' *Quarterly Journal of Mechanics and Applied Mathematics* **11**, pp. 302-325.

WERLÉ, H. 1962 'Separation on axisymmetrical bodies at low speed.' *Recherche Aérospatial* **90**: 3-14.

WILLIAMS, J. C., III 1977 'Incompressible boundary-layer separation.' *Annual Review of Fluid Mechanics* **9**: 113-144.

WINKELMANN, A. E. & BARLOW, J. B. 1980 'Flowfield model for a rectangular planform wing beyond stall.' *AIAA Journal* **18**: 1006-1008.

WINKELMANN, A. E. 1981 'An experimental study of separated flow on a finite wing.' AIAA-81-1882.

WOOD, N. J., LEE, K. T. & ROBERTS, L. 1988 'Dynamic control of vortical flow on delta wings at high angles of attack.' AIAA Paper 88-4333.

YOUNG, A. D. 1977 'Some special boundary layer problems.' *Zeitschrift für Flugwissenschaften und Weltraumforschung.* **1**, Heft 6:401-414.
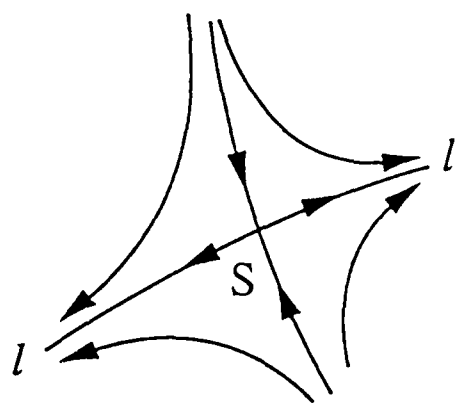
(a)   S = saddle point

l-l = separation line
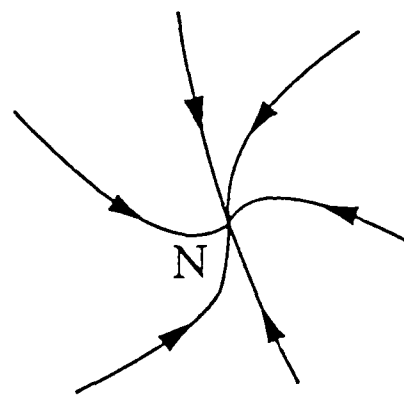
(b)   N = node
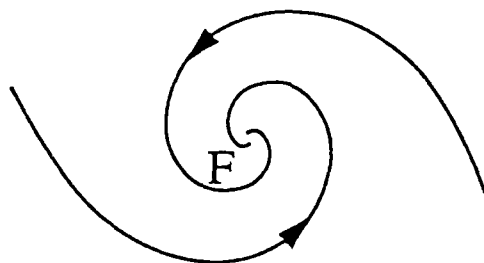
(c)   F = focus
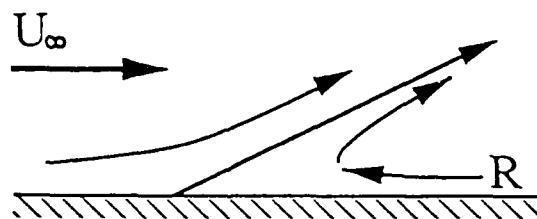
(d) R = reversed flow

Figure 2.1   Defining diagrams: Skin-friction lines characteristic of a (a) "saddle point," (b) a "node," and (c) a "focus." (d) Schematic of reversed flow..

Definitions that pertain to separated flows.

Boundary-Layer Edge

Free Stream Flow

Laminar

Turbulent

Dead Air Region

Recirculating Vortex

S(Separation)

T(Transition)

R(Reattachment)
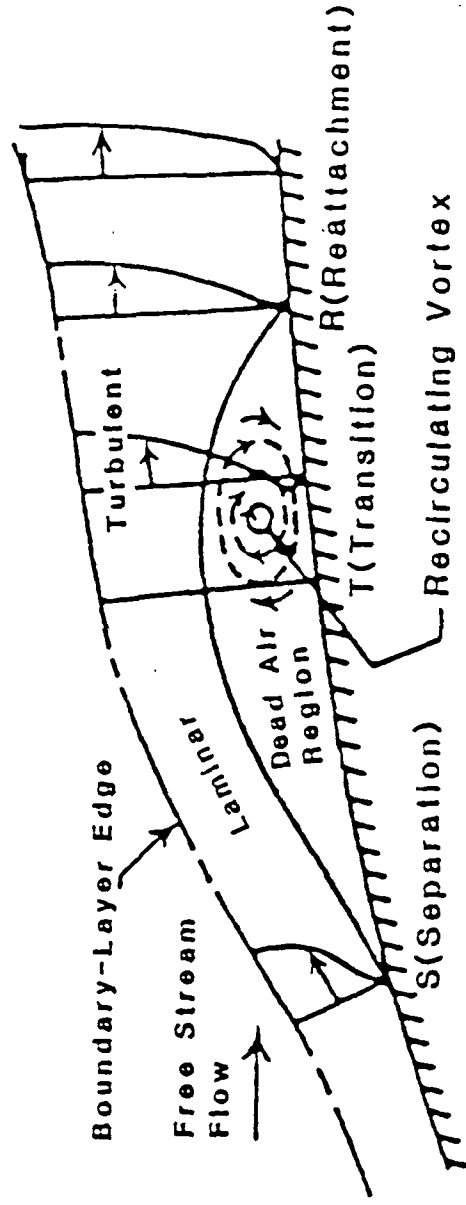
Figure 2.2   Stationary, two-dimensional separation, from Horton (1968).

(a)

(b)

Downstream-
moving
separation

Upstream-
moving
separation
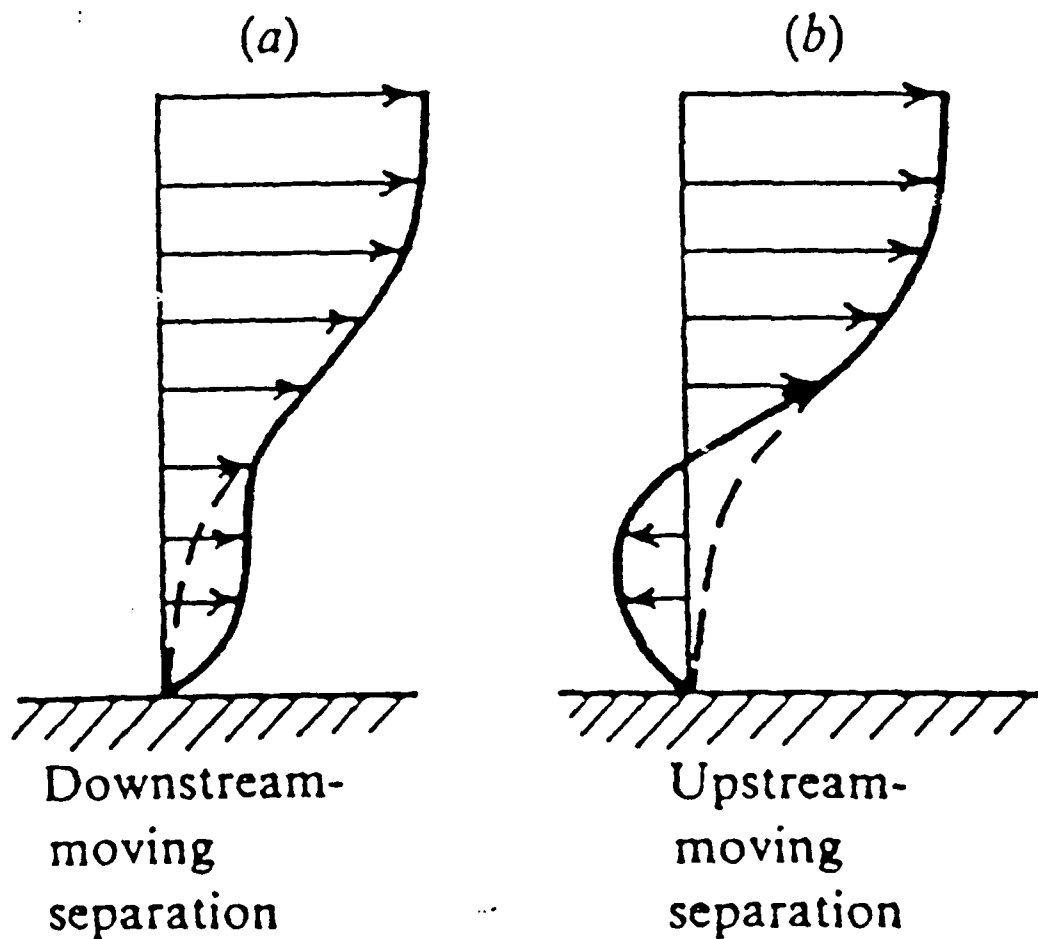
locity profiles in separated flows. - - -, steady separation;
—— unsteady separation velocity profile.

Figure 2.3   Upstream- and downstream-moving MRS 'separations' (Didden and
Ho, 1985).
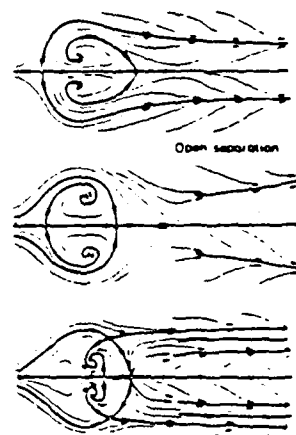
Figure   A variety of skin-friction patterns are found on a
hemisphere-cylinder at incidence: (a) $\alpha = 10°$, (b) $\alpha = 15°$,
(c) $\alpha = 33.5°$. Bippes (1986).

Figure 2.4   Limiting streamlines visualized for flow about an axisymmetrical
body at an angle of attack (Bippes, 1987).
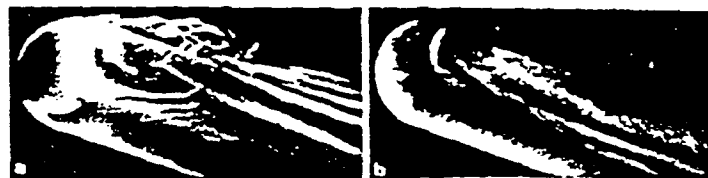
Figure   Owl-face separation structure on an axisymmetric body at
incidence (a) spatial structure visualized by dye, (b) skin-
friction pattern. Bippes (1986).

Figure   Owl-face skin-friction pattern on a rectangular wing at
incidence. Bippes (1986).

Figure 2.5   Owl face of the first kind separation on an axisymmetrical body and
on an airfoil each at an angle of attack (Bippes, 1987).
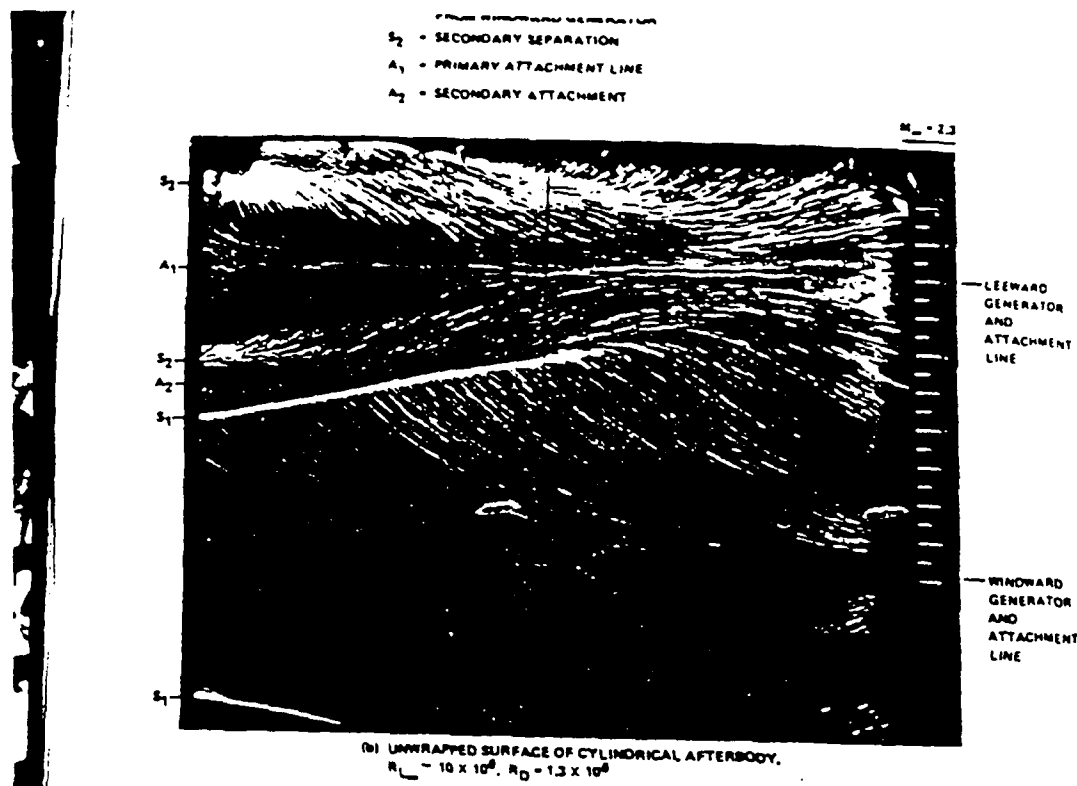
Figure 2.6   Surface oil flow patterns on θ_{cone} blunted cone-cylinder at $\overline{\alpha} = 0.6$, Mach 2.3 with turbulent boundary layers (Boersen, 1975).

3-D Separation At A Wall With
No Singularity Of Shear Stress
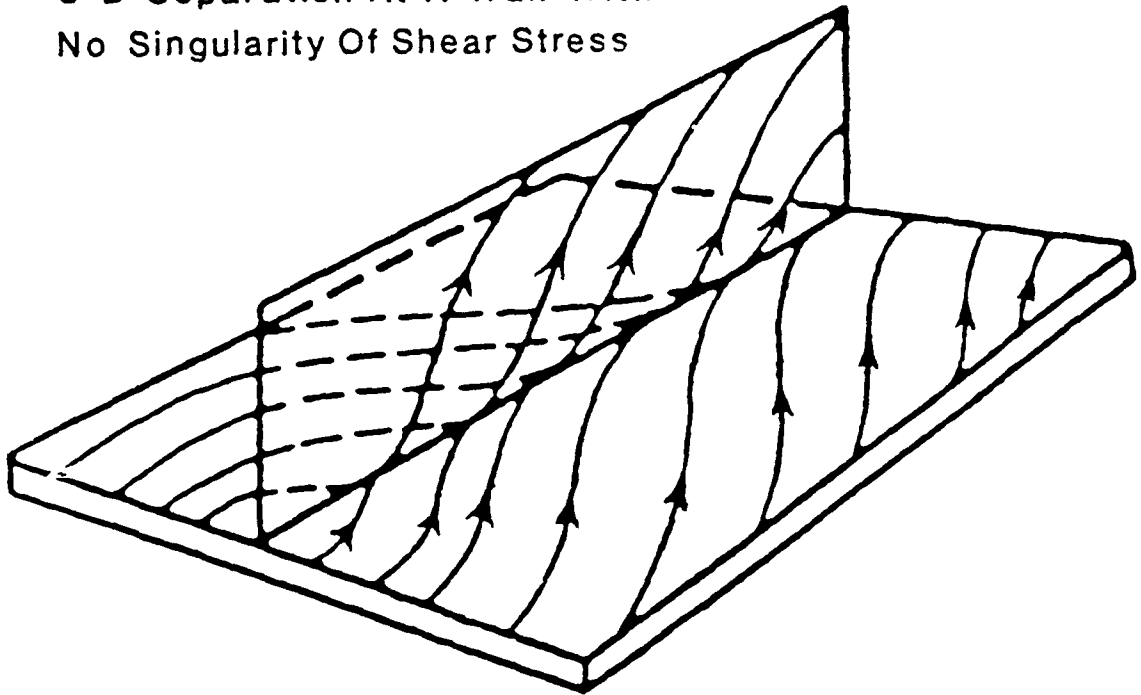
Streamsurfaces Generated Near

A Negative Bifurcation
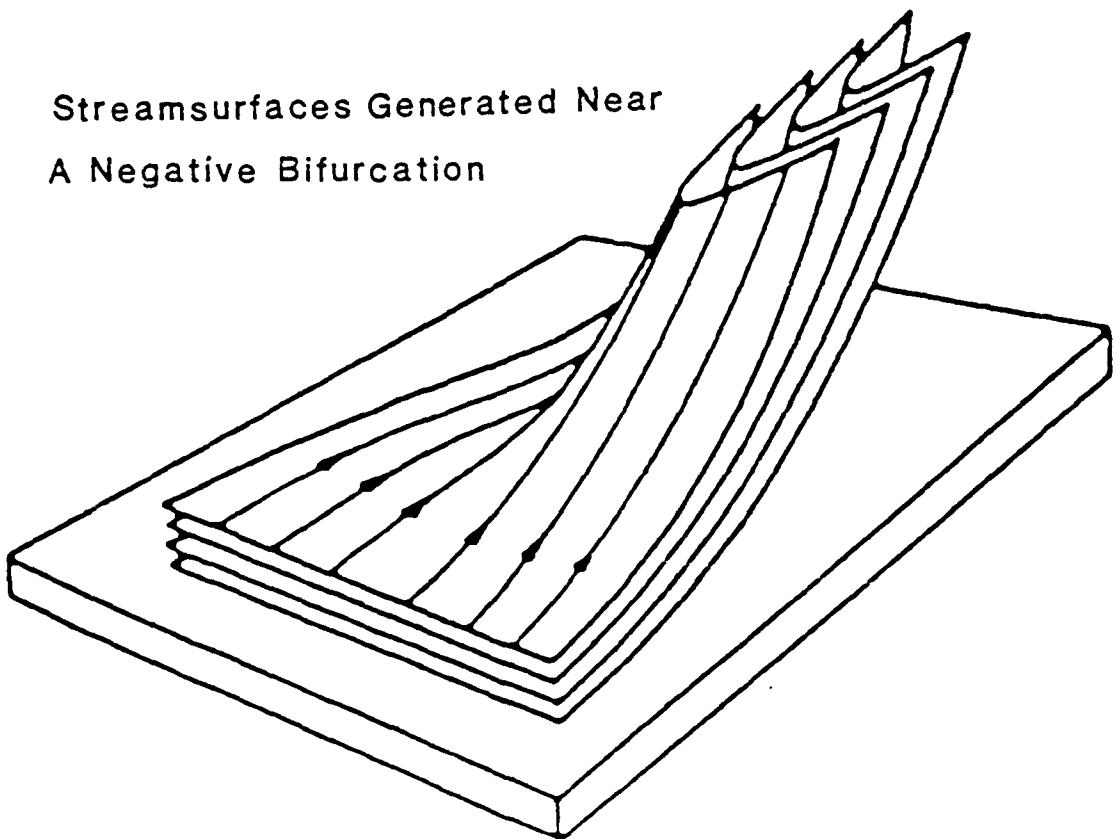
Figure 2.7   Convergent streamlines without separation: Hornung and Perry (1984).

Surface patterns on a stalled airfoil reveal three-dimensional separations.

Time-averaged wall
streamlines and
vortical structures
of rectangular wing
attached to a wall.
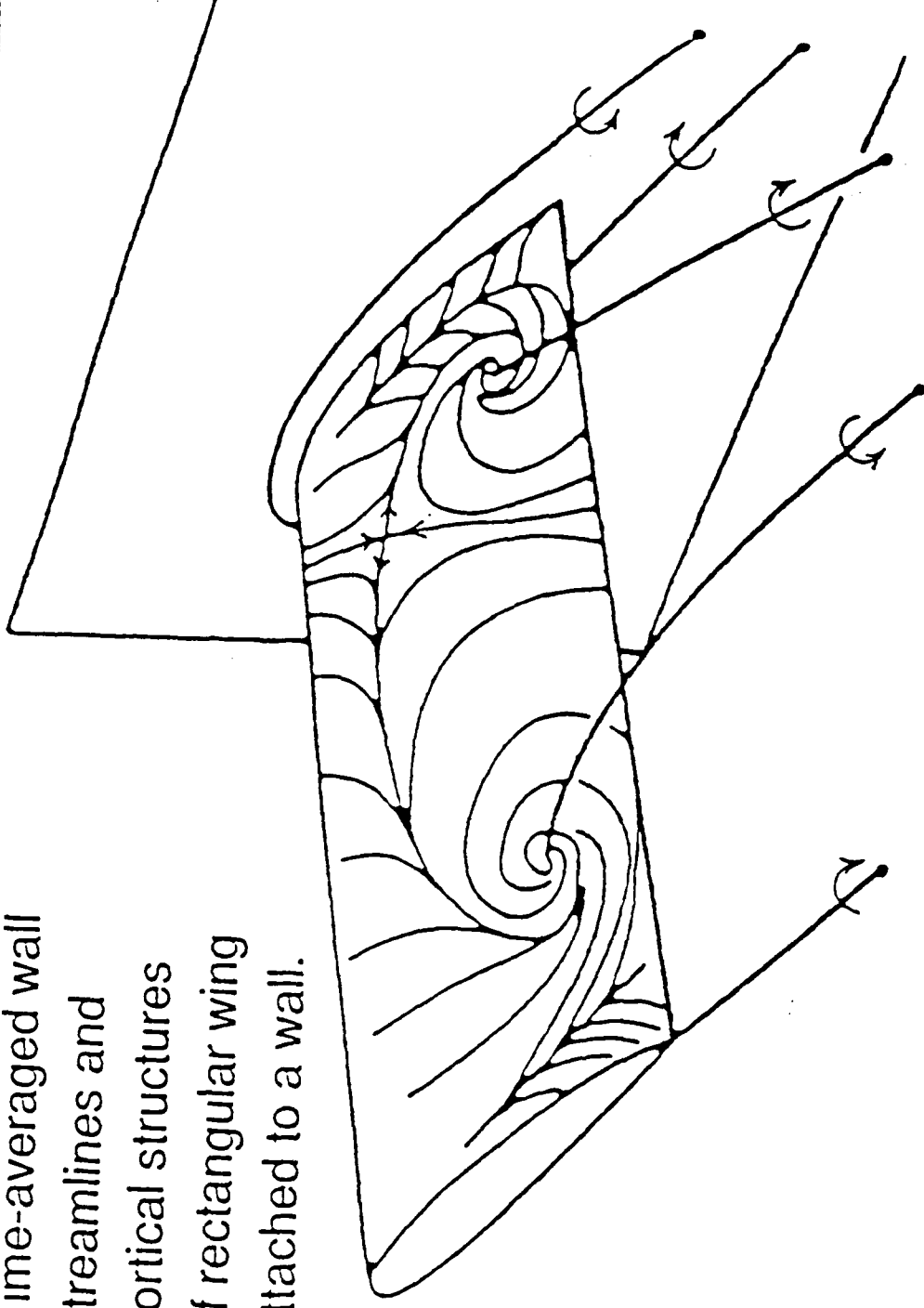
Figure 2.8   Limiting streamlines and vortex skeletons on a stalled airfoil, Perry and Hornung (1984).
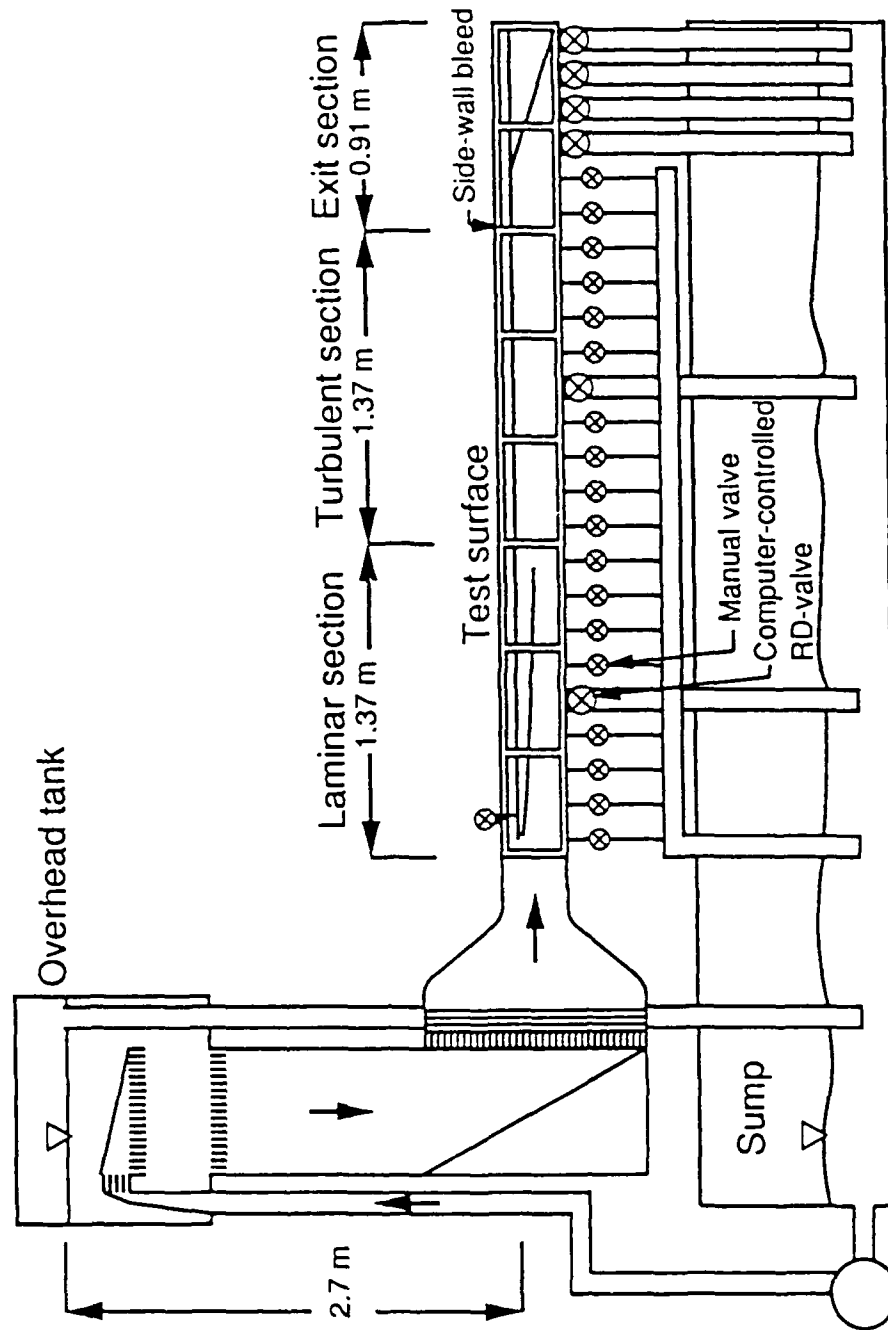
Figure 3.1 Schematic of the Stanford, Unsteady Boundary Layer, Research Water Tunnel.

Inside the test section

Plates are perforated to
tailor suction through wall.

Honeycomb and contraction guide
flow uniformly across span.

Wet
pulley

Revolving-disc seals against
a Delrin bearing for low-
friction area adjustment.

Downcomer conducts water to
sump. Atmospheric pressure
is maintained at valve exit.

Flat dc motor produces high torque
for high-speed valve positioning.

RVDT monitors shaft position for
analog-feedback control.

All electrical components are dry and
multiply-sealed against moisture.

Figure 3.2   Schematic of the Revolving-Disk Valve Assembly.
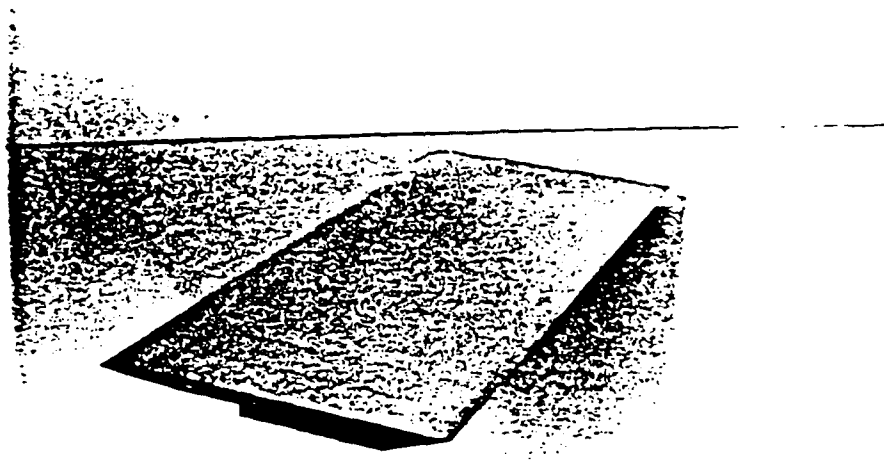
Figure 3.3   Photograph of the finished leading edge. The smooth transition from the half-ellipse to a flat plane is visible on the top surface. The tail is sloped at 22.5° to butt against the edge glass test surface and to set the slope of the dye slot.
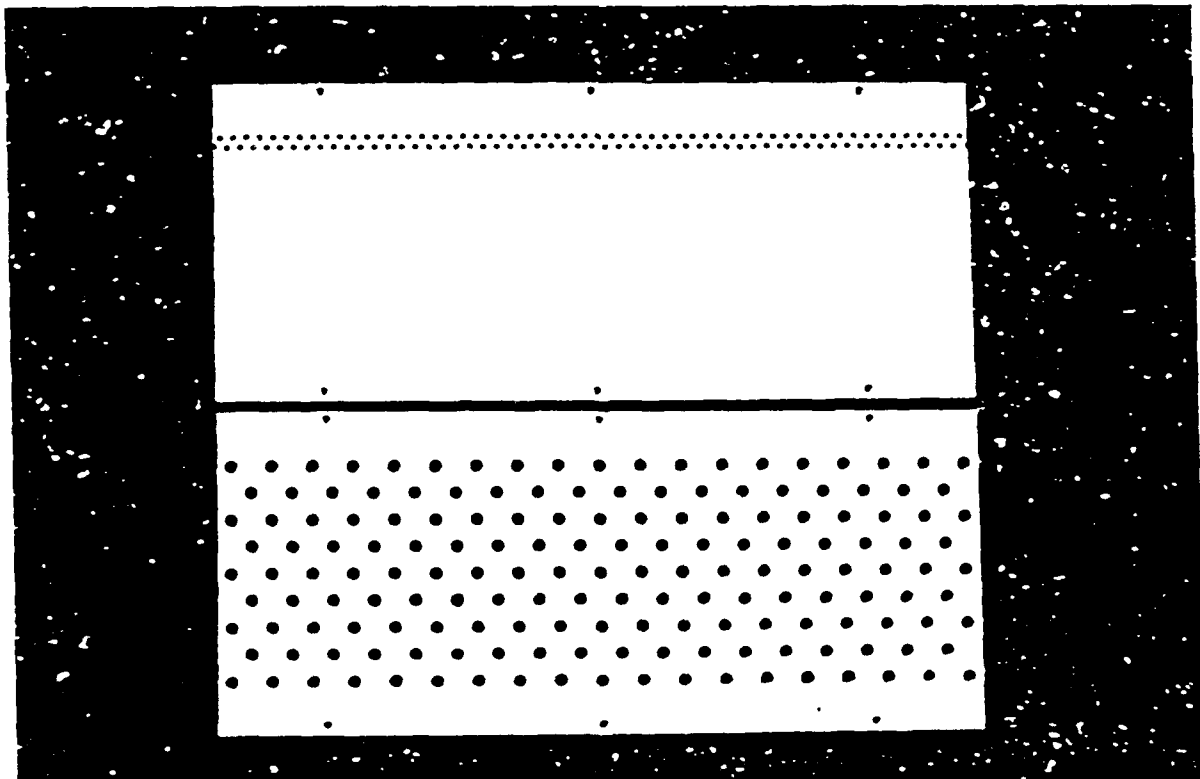
Figure 3.5   Photograph perforated control-wall plates: (a) type 1 plate. (b) type 2 plate.

Bypass Bleed

Nozzle

Dye Inlet

Glass

Inlet Flow

Boundary layer begins on elliptic leading edge
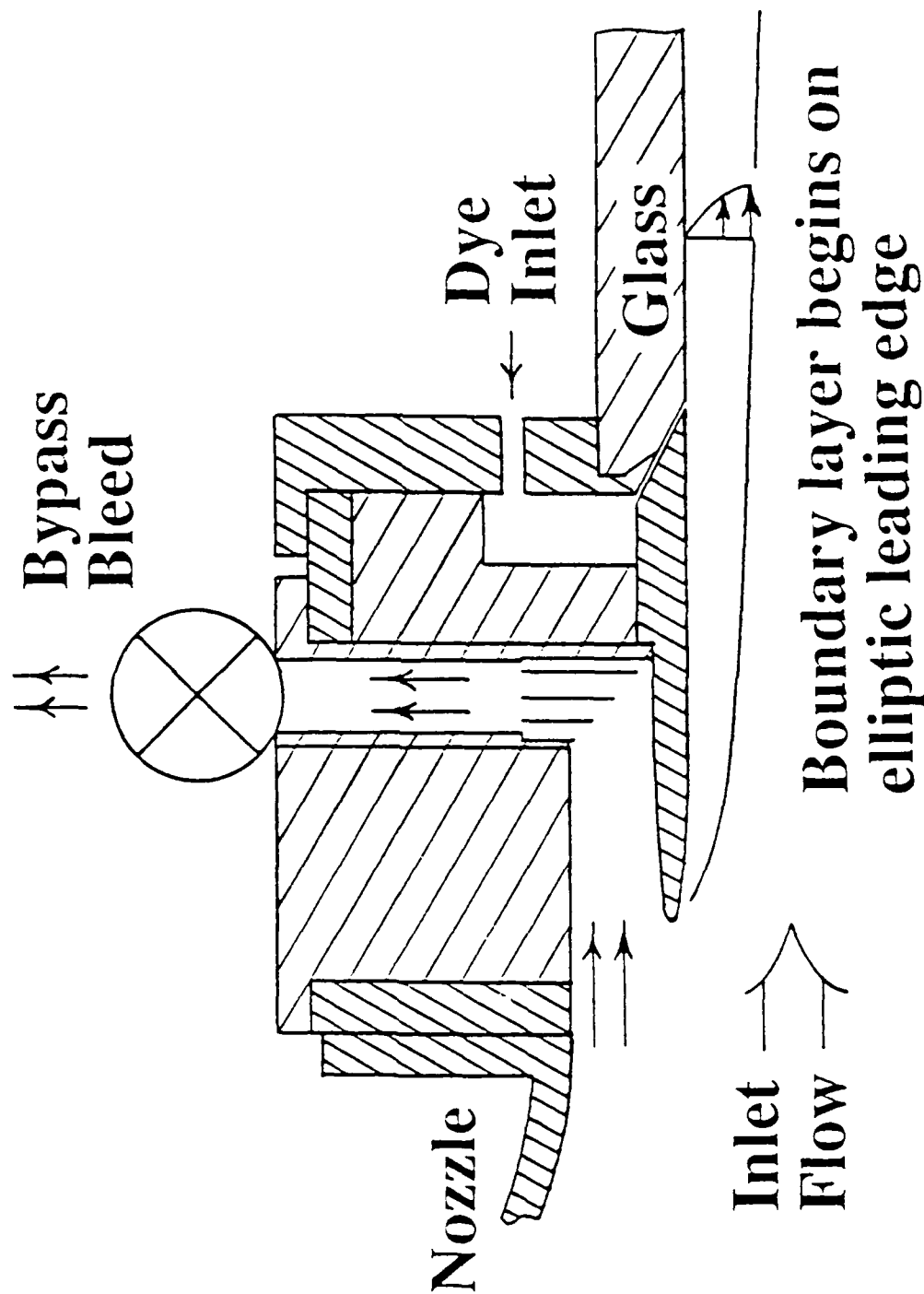
Figure 3.4 Schematic of the leading-edge and bypass-bleed assemblies in the test section. A fresh boundary layer is grown on the lower side of the leading edge. The bypass bleed is used to set the stagnation point on the leading edge. Bypass fluid is returned to the sump. A dye slot is formed at the junction of the leading edge with the test
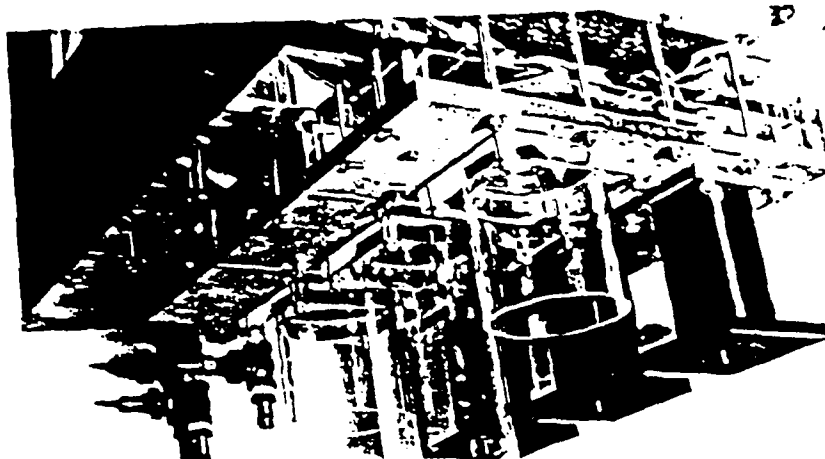
Figure 3.6   Photograph of two manual and three Revolving-Disc valves mounted
under the control wall of the test section.

Figure 3.7   *Photograph of a partially disassembled Revolving-Disc valve. The
Delrin bearing/seal, the drive sprocket and drive cylinder are shown
attached to the stainless-steel valve plate. Also shown are a coarse
disc, a fine disc, a drive belt, a nylon shaft bearing, a spring, two
washers and a snap ring.*
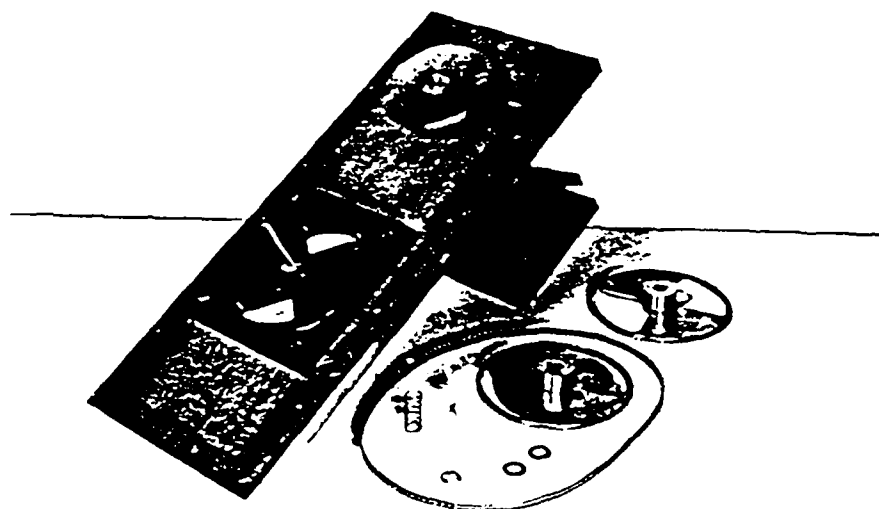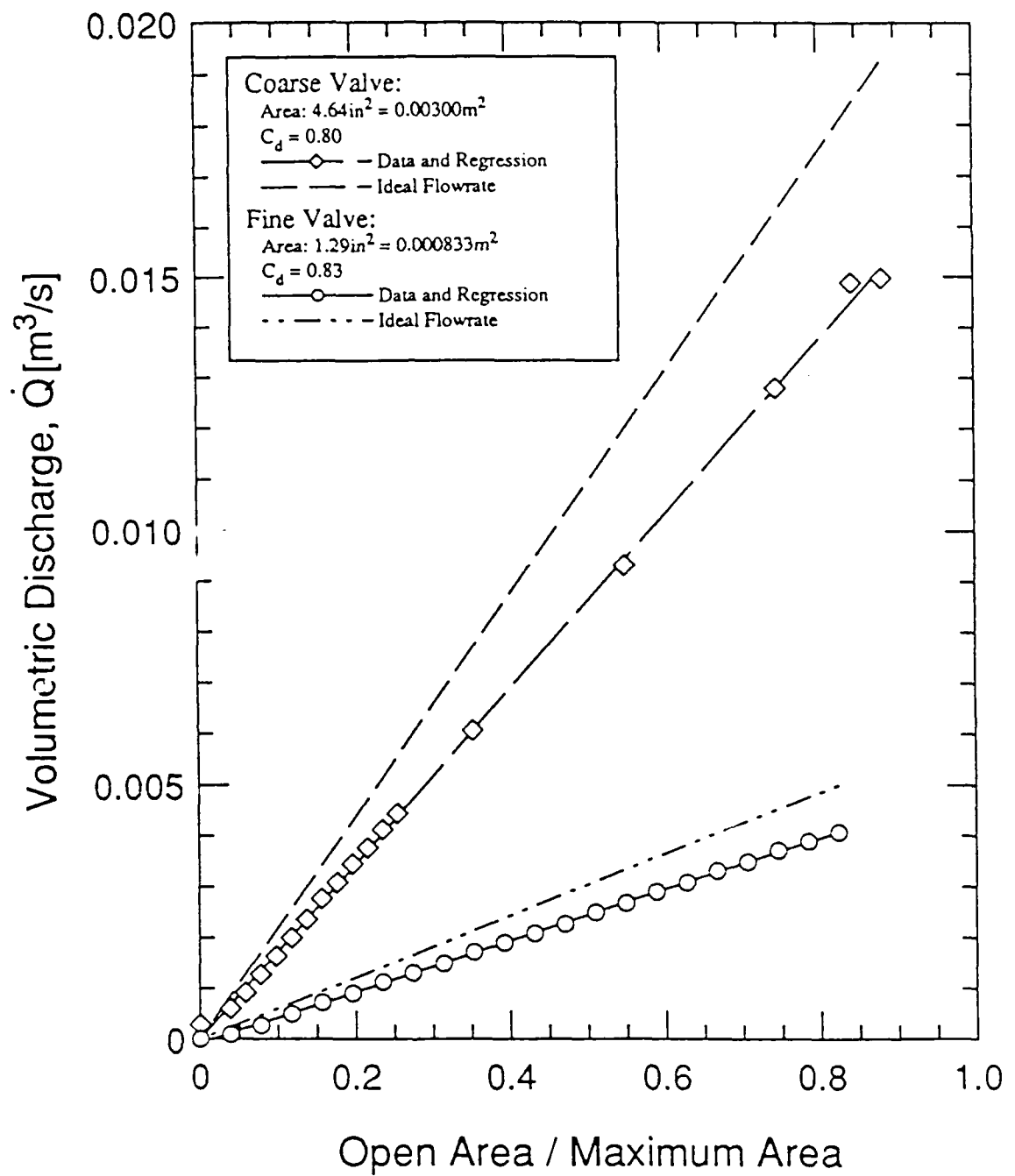
Figure 3.8   Volume flowrates for the Revolving-Disc valve versus open angle, α. Results for two versions of the revolving disc are shown.

Parameter	Value at integral upper limit	
limit	$y \rightarrow \infty$	$y = \delta_{99}$
δ^*	1.72108	1.715
θ	0.664103	0.6533
H	2.5916	2.605

TABLE 4.1 Comparision of integral parameters for the Blasius zero pressure-gradient velocity profile for two upper limits to the integral.
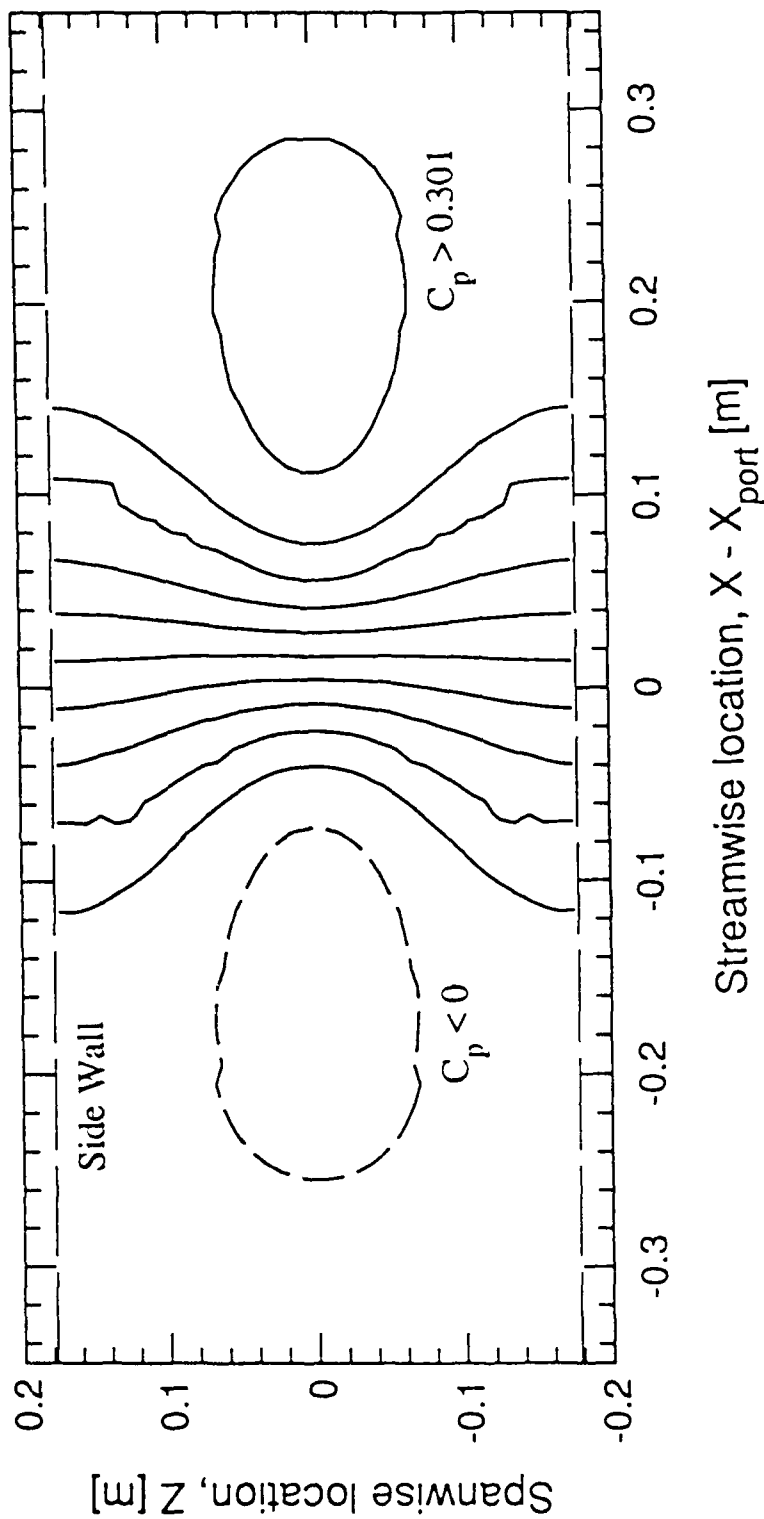
Figure 4.1   Contour plot of potential-flow C_p for base case flow: Case 10.

Integral Area Algorithms

O d:\march_89\@lp_b\m0910ss0.dat

Dark Area $\leq \delta_{99}$

U_∞[m/s]:   0.214

δ^*[m]:   0.00751

θ[m]:   0.00129

Light and Dark Area

U_{max}[m/s]: 0.223

δ^*[m]:   0.00860

θ[m]:   0.00225

δ_{99}

y/H

U [m/s]
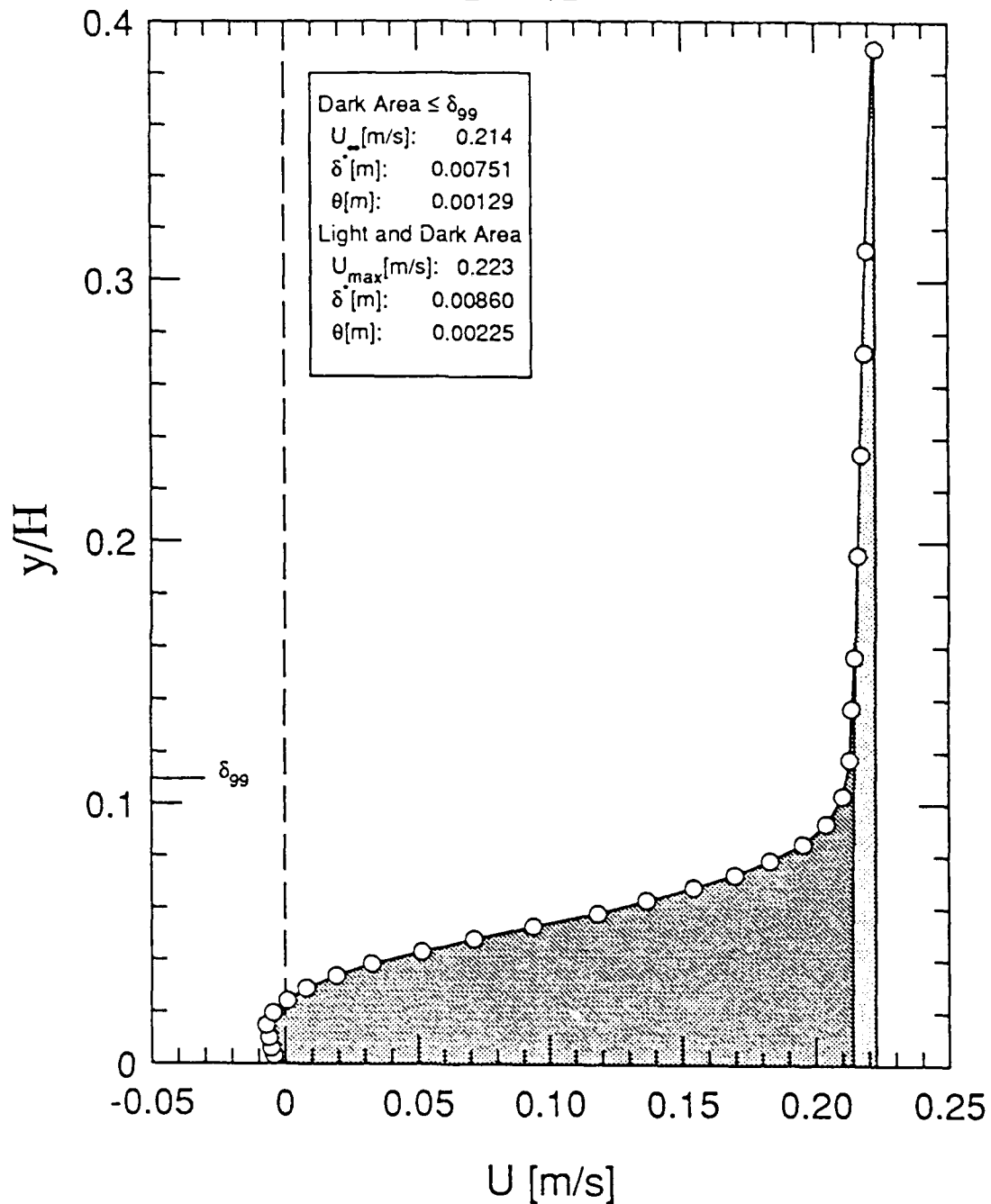
Figure 4.2   The area of the displacement thickness as estimated by two candidate algorithms is shown. Algorithm (1), which used a $g(y)$ fit to the potential flowfield, computes the area filled with dark gray up to δ_{99}. The polynomial $g(y)$ shows an excellent fit to the outer six points of the time-averaged velocity profile. Algorithm (2) computes the area filled with light and dark gray..
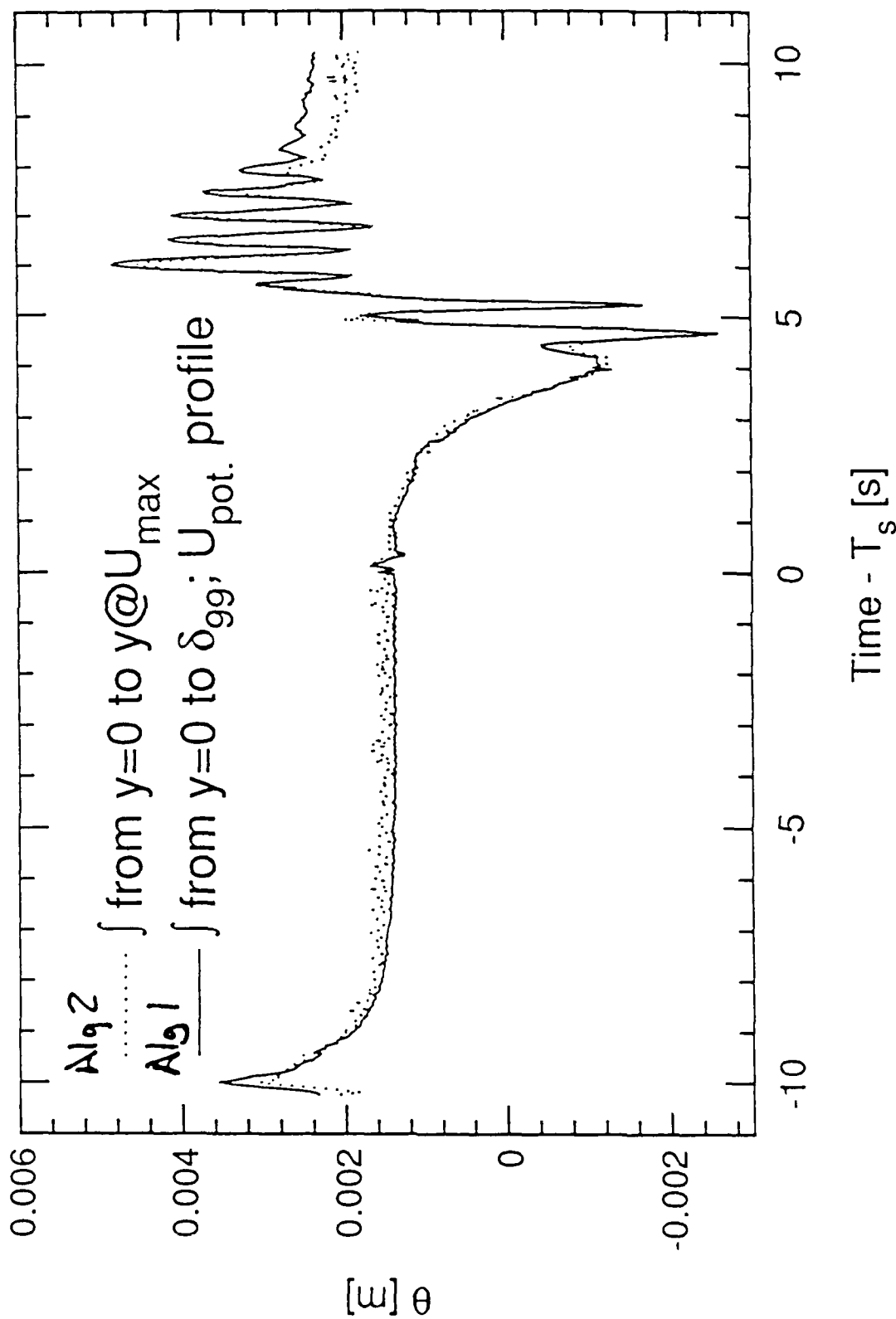
Figure 4.3   Evolution of the momentum thickness over time is shown for phase-averaged velocity profiles at LP:1.   The results of algorithms (1) and (2) for finding the upper limit to the integral are compared.
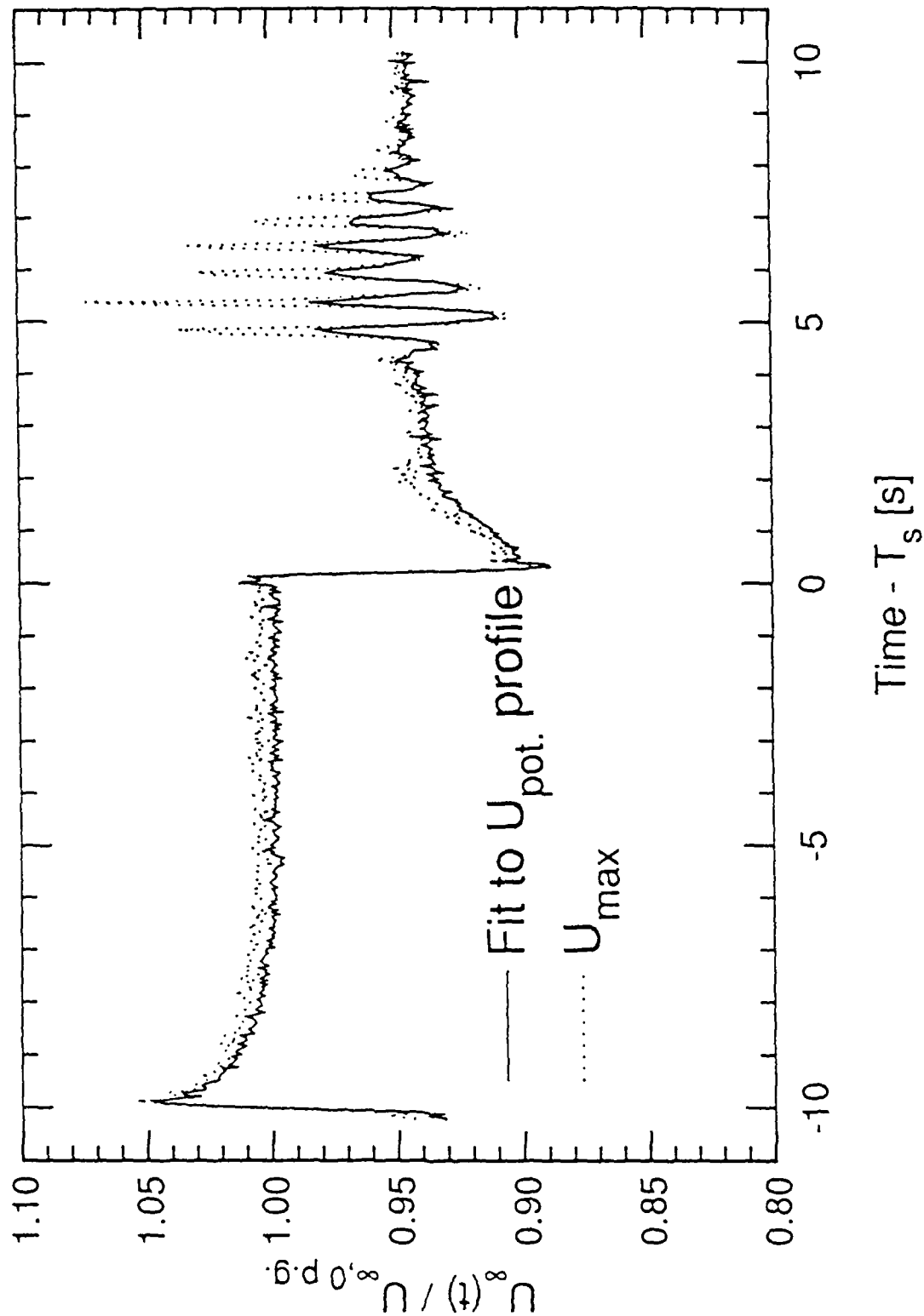
Figure 4.4   Evolution of the estimated freestream velocity over time is shown for phase-averaged velocity profiles at LP:1. Two algorithms for determining U_∞ are compared.

Initial Conditions					
U_0	0.189	0.214	0.250	0.135	[m/s]
Inlet Flowrate	0.00864	0.00979	0.0114	0.00617	[m³/s]
$\theta_{0\,P.G.}$	0.00143	0.00133	0.00124	0.00165	[m]
Re_θ	247	265	284	213	

Note: $\theta_{0\,P.G.}$ and Re_θ at location LP:B a: · from fit of theory to data.

TABLE 5.2a   Initial conditions for all flow cases.

	U_0 [m/s]				
	0.189	0.214	0.250	0.135	
Waveform	Suction Flowrate, % of Inlet Flowrate				Volume [m³/s]
0.Wav	18.6	16.4	14.1		0.00161
1.Wav	16.3	14.4	12.3		0.00141
2.Wav	13.9	12.3	10.5		0.00120
3.Wav	11.6	10.3	8.8		0.00100
4.Wav	9.3	8.2	7.0	13.0	0.00080
5.Wav	7.0	6.2	5.3		0.00060
Waveform	Maximum $\partial C_p / \partial x$ [m⁻¹] ; Potential flow estimate				
0.Wav	2.86	2.52	2.19		
1.Wav	2.53	2.22	1.93		
2.Wav	2.16	1.90	1.66		
3.Wav	1.86	1.63	1.42		
4.Wav	1.51	1.32	1.14	2.04	
5.Wav	1.14	1.00	0.86		
Waveform	$(\partial C_p / \partial z)_{max} / (\partial C_p / \partial x)_{max}$; Potential flow estimate				
0.Wav	0.106	0.106	0.105		
1.Wav	0.105	0.105	0.105		
2.Wav	0.104	0.105	0.104		
3.Wav	0.094	0.095	0.096		
4.Wav	0.091	0.092	0.093	0.093	
5.Wav	0.097	0.097	0.098		
Waveform	Case Numbers for textual reference				
Zero P.G.	0Z	1Z	2Z	3Z	
0.Wav	00	10	20		
1.Wav	01	11	21		
2.Wav	02	12	22		
3.Wav	03	13	23		
4.Wav	04	14	24	34	
5.Wav	05	15	25		

TABLE 5.1   Flow Parameters: (a) Upstream conditions for the four U_0 cases; (b) Four uniform velocity and nineteen adverse, velocity gradient cases by case number, per cent suction and pressure-gradient estimate.

Integral Parameters for Zero Pressure-Gradient Conditions						
from Time-averaged profiles under steady conditions						
U_0	x [m]	Station	δ^*	$\%\Delta$	θ	$\%\Delta$
0.139	0.555	LP:A	0.00437	1.9	0.00172	5.2
	0.575	LP:B	0.00453	4.2	0.00167	1.0
	0.613	LP:D	0.00423	−4.7	0.00157	−7.5
	0.651	LP:1	0.00538	18.6	0.00186	7.5
	0.689	LP:2	0.00521	12.5	0.00166	−5.7
0.187	0.575	LP:B	0.00352	−6.1	0.00136	−4.7
	0.613	LP:D	0.00361	−5.7	0.00135	−7.6
	0.651	LP:1	0.00415	5.9	0.00156	4.4
	0.651	LP:1	0.00379	−3.1	0.00143	−4.2
	0.689	LP:2	0.00418	4.6	0.00156	2.4
0.215	0.555	LP:A	0.00302	−12.4	0.00116	−11.9
	0.575	LP:B	0.00331	−5.3	0.00126	−5.4
	0.575	LP:B	0.00344	−1.5	0.00125	−6.0
	0.613	LP:D	0.00365	2.1	0.00135	−0.9
	0.613	LP:D	0.00364	1.9	0.00139	2.3
	0.651	LP:1	0.00354	−3.1	0.00136	−2.3
	0.651	LP:1	0.00376	3.0	0.00142	2.1
	0.651	LP:1	0.00390	6.8	0.00154	11.0
	0.689	LP:2	0.00404	8.3	0.00153	8.1
	0.689	LP:2	0.00356	−4.5	0.00132	−6.9
	0.727	LP:3	0.00402	5.6	0.00158	9.1
	0.775	LP:4	0.00353	−9.3	0.00148	−0.2
	0.775	LP:4	0.00392	0.7	0.00150	1.0
0.248	0.575	LP:B	0.00302	−7.2	0.00125	0.7
	0.613	LP:D	0.00338	1.6	0.00133	5.0
	0.651	LP:1	0.00331	−2.6	0.00125	−3.8
	0.689	LP:2	0.00376	8.4	0.00158	19.2
	0.689	LP:2	0.00358	3.2	0.00137	3.9
from Phase-averaged profiles						
0.214	0.575	LP:B	0.00308	−12.2	0.00113	−15.7
	0.613	LP_D	0.00356	−0.6	0.00142	4.3
	0.651	LP:1	0.00353	−3.6	0.00137	−1.7
	0.689	LP:2	0.00405	8.3	0.00161	12.8
	0.727	LP:3	0.00373	−2.3	0.00132	−8.8
	0.775	LP:4	0.00366	−6.4	0.00141	−5.1

TABLE 5.2 Boundary-layer integral parameters for cases 0Z, 1Z, 2Z, and 3Z at several streamwise locations. Results from nonstationary case 10 are also listed for the boundary layer after adverse conditions have been released.

Vel. Case	Suction valve status	Streamwise Velocity U				
		mean [m/s]	Std. Dev. [m/s]	%	(max-min)/2 [m/s]	%
0	leak-tight	0.1817	0.0020	1.1	0.0041	2.3
	closed	0.1832	0.0018	1.0	0.0037	2.0
1	leak-tight	0.2110	0.0015	0.7	0.0029	1.4
	closed	0.2125	0.0012	0.6	0.0024	1.1
2	leak-tight	0.2477	0.0027	1.1	0.0056	2.2
	closed	0.2500	0.0026	1.0	0.0044	1.8
3	leak-tight	0.1354	0.0013	1.0	0.0022	1.6
	closed	0.1388	0.0019	1.4	0.0033	2.4

TABLE 5.3 Uniformity of freestream velocities along the centerline confirms zero pressure-gradient Blasius boundary layer.

location	profile	u_tau	u_inf/u	delta	theta	shapeFac
...@lp_A	...iilssi0	0.0147	0.211	0.00567	0.00141	3.96
...@lp_B	...iilssi0	0.0141	0.211	0.00751	0.00129	5.34
...@lp_D	...iilssi0	0.0191	0.209	0.00057	0.00094	12.50
...@lp_1	...iilssi0	0.0021	0.207	0.00670	0.00129	7.40
...@lp_2	...iilssi0	0.0014	0.207	0.01566	0.00206	8.07
...@lp_3	...iilssi0	0.0076	0.205	0.01616	0.00205	7.93
...@lp_7	...iilssi0	0.0092	0.202	0.01743	0.00355	4.99
...@lp_7	...iilssi0	0.0050	0.172	0.01667	0.00217	8.73
...@lp_1	...iilssi0	0.0076	0.176	0.01737	0.00445	3.87
...@lp_1	...iilssi0	0.0241	0.185	0.01514	0.00506	2.54
...@lp_A	...iilssi	0.0141	0.211	0.00561	0.00143	3.51
...@lp_B	...iilssi	0.0145	0.209	0.00571	0.00142	4.74
...@lp_D	...iilssi	0.0157	0.213	0.00791	0.00132	8.29
...@lp_1	...iilssi	0.0225	0.203	0.01466	0.00095	15.51
...@lp_2	...iilssi	0.0246	0.201	0.01509	0.00237	6.36
...@lp_3	...iilssi0	0.0249	0.198	0.01548	0.00236	6.97
...@lp_7	...iilssi	0.0238	0.200	0.01477	0.00350	4.22
...@lp_4	...iilssi	0.0320	0.190	0.01278	0.00496	2.58
...@lp_A	...iiItss2	0.0140	0.212	0.00450	0.00143	3.15
...@lp_B	...iiItss2	0.0142	0.210	0.00582	0.00148	3.94
...@lp_C	...iiItss2	0.0163	0.210	0.00380	0.00150	5.87
...@lp_1	...iiItss2	0.0190	0.203	0.01193	0.00120	9.91
...@lp_2	...iiItss2	0.0199	0.204	0.01432	0.00132	10.81
...@lp_3	...iiItss2	0.0240	0.201	0.01336	0.00275	4.86
...@lp_4	...iiItss2	0.0275	0.196	0.01085	0.00414	2.62
...@lp_A	...iiItss3	0.0143	0.209	0.00413	0.00145	2.95
...@lp_B	...iiItss3	0.0140	0.211	0.00509	0.00146	3.43
...@lp_D	...iiItss3	0.0135	0.205	0.00765	0.00157	4.86
...@lp_1	...iiItss3	0.0159	0.202	0.00977	0.00139	7.03
...@lp_2	...iiItss3	0.0168	0.201	0.01164	0.00122	6.35
...@lp_3	...iiItss3	0.0184	0.203	0.01177	0.00150	7.87
...@lp_4	...iiItss3	.0194	0.197	0.00967	0.00237	3.36
...@lp_A	...iiItss4	0.0141	0.212	0.00534	0.00141	2.72
...@lp_B	...iiItss4	0.0145	0.211	0.00446	0.00152	2.91
...@lp_D	...iiItss4	0.0157	0.208	0.00612	0.00148	4.25
...@lp_1	...iiItss4	0.0154	0.204	0.00775	0.00149	5.20
...@lp_2	...iiItss4	0.0161	0.203	0.00572	0.00142	6.89
...@lp_3	...iiItss4	0.0170	0.203	0.01041	0.00145	7.21
...@lp_4	...iiItss4	0.0177	0.201	0.00911	0.00217	4.21
...@lp_A	...iiItss5	0.0174	0.212	0.00749	0.00154	2.60
...@lp_B	...iiItss5	0.0131	0.212	0.00912	0.00143	2.72
...@lp_D	...iiItss5	0.0176	0.210	0.00522	0.00151	3.46
...@lp_1	...iiItss5	0.0012	0.206	0.00572	0.00136	4.09
...@lp_2	...iiItss5		0.204	0.00578	0.00148	4.75
...@lp_3	...iiItss5	0.0097	0.204	0.00564	0.00173	4.15
...@lp_4	...iiItss5		0.205	0.00778	0.00168	4.54
...@lp_A	...iiItss6	0.0010	0.209	0.00511	0.00151	4.15
...@lp_B	...iiItss6	0.0117	0.211	0.00515	0.00134	3.77
...@lp_D	...iiItss6					

TABLE 5.4 Boundary-layer parameters along the centerline for all velocity and suction cases.

Valve position

Pipe
Riindeload ← → Piston

Closed

5. WAV

4. WAV

3. WAV

2. WAV

1. WAV

0. WAV

-60

-80

-100

|Δvel|

-0,02

-0,03

0,04

0,05 m/s

0

t
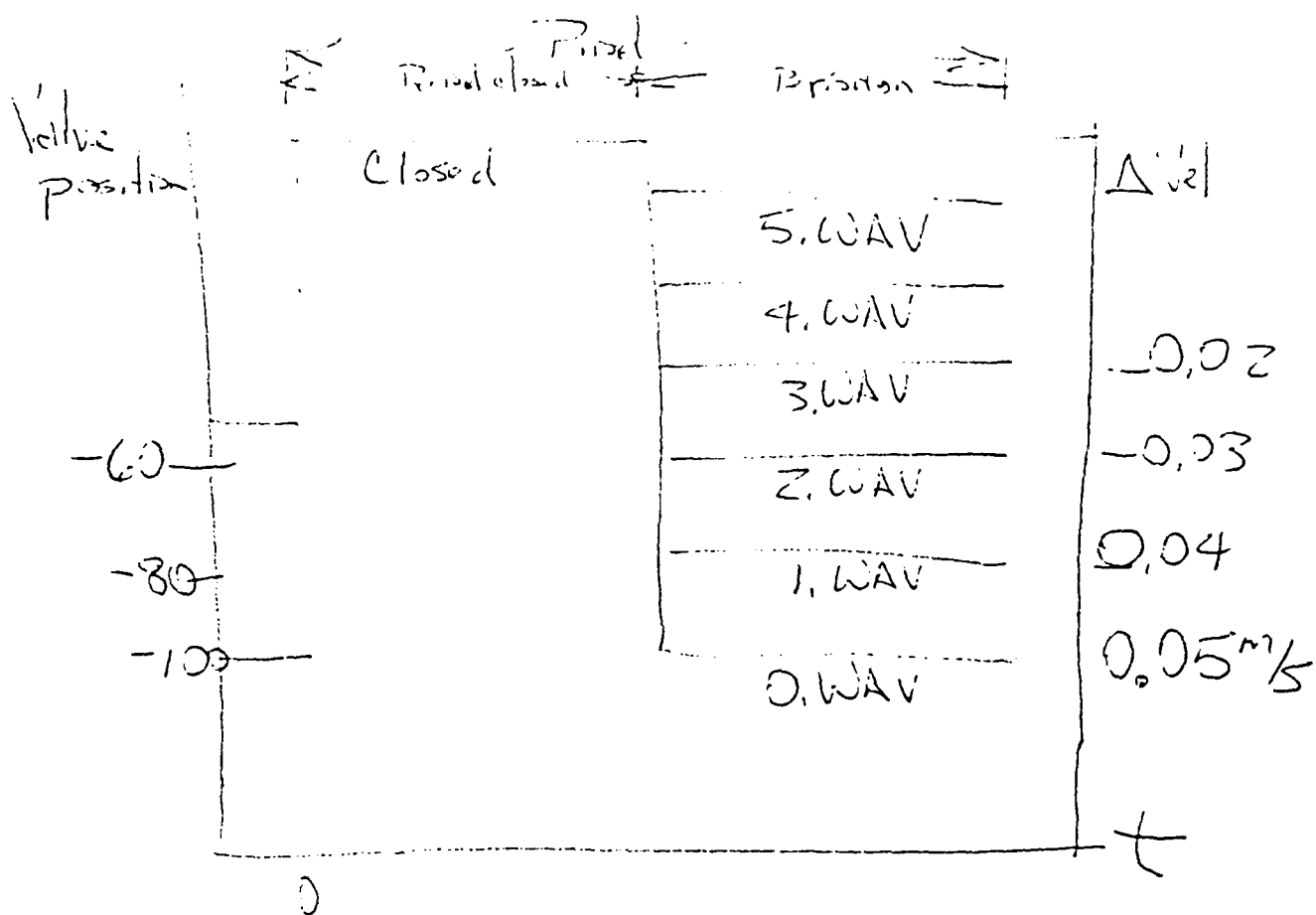
Figure 5.1   These suction waveforms are input to the RD-valve for nonstation-
ary forcing of the freestream. During stationary, adverse freestream-
gradient conditions the suction S is maintained at the volume flow-
rate for "valve open".

(a) Plan View of Separation and Tunnel Geometry

Side Wall

5cm

x

z

Separation line

Saddle point

Image of suction port
on control wall

a

a

CL

A   B   D   1   2   3   4

(b) Section a-a,   Cross-section of Separation

Separation streakline

y

U_∞

x

Separation wake

Test Surface

A   B   D   1   2   3   4
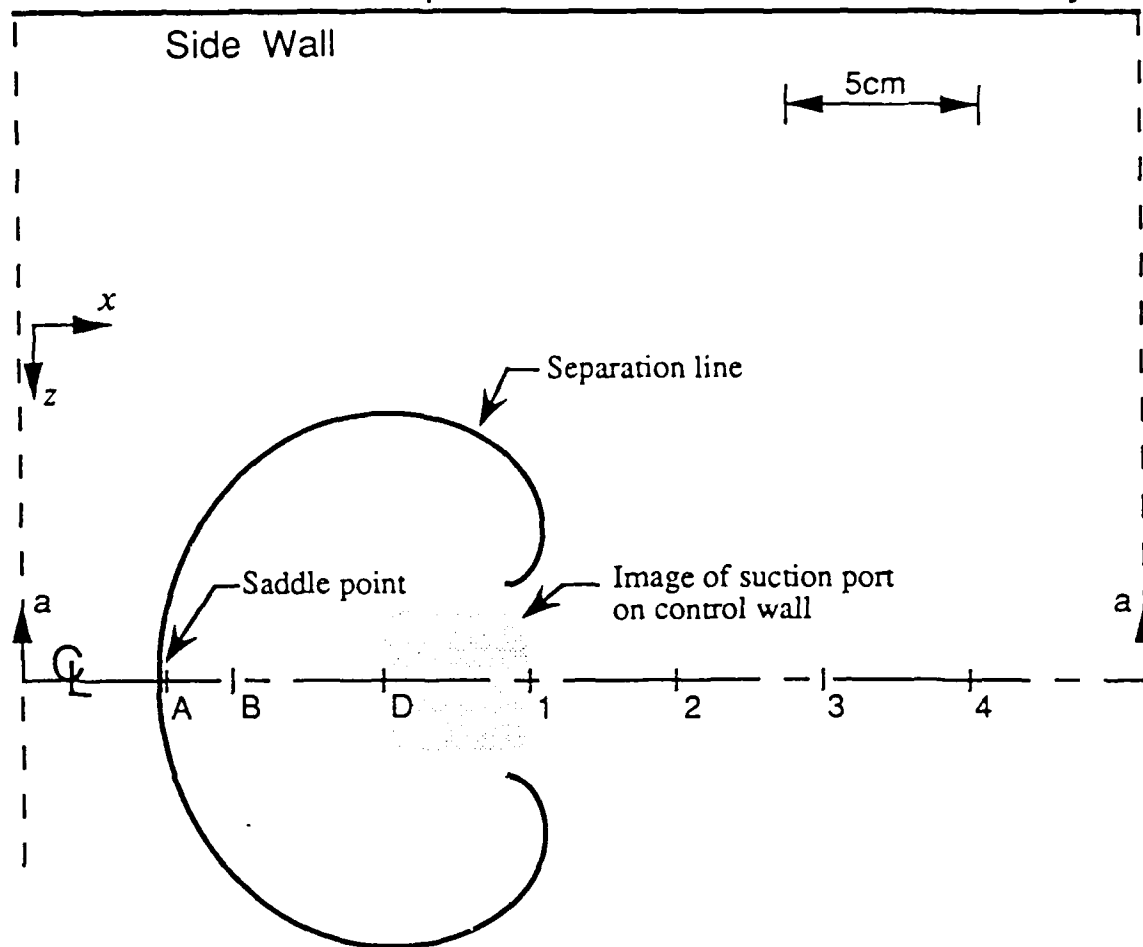
Measurement Stations, LP: ⊔
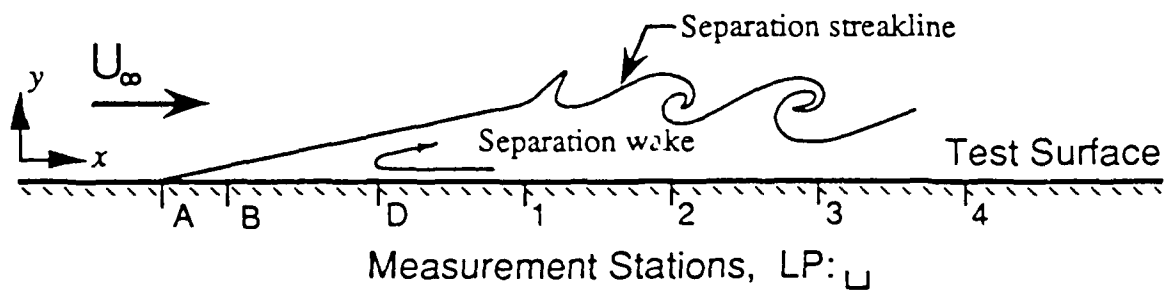
Figure 5.2   A schematic of tunnel geometry and separation structure shows lo-
cation of measurement stations.

Figure 5. Zero Pressure-Gradient Velocity Development - U
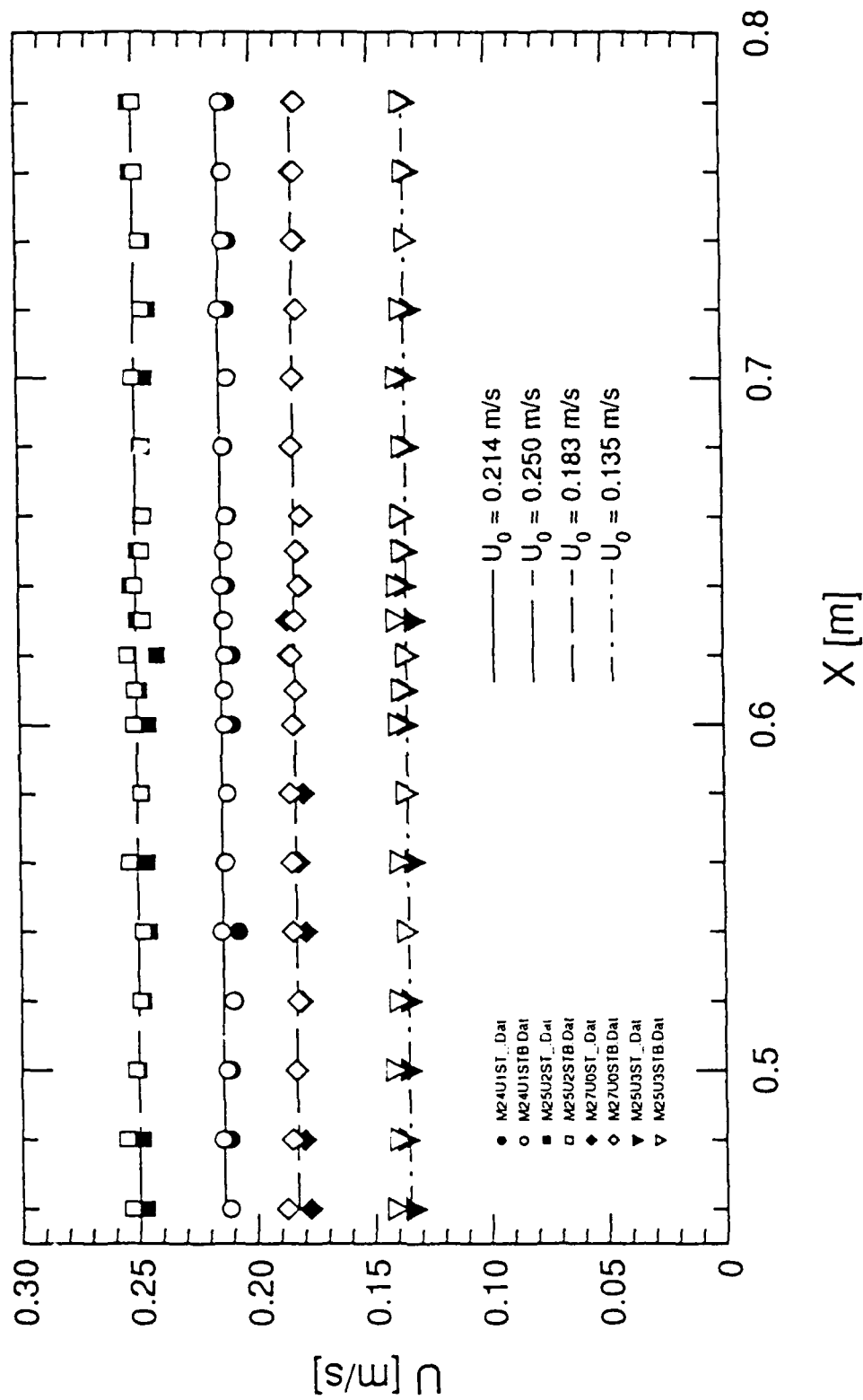
Figure 5.3   Uniformity of freestream velocities along the tunnel centerline indi-
cates zero pressure gradient.
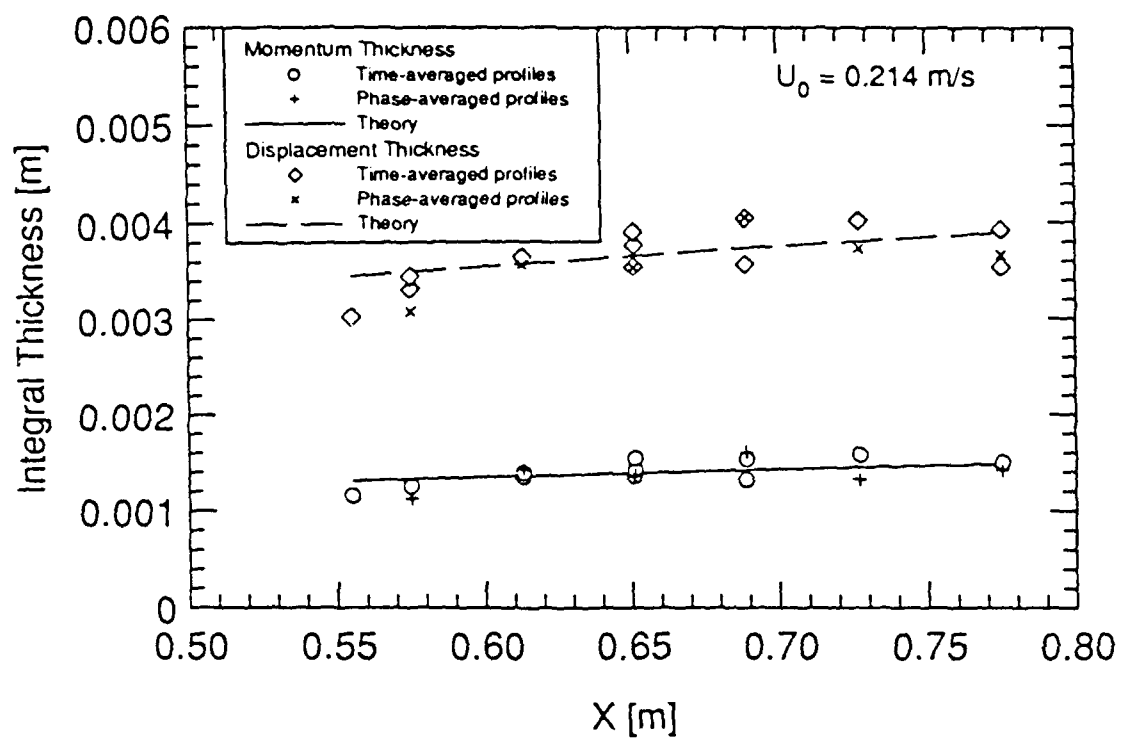
Integral Thickness Development: U1

Figure 5.4   Boundary-layer integral parameters for case 1Z along the centerline of the tunnel.
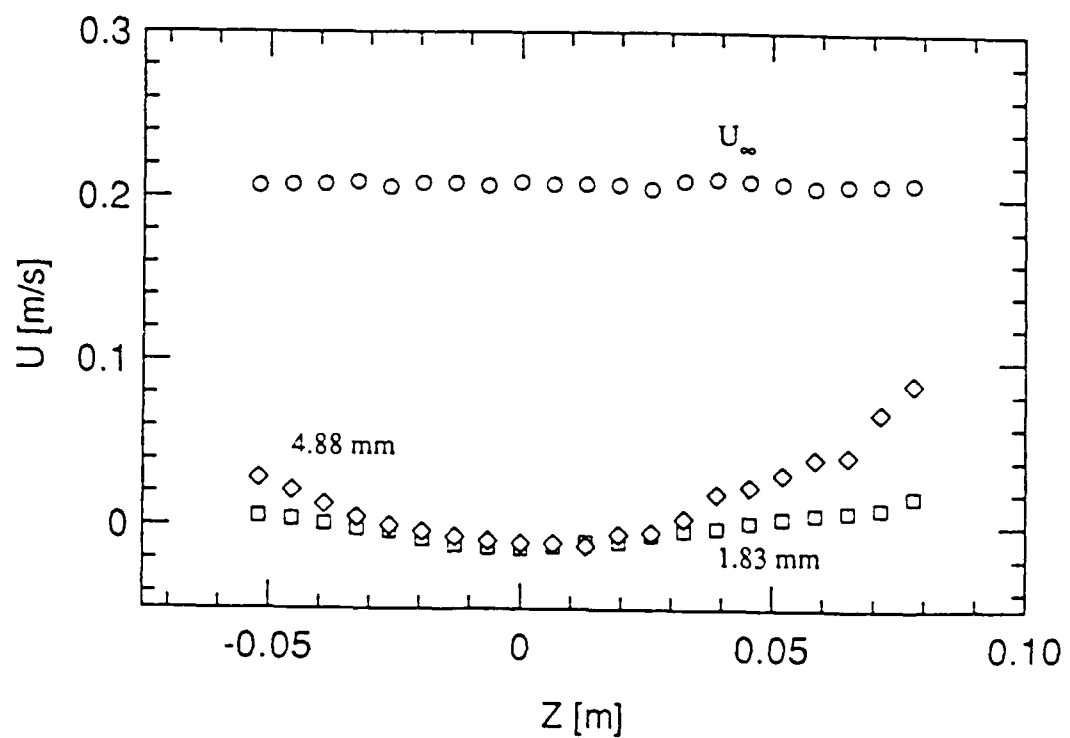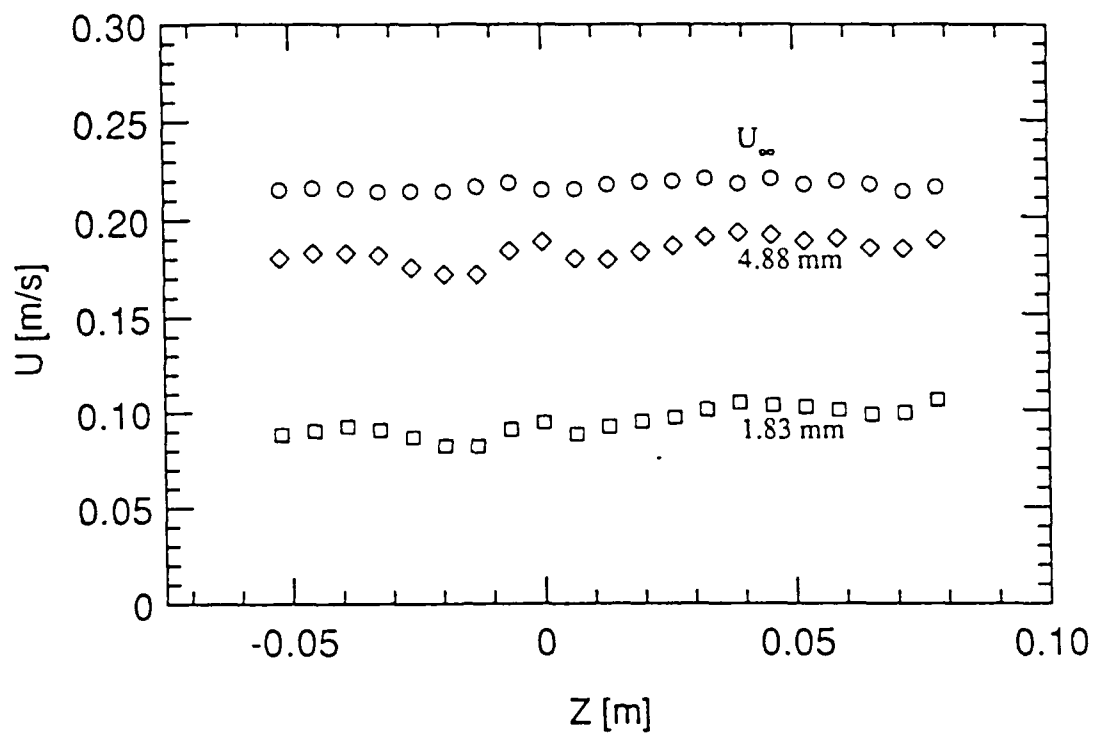
Figure 5.5   Spanwise velocity profiles during (a) uniform freestream conditions,
(b) adverse freestream-velocity gradient conditions.
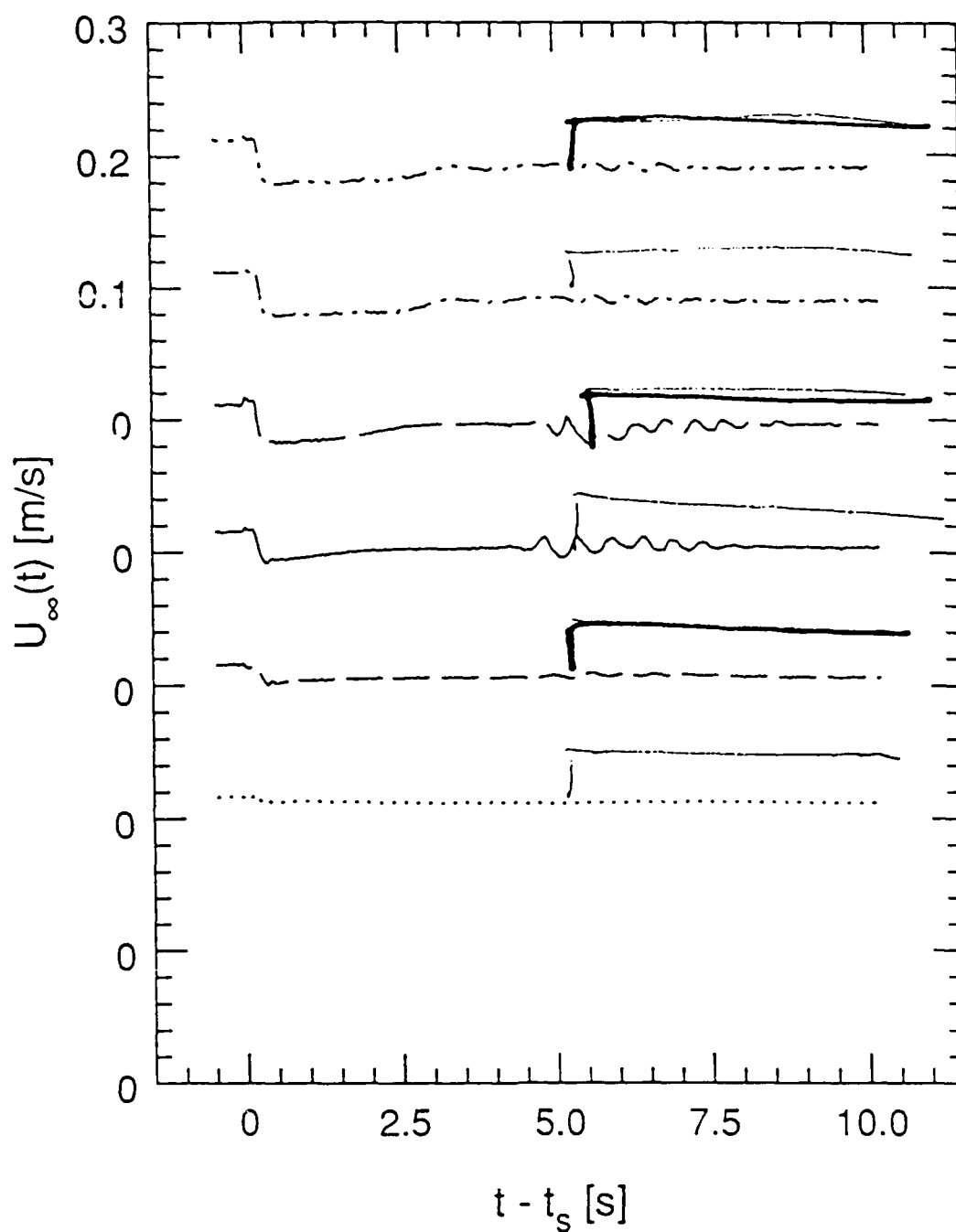
Figure 5.6   Freestream $\langle u \rangle$-velocity versus phase at three locations along the centerline.

Figure   Histories of potential U_∞ for the developing separation:

Freestream U-velocity vs. Chord and Phase
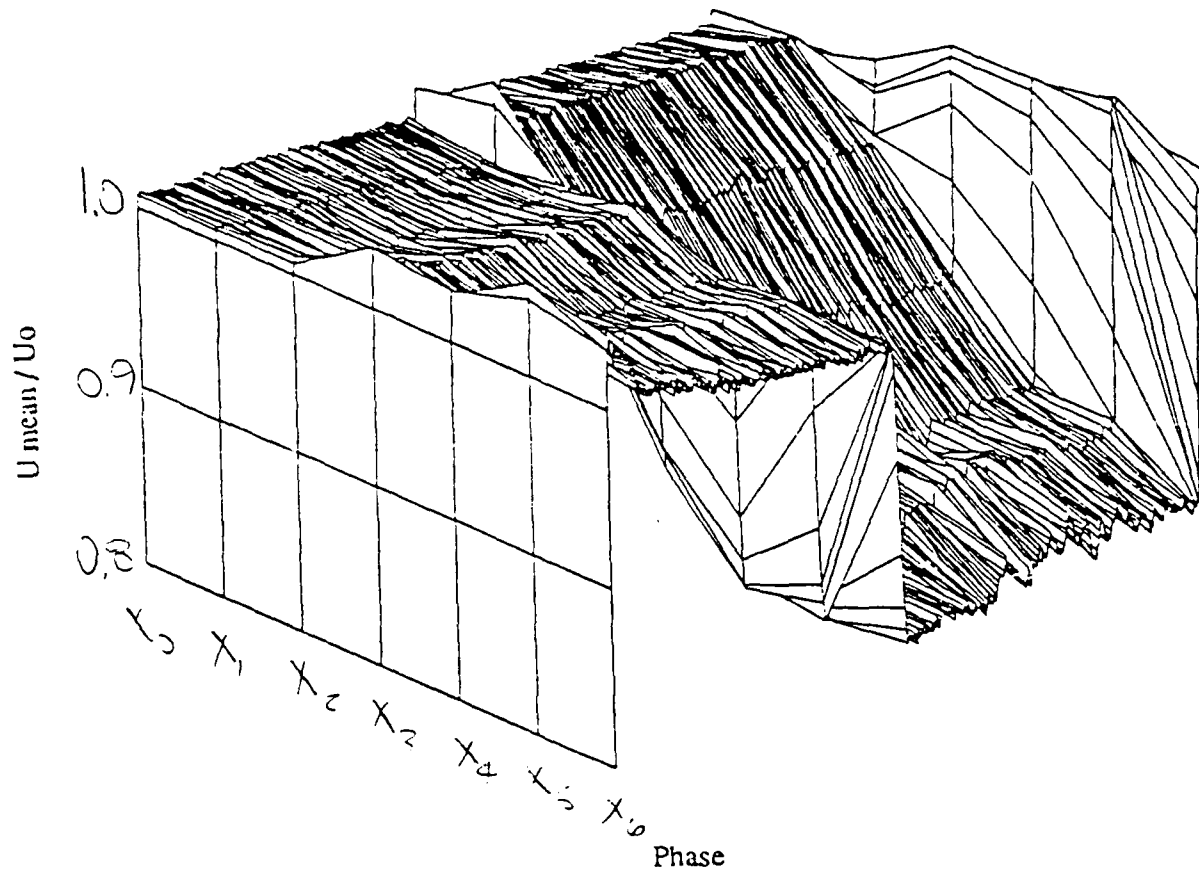
Figure 5.7   Freestream ⟨u⟩-velocity versus chord and phase.
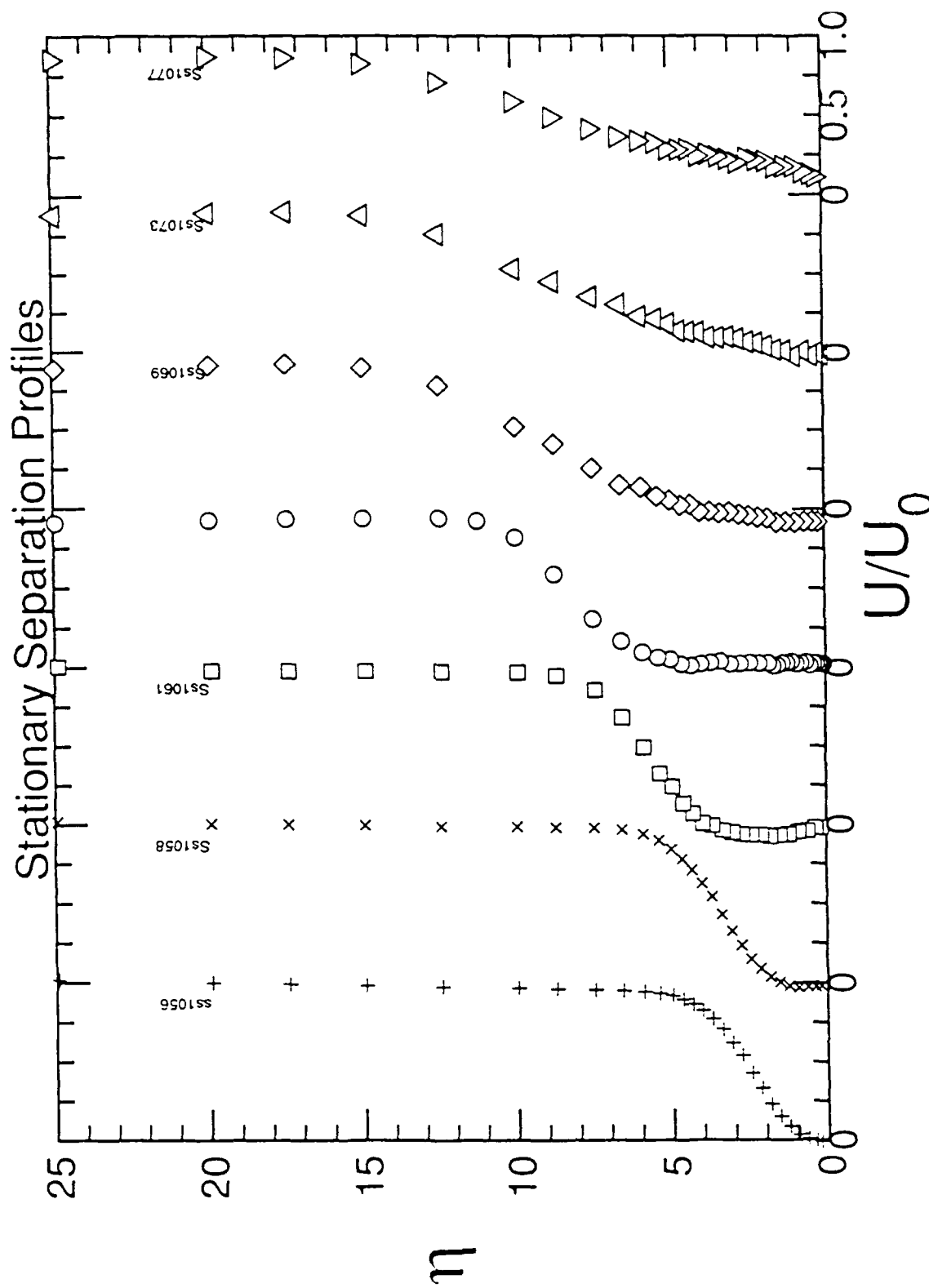
Figure 5.8   Boundary-layer development along the centerline for stationary separation: case 10.
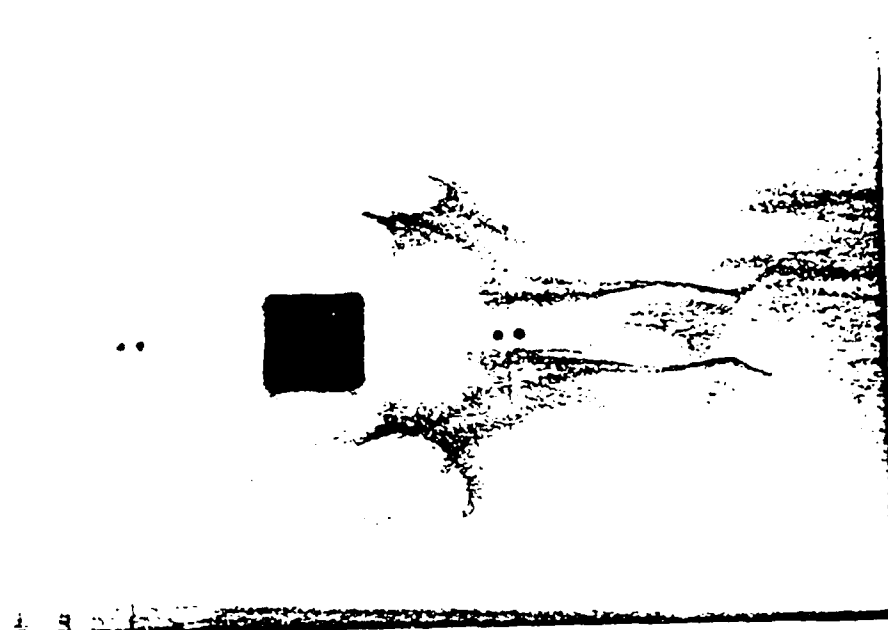
Figure 6.1   The owl-face separation structure: (a) Plan view as seen through the glass test surface. An image of the square port in a type 3 plate on the control wall is also visible; (b) Side view cross-section.

Better pictures on following 2 page

3.6

3.2

6.1a
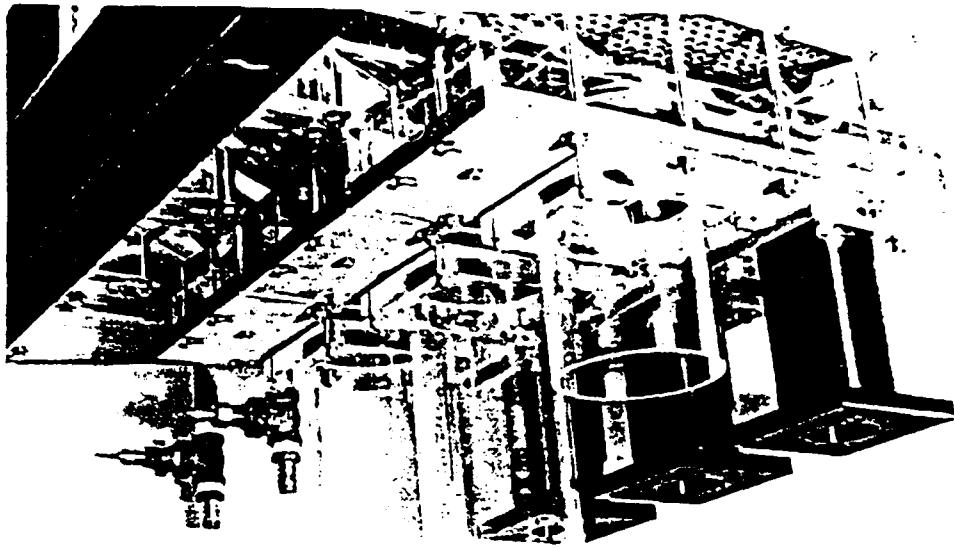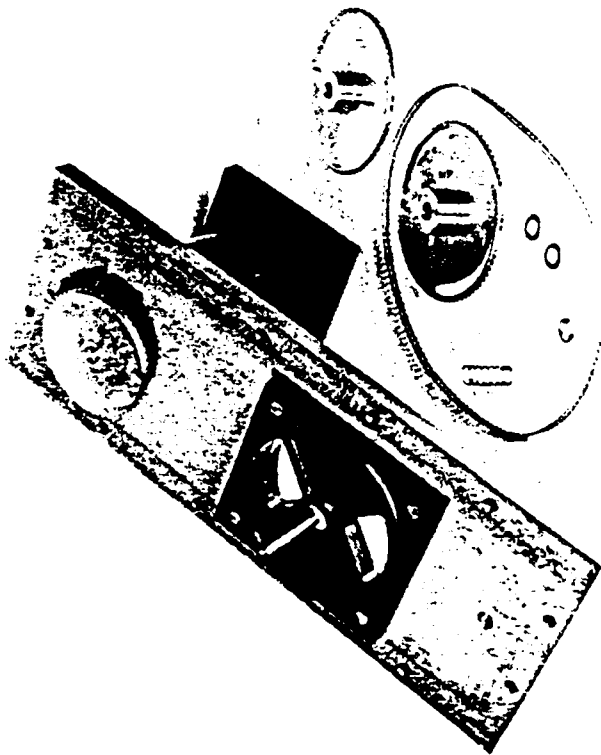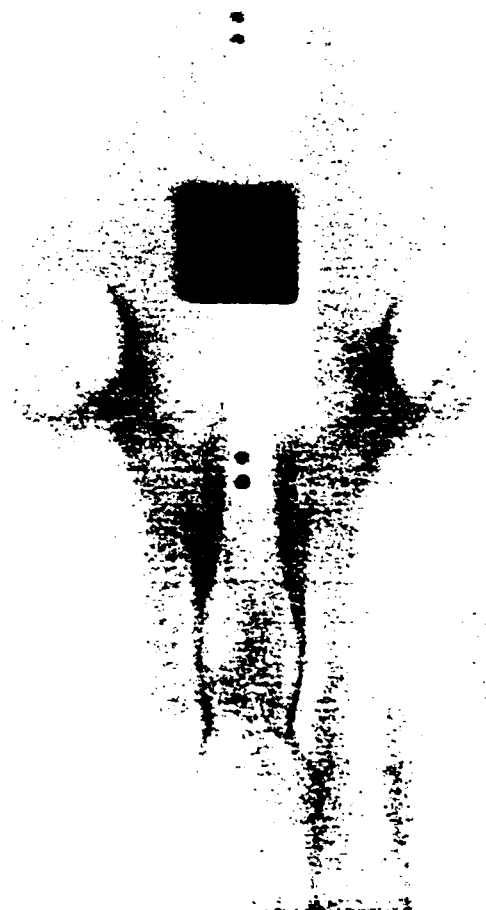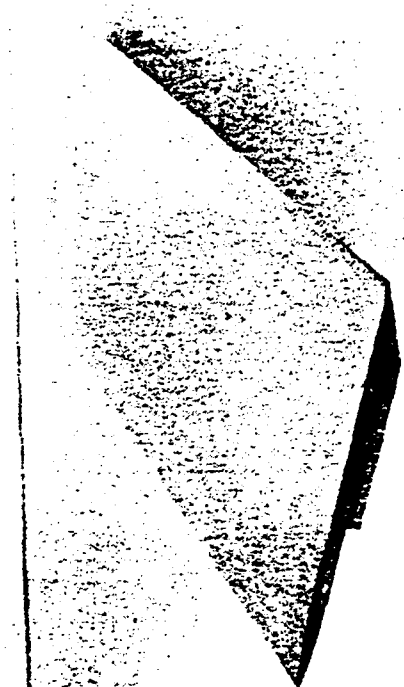
(a) Plan view of separation zones and tunnel geometry

Side Wall

Zone I

Zone V

5cm

x

z

Separation line

Zone IV

Saddle point

Zone III

a

C_L

A   B   D   1   2   3   4   a

Zone II

(b) Section a-a,   Cross-section of Separation

Separation streakline

y

U_∞

x

Separation wake

Test Surface

A   B   D   1   2   3   4

Measurement Stations, LP: ⊔
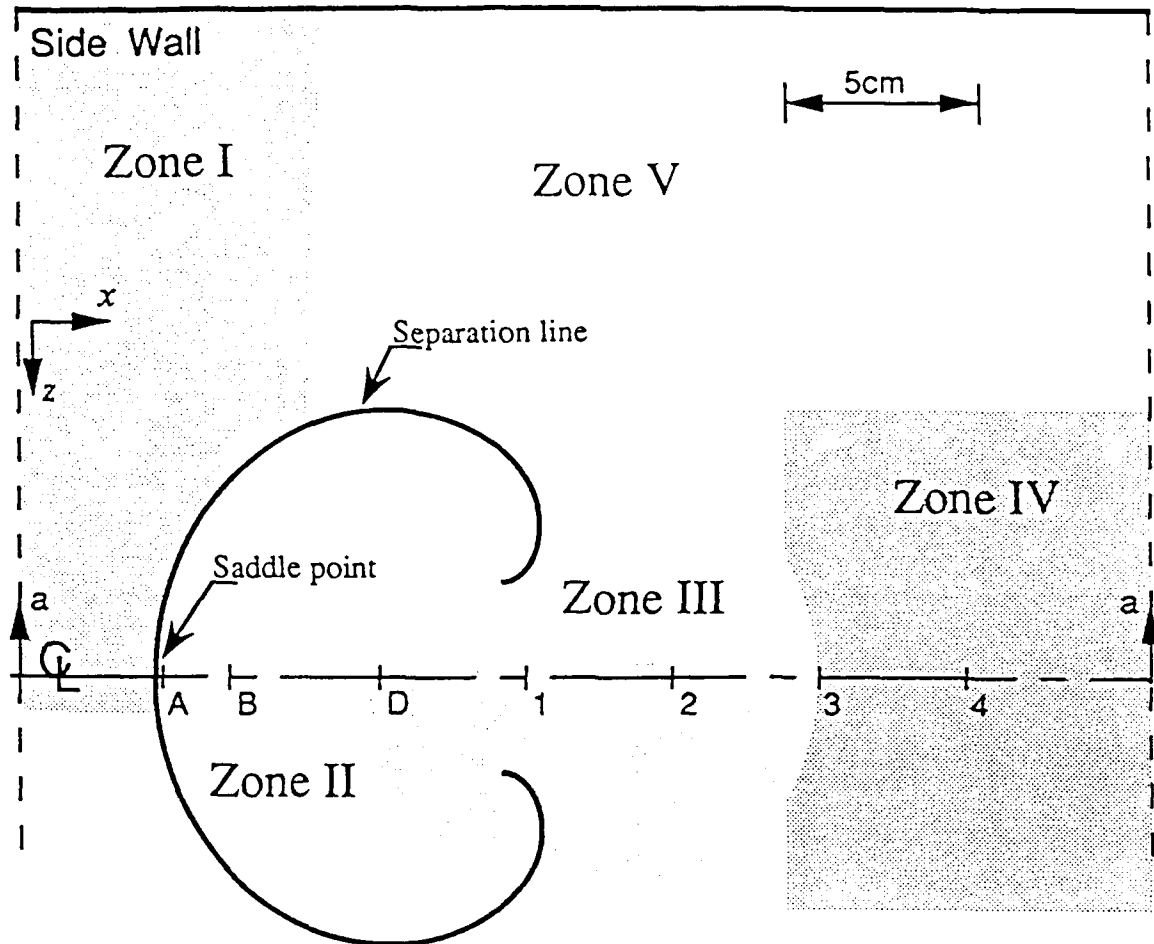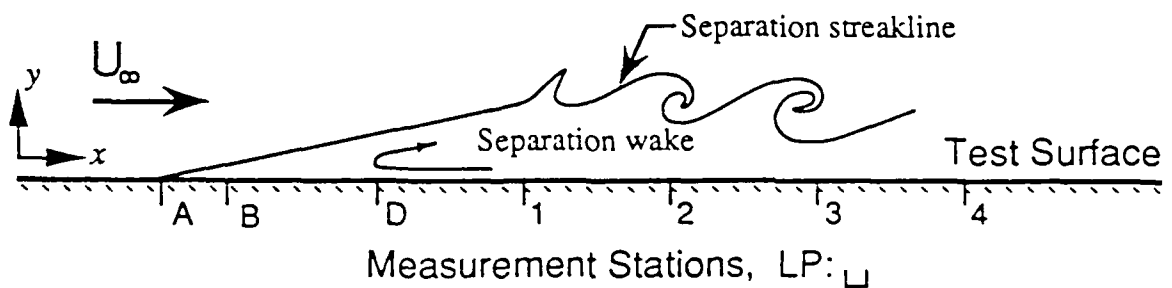
Figure 6.2   Zones of the quasi-steady separation structure. Forward, laminar flow at all times during nonstationary forcing characterized Zone I. Quiescent forward or reversed laminar flow distinguishes Zone II. Zone III experiences large-scale unsteadiness. Zone IV is downstream of the saddle point at mean reattachment. Zone V is outside the principal separation structure. Fresh fluid continually feeds into Zones II and III, which comprise the separation wake.
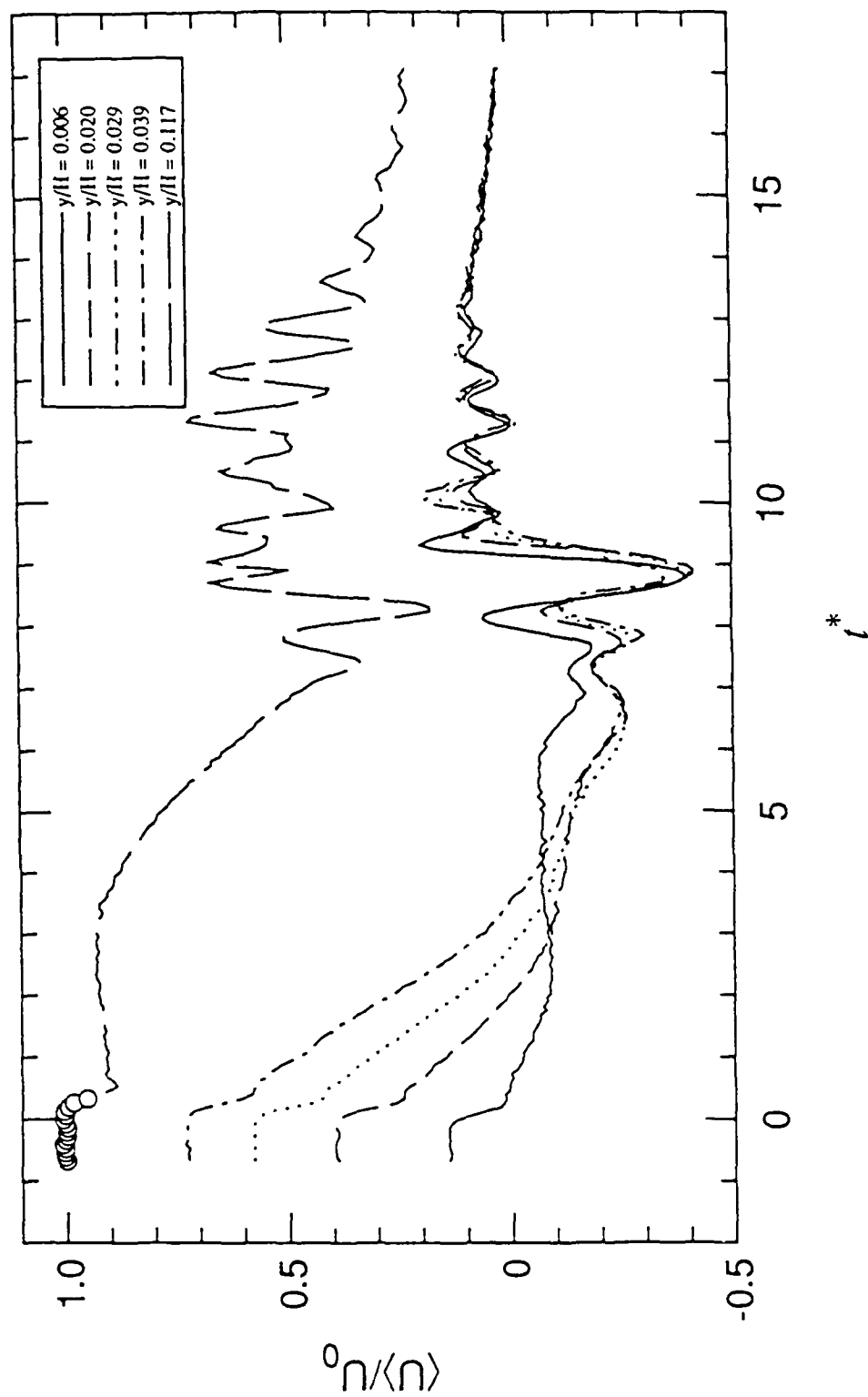
Figure 6.3 Velocity histories at five distances from the wall during separation development: (a) at LP:1, (b) at LP:2, (c) at LP:3, and (d) at LP:4.

636

6.30

6.3e

639
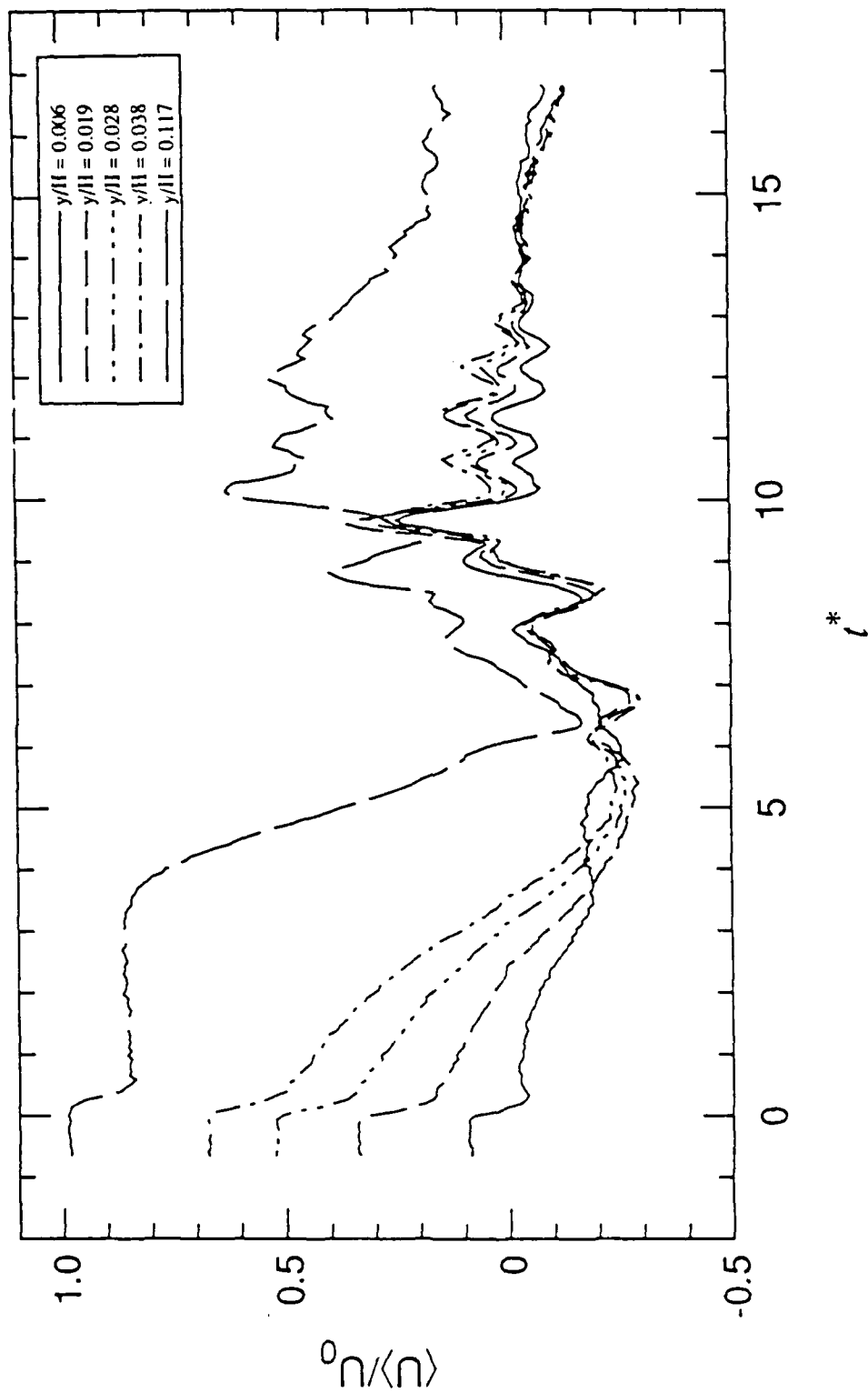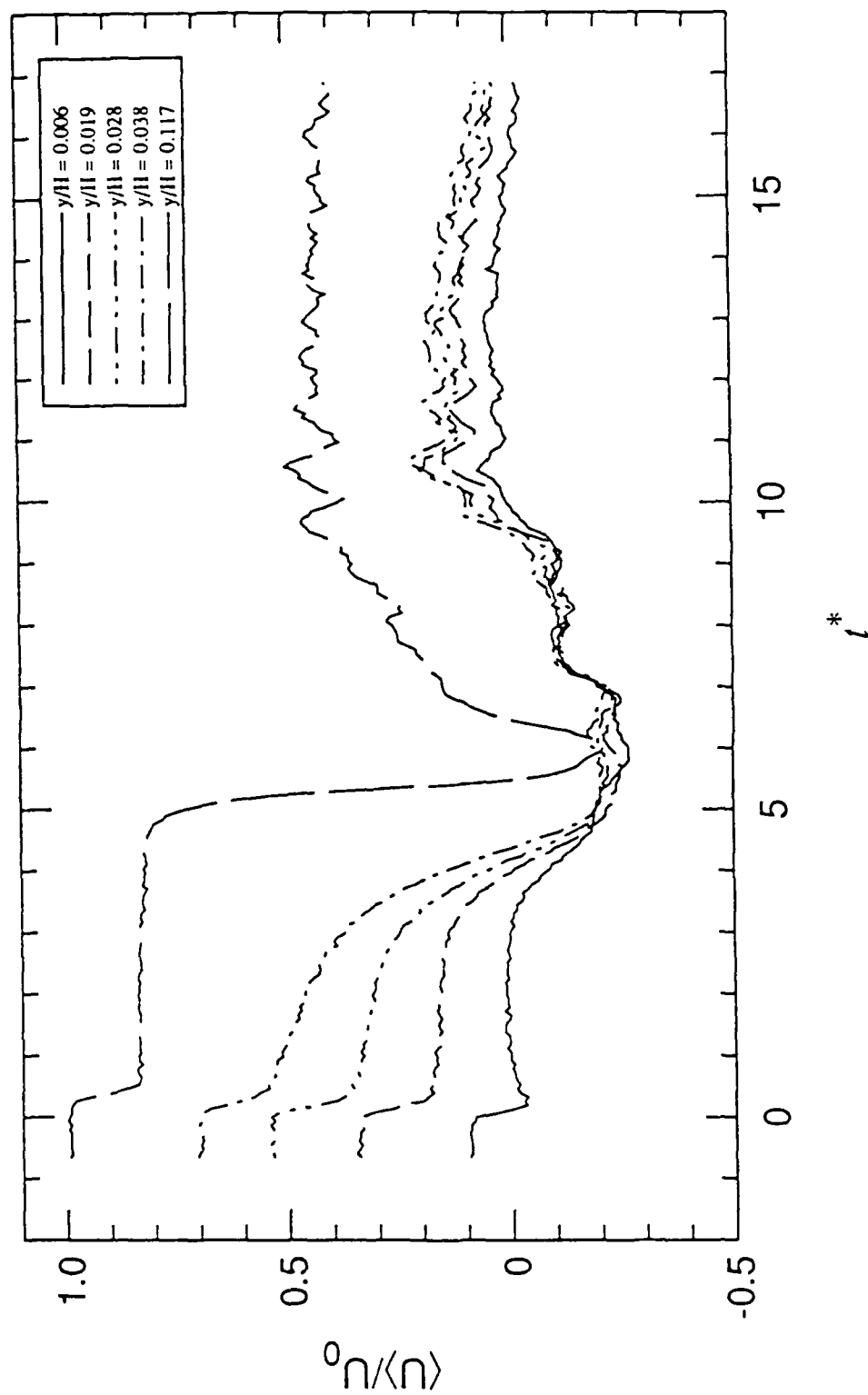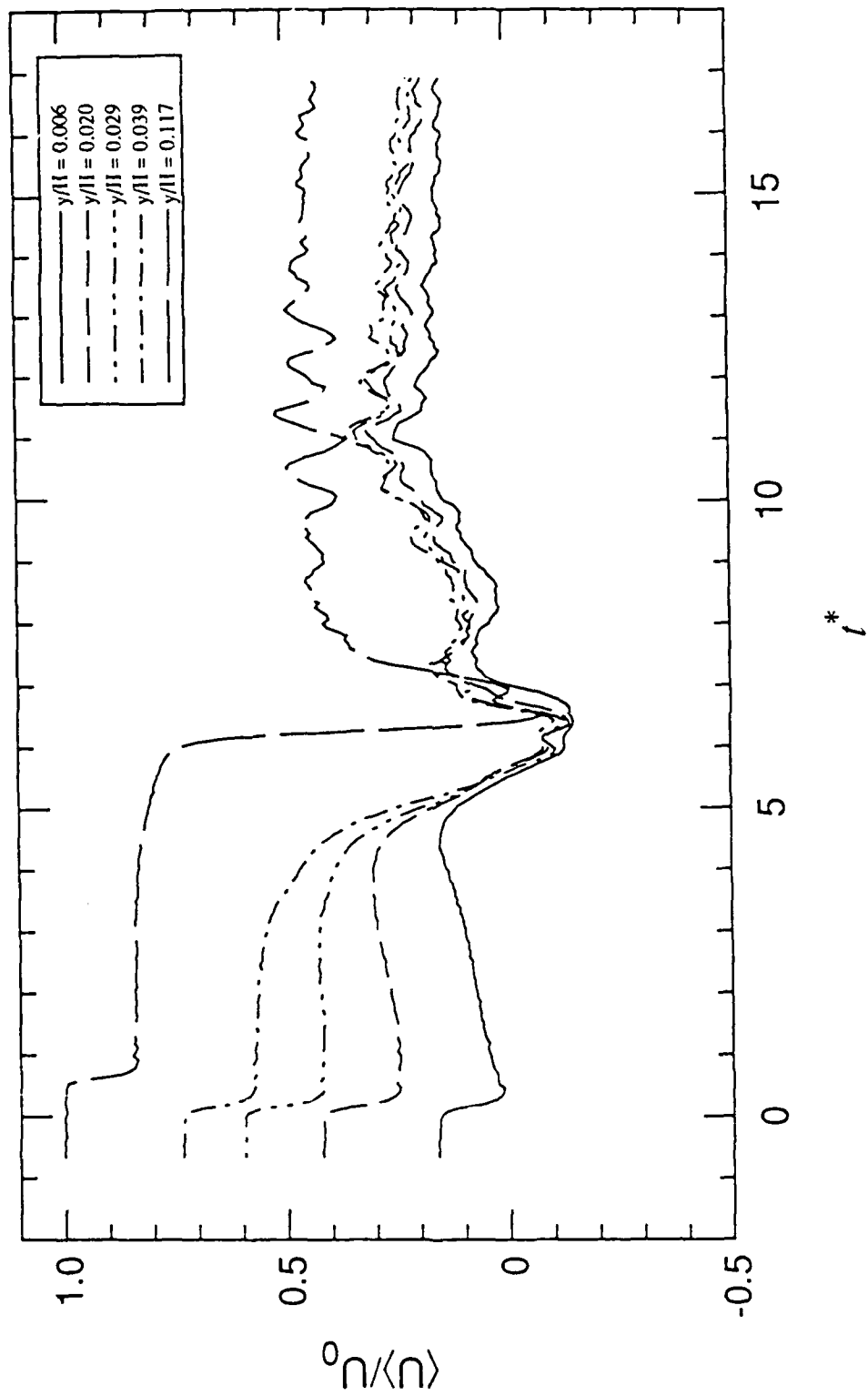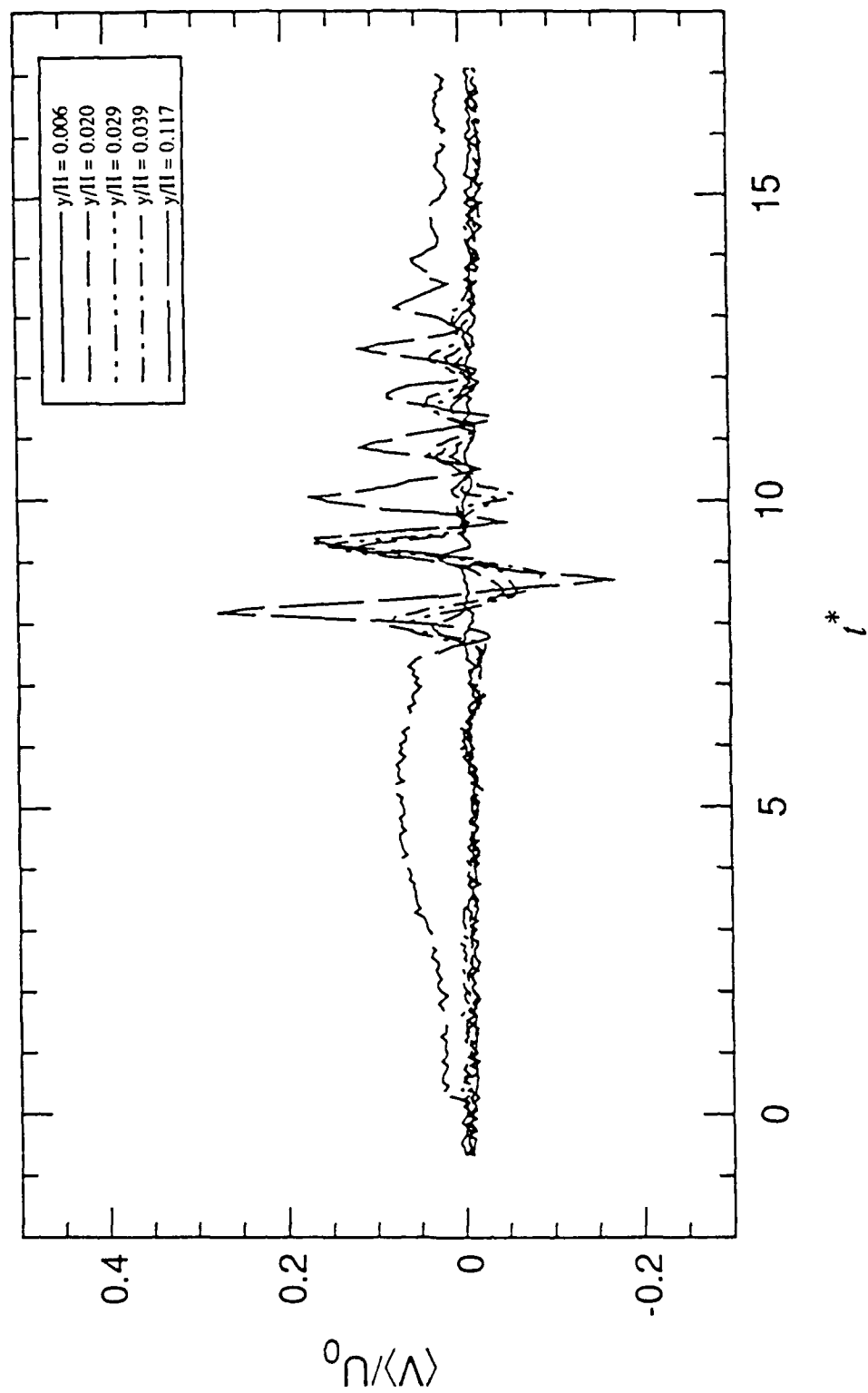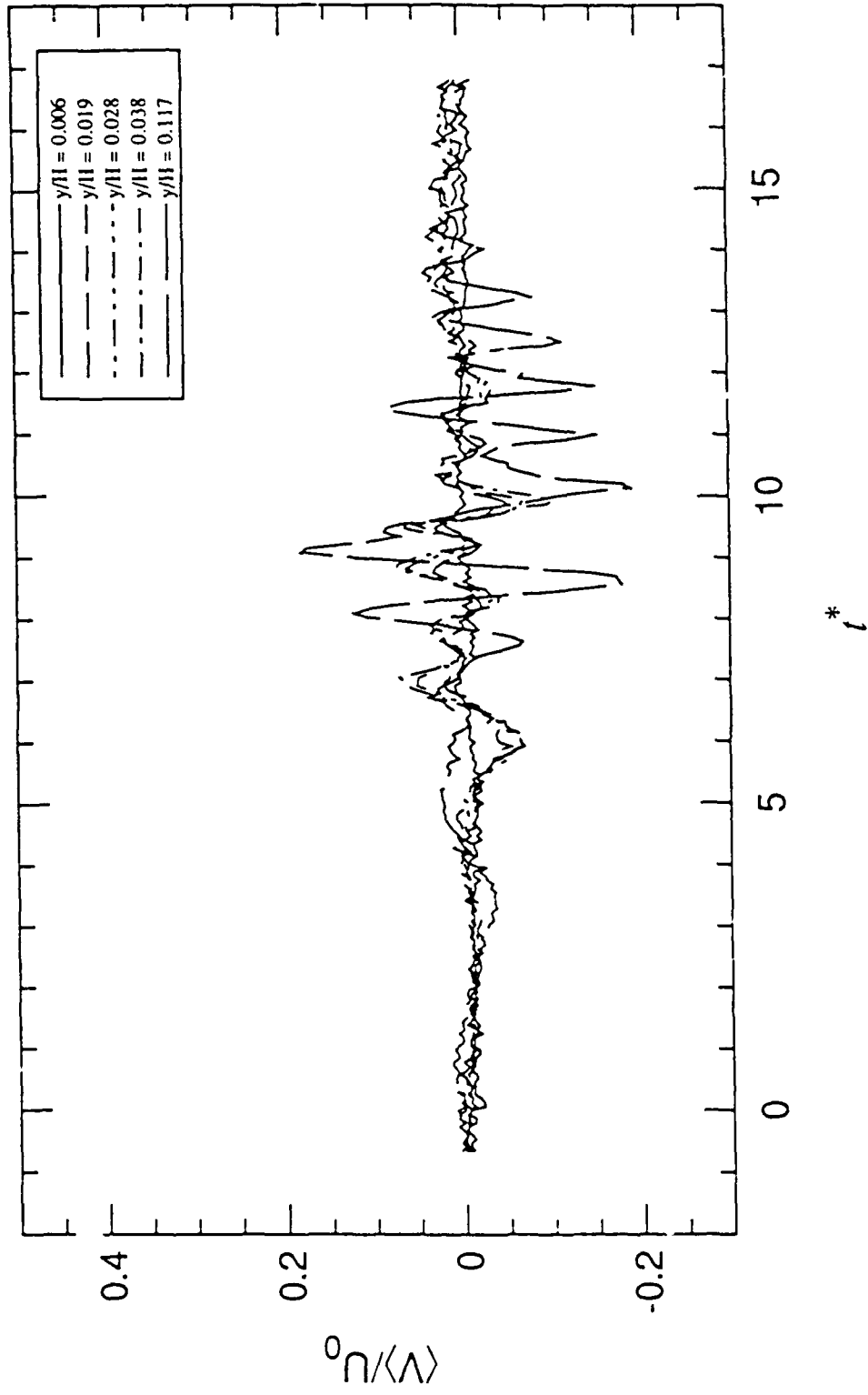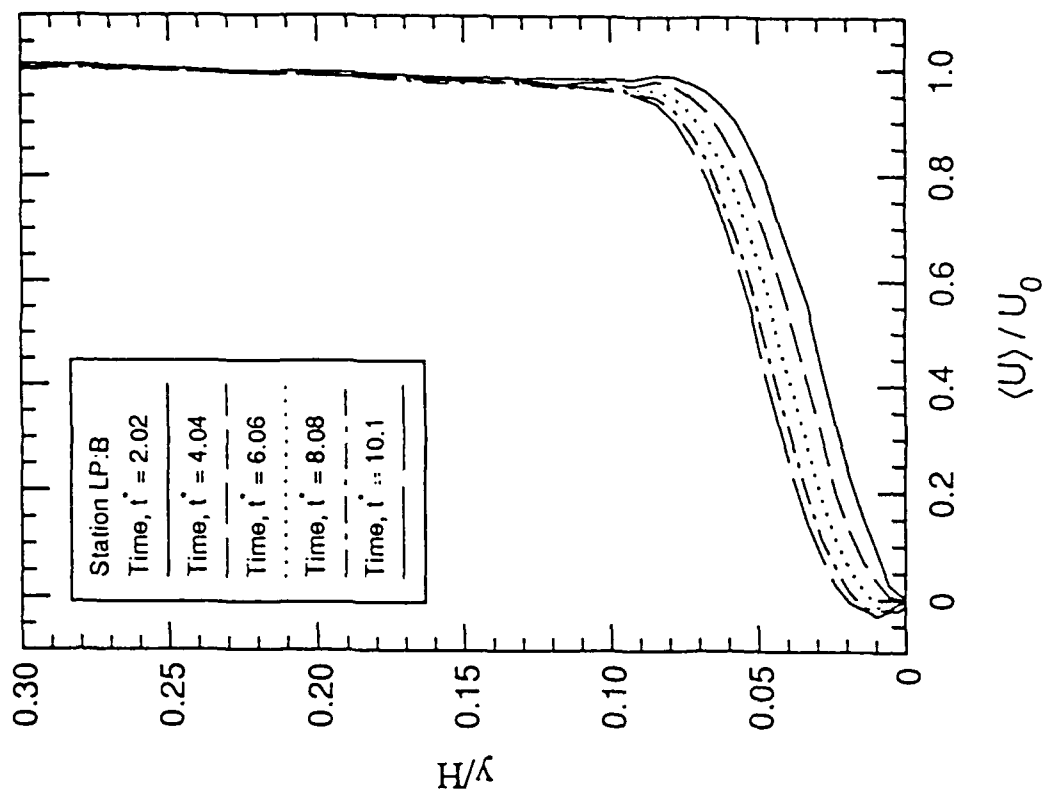
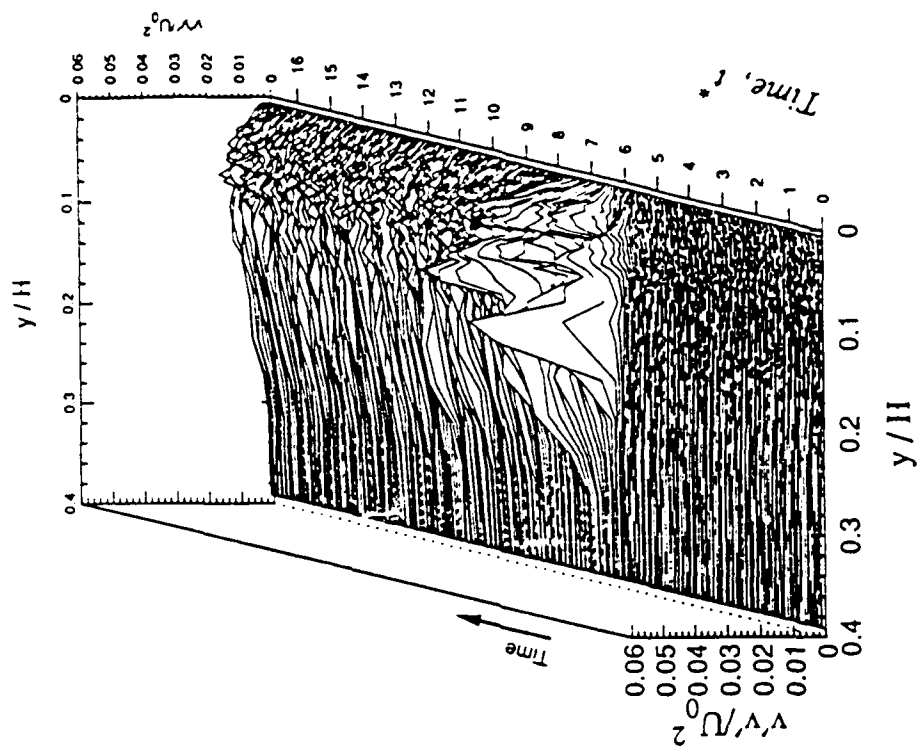Figure 6.4   Development of the phase-averaged $\langle u \rangle$-velocity profiles during separation development. Results are compared alongside with Pauley, *et al.* (1988). Figure numbers ending with a 1 are from Pauley; figures ending with a 2 are experimental: (a1) and (a2) at LP:B, (b1) and (b2) at LP:D, (c1) and (c2) at LP:1.

Figure legend:
Station LP:D
Time, $t^* = 2.01$
Time, $t^* = 4.02$
Time, $t^* = 6.03$
Time, $t^* = 8.04$
Time, $t^* = 10.05$

Y-axis: y/H
X-axis: $\langle U \rangle / U_0$

6.4 b

Developing Separatic

Pauley, *et al.* (1988)

Legend (right plot):
Station LP:1
Time, $t^* = 2.01$
Time, $t^* = 4.02$
Time, $t^* = 6.03$
Time, $t^* = 8.04$
Time, $t^* = 10.05$

Right plot axes: y/H vs $\langle U \rangle / U_0$

Left plot axis: U
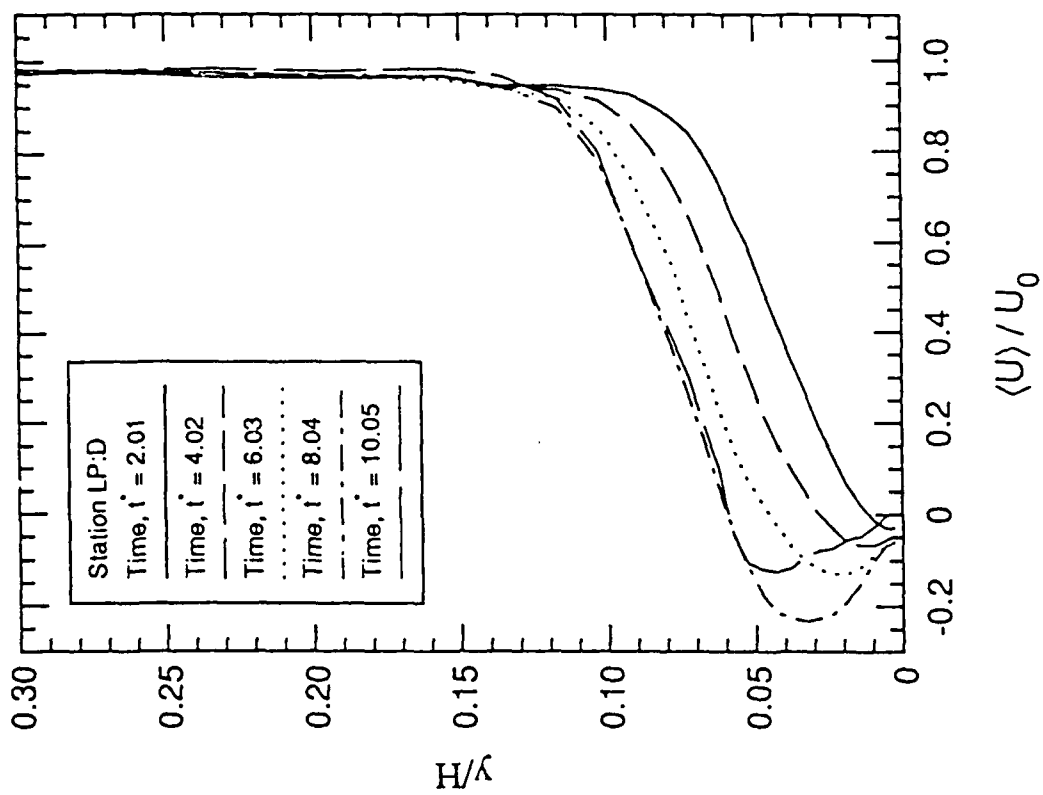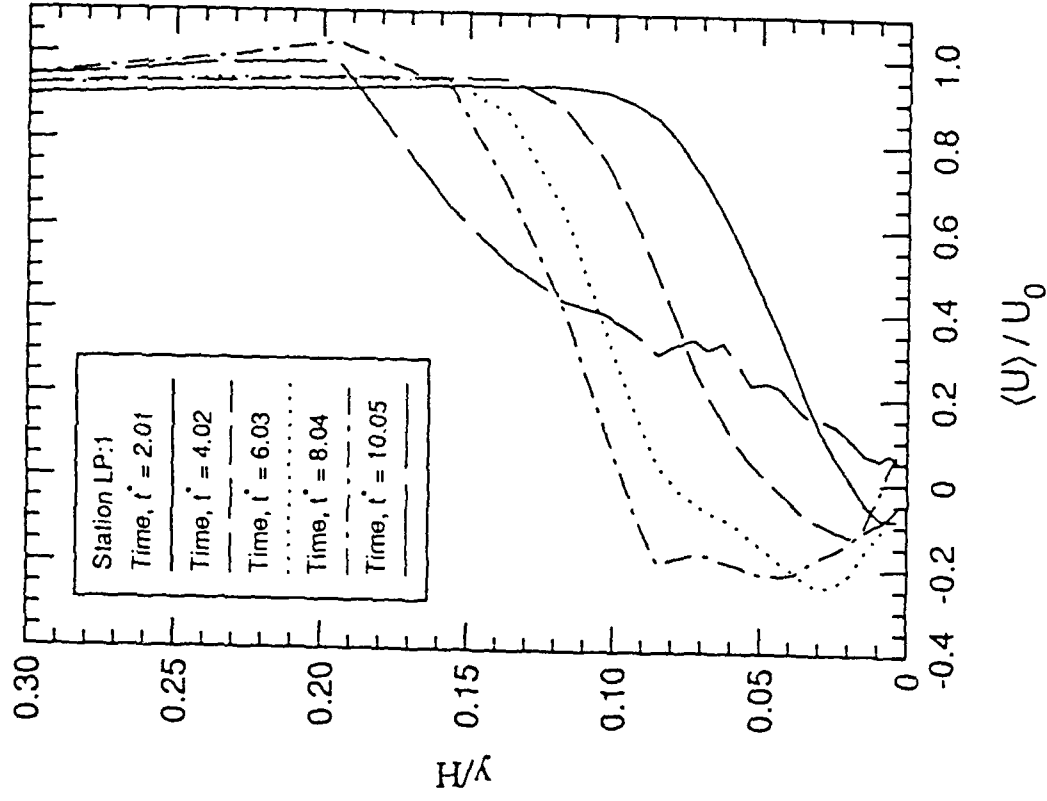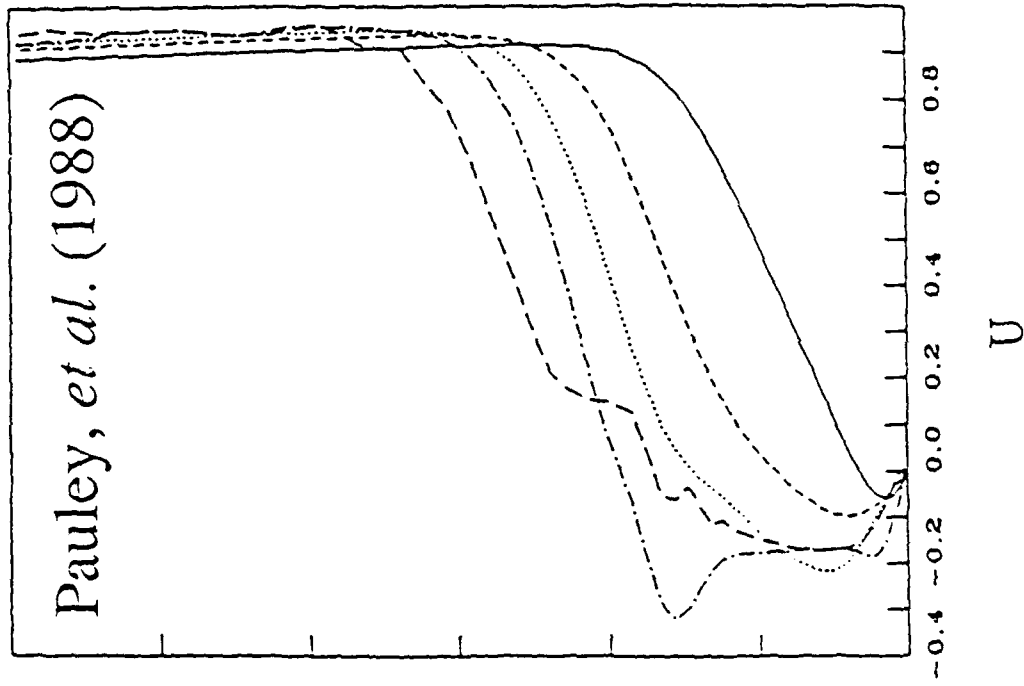
64c
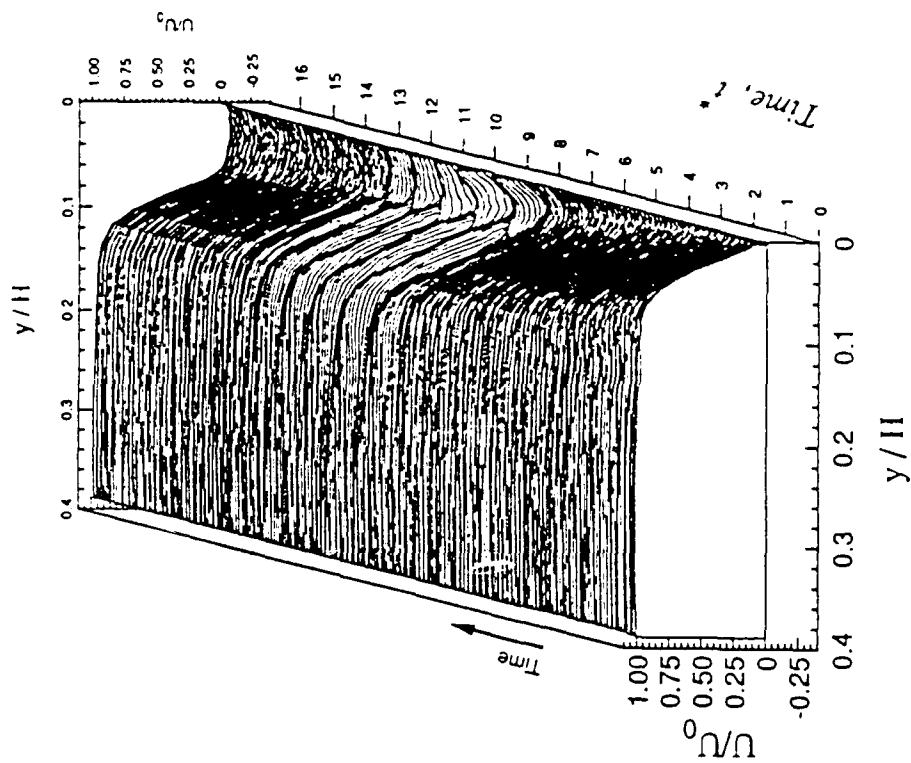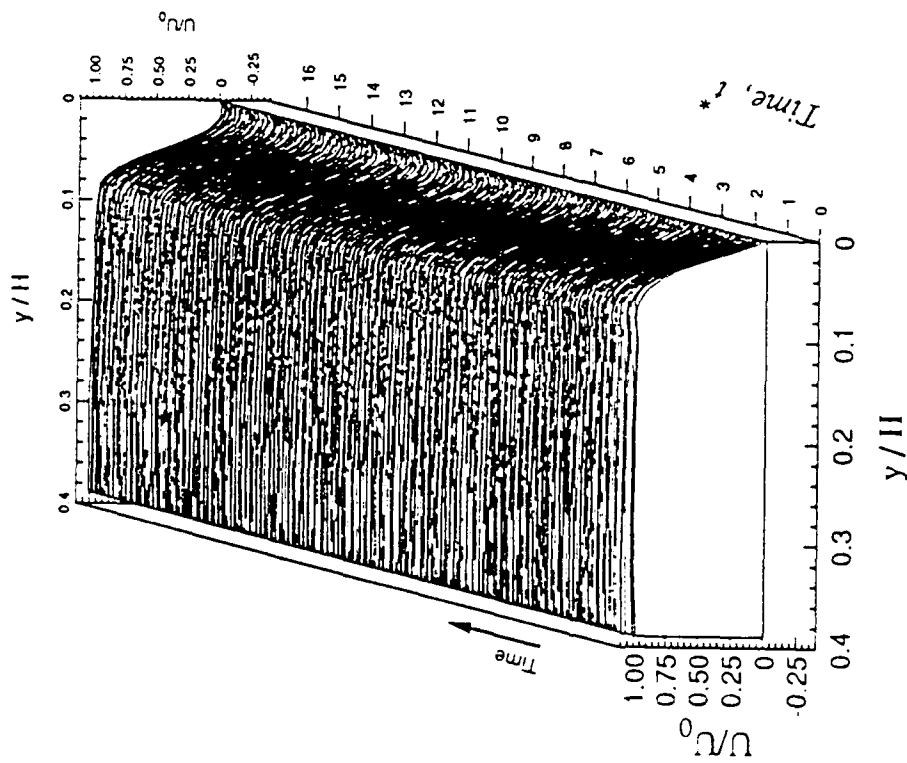
Figure 6.5 Evolution of the phase-averaged $\langle u \rangle$-velocity profiles during separation development: (a) at LP:B, (b) at LP:D, (c) at LP:1, (d) at LP:2, (e) at LP:3, and (f) at LP:4.
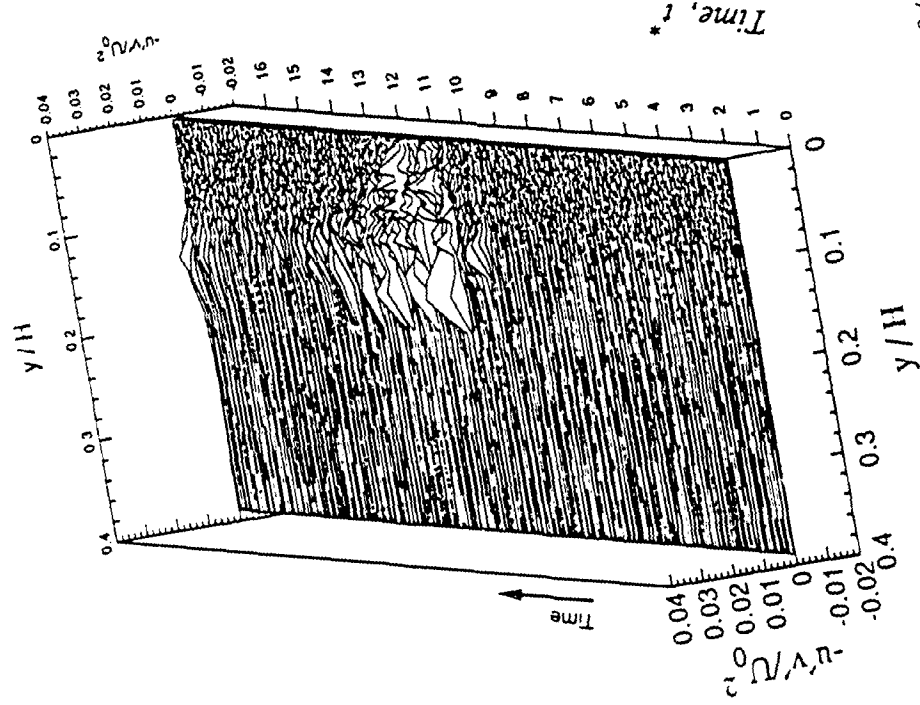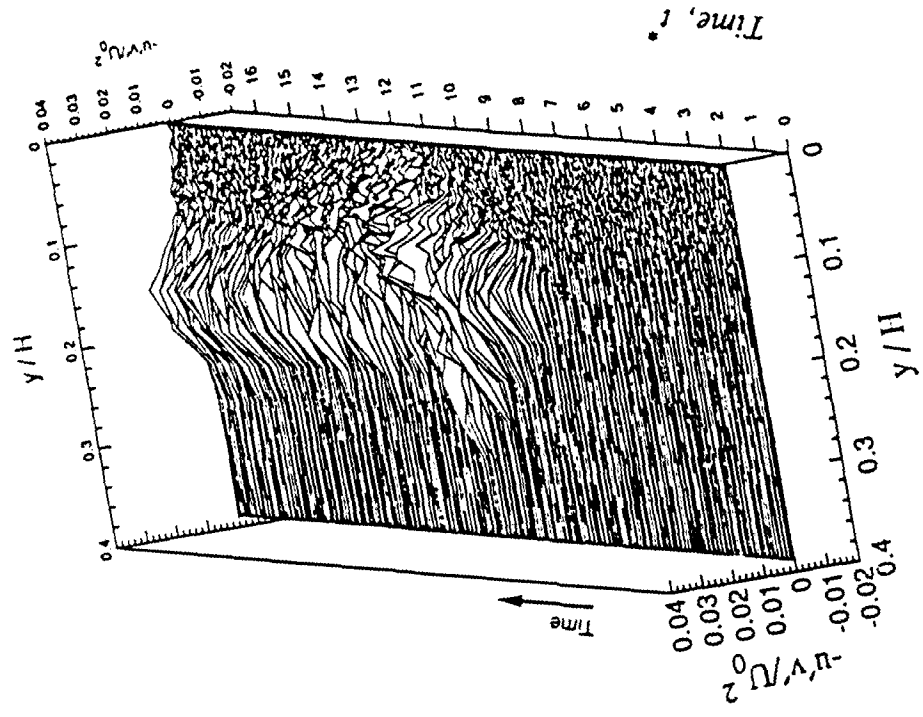
6.5 e

6.5 f
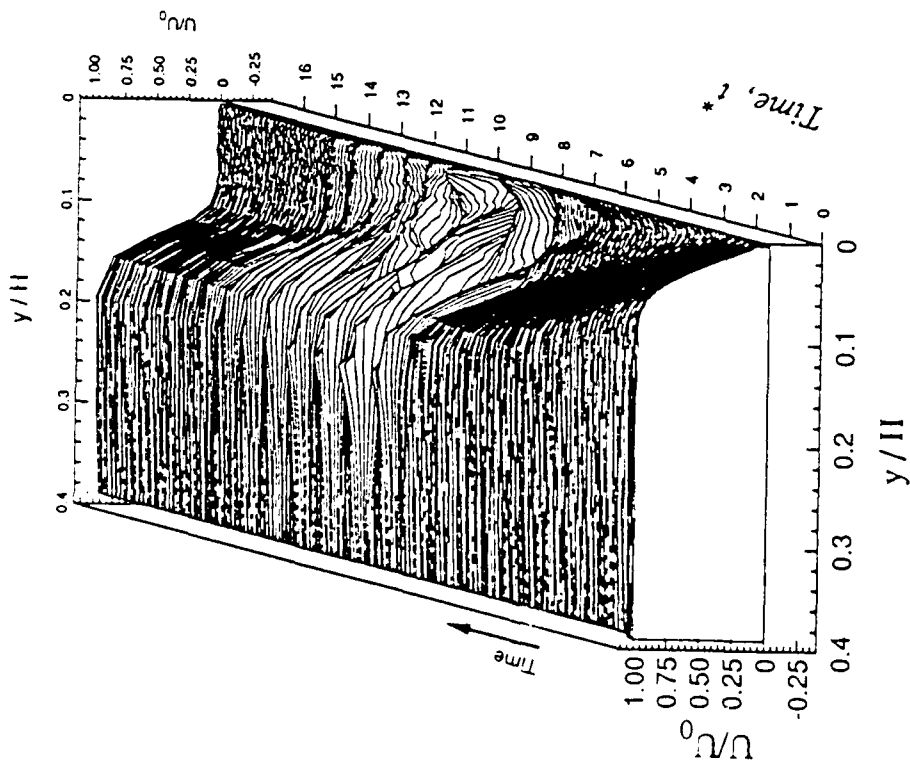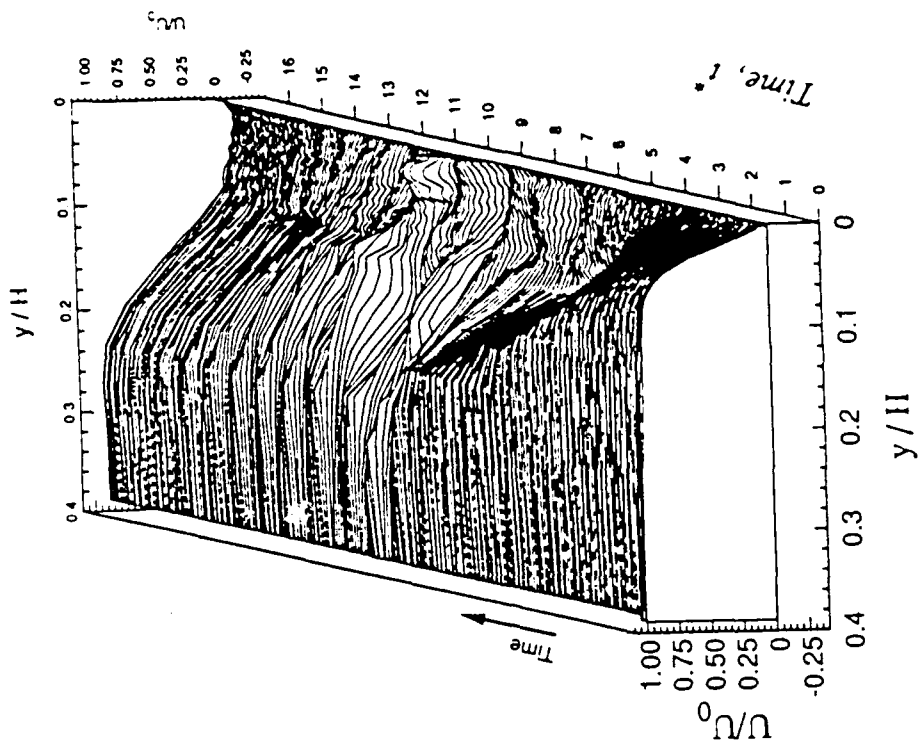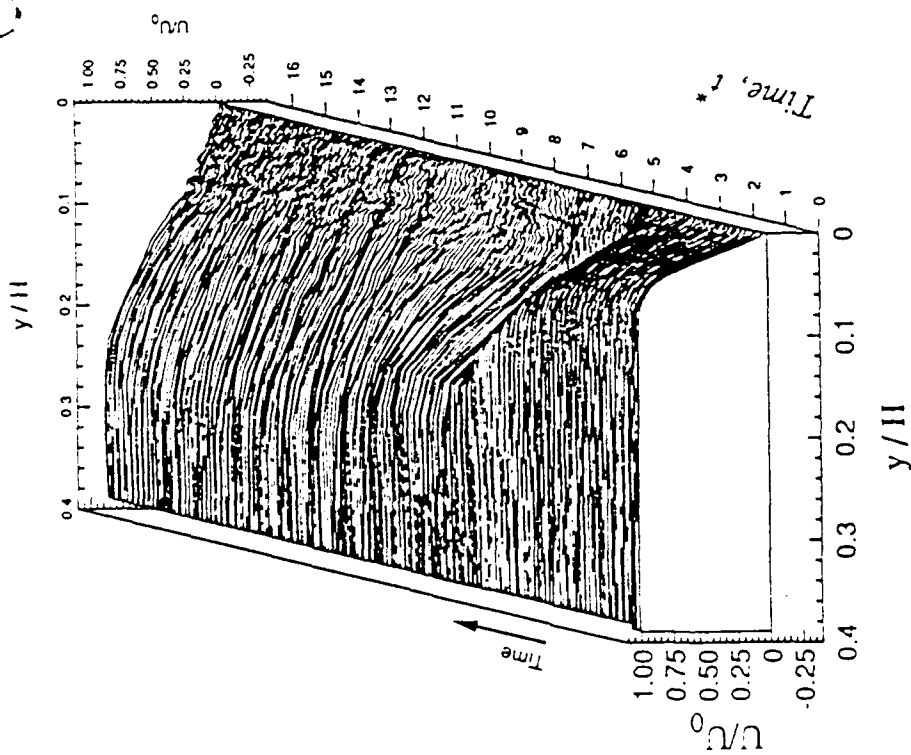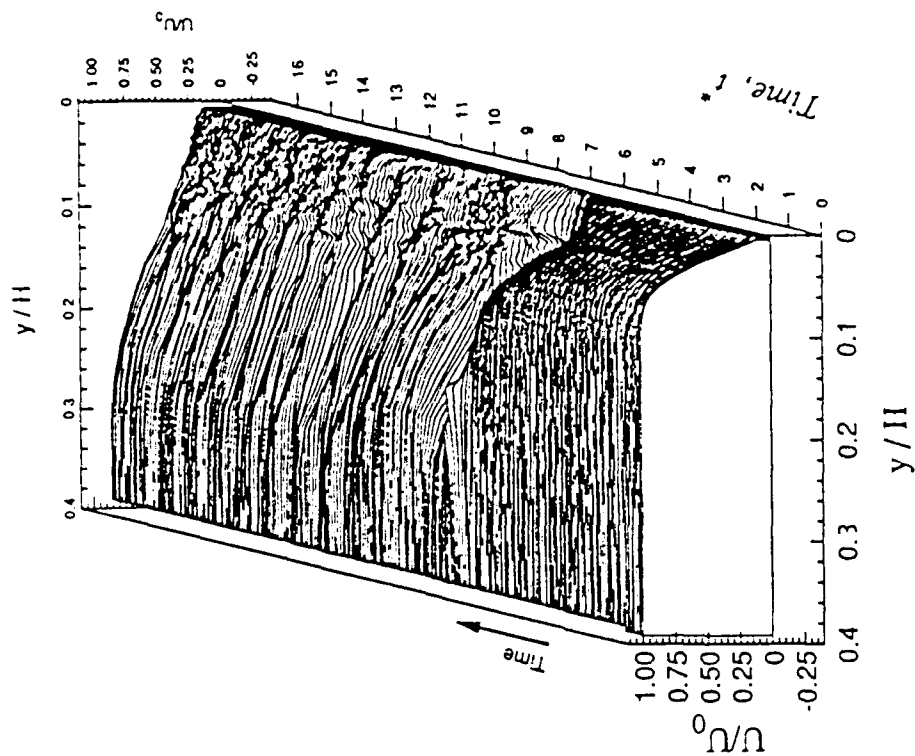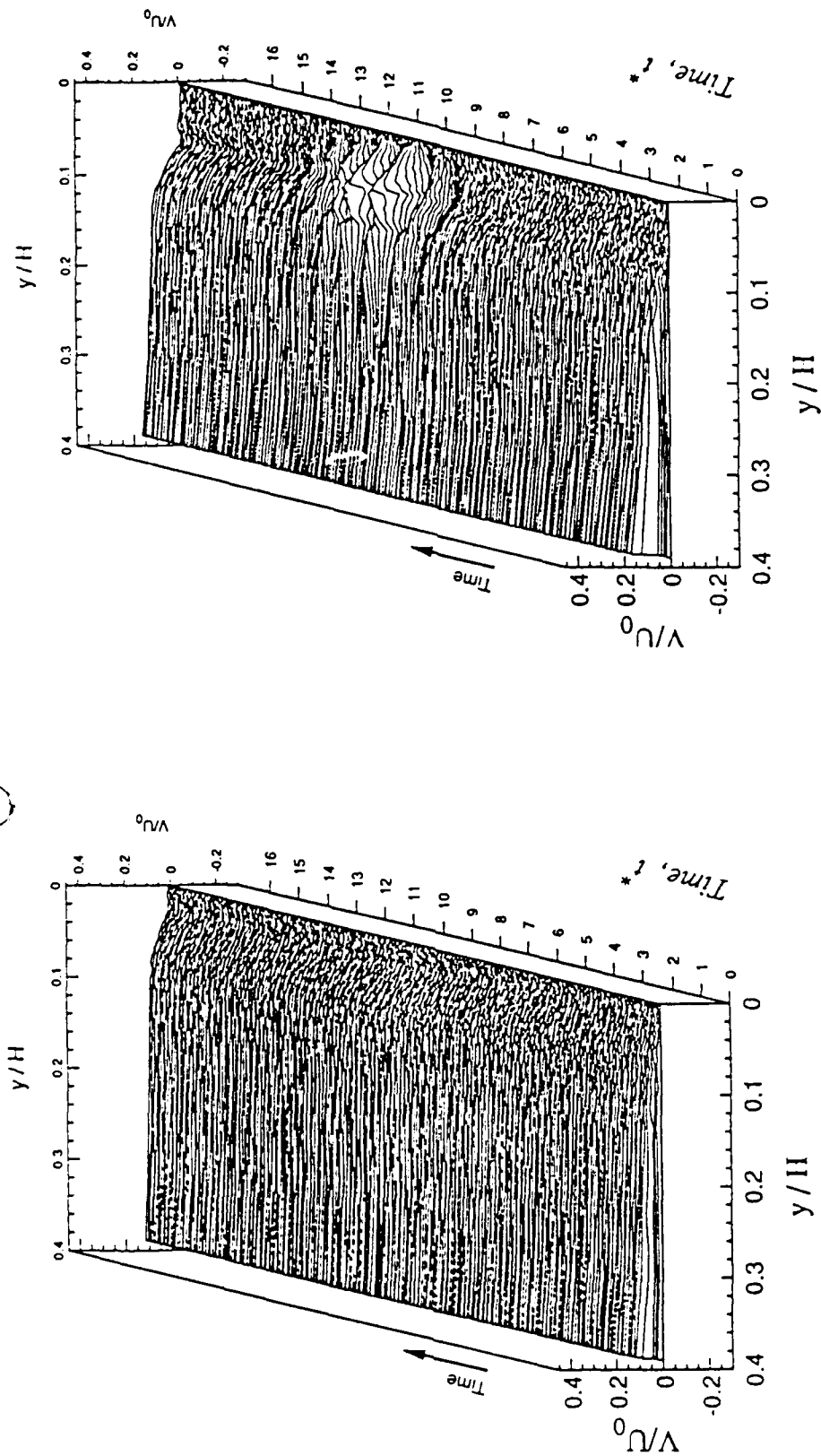
Figure 6.6   Evolution of the phase-averaged $\langle v \rangle$-velocity profiles during separation development: (a) at LP:B, (b) at LP:D, (c) at LP:1, (d) at LP:2, (e) at LP:3, and (f) at LP:4.
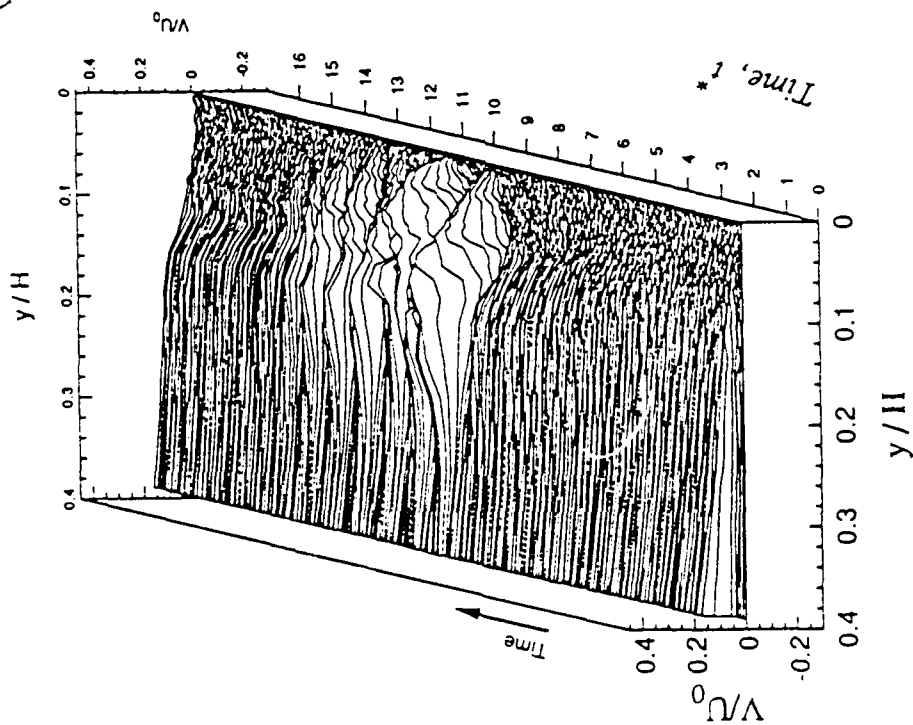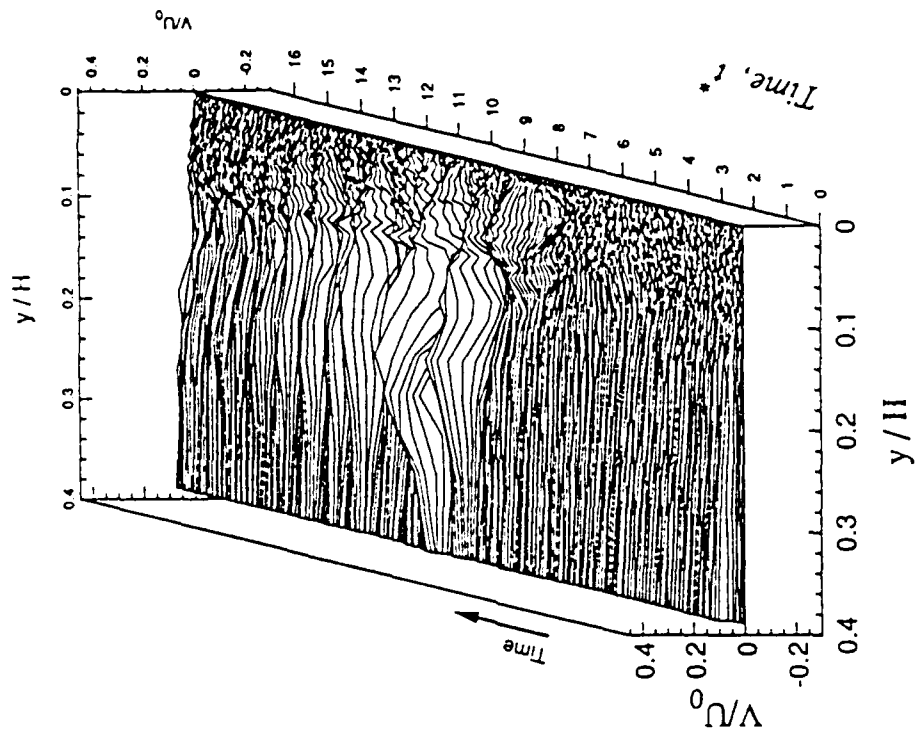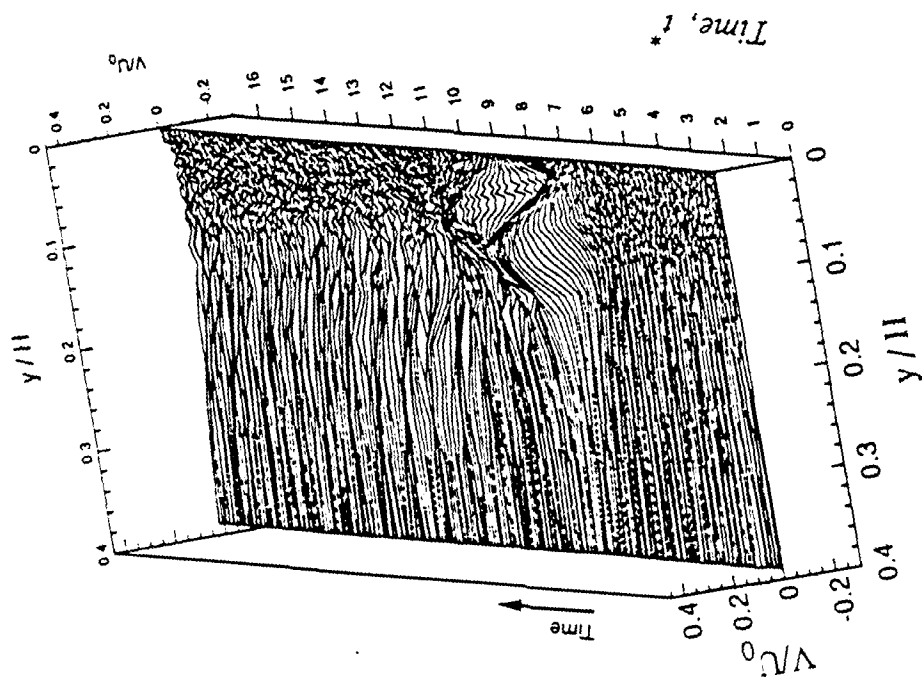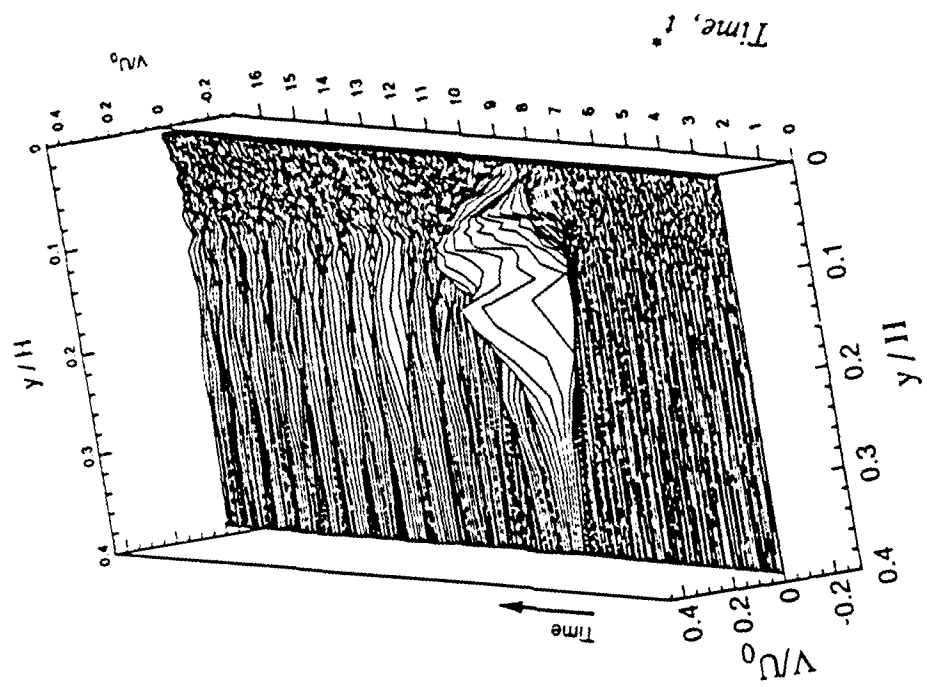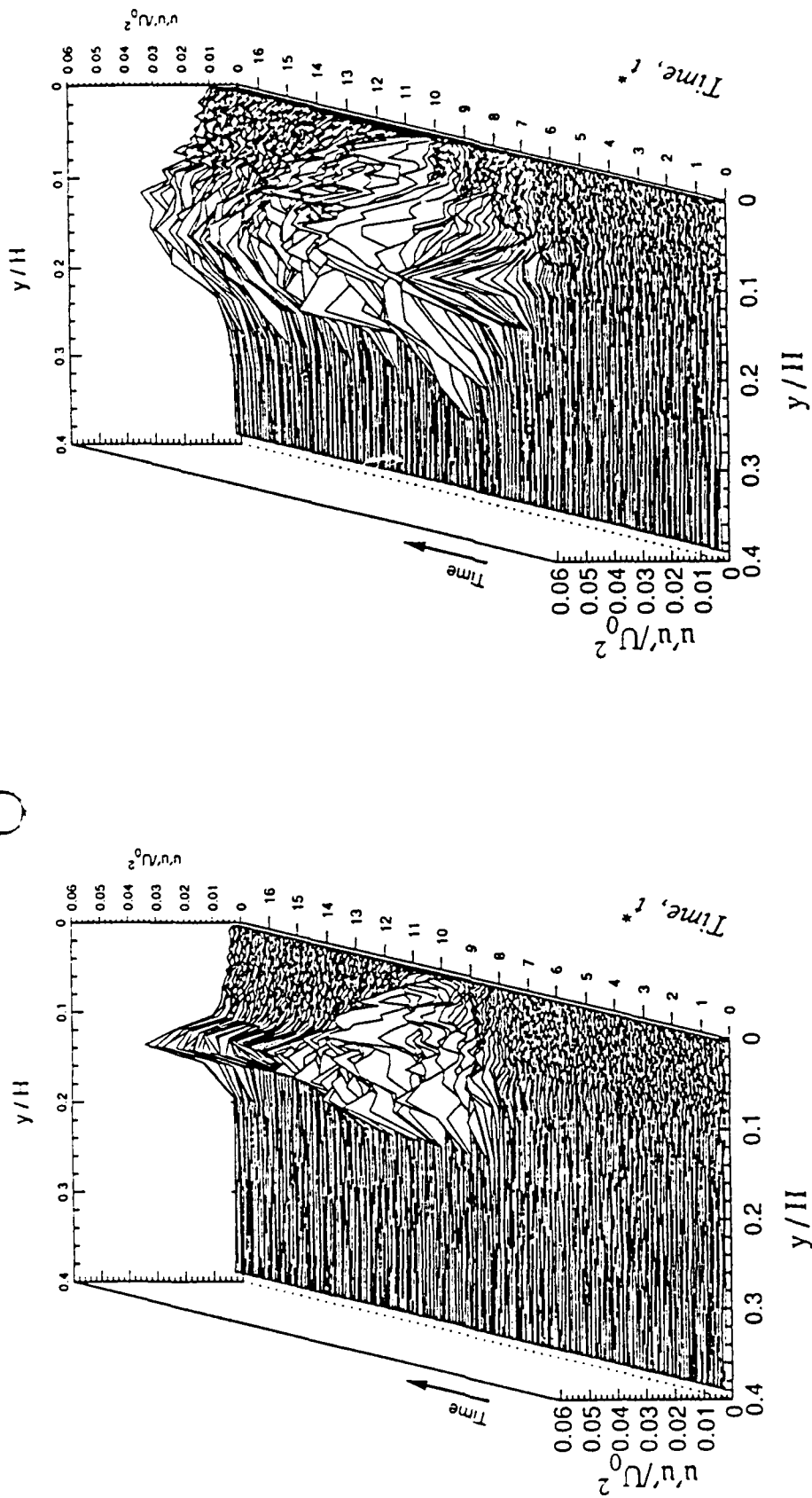
Figure 6.7   Evolution of the phase-averaged $\langle u'u' \rangle$-velocity profiles during separation development: (a) at LP:1, (b) at LP:2, (c) at LP:3, and (d) at LP:4.
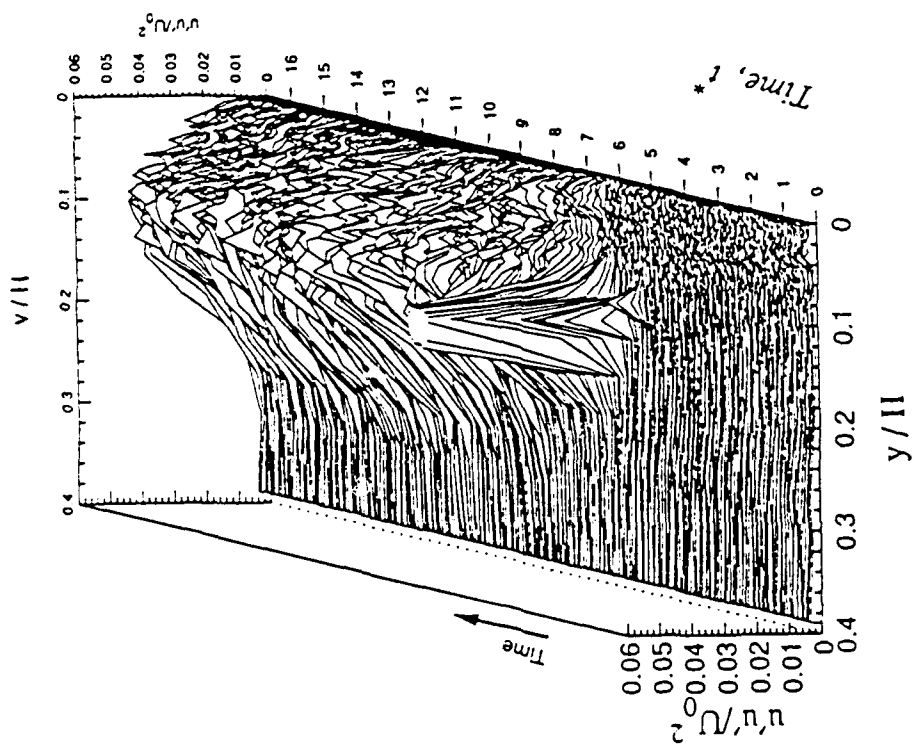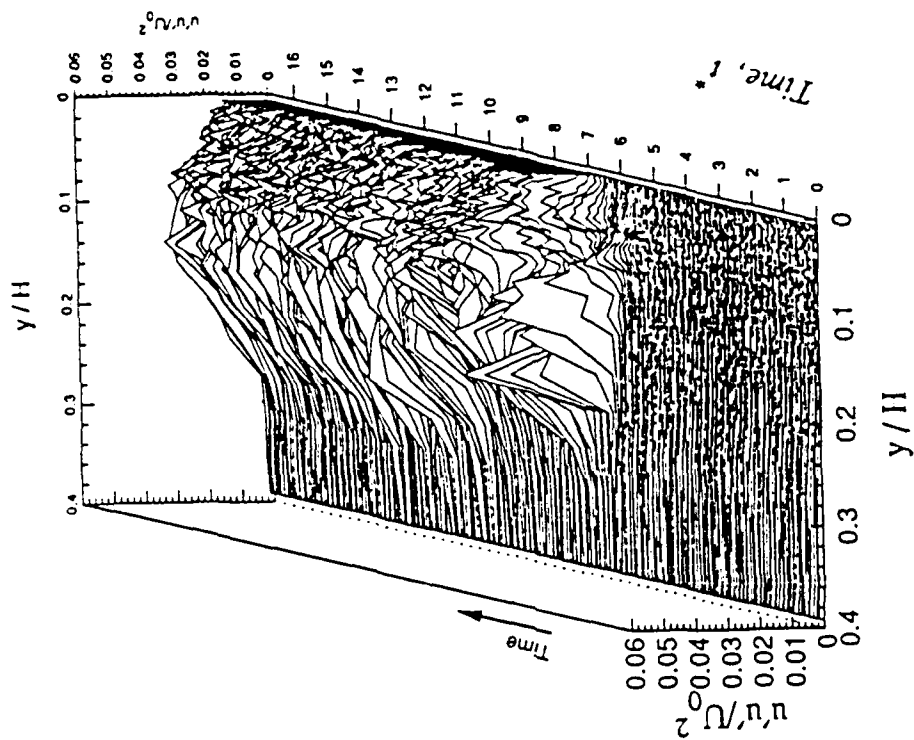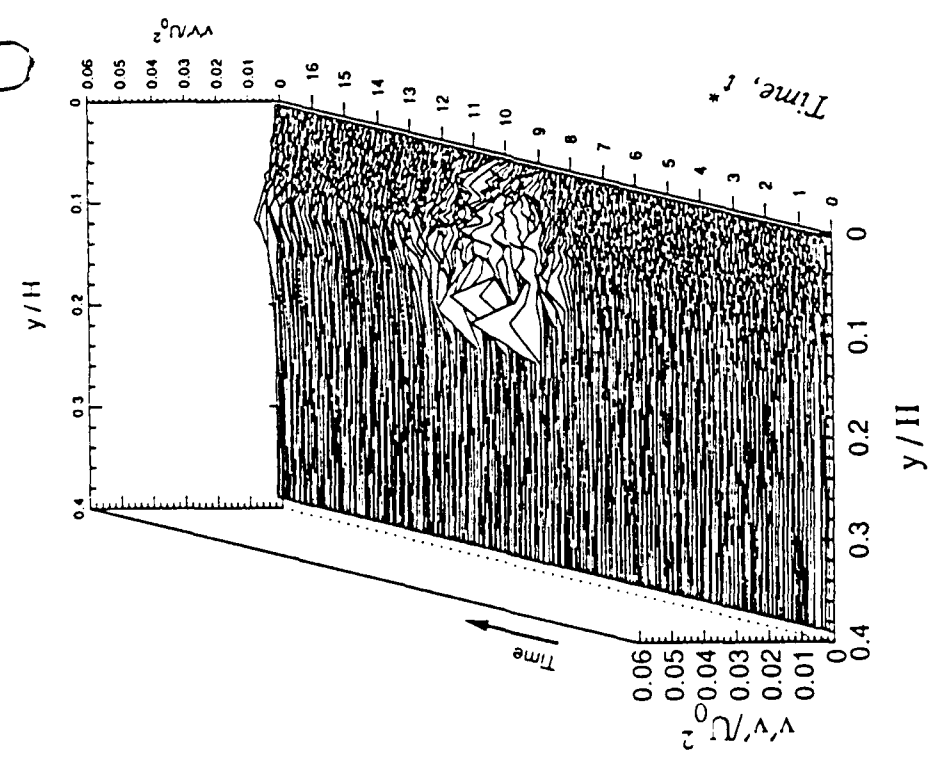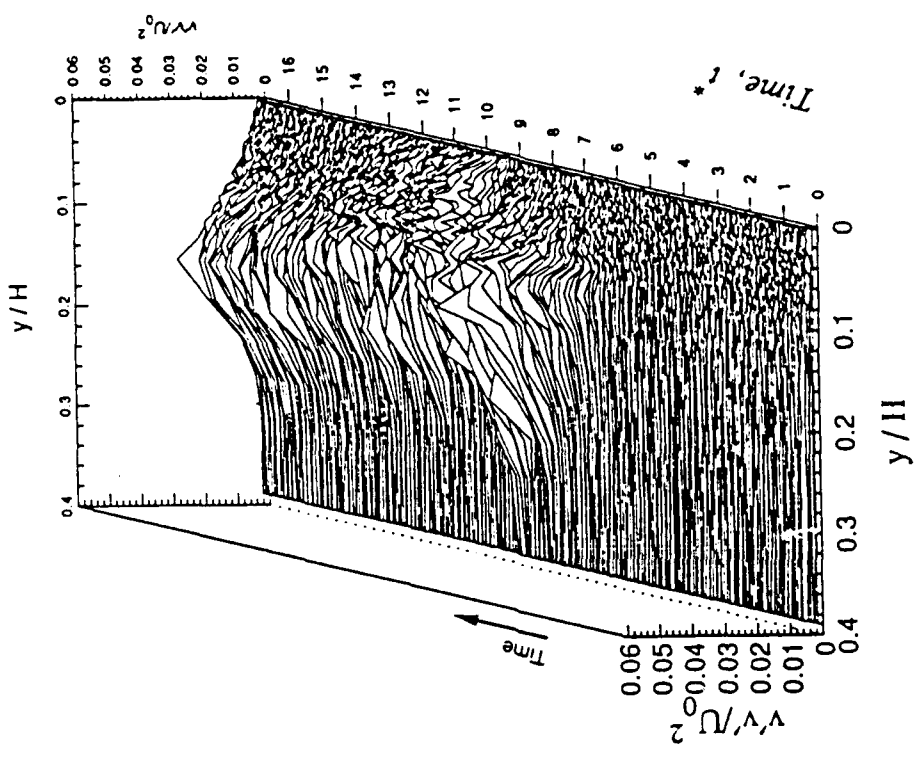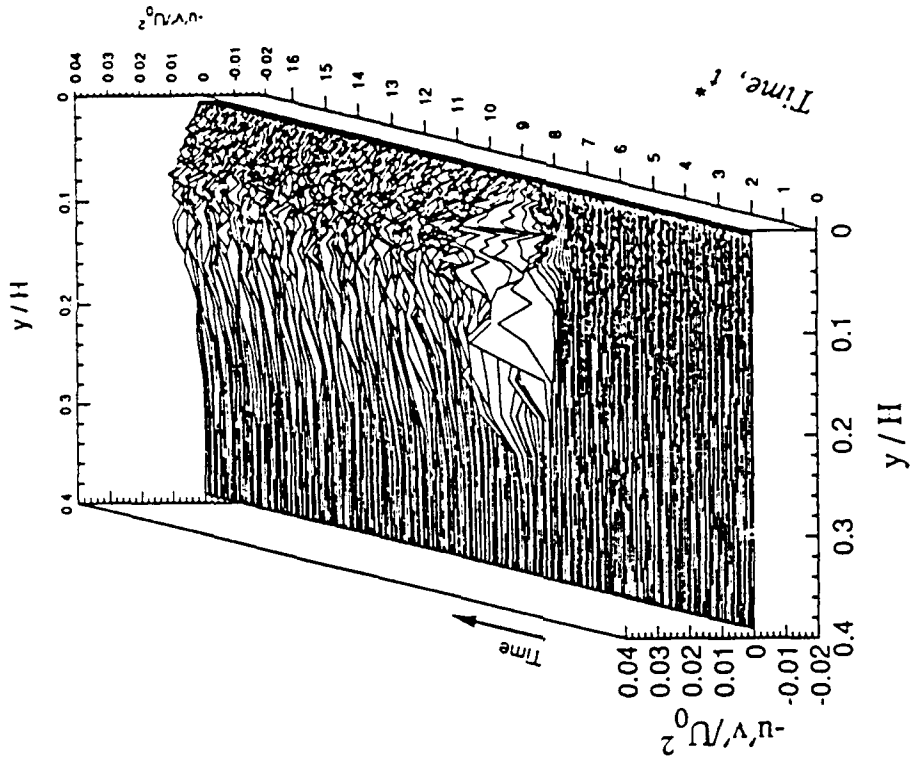
Figure 6.8 Evolution of the phase-averaged $\langle v'v' \rangle$-velocity profiles during separation development: (a) at LP:1, (b) at LP:2, (c) at LP:3, and (d) at LP:4.
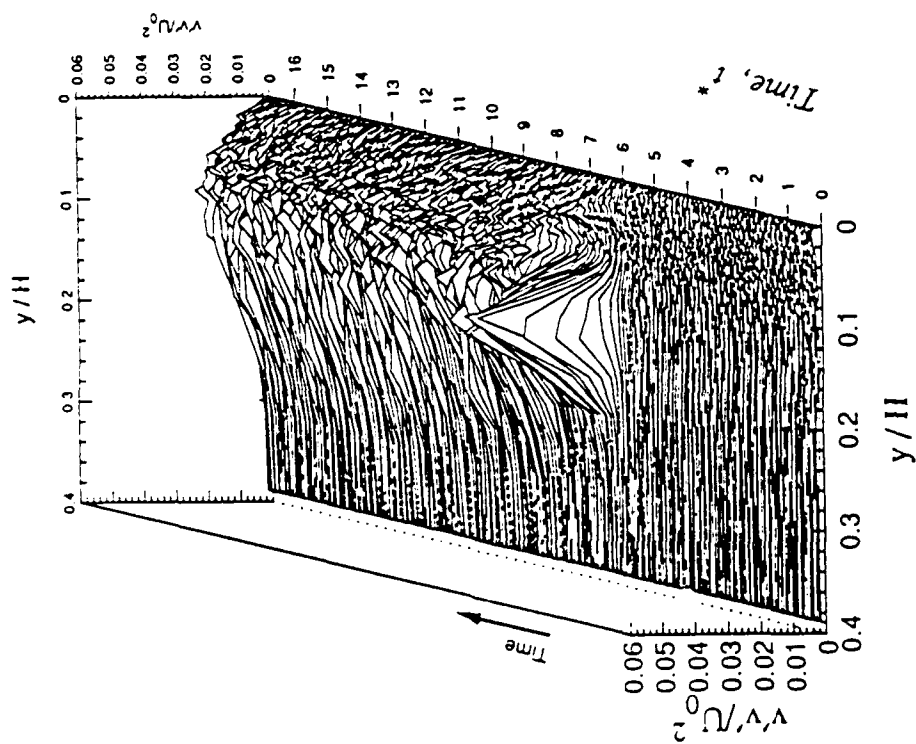
Figure 6.9 Evolution of the phase-averaged $\langle u'v'\rangle$-velocity profiles during separation development: (a) at LP:1, (b) at LP:2, (c) at LP:3, and (d) at LP:4.
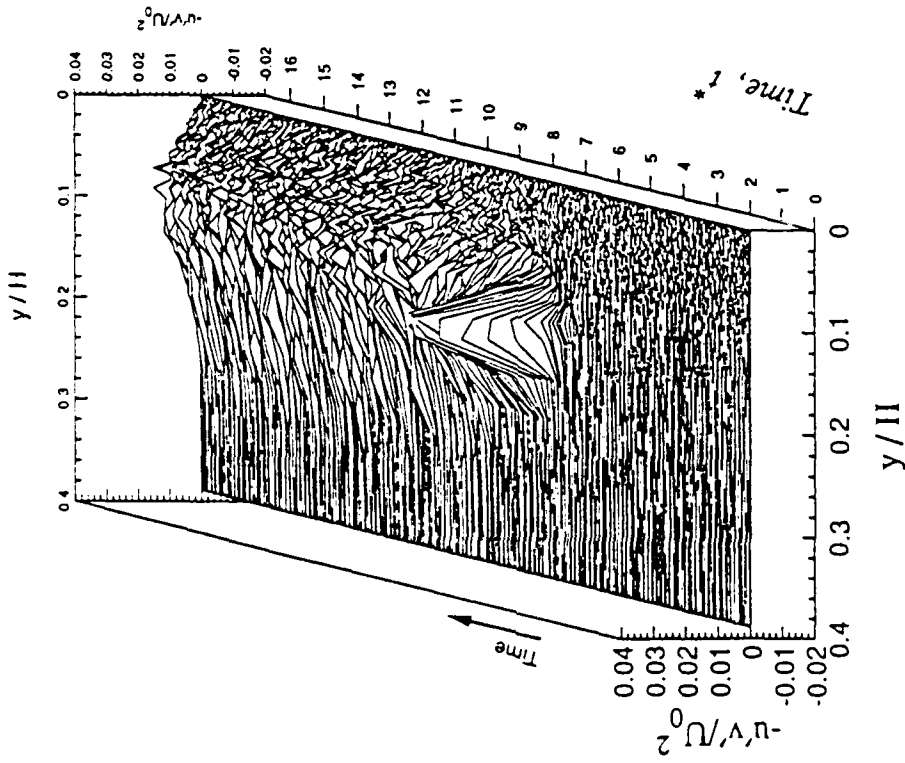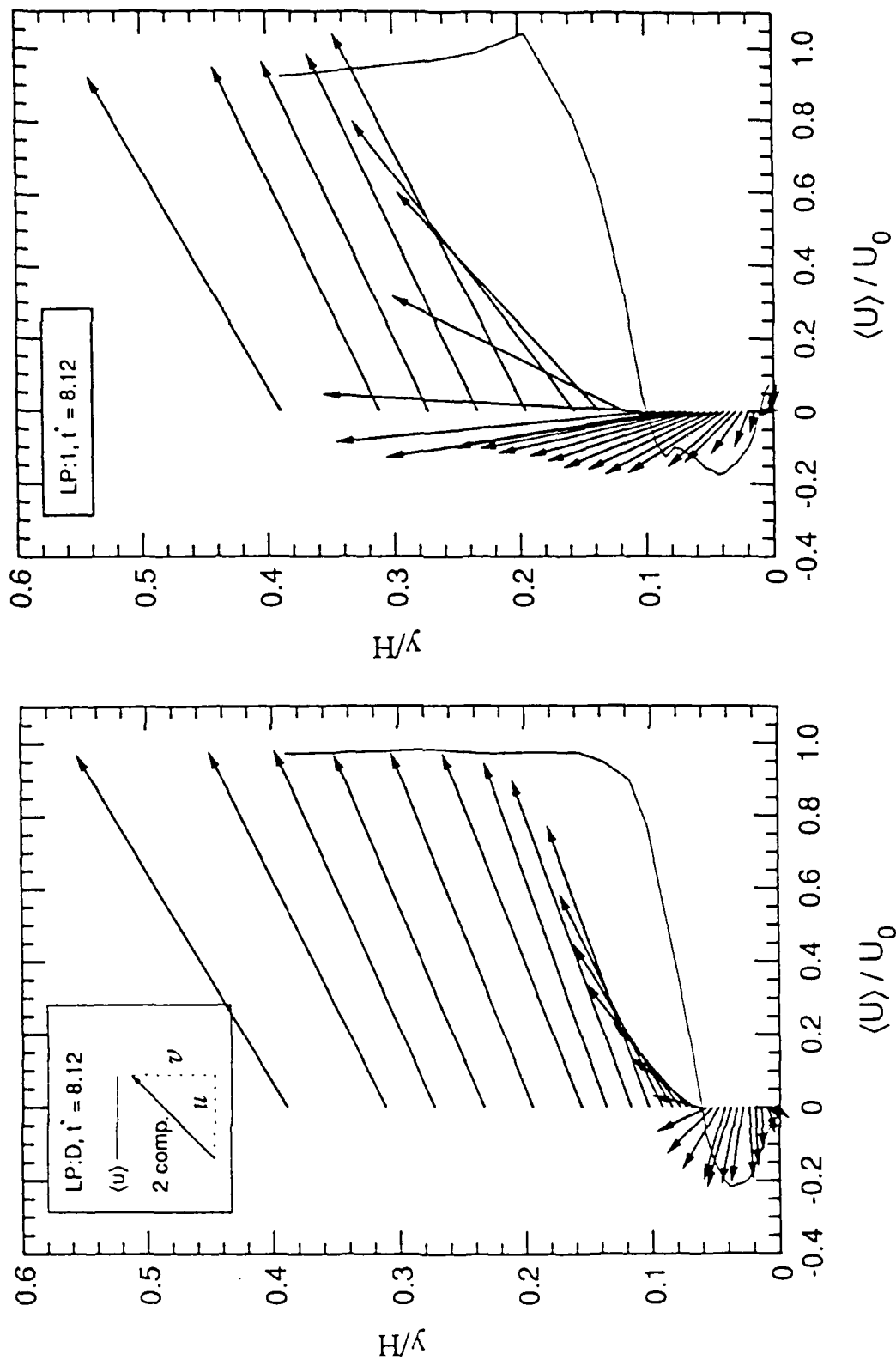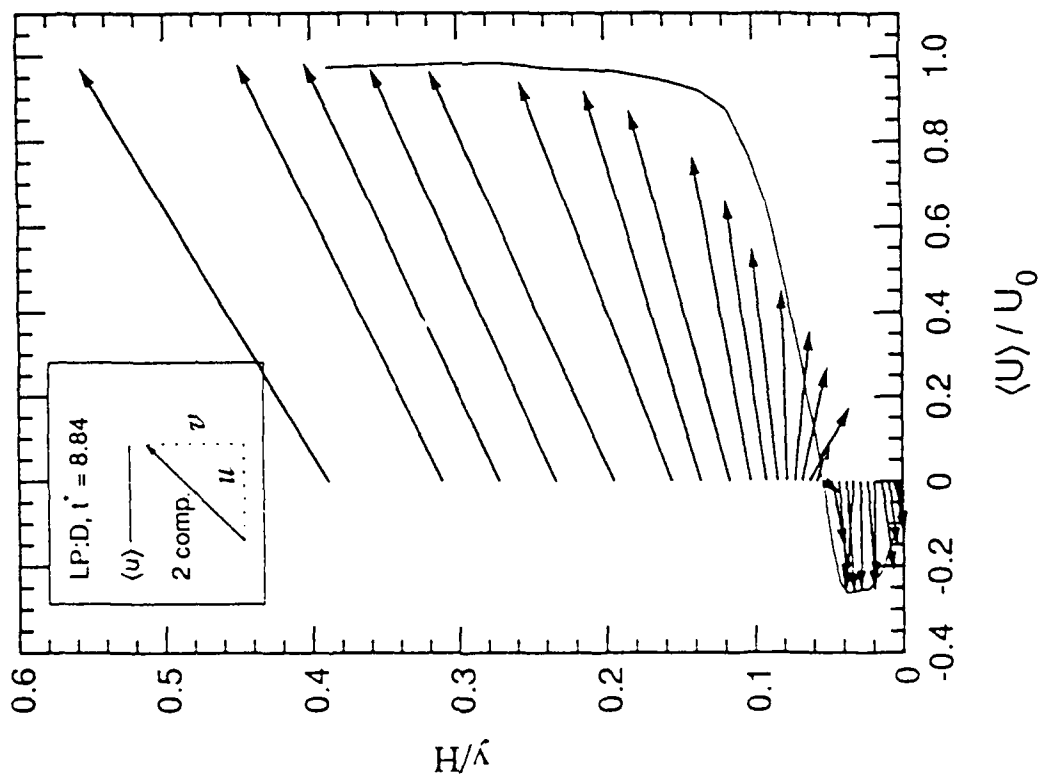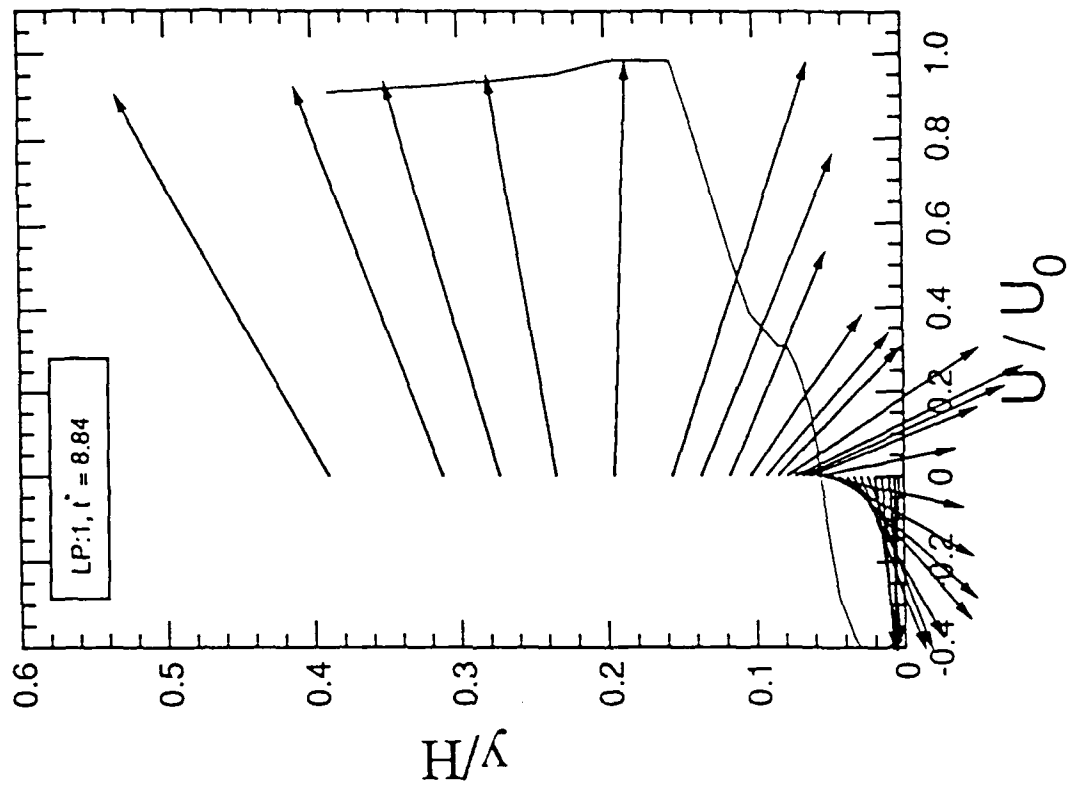
Figure 6.10 Selected velocity profiles and two-component velocity vectors reveal large-scale unsteadiness: (a) LP:D and LP:1 at $t^* = 8.12$; (b) LP:D and LP:1 at $t^* = 8.84$.

LP:1, $t^* = 8.84$

LP:D, $t^* = 8.84$

$\langle u \rangle$ ——

2 comp. v u

y/H

y/H

U/U_0

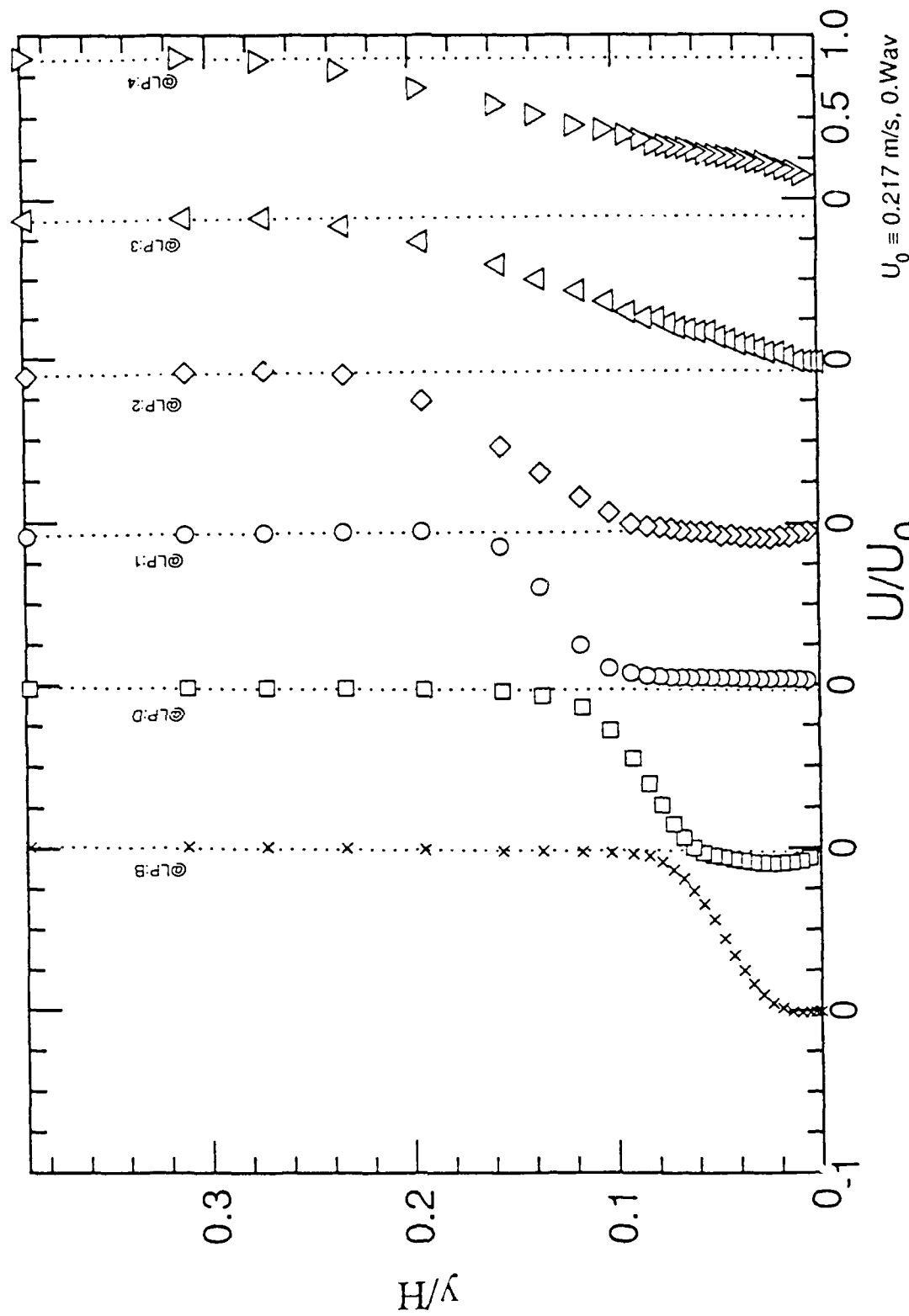$\langle U \rangle / U_0$

Quasi-steady Separation Profiles

Figure 6. Quasi-steady separation profiles along the centerline. Dotted lines are respective potential-flow velocity profiles.

Figure 6.11 Phase-averaged velocity profiles along the centerline during quasi-steady separation.
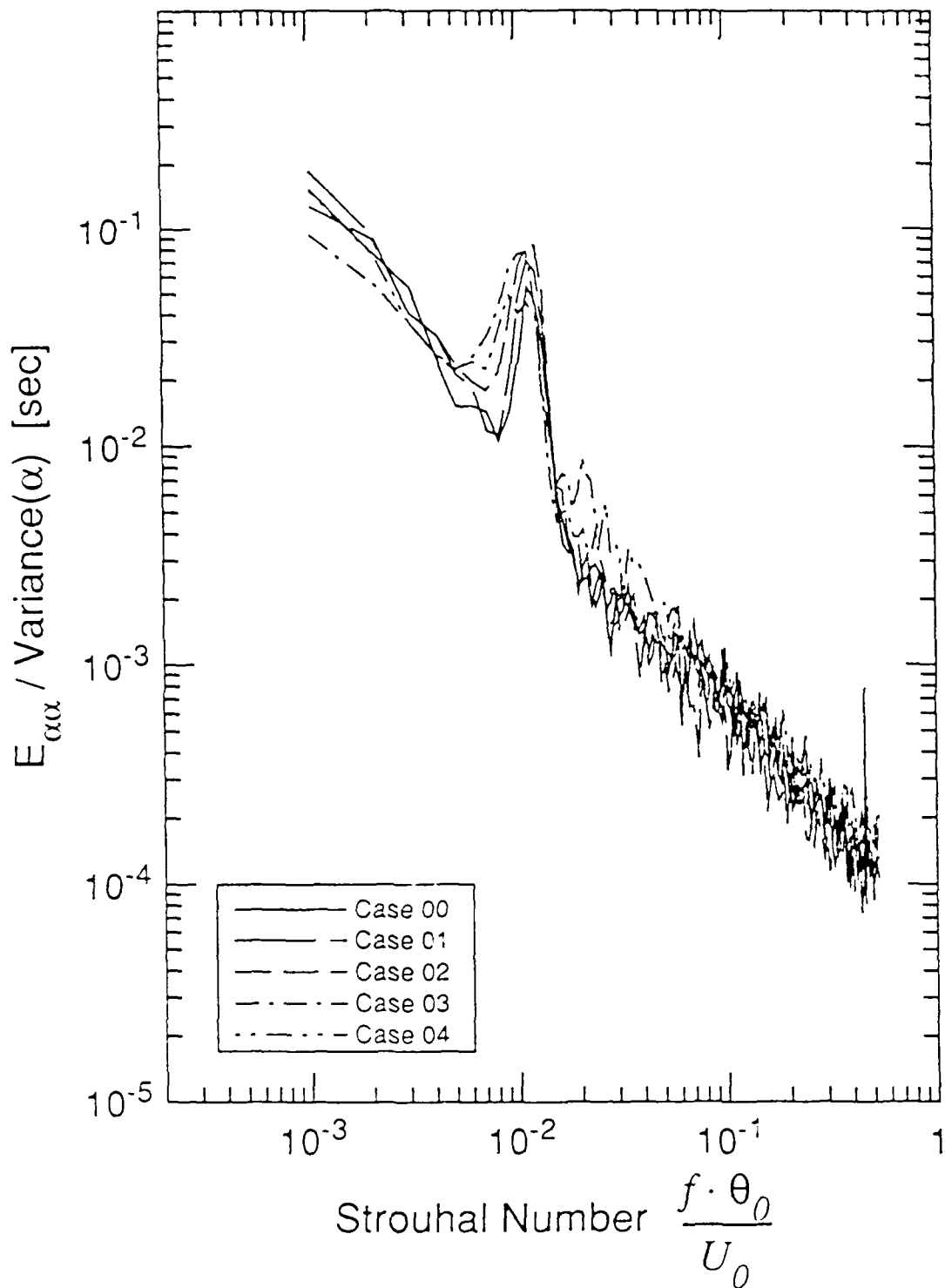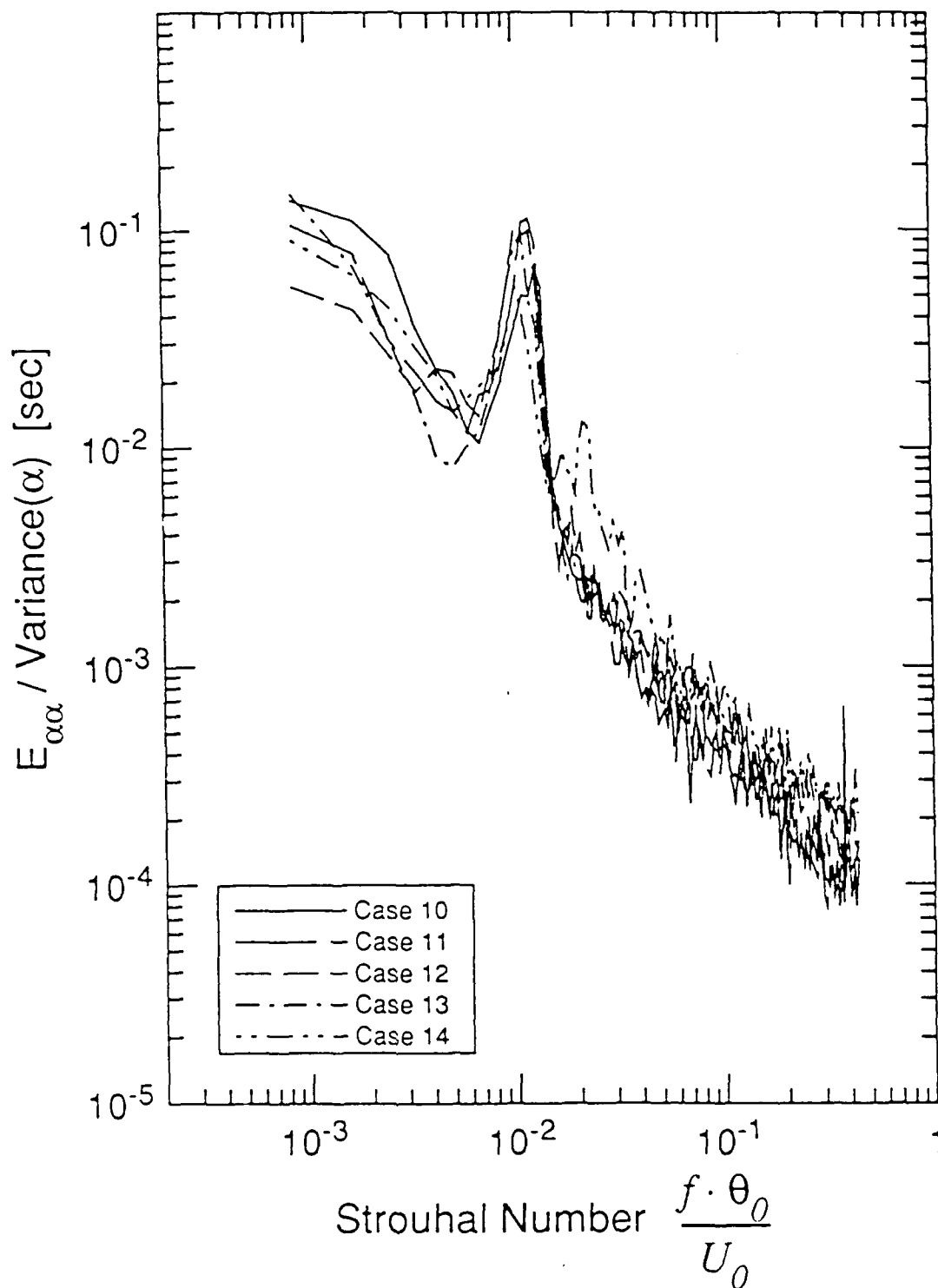
U Power Spectra

Flow cases: 0?

Figure 6.12 Strouhal number for a single U_0 for various suction cases: (a) cases $0_\sqcup$, (b) cases $1_\sqcup$, and (c) cases $2_\sqcup$.

U Power Spectra

Flow cases: 1?

6,12 b

U Power Spectra

Flow cases: 2?

Legend:
- Case 20
- Case 21
- Case 22
- Case 23
- Case 24

Y-axis: $E_{\alpha\alpha}$ / Variance(α) [sec]

X-axis: Strouhal Number $\dfrac{f \cdot \theta_0}{U_0}$
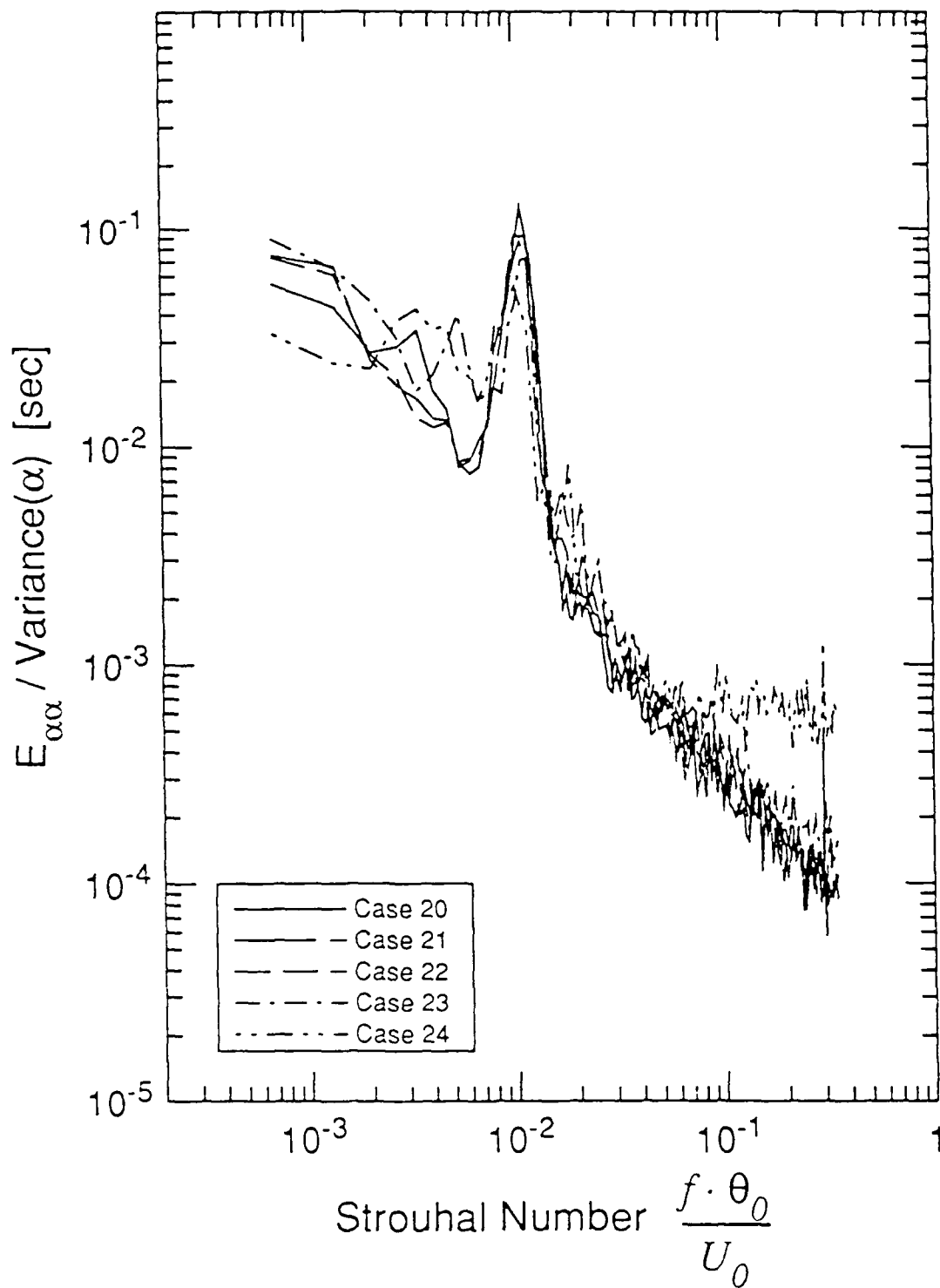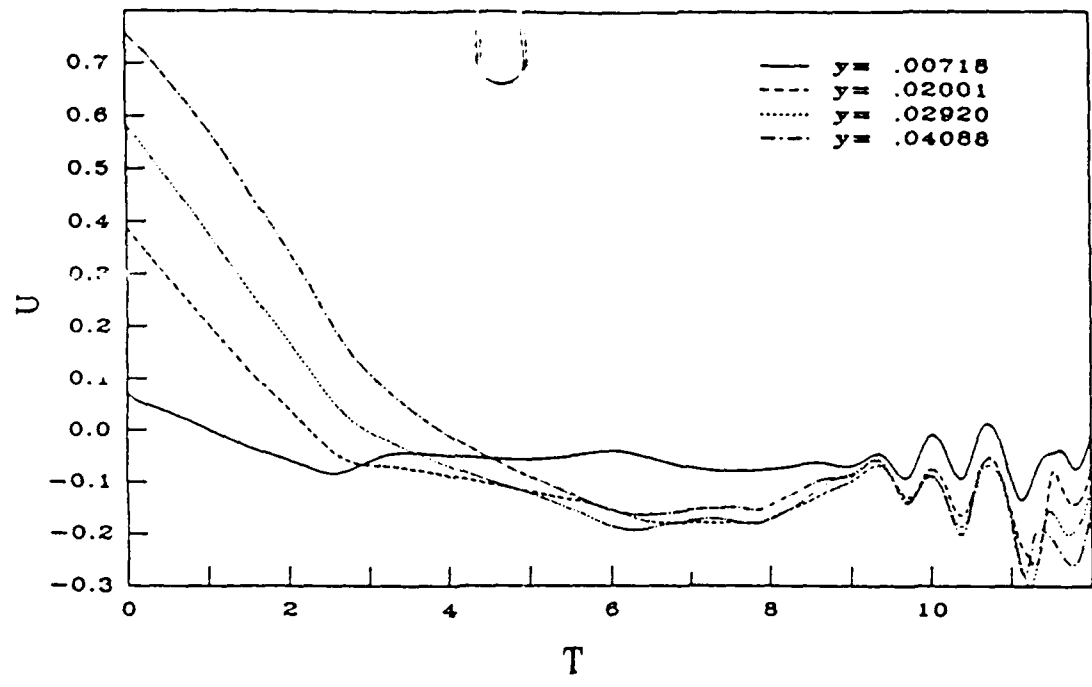
6.12c

Figure 4.15 Velocity histories at four distances from the wall.   a) Location 1.
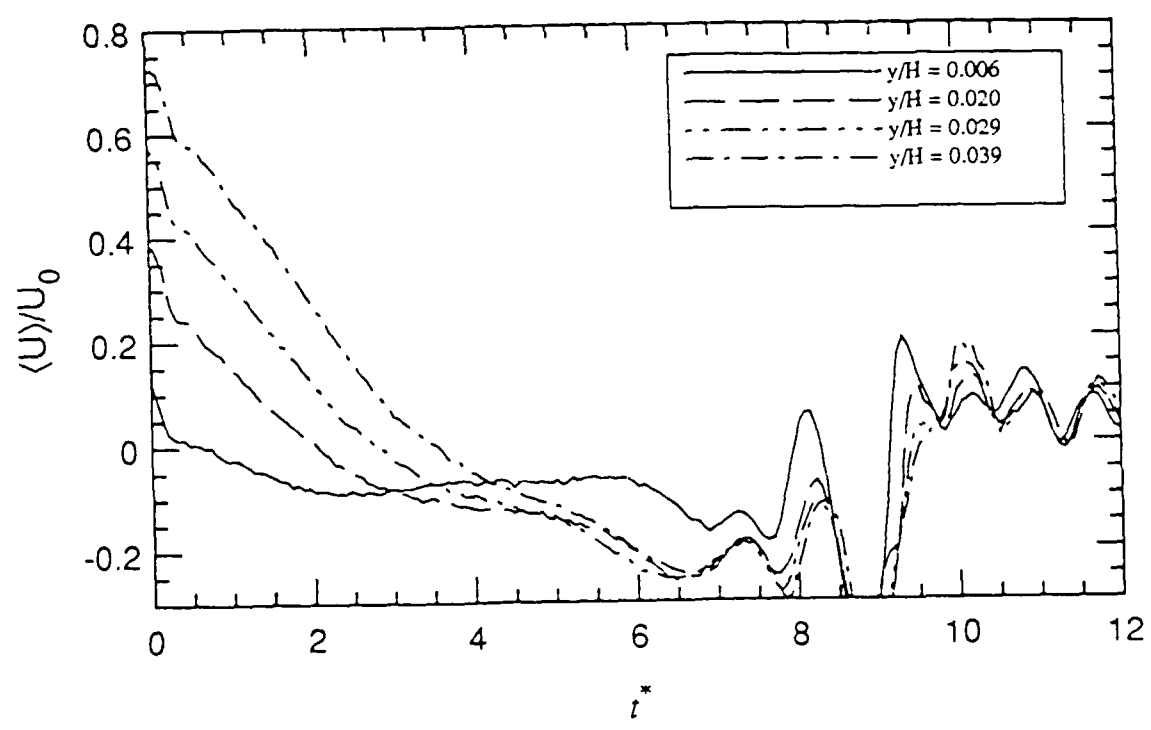
Figure 6.13   Velocity histories at station LP:1 and at several distances. y/H. from the wall during separation development: (a) results of DNS by Pauley. et al. (1988). (b) results of the experiment. shown in figure 6.3a. re-scaled for comparison.

3
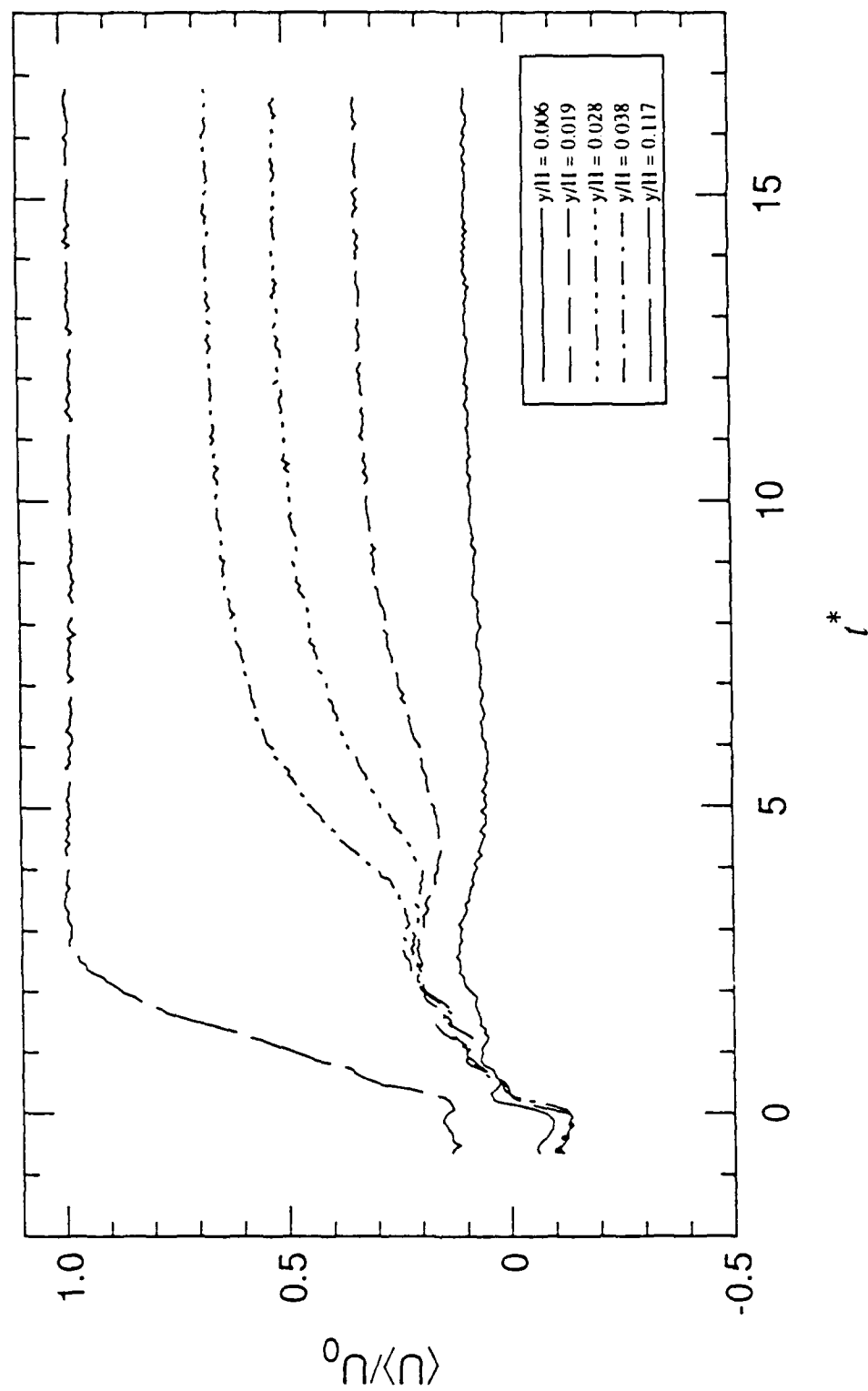
Figure 6.14   Velocity histories at five distances from the wall during separation
decay at station LP:2.

Decaying Separation: Diffusion of Vorticity
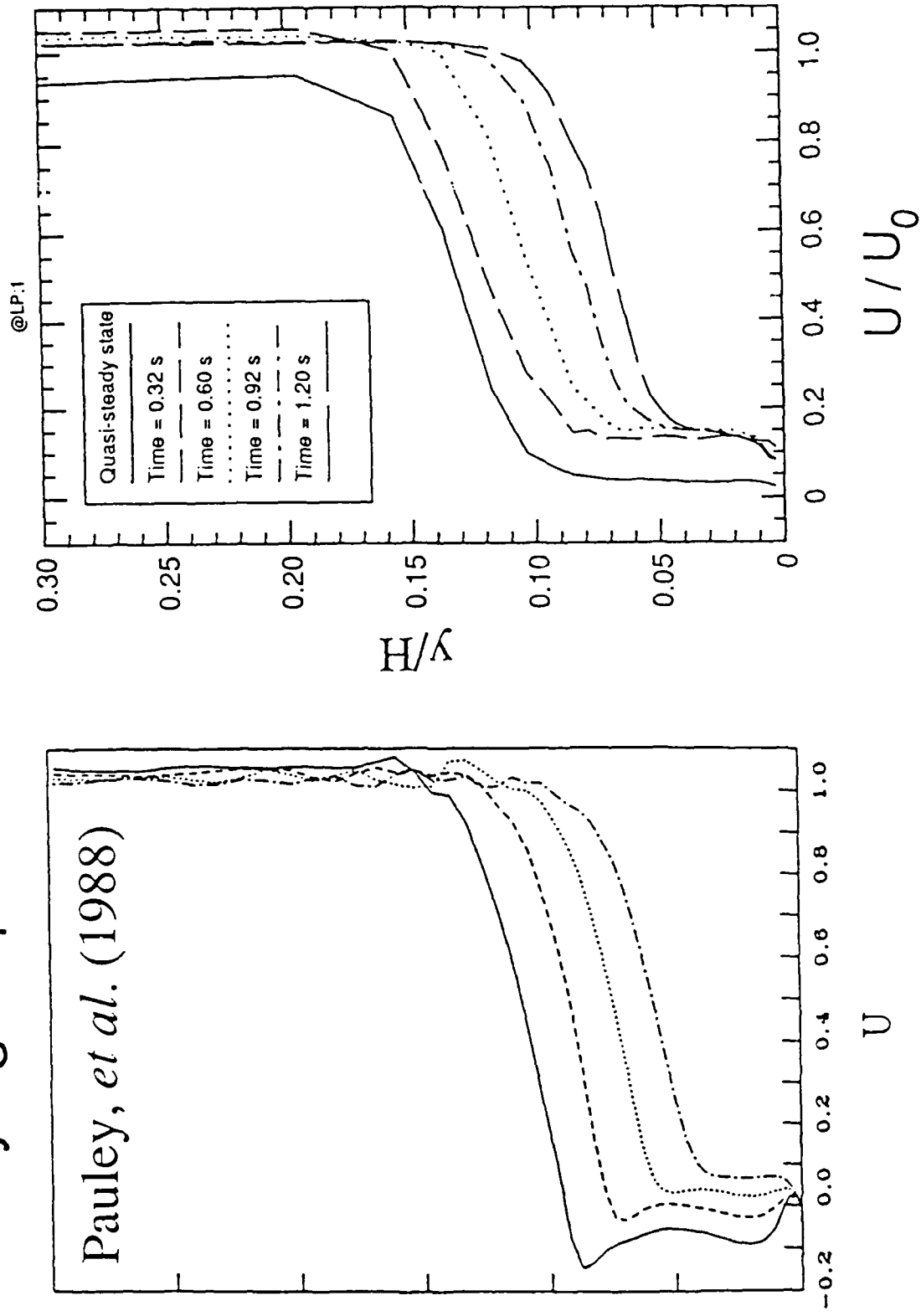
Figure 6.15   Velocity profiles during separation decay are compared alongside the computational results of Pauley, *et al.* (1988): (a1) and (a2) at LP:D, (b1) and (b2) at LP:1.
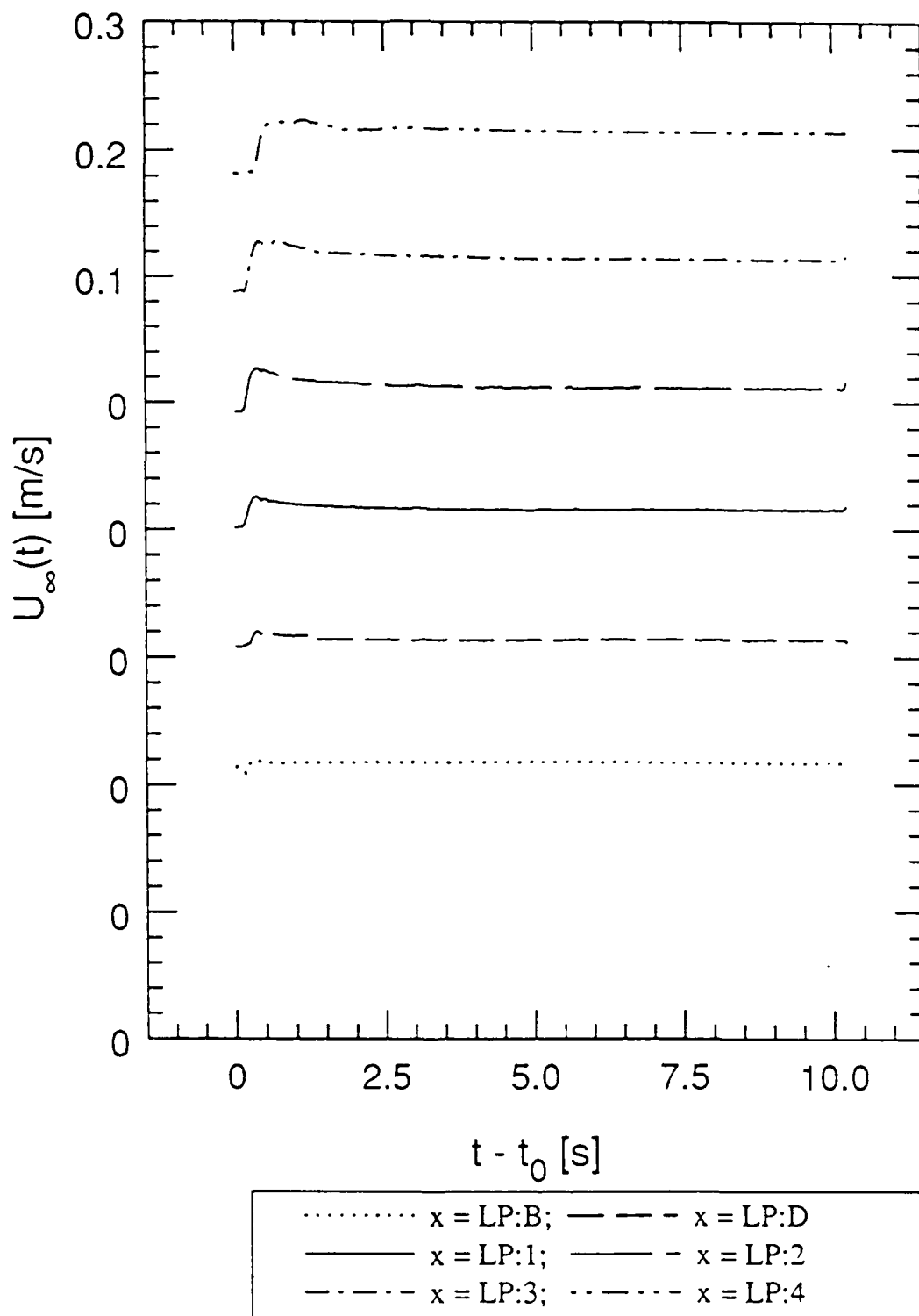
Figure 6.16 Time history of the local U_∞ along the centerline of the decaying separation.
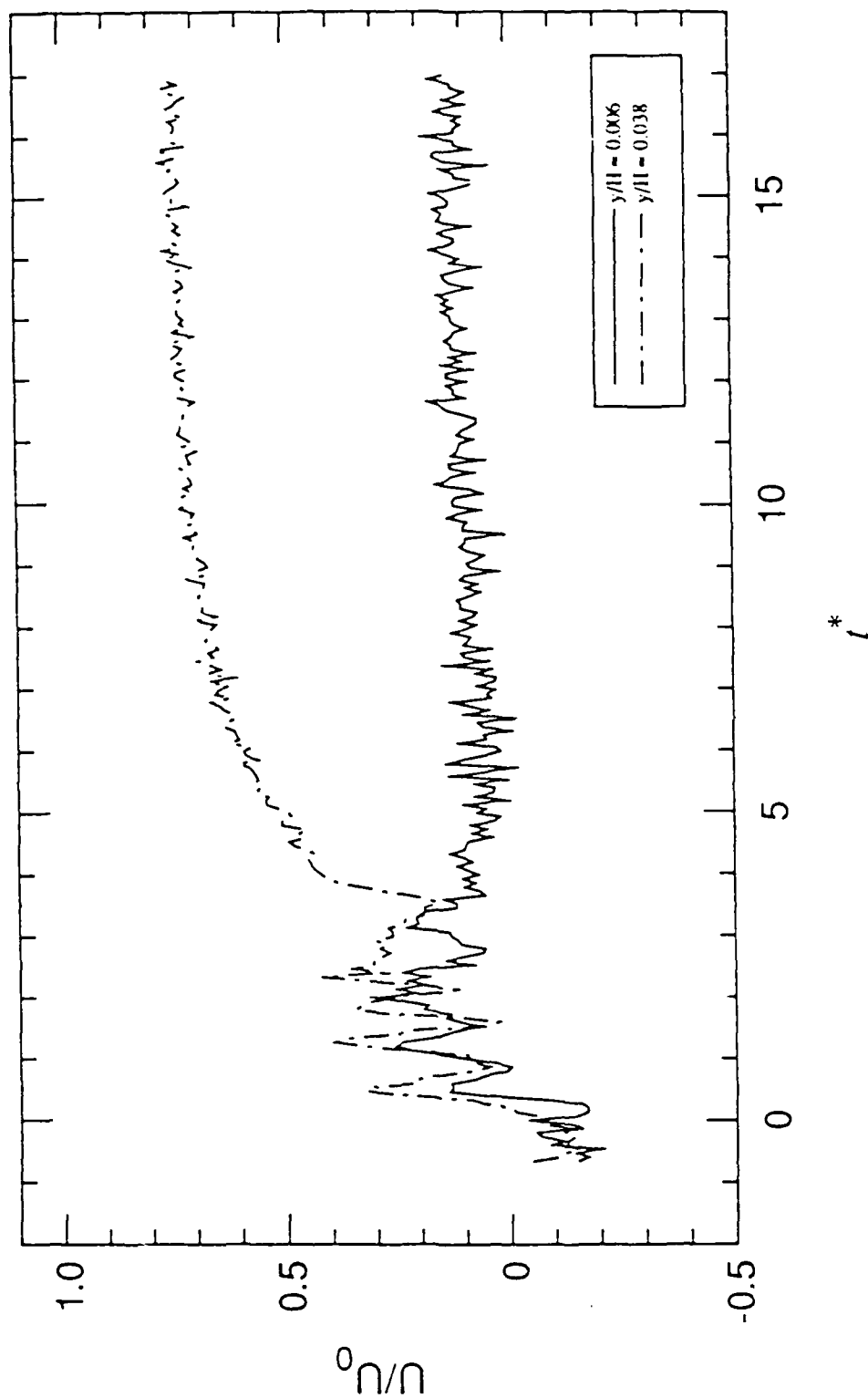
Figure 6.17 Velocity histories of the decaying separation at four distances from the wall at station LP:2: non-simultaneous individual realizations.
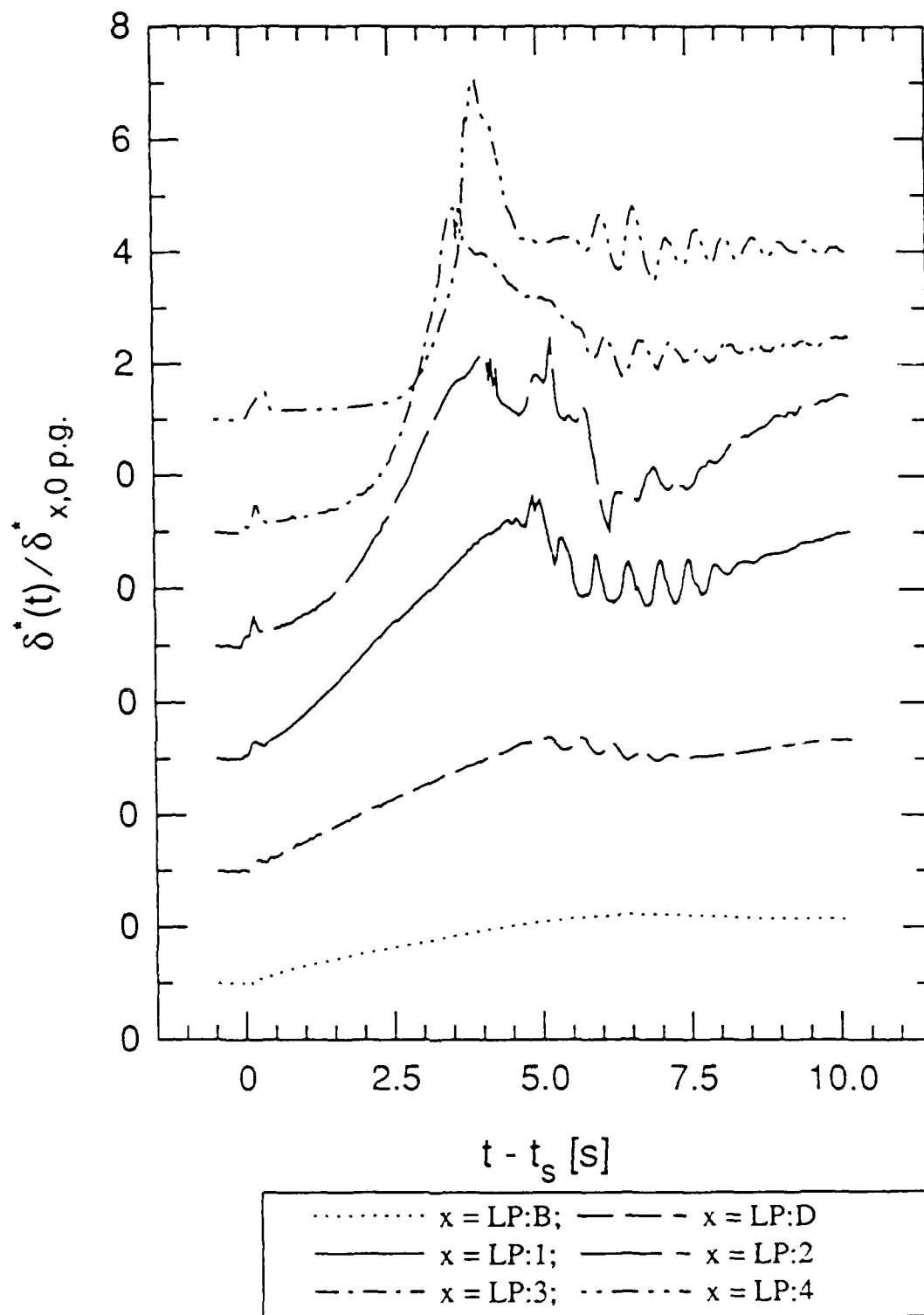
Figure 6.18   Time history of the displacement thickness, δ^*, along the centerline of the developing separation. Values are normalized to the value of the local δ^* during zero pressure-gradient conditions.
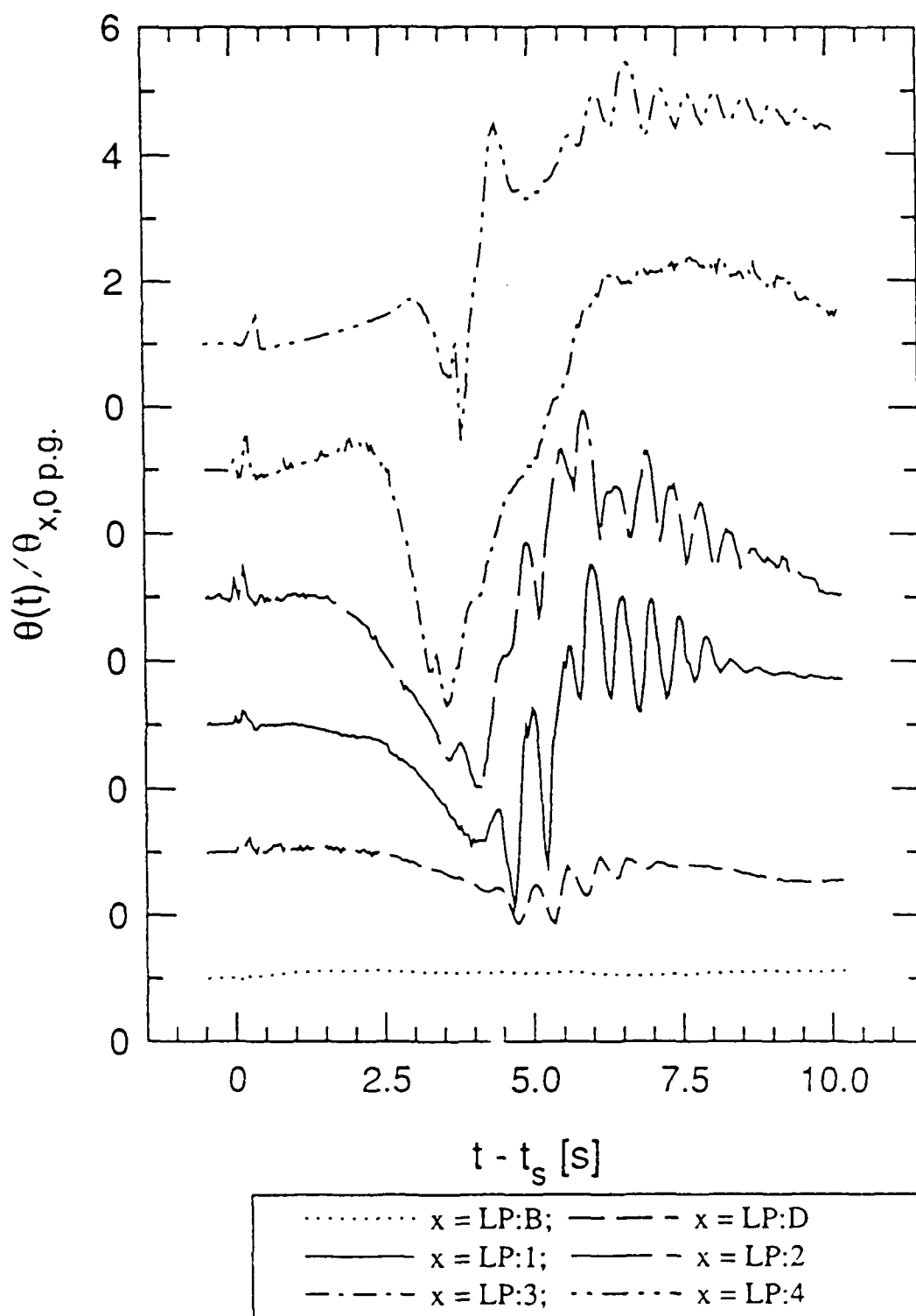
Figure 6.19   Time history of the momentum thickness, θ, along the centerline of
the developing separation. Values are normalized to the value of the
local θ during zero pressure-gradient conditions.

Figure 6.20 Time history of the displacement thickness, δ^*, along the centerline of the decaying separation. Values are normalized to the value of the local δ^* during zero pressure-gradient conditions.

Figure 6.21 Time history of the momentum thickness, θ, along the centerline of the decaying separation. Values are normalized to the value of the local θ during zero pressure-gradient conditions.

Figure 6.22 Time history of the local U_∞ along the centerline of the developing separation.

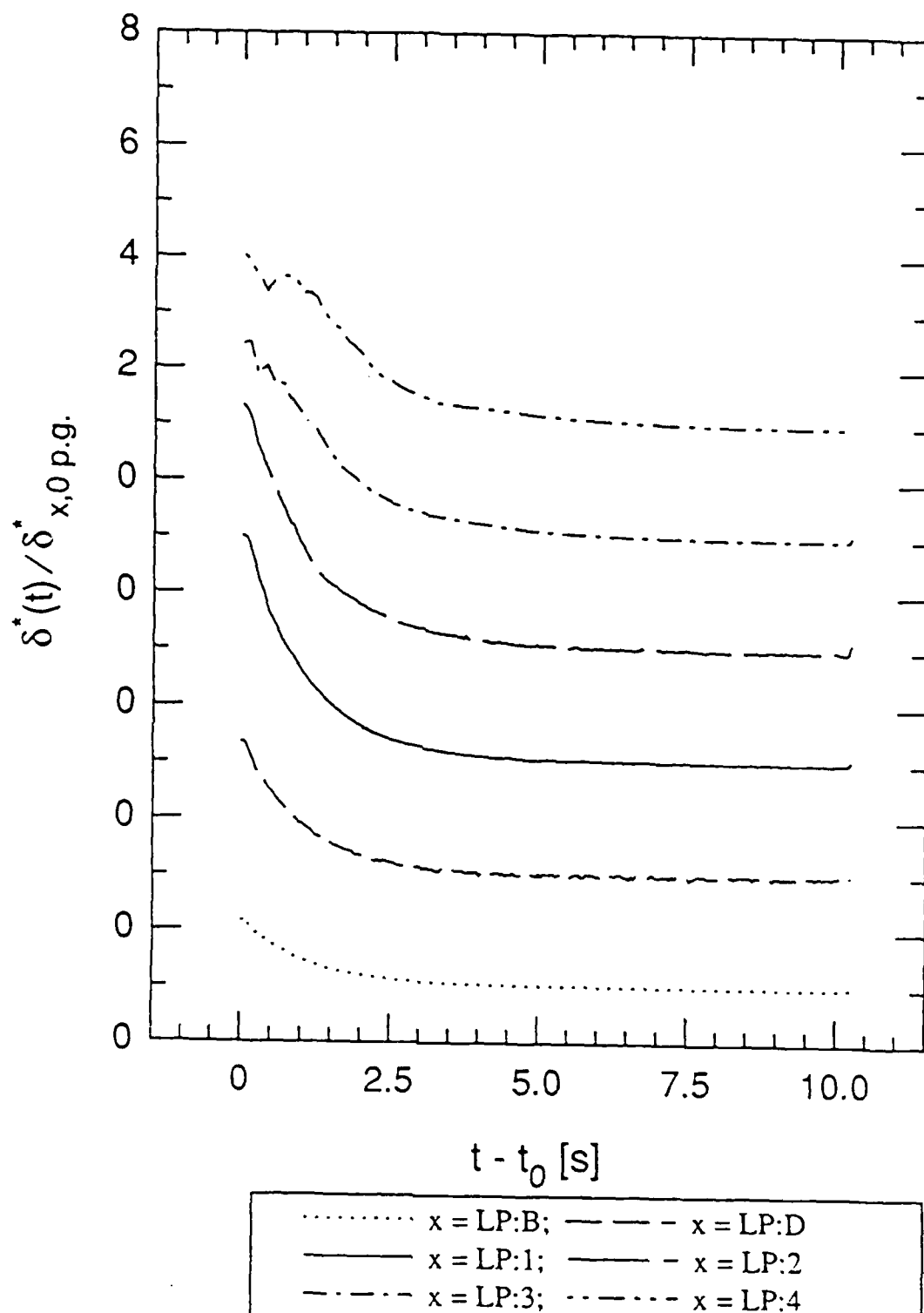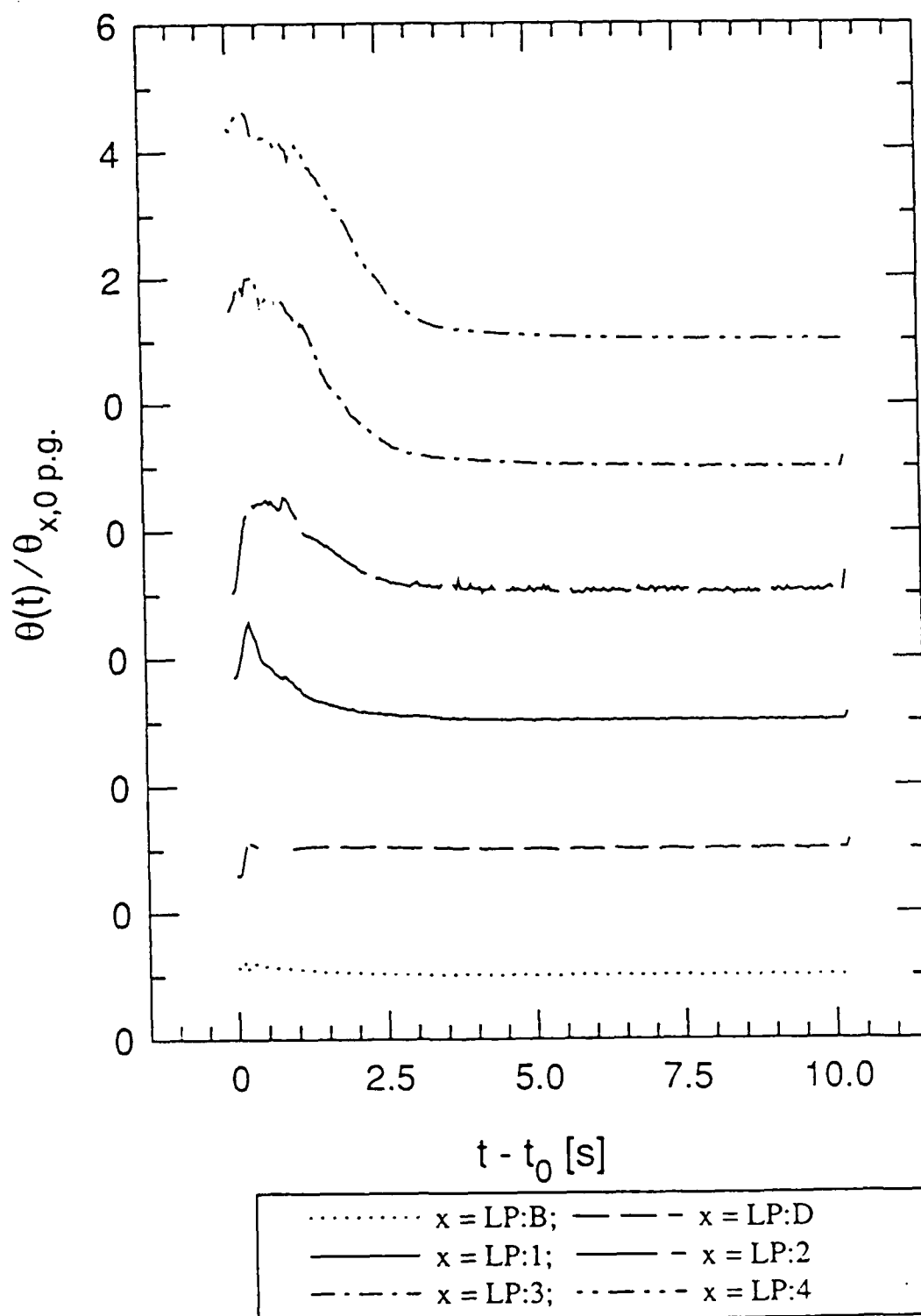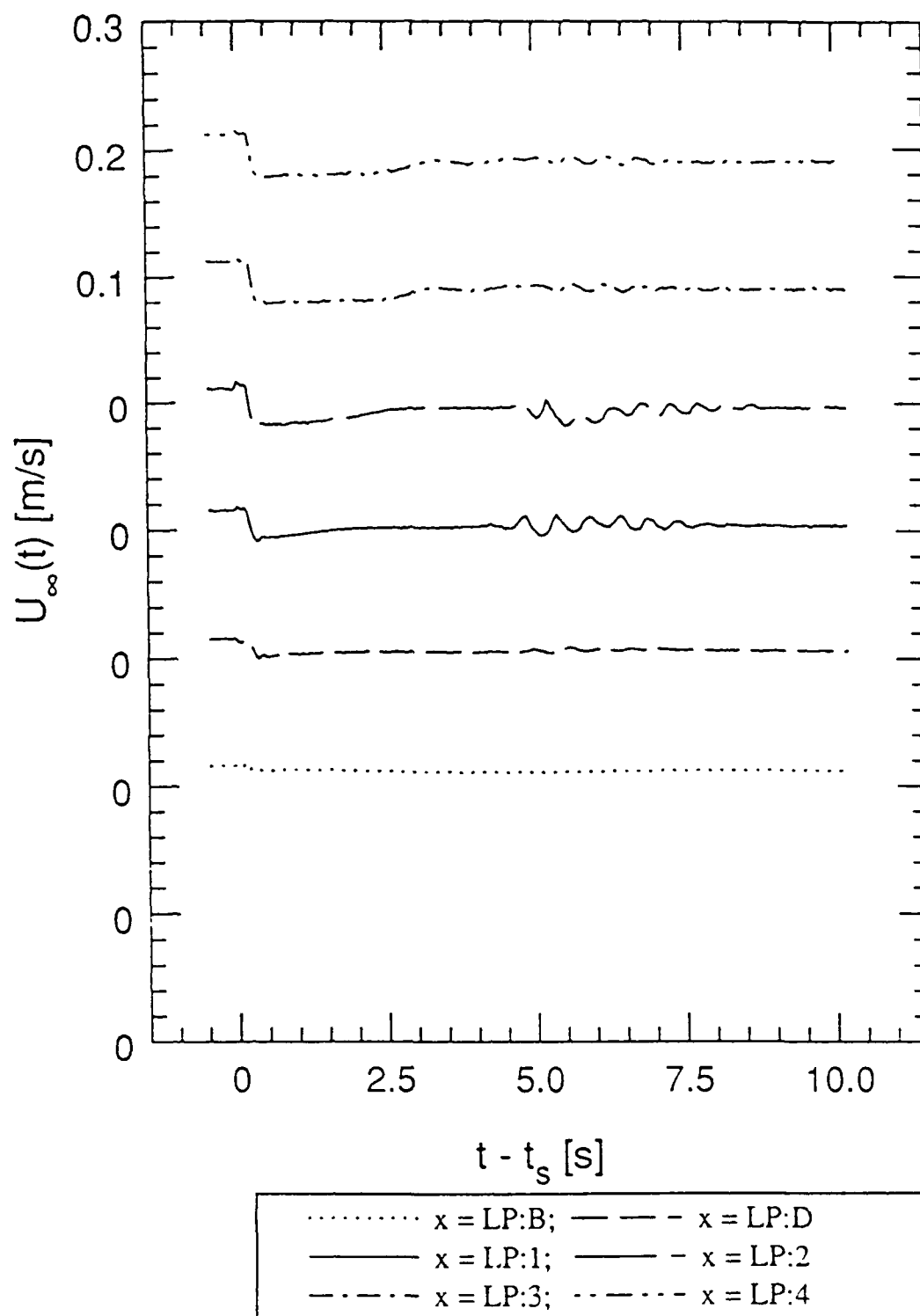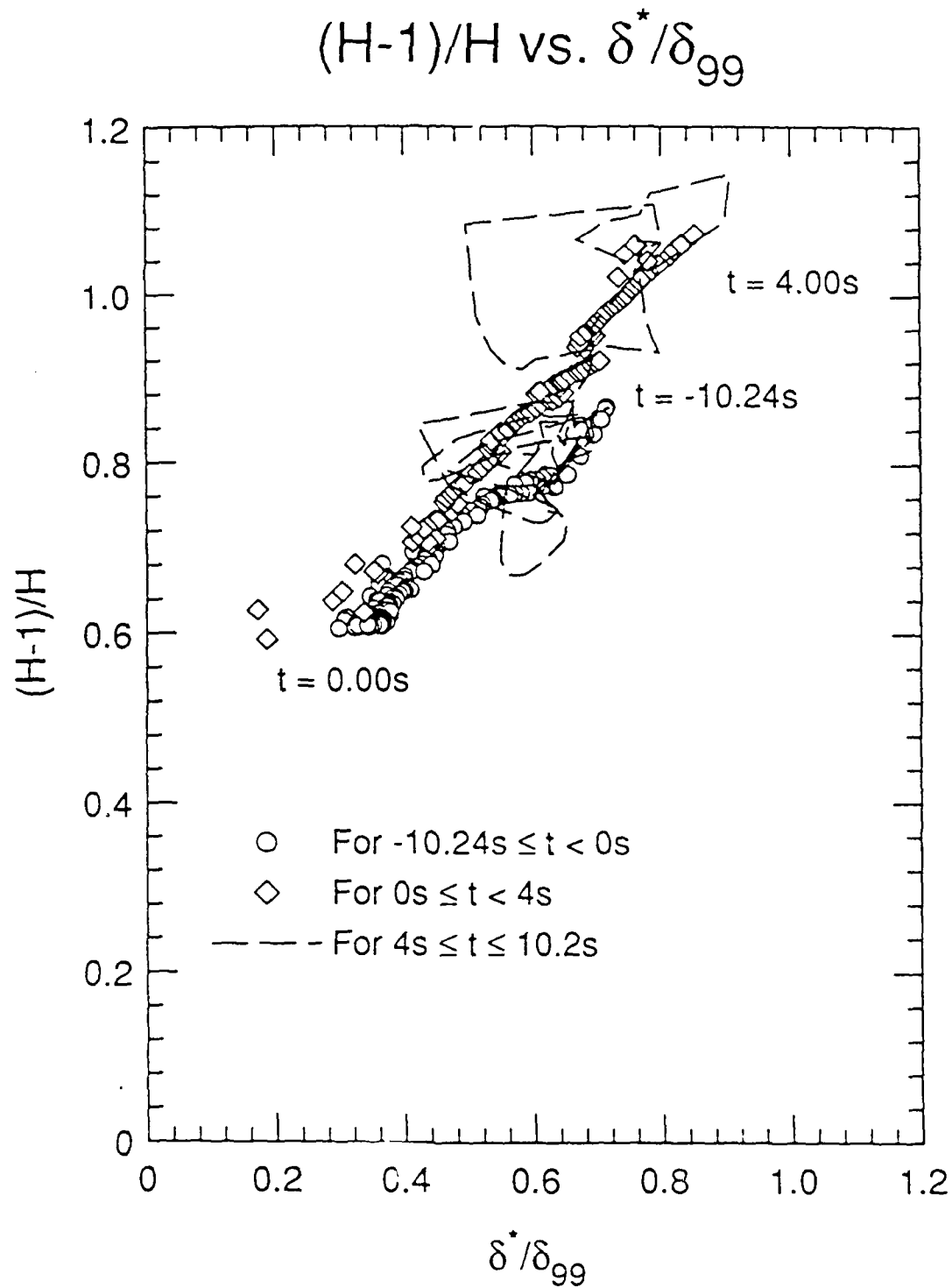Figure 6.23 Trajectory of the relation $h = (H-1)/H$ vs. δ^*/δ_{99} at station LP:1 during the development and the decay of separation.

PART 4. COMPLETED UNSTEADY 2-D COMPUTATIONAL WORK

1 INTRODUCTION

Separation is a critical consideration in a variety of technical situations, including the design of low-speed aircraft, i.e., long-endurance vehicles at high altitudes, high aspect ratio sailplane wings, remotely piloted vehicles at low altitudes, ultra-light aircraft, jet engine fan blades, inboard sections of helicopter rotors, and canards on generator aviation aircraft. Separation depends on many factors, including unsteadiness, adverse pressure gradient, freestream turbulence intensities and spectra, compressibility, and three-dimensionality of the flow. In this effort the effects of adverse pressure gradient and unsteadiness are studied by computation. In order to isolate these effects, the test flow consists of a laminar, incompressible boundary-layer flow with a predictable, well-described unsteady freestream pressure gradient applied. Cases for impulsively (gusts and lolls) and sinusoidally fluctuating pressure distributions are possible in the computations. The response of the boundary layer to these fluctuations is observed, in particular, separation location and structure and the rate at which separation regions develop and decay. If these zones develop slowly, there may be no serious problems; but if the off-design unsteady conditions persist sufficiently long, the buildup of these separated regions could be fatal to a low Reynolds number vehicle (chord Reynolds numbers of 50,000-500,000). The recent conference on Low Reynolds Number Aerodynamics at Notre Dame in 1989 (see T.J. Mueller 1989) was focused on the performance of these vehicles.

Crouch and Saric (1986) state that in this lower range of chord Reynolds numbers (down to 10,000), the airfoil performance rapidly deteriorates. This drop in performance is due to the increase in skin friction (thus, increase in drag) and the fact that the airfoil can behave as a flat plate. To account for the increase in drag, airfoils have been designed with strong adverse pressure gradients to increase lift. However, a laminar separation bubble is formed when a previously attached laminar boundary layer encounters an adverse pressure gradient of sufficient magnitude to cause the flow to separate. This phenomena is illustrated in Figure 1. In particular, the flow phenomena associated with the formation of laminar separation bubbles play an

important role in the development of the boundary layer. For example, two of the most characteristic features of separation are the sudden thickening of the boundary layer and the generation of a slow-moving turbulent wake composed of large-scale vortices.

The laminar boundary layer separates from the airfoil surface at S and reattaches at the point R downstream of point S. The flow can roughly be divided into two regions (O'Meara & Mueller, 1987; Roberts, 1980). The first region is bounded by the mean dividing streamline and the airfoil surface. The mean dividing streamline is the collection of points across each velocity profile at which the integrated mass flow is zero. The second region of flow consists of the free shear layer contained between the outer edge of the viscous region and the mean dividing streamline. The unstable character of the free shear layer results in transition to turbulence at a location denoted by T. Momentum transfer due to turbulent mixing eventually eliminates the reversed flow near the w :¹ and the flow reattaches at point R.

The determination of point S and the flow properties in the neighborhood of point S under both steady and unsteady conditions is essential because this controls the size and shape of the wake and, thereby, the basic characteristics of lifting surfaces. The classical boundary-layer criterion of separation for steady flows, that is, the vanishing of skin friction, has been used successfully in the prediction of the location of separation even though the boundary-layer approximation breaks down in the neighborhood of separation. Moore (1957), Rott (1956), and Sears (1956) argue that the boundary-layer equations can also be used to predict unsteady separation. Sears (1956) suggests as a criterion the simultaneous vanishing of the shear and the velocity at a point within the boundary layer or the MRS point in a frame of reference moving with separation. A *complete* discussion of this condition is contained in Henk, Reynolds & Reed (1990).

The entire flow field can be predicted with the full Navier-Stokes equations since these equations are free of singularities. This is the approach we adopt.

2 TECHNICAL APPROACH

Direct numerical simulations are playing an increasingly important role in the

investigation of separation; the literature is growing, especially recently. This trend is likely to continue as considerable progress is expected towards the development of new, extremely powerful supercomputers. In such simulations, the full Navier-Stokes equations are solved directly by employing numerical methods, such as finite-difference or spectral methods. The direct-simulation approach is widely applicable since it avoids many of the restrictions that usually have to be imposed in theoretical models.

The principle goal of this work is the development of a computational method for the simulation of the process of unsteady separation on the upper surface of a wing. By varying the freestream conditions (oscillations, ramps), the intermittent off-design conditions low-Reynolds-number flight vehicles are likely to encounter, such as variations in angle-of-attack or the passage of a gust, can be simulated and the rate at which separated regions develop and decay can be studied. In this way it is also possible to verify the length and time scales predicted by triple-deck theory. The existence of such a method will provide a tool which will enable computation to complement theoretical and experimental contributions to further the understanding of the physics of these flows and, ultimately, will provide a tool for the prediction and modeling of these flows.

Basically, this model involves the use of the unsteady inviscid solution for the airfoil or wing shape as an edge boundary condition for a Navier-Stokes solution near the wall. The inviscid solution is described in Section 2.1 and the viscous solution is described in Section 2.2. Once the viscous solution is obtained, the pressure distribution is determined at the wall and the "actual" lift and drag histories for the airfoil under unsteady, off-design conditions can be obtained.

2.1 UNSTEADY INVISCID METHOD

A vortex panel method is used to compute the inviscid unsteady flow around a given airfoil or wing shape. The unsteady Kutta condition is used as well as conservation of vorticity and the fact that each point of the wake must be aligned in the force-free position. Changes in angle of attack or speed cause vorticity to be shed from the trailing edge of the airfoil. This

vorticity is then convected along aft of the airfoil according to the local velocity vector.

The resulting velocity field is then applied as the edge condition for the Navier-Stokes calculation presented in the next section.

2.2 UNSTEADY VISCOUS METHOD

2.2.1 PRIMARY EQUATIONS

The partial differential equations governing the motion of a two-dimensional, incompressible flow of a Newtonian fluid with no body forces and constant fluid properties are the two momentum equations (Navier-Stokes) and the continuity equation (presented here in two-dimensional form, for simplicity). Using Cartesian coordinates and allowing for time dependence, the nonconservative forms of these equations are:

$$\partial u/\partial t + u\partial u/\partial x + v\partial u/\partial y = -(1/\rho)\partial p/\partial x + \upsilon(\partial^2 u/\partial x^2 + \partial^2 u/\partial y^2) \tag{1}$$

$$\partial v/\partial t + u\partial v/\partial x + v\partial v/\partial y = -(1/\rho)\partial p/\partial y + \upsilon(\partial^2 v/\partial x^2 + \partial^2 v/\partial y^2) \tag{2}$$

$$\partial u/\partial x + \partial v/\partial y = 0 \tag{3}$$

In Equations (1) through (3), x is the streamwise coordinate, y is the transverse coordinate, and u and v are the velocity components in the streamwise and transverse directions, respectively, p is the pressure, υ is the kinematic viscosity, ρ is the mass density, and t is time. The overbars represent dimensional quantities.

Introducing the definition of a substantial derivative

$$D(\ )/Dt = \partial(\ )/\partial t + (V \bullet \nabla)(\ ) \tag{4}$$

where ∇ is the gradient operator

$$\nabla = \left(\partial/\partial x, \partial/\partial y\right) \tag{5}$$

and

$$V = (u,v) \tag{6}$$

Equations (1) and (2) become the two-dimensional vector momentum equation

$$DV/Dt = -(1/\rho)\nabla p + \upsilon\nabla^2 V \tag{7}$$

where ∇^2 is the Laplacian operator

$$\nabla^2 = \partial^2/\partial x^2 + \partial^2/\partial y^2 \tag{8}$$

By the definition of the gradient operator as given in Equation (5), the continuity equation can be written in the form

$$\nabla \bullet V = 0 \tag{9}$$

2.2.2 VORTICITY AND STREAM-FUNCTION EQUATIONS

The pressure is eliminated from Equations (1) and (2) by taking the curl of Equation (7), i.e., cross-differentiating Equation (1) with respect to y, (2) with respect to x, and combining equations. The result is

$$\partial/\partial t(\partial u/\partial y - \partial v/\partial x) + u[\partial/\partial x(\partial u/\partial y - \partial v/\partial x)] + v[\partial/\partial y(\partial u/\partial y - \partial v/\partial x)] =$$
$$\upsilon[\partial^2/\partial x^2(\partial u/\partial y - \partial v/\partial x) + \partial^2/\partial y^2(\partial u/\partial y - \partial v/\partial x)] \tag{10}$$

Defining the vorticity as

$$\omega = (\partial u/\partial y - \partial v/\partial x) \tag{11}$$

Equation (10) becomes the vorticity-transport equation,

$$\partial \omega/\partial t = -u\,\partial \omega/\partial x - v\,\partial \omega/\partial y + \upsilon(\partial^2\omega/\partial x^2 + \partial^2\omega/\partial y^2)$$

or

$$\partial \omega/\partial t = -V \bullet (\nabla \omega) + \upsilon \nabla^2 \omega \tag{12}$$

In three-dimensions, the vorticity vector is defined by

$$\omega = \nabla \times V \tag{13}$$

If $V = V(x,y,t)$, the vorticity vector is perpendicular to the gradient of V and reduces to one component ω_z, the negative of the present definition.

Equation (3), the continuity equation, is satisfied by the direct substitution of a stream function $\psi(x,y,t)$ defined by

$$u = \partial \psi/\partial y , v = - \partial \psi/\partial x \tag{14}$$

Therefore, the continuity equation is replaced by stream function and the number of independent variables reduces to one. Combining Equation (11) and (14) yields the Poisson equation

$$\omega = \partial^2 \psi/\partial x^2 + \partial^2 \psi/\partial y^2 \tag{15}$$

The vorticity-transport equation is parabolic and poses a mixed initial- and boundary-value problem in which the solution is computed by marching outward from some initial condition while satisfying the boundary conditions. The equation is nonlinear because u and v are functions of the dependent variable through Equations (14) and (15). The stream function equation, Equation (15), is elliptic and poses a boundary-value problem which is solved by specifying the boundary conditions on a complete contour enclosing the region.

As a result of the change of independent variables which replaced the velocity components with vorticity and stream function, the Navier-Stokes equations separate into one parabolic equation (the vorticity-transport equation) and one elliptic equation (the Poisson or stream-function equation). Therefore, only one transport equation needs to be solved.

2.2.3 NONDIMENSIONAL FORM OF THE EQUATION

The normalizing system used to nondimensionalize the governing equations and boundary conditions is based on airfoil chord c and freestream velocity U_∞. The dimensionless variables are defined by

$$u = u/U_\infty, \ v = v/U_\infty$$

$$x = x/c, \ y = y/c$$

$$\omega = \omega/(U_\infty/c) \tag{16}$$

$$\psi = \psi/U_\infty c$$

$$t = t/(c/U_\infty)$$

Substituting these variables into Equations (12), (14) and (15) and rearranging yields

$$\partial\omega/\partial t + u\partial u/\partial x + v\partial u/\partial y = (1/Re) \left(\partial^2\omega/\partial x^2 + \partial^2\omega/\partial y^2\right) \tag{17}$$

$$\omega = \left(\partial^2\psi/\partial x^2 + \partial^2\psi/\partial y^2\right) \tag{18}$$

$$u = \partial\psi/\partial y, \ v = - \partial\psi/\partial x \tag{19}$$

where Re is the dimensionless Reynolds number defined by

$$Re = U_\infty c/\upsilon \tag{20}$$

Thus, by nondimensionalizing the governing equations, the flow is characterized by one dimensionless parameter, the chord Reynolds number.

2.2.4 TRANSFORMED EQUATIONS

In the physical plane (x,y), grid points will be moved in time in response to the developing solution in order to concentrate grid points in regions of large solution variation. (See Section 2.4.) In order for all numerical computations to be done on a uniformly spaced grid, the governing equations and boundary conditions must be transformed from the physical plane (x,y) to a computation plane (ξ,η) which will be fixed in time and where (ξ,η) are curvilinear coordinates. The general transformation of the physical plane to the computational

plane is given by

$$\xi = \xi(x,y), \ \eta = \eta(x,y) \qquad (21)$$

and the inverse transformation is given by

$$x = x(\xi,\eta), \ y = y(\xi,\eta) \qquad (22)$$

Derivatives are transformed as follows (see Anderson, Tannehill and Pletcher, 1984):

$$f_x = \left(y_\eta f_\xi - y_\xi f_\eta\right)/J \qquad (23)$$

$$f_y = \left(-x_\eta f_\xi + x_\xi f_\eta\right)/J \qquad (24)$$

$$f_{xx} = [y_\eta^2 f_{\xi\xi} - 2y_\xi y_\eta f_{\xi\eta} + y_\xi^2 f_{\eta\eta}]/J^2 + [(x_\eta f_\xi - x_\xi f_\eta)(y_\eta^2 y_{\xi\xi} - 2y_\xi y_\eta y_{\xi\eta}$$
$$+ y_\xi^2 y_{\eta\eta}) + (-y_\eta f_\xi + y_\xi f_\eta)(y_\eta^2 x_{\xi\xi} - 2y_\xi y_\eta x_{\xi\eta} + y_\xi^2 x_{\eta\eta})]/J^3 \qquad (25)$$

$$f_{yy} = [x_\eta^2 f_{\xi\xi} - 2x_\xi x_\eta f_{\xi\eta} + x_\xi^2 f_{\eta\eta}]/J^2 + [(x_\eta f_\xi - x_\xi f_\eta)(x_\eta^2 y_{\xi\xi} - 2x_\xi x_\eta y_{\xi\eta}$$
$$+ x_\xi^2 y_{\eta\eta}) + (-y_\eta f_\xi + y_\xi f_\eta)(x_\eta^2 x_{\xi\xi} - 2x_\xi x_\eta y_{\xi\eta} + x_\xi^2 y_{\eta\eta})]/J^3 \qquad (26)$$

$$f_t = (-y_\eta x_t + x_\eta y_t) f_\xi/J + (-y_\xi x_t - x_\xi y_t) f_\eta/J + f_t(\xi,\eta) \qquad (27)$$

where J is the Jacobian of the transformation

$$J = \partial(\xi,\eta)/\partial(x,y) = (x_\xi y_\eta - x_\eta y_\xi) \qquad (28)$$

In a two-dimensional problem, the Jacobian of the transformation controls the magnification of area elements between the physical and computational planes (Anderson, Tannehill and Pletcher, 1984). In order for the transformation given by Equation (21) to be nonsingular, which insures that a one to one relationship exists between (x,y) and (ξ,η) the Jacobian must be nonzero. Substituting Equations (23) through (27) into Equations (17), (18) and (19) yields:

Vorticity-Transport Equation

$$\omega_t + \omega_\xi \left[y_\eta(u-x_t) - x_\eta(v-y_t)\right]/J + \omega_\eta \left[-y_\xi(u-x_t) + x_\xi(v-y_t)\right]/J =$$
$$\left[\tau\omega_\xi + \sigma\omega_\eta + \alpha\omega_{\xi\xi} - 2\beta\omega_{\xi\eta} + \gamma\omega_{\eta\eta}\right]/(ReJ^2) \qquad (29)$$

Stream-Function Equation

$$\alpha\psi_{\xi\xi} - 2\beta\psi_{\xi\eta} + \gamma\psi_{\eta\eta} + \tau\psi_\xi + \sigma\psi_\eta = J^2\omega \qquad (30)$$

Velocity-Component Equations

$$u = (-x_\eta\psi_\xi + x_\xi\psi_\eta)/J \qquad (31)$$

$$v = (-y_\eta\psi_\xi + y_\xi\psi_\eta)/J \qquad (32)$$

where

$$\alpha = x_\eta^2 + y_\eta^2 \qquad (33)$$

$$\beta = y_\xi y_\eta + x_\xi x_\eta \qquad (34)$$

$$\gamma = x_\xi^2 + y_\xi^2 \tag{35}$$

$$\tau = (-y_\eta (Dx) + x_\eta(Dy))/J \tag{36}$$

$$\sigma = (y_\xi (Dx) - x_\xi(Dy))/J \tag{37}$$

$$Dx = \alpha x_{\xi\xi} - 2\beta y_{\xi\eta} + \gamma x_{\eta\eta} \tag{38}$$

$$Dy = \alpha y_{\xi\xi} - 2\beta y_{\xi\eta} + \gamma y_{\eta\eta} \tag{39}$$

Equations (29) through (32) are solved numerically on a uniform rectangular computational plane. Therefore, the movement of a grid point in the physical plane results in a change of the physical coordinate (x,y) at the corresponding fixed grid point (ξ,η) in the computational plane.

The computational approach is applied in the immediate vicinity of the separation bubble. In this region it was assumed that the body surface can be represented by a flat plate. Modifications of the proposed numerical method could be made to include curvature by expressing the governing equation in normal coordinates. The remainder of the flow field is to be "patched" to the Navier-Stokes solutions by means of appropriate boundary-layer theory and inviscid-flow analysis.

2.3 COMPUTATIONAL SCHEME

The procedure for solving Equations (29) through (32) starts with the establishment of initial values of vorticity, stream function and velocity components everywhere at time t = 0. Then the vorticity-transport equation is advanced through time using a finite-difference representation of Equation (29). The vorticity field then serves as a forcing function in Equation (30), which is solved numerically for the stream function. The coefficients, u and v, in the vorticity-transport equation are computed by a finite-difference representation of Equations (31) and (32). This procedure is repeated until the desired time is reached or until some accepted convergence criteria for a steady-state solution is satisfied.

2.3.1 VORTICITY-TRANSPORT EQUATION

The computational scheme used to solve the vorticity-transport equation is an alternating-direction-implicit (ADI) method for parabolic equations based on that of Peaceman and Rachford (1955). The advancement of Equation (29) over a time step index Δt is accomplished

by splitting a finite-difference algorithm into a sequence of one-dimensional operations. The following equation approximates Equation (29) for the first half time step:

$$(\omega_{i,j}^{n+1/2}-\omega_{i,j}^n)/(1/2\Delta t) + [u\delta y/\delta\eta - v\delta x/\delta\eta]\ \delta\omega_{i,j}^{n+1/2}/\delta\xi + [-u\delta y/\delta\xi +$$
$$v\delta x/\delta\xi]\delta\omega_{i,j}^n/\delta\eta = (ReJ^2_{i,j})^{-1}\ [\tau_{i,j}\delta\omega_{i,j}^{n+1/2}/\delta\xi + \sigma_{i,j}\delta\omega_{i,j}^n/\delta\eta +$$
$$\alpha_{i,j}\delta^2\omega_{i,j}^{n+1/2}/\delta\xi^2 - 2\beta_{i,j}\delta^2\omega_{i,j}^n/\delta\xi\delta\eta + \gamma_{i,j}\delta^2\omega_{i,j}^n/\delta\eta^2] \qquad (40a)$$

The equation for the second half step is

$$(\omega_{i,j}^{n+1}-\omega_{i,j}^{n+1/2})/(1/2\Delta t) + [u\delta y/\delta\eta - v\delta x/\delta\eta]\ \delta\omega_{i,j}^{n+1/2}/\delta\xi + [-u\delta y/\delta\xi +$$
$$v\delta x/\delta\xi]\delta\omega_{i,j}^{n+1}/\delta\eta = (ReJ^2_{i,j})^{-1}\ [\tau_{i,j}\delta\omega_{i,j}^{n+1/2}/\delta\xi + \sigma_{i,j}\delta\omega_{i,j}^{n+1}/\delta\eta +$$
$$\alpha_{i,j}\delta^2\omega_{i,j}^{n+1/2}/\delta\xi^2 - 2\beta_{i,j}\delta^2\omega_{i,j}^{n+1}/\delta\xi\delta\eta + \gamma_{i,j}\delta^2\omega_{i,j}^{n+1}/\delta\eta^2] \qquad (40b)$$

where the central finite-difference operators δ and δ^2 are defined by

$$\delta f/\delta\xi = (f_{i+1,j} - f_{i-1,j})/(2\Delta\xi) + O(\Delta\xi^2) \qquad (41)$$

$$\delta f/\delta\eta = (f_{i,j+1} - f_{i,j-1})/(2\Delta\eta) + O(\Delta\eta^2) \qquad (42)$$

$$(\delta^2 f/\delta\xi^2) = (f_{i+1,j} - 2f_{i,j} + f_{i-1,j})/(2\Delta\xi^2) + O(\Delta\xi^2) \qquad (43)$$

$$\delta^2 f/\delta\eta^2 = (f_{i,j+1} - 2f_{i,j} + f_{i,j-1})/(2\Delta\eta^2) + O(\Delta\eta^2) \qquad (44)$$

$$\delta^2 f/\delta\xi\delta\eta = (f_{i+1,j+1} - f_{i+1,j-1} - f_{i-1,j+1} + f_{i-1,j-1})/(4\Delta\xi\Delta\eta) + O[(\Delta\xi)^2,(\Delta\eta)^2] \qquad (45)$$

The notation of subscripts i,j denotes the position (ξ,η) and superscript n denotes a particular time t:

$$f_{i,j}^n = f(\xi = j\Delta\xi, \eta = i\Delta\eta, t = n\Delta t)$$

with mesh size $(\Delta\xi, \Delta\eta, \Delta t)$ \qquad (46)

The coefficients $\alpha_{i,j}$, $\beta_{i,j}$, $\gamma_{i,j}$, $\tau_{,i,j}$ and $\sigma_{i,j}$ are computed as follows for interior grid points (i = 2,M-1), and j = 2,N-1):

$$\alpha_{i,j} = \delta^2 x/\delta\eta^2 + \delta^2 y/\delta\eta^2 \qquad (47)$$

$$\beta_{i,j} = \delta y/\delta\xi\ \delta y/\delta\eta + \delta x/\delta\xi\ \delta x/\delta\eta \qquad (48)$$

$$\gamma_{i,j} = \delta^2 x/\delta\xi^2 + \delta^2 y/\delta\xi^2 \qquad (49)$$

$$\tau_{i,j} = (-\ \delta y/d\eta(Dx_{i,j}) + \delta x/\delta\eta(Dy_{i,j}))/J_{i,j} \qquad (50)$$

$$\sigma_{i,j} = (\delta y/\delta\xi(Dx_{i,j}) - \delta x/\delta\xi(Dy_{i,j}))/J_{i,j} \qquad (51)$$

where

$$Dx_{i,j} = \alpha_{i,j}\ \delta^2 x/\delta\xi^2 - 2\beta_{i,j}\delta^2 x/\delta\xi\delta\eta - \gamma_{i,j}\delta^2 x/\delta\eta^2 \qquad (52)$$

$$Dy_{i,j} = \alpha_{i,j}\ \delta^2 y/\delta\xi^2 - 2\beta_{i,j}\ \delta^2 y/\delta\xi\delta\eta - \gamma_{i,j}\delta^2 y/\delta\eta^2 \qquad (53)$$

$$J_{i,j} = \delta x/\delta\xi\ \delta y/\delta\eta - \delta x/\delta\eta\ \delta y/\delta\xi \qquad (54)$$

On the boundaries, backward and forward finite-differencing formulas were derived using a

cubic Lagrangian interpolating polynomial.

Equation (40a) contains implicit unknowns $\omega_{i-1,j}^{n+1/2}$, $\omega_{i,j}^{n+1/2}$ and $\omega_{i+1,j}^{n+1/2}$ while Equation (40b) contains implicit unknowns $\omega_{i,j-1}^{n+1}$, $\omega_{i,j}^{n+1}$, $\omega_{i,j+1}^{n+1}$. Thus, the result of splitting in the ADI method is that only tridiagonal systems of linear algebraic equations need to be solved. A technique for rapidly solving a tridiagonal system of linear algebraic equations is due to Thomas (1949) and is called the Thomas Algorithm. In this algorithm the system of equations is put in upper triangular form and the unknowns are computed using back substitution.

The grid speed terms x_t and y_t were dropped in the finite-difference representation (40) of the vorticity-transport Equation (29) because the grid points in the physical space will only change at selected time steps. Since the influence of the motion of the physical grid points is registered through the grid speed terms, interpolation must be used to transfer the values of vorticity, stream function and velocity components from the old grid to the new. This was accomplished by cubic-spline interpolation.

According to a von Neumann stability analysis, the ADI method applied to the linearized, two-dimensional vorticity-transport equation (nontransformed) is unconditionally stable for all time steps. However, Roache (1972) points out that the implicit wall boundary values of vorticity actually give a time-step restriction which depends on the physical problem and the convergence requirement.

The ADI method as applied to the vorticity-transport equation has a truncation error of O $(\Delta t^2, \Delta\xi^2, \Delta\eta^2)$. The full second-order accuracy of the method can be deteriorated by the evaluation of the nonlinear terms. In Equation (40a), u and v should be evaluated at (n+1/2) and (n), respectively. While in Equation (40b), they should be evaluated at (n+1/2) and (n+1). Since u and v are calculated from ψ, which is obtained from the stream-function equation, this procedure would require the implicit coupled solution of ω and ψ at both (n+1/2) and (n+1), which is not feasible. In this study, the nonlinear coefficients u and v were re-evaluated during each time-iteration cycle, thereby converging along with the wall vorticity.

2.3.2 STREAM-FUNCTION EQUATION

The solution of steady elliptic equations by iteration is analogous to solving a time-dependent problem to an asymptotic steady state (Frankel, 1950). Therefore, the stream-function equation, Equation (30), was solved by the ADI method for elliptic equations as described by Peaceman and Rachford (1955). The iteration is performed first implicitly by rows and then by columns using the following difference equations:

$$\psi_{i,j}^{q+1/2} = \psi_{i,j}^q + \Delta t/(2\Delta\xi\Delta\eta) \left[\alpha_{i,j} \Delta\eta/\Delta\xi \, \delta_\xi^2 \, \psi^{q+1/2} - \beta_{i,j}/2 \, \delta_{\xi\eta}^2 \, \psi^q + \right.$$
$$\left. \gamma_{i,j} \Delta\xi/\Delta\eta \, \delta_\eta^2\psi^q + \tau_{i,j}\Delta\eta/2 \, \delta_\xi\psi^{q+1/2} + \sigma_{i,j}/2 \, \Delta\xi\delta_\eta \psi^q - \Delta\xi\Delta\eta^2 J_{i,j}, \, \omega_{i,j} \right] \text{(55a)}$$

$$\psi_{i,j}^{q+1} = \psi_{i,j}^{q+1/2} + \Delta t/(2\Delta\xi\Delta\eta) \left[\alpha_{i,j} \Delta\eta/\Delta\xi \, \delta_\xi^2 \, \psi^{q+1/2} - \beta_{i,j}/2 \, \delta_{\xi\eta}^2 \, \psi^{q+1/2} + \right.$$
$$\left. \gamma_{i,j} \Delta\xi/\Delta\eta \, \delta_\eta^2\psi^{q+1} + \tau_{i,j}\Delta_\eta/2 \, \delta_\xi\psi^{q+1/2} + \sigma_{i,j}/2 \, \Delta\xi\delta_\eta\psi^{q+1} - \Delta\xi\Delta\eta^2 J_{i,j}, \, \omega_{i,j} \right] \text{(55b)}$$

where

$$\delta_\xi\psi = \psi_{i+1,j} - \psi_{i-1,j} \tag{56}$$

$$\delta_\eta\psi = \psi_{i,j+1} - \psi_{i,j-1} \tag{57}$$

$$\delta^2_\xi\psi = \psi_{i+1,j} - 2\psi_{i,j} + \psi_{i-1,j} \tag{58}$$

$$\delta^2_\eta\psi = \psi_{i,j+1} - 2\psi_{i,j} + \psi_{i,j-1} \tag{59}$$

$$\delta^2_{\xi\eta}\psi = \psi_{i+1,j+1} - \psi_{i+1,j-1} - \psi_{i-1,j+1} + \psi_{i-1,j-1} \tag{60}$$

and q is the iteration index.

The equations may be written in the following form, after multiplying by $\rho = 2\Delta\xi\Delta\eta/\Delta t$:

$$\psi_{i-1,j}^{q+1/2} \left(\tau_{i,j}\Delta\eta/2 - \alpha_{i,j}\Delta\eta/\Delta\xi \right) + \psi_{i,j}^{q+1/2} \left(\rho + 2\alpha_{i,j}\Delta\eta/\Delta\xi \right) +$$
$$\psi_{i+1,j}^{q+1/2}\left(-\tau\Delta\eta/2 - \alpha_{i,j}\Delta\eta/\Delta\xi \right) = \rho\psi_{i,j}^q - \Delta\xi\Delta\eta J_{i,j}^2\omega_{i,j} +$$
$$\gamma_{i,j}\Delta\xi/\Delta\eta \left(\delta_\eta^2 \psi^q \right) + \sigma_{i,j}\Delta\xi/2 \left(\delta_\eta\psi^q \right) - \beta_{i,j}/2 \left(\delta_{\xi\eta}^2\psi^q \right) \tag{61a}$$

$$\psi_{i,j-1}^{q+1} \left(\sigma_{i,j}\Delta\xi/2 - \gamma_{i,j}\Delta\xi/\Delta\eta \right) + \psi_{i,j}^{q+1} \left(\rho + 2\gamma_{i,j}\Delta\xi/\Delta\eta \right) +$$
$$\psi_{i,j+1}^{q+1}\left(-\sigma_{i,j}\Delta\xi/2 - \gamma_{i,j}\Delta\xi/\Delta\eta \right) = \rho\psi_{i,j}^{q+1/2} - \Delta\xi\Delta\eta J_{i,j}^2\omega_{i,j} +$$
$$\alpha_{i,j}\Delta\eta/\Delta\xi \left(\delta_\xi^2 \psi^{q+1/2} \right) + \tau_{i,j}\Delta\eta/2 \left(\delta_\xi\psi^{q+1/2} \right) - \beta_{i,j}/2 \left(\delta_{\xi\eta}^2 \psi^{q+1/2} \right) \tag{61b}$$

The parameter ρ is a positive parameter chosen to accelerate the convergence of the method and to insure diagonal dominance in the tridiagonal matrix.

2.3.3 U-V COMPONENT OF VELOCITY

The velocity components, Equations (31) and (32), are computed from the following finite difference approximations:

$$u_{i,j} = \left[-x_\eta\psi_\xi + x_\xi\psi_\eta \right]/J_{i,j} \tag{62}$$

$$v_{i,j} = \left[-y_\eta \psi_\xi + y_\xi \psi_\eta \right]/J_{i,j} \tag{63}$$

where for i=2, M-1 and j=3, N-1

$$\psi_\xi = (\psi_{i+1,j} - \psi_{i-1,j})/(2\Delta\xi) \tag{64}$$

$$\psi_\eta = (\psi_{i+1,j} - \psi_{i-1,j})/(2\Delta\eta) \tag{65}$$

and for i=2, M-1 and j=2

$$\psi_\xi = (\psi_{i+1,j} - \psi_{i-1,j})/(2\Delta\xi) \tag{66}$$

$$\psi_\eta = (-5\psi_{i,1} + 4\psi_{i,2} + \psi_{i,3})/(4\Delta\eta) \tag{67}$$

Equation (67) will be derived in Section 2.3.4.

Along the downstream boundary and outer-flow boundary, three-point backward-differencing formulas are used. For example, for i = M, j = 3, N-1,

$$\psi_\xi = (3\psi_{M,j} - 4\psi_{M-1} + \psi_{M-2,j})/(2\Delta\xi) \tag{68}$$

$$\psi_\eta = (\psi_{i,j+1} - \psi_{i,j-1})/(2\Delta\eta) \tag{69}$$

2.3.4 BOUNDARY CONDITIONS

As discussed above, the computational approach of the problem does not take into account the entire flow field, but limits the domain of the solution to the immediate vicinity of the separation bubble. Therefore, the specification of boundary conditions is important in order for the "patching" of the Navier-Stokes solution to the remainder of the flow. Boundary conditions need to be specified on: (1) the solid wall, (2) the upstream boundary, (3) the outer-flow boundary, and (4) the downstream boundary.

Upstream Boundary

It was pointed out in Geibler, Carr & Cebeci (1988) that for oscillating airfoils the front stagnation point is moving in time. Therefore, the boundary-layer calculations need to be started at the instantaneous positions of the stagnation points which are known from the inviscid calculations of Section 2.1. Since this work only considers small-amplitude oscillations, it is assumed that the unsteady effects in the boundary layer in the region near the stagnation point are negligible. Therefore the upstream boundary conditions were obtained by the solution of the two-dimensional laminar boundary-layer equations on a quasi-steady basis. The modification to include stagnation-point motion as in Geibler, Carr & Cebeci (1988) is straightforward.

The two-dimensional boundary-layer equations are:

$$\partial u/\partial s + \partial v/\partial y = 0 \tag{70}$$

$$u\partial u/\partial s + v\partial u/\partial y = U_e \, dU_e/ds + \upsilon \, \partial^2 u/\partial y^2 \tag{71}$$

with the boundary conditions

$$u(s, y = 0) = v(s, y = 0) = 0 \tag{72}$$

$$u(s, y \to \infty) = U_e(s) \tag{73}$$

$$u(s = 0, y) = u_i \tag{74}$$

Introducing the Falkner-Skan-like variables

$$\xi = s, \eta = y \left[\xi/(ReU_e(\xi)) \right]^{-1/2} \tag{75}$$

$$u = U_e(\xi) \, f'(\xi,\eta) \tag{76}$$

$$V(\xi,\eta) = v \left[Re\xi/U_e(\xi) \right]^{1/2} \tag{77}$$

where s is the dimensionless distance measured along the surface of the airfoil, y is the dimensionless distance normal to the surface and the prime indicates differentiation with respect to η.

We rewrite Equations (70) and (71) as

$$\xi\partial f'/\partial\xi + \beta f' + \eta/2 \, (\beta\text{-}1)\partial f'/\partial\eta \; \partial V/\partial\eta = 0 \tag{78}$$

$$f'\xi\partial f'/\partial\xi + V\partial f'/\partial\eta = [1\text{-}f'^2]\beta + \partial^2 f'/\partial\eta^2 \tag{79}$$

where

$$\beta(\xi) = x/U_e \, dU_e/d\xi \tag{80}$$

and

$$V = V + \eta f' \, (\beta\text{-}1)/2 \tag{81}$$

The boundary conditions transform to

$$f'(\xi,0) = 0, V(\xi,0) = 0 \tag{82}$$

$$f'(\xi,\eta \to \infty) = 1 \tag{83}$$

$$f'(0,\eta) = f_i'(\eta) \tag{84}$$

Equations (78) through (84) are solved using the Crank-Nicolson method described in Panton (1984) with initial conditions supplied by the Falkner-Skan profile of $\beta_i = 1$, the plane stagnation-point solution. It should be noted that ξ,η defined in Equation (75) are not related to the curvilinear cordinates (ξ,η).

Solid Wall

Along the wall, $\psi = 0$, which implies the no-penetration condition, $v = 0$. The no-slip condition

$$u_{i,1} = J^{-1} (x_\xi \psi_\eta) \Big|_{wall} = 0 \qquad (85)$$

is also applied at the wall.

At the wall the stream-function equation reduces to

$$\omega_{i,1} = \gamma J^{-2} \psi_{\eta\eta} \Big|_{wall} \qquad (86)$$

Equation (86) does not provide a direct boundary condition for vorticity, and the accepted procedure is to calculate the vorticity from Equation (86) using a difference formula which implicitly satisfies Equation (85) (Briley, 1972). To derive such a formula, a cubic Lagrangian interpolating polynomial is passed though the points (i,0), (i,1), (i,2) and (i,3). The formula for this cubic is

$$\psi_i = [-(\eta - \eta_1)(\eta - \eta_2)(\eta - \eta_3)\psi_{i,0} + 3(\eta - \eta_0)(\eta - \eta_2)(\eta - \eta_3)\psi_{i,1} -$$
$$3(\eta - \eta_0)(\eta - \eta_1)(\eta - \eta_3)\psi_{i,2} + (\eta - \eta_0)(\eta - \eta_1)(\eta - \eta_2)\psi_{i,3}]/[6(\Delta\eta^3)] \qquad (87)$$

where η_k denotes η at the point (i,k). Differentiating Equation (87) with respect to η gives

$$\partial\psi_i/\partial\eta = \{[-3\eta_2 + 2(\eta_1 + \eta_2 + \eta_3)\eta - (\eta_1\eta_2 + \eta_1\eta_3 + \eta_2\eta_3)]\psi_{i,0} +$$
$$[9\eta^2 - 6(\eta_0 + \eta_2 + \eta_3)\eta + 3(\eta_0\eta_2 + \eta_0\eta_3 + \eta_2\eta_3)]\psi_{i,1} +$$
$$[-9\eta^2 + 6(\eta_0 + \eta_1 + \eta_3)\eta - 3(\eta_0\eta_1 + \eta_0\eta_3 + \eta_1\eta_3)]\psi_{i,2} +$$
$$[3\eta^2 - 2(\eta_0 + \eta_1 + \eta_2)\eta + (\eta_0\eta_1 + \eta_0\eta_2 + \eta_1\eta_2)]\psi_{i,3}\}/[6(\Delta\eta^3)] \qquad (88)$$

Differentiating Equation (88) with respect to η gives

$$\partial^2\psi_i/\partial\eta^2 = \{[-6\eta + 2(\eta_1 + \eta_2 + \eta_3)]\psi_{i,0} +$$
$$[18\eta - 6(\eta_0 + \eta_2 + \eta_3)]\psi_{i,1} + [-6\eta + 6(\eta_0 + \eta_1 + \eta_3)]\psi_{i,2} +$$
$$[6\eta - 2(\eta_0 + \eta_1 + \eta_2)]\psi_{i,3}\}/[6(\Delta\eta^3)] \qquad (89)$$

Evaluating Equation (88) at $\eta = \eta_1 = \eta_{wall}$ gives

$$\partial\psi/\partial\eta \Big|_{i,wall} = (-2\psi_{i,0} - 3\psi_{i,1} - 6\psi_{i,2} - \psi_{i,3})/[6\Delta\eta] \qquad (90)$$

Evaluating Equation (89) at $\eta = \eta_1 = \eta_{wall}$ gives

$$\partial^2\psi/\partial\eta^2 \Big|_{i,wall} = (\psi_{i,0} - 2\psi_{i,1} + \psi_{i,2})/[\Delta\eta^2] \qquad (91)$$

The no-slip condition is now

$$u_{i,wall} = x_\xi/J \ \partial\psi/\partial\eta \Big|_{i,wall} = x_\xi(-2\psi_{i,0} - 3\psi_{i,1} + 6\psi_{i,2} - \psi_{i,3})/[6J\Delta\eta] = 0 \qquad (92)$$

The difference formula for vorticity at the wall is calculated by eliminating ψ at the point (i,0) from Equations (91) and (92), and substituting (91) into Equation (86). The result is

$$\omega_{i,1} = \gamma_{i,1}(-7\psi_{i,1} + 8\psi_{i,2} - \psi_{i,3})/(2\Delta\eta^2 J_{i,1}^2) \qquad (93)$$

To be consistent, the same cubic, Equation (87), should be used to derive a second-order difference approximation for ψ_η and $\psi_{\eta\eta}$ at the point (i,2). Setting $\eta = \eta_2$, Equations (88) and (89) become:

$$\partial\psi/\partial\eta \Big|_{i,2} = (\psi_{i,0} - 6\psi_{i,1} + 3\psi_{i,2} + 2\psi_{i,3})/(6\Delta\eta) \qquad (94)$$

$$\partial^2\psi/\partial\eta^2 \Big|_{i,2} = (\psi_{i,1} - 2\psi_{i,2} + \psi_{i,3})/\Delta\eta^2 \qquad (95)$$

Eliminating ψ at the point (i,0) from Equation (92) and (94),

$$\partial\psi/\partial\eta \Big|_{i,2} = (-5\psi_{i,1} + 4\psi_{i,2} + \psi_{i,3})/(4\Delta\eta) \qquad (96)$$

Equation (95) is identical to the standard central-difference formula obtained using Taylor-series expansions or a quadratic polynomial. However, Equation (96) is not consistent with Equation (42). Therefore, at the row of points adjacent to the wall, Equation (96) should be used to represent the coefficients $u_{i,j}$ and $v_{i,j}$ in order to be consistent with the treatment of the vorticity boundary condition at the wall.

Lagging of vorticity at the wall arises with an implicit method because the boundary values of vorticity at the (n+1) time level are needed to solve the vorticity equation before the stream-function values at this time level are available to eliminate them. This problem was solved by using the wall values of vorticity at the (n) time level as boundary conditions for the vorticity equation at the (n+1) time level. Then, after the stream function has been calculated at the (n+1) time level, the values of wall vorticity are updated by Equation (93). This procedure was continued in an iterative manner over the time step.

Outer-Flow Boundary

At this boundary, the u-component of velocity is prescribed by the unsteady inviscid calculations of Section 2.1. The application of Equation (61) requires values of ψ at an imaginary row of points just outside the boundary. The values are eliminated by solving the following finite-difference representation of the prescribed values of u for $\psi_{i,N+1}$.

$$u_{i,N} = \left[-x_\eta(\psi_{i+1,N} - \psi_{i-1,N})/(2\Delta\xi) + x_\xi(\psi_{i,N+1} - \psi_{i,N-1})/(2\Delta\eta) \right]/$$
$$J_{i,N}, \quad (i = 2, M-1) \qquad (97)$$

$$u_{M,N} = \left[-x_\eta(3\psi_{M,N} - 4\psi_{M-1,N} + \psi_{M-2,N})/(2\Delta\xi) + x_\xi(\psi_{M,N+1} - \psi_{M,N-1})/(2\Delta\eta) \right]/J_{M,N} \qquad (98)$$

The flow is also required to be irrotational by setting the vorticity equal to zero.

The boundary is located at a distance y_e

$$y_e = \eta_\infty \left[\xi_1/(R_e U_e(\xi_1)) \right]^{1/2} \tag{99}$$

where $\eta = \infty$ is taken to be the finite position $\eta = 8$, and ξ_1 is the location of the upstream boundary.

Downstream Boundary

At this boundary it is assumed that a fully rehabilitated boundary layer exists. Therefore, the boundary conditions are given by the boundary-layer approximations

$$\partial^2\psi/\partial x^2 = \partial^2\omega/\partial x^2 = 0 \tag{100}$$

These boundary conditions must be transformed to the computational plane by Equations (23) through (27). The equation governing the vorticity boundary condition is

$$y_\eta^2\omega_{\xi\xi} - 2y_\xi y_\eta\omega_{\xi\eta} + y_\xi^2\omega_{\eta\eta} + \left[(x_\eta\omega_\xi - x_\xi\omega_\eta)(y_\eta^2 y_{\xi\xi} - 2y_{\xi\eta}y_\xi y_\eta + y_\xi^2 y_{\eta\eta}) + (y_\xi\omega_\eta - y_\eta\omega_\xi)(y_\eta^2 x_{\xi\xi} - 2x_{\xi\eta}y_\xi y_\eta - y_\xi^2 x_{\eta\eta}) \right]/J = 0 \tag{101}$$

The finite-difference form of Equation (101) is then

$$\omega_{M+1,j}\left(1 + Dx_\eta\Delta\xi/[2AJ] - Ey_\eta/[2AJ]\right)_{M,j} = 2\omega_{M,j}\left(1 + C\Delta\xi^2/[A\Delta\eta^2]\right)_{M,j} +$$
$$\omega_{M-1}\left(Dx_\eta\Delta\xi/[2AJ] - Ey_\eta\Delta\xi/[2AJ] - 1\right)_{M,j} - \left(C\Delta\xi^2/[A\Delta\eta^2]\right)_{M,j}$$
$$\left(\omega_{M,j+1} - \omega_{M,j-1}\right) + \left(B\Delta\xi/[2A\Delta\eta]\right)_{M,j}\left(\omega_{\xi\eta}\right)_{M,j} \tag{102}$$

where

$$A_{M,j} = (y_\eta)^2 \tag{103}$$

$$B_{M,j} = (y_\xi y_\eta) \tag{104}$$

$$C_{M,j} = (y_\xi)^2 \tag{105}$$

$$D_{M,j} = A_{M,j}(y_{\xi\xi}) - 2B_{M,j}(y_{\xi\eta}) + C_{M,j}(y_{\eta\eta}) \tag{106}$$

$$E_{M,j} = A_{M,j}(x_{\xi\xi}) - 2B_{M,j}(x_{\xi\eta}) + C_{M,j}(x_{\eta\eta}) \tag{107}$$

$$\left(\omega_{\xi\eta}\right)_{M,j} = (9\omega_{M,j} - 12\omega_{M-1,j} + 3\omega_{M-2,j}) + (-12\omega_{M,j-1} + 16\omega_{M-1,j-1} - 4\omega_{M-2,j-1}) + (3\omega_{M,j-2} - 4\omega_{M-1,j-2} + \omega_{M-2,j-2}) \tag{108}$$

The equation governing the stream-function boundary condition and its finite-difference form is obtained by replacing ω with ψ in Equations (101) through (108). The application of Equations (40) and (61) at the downstream boundary requires values of vorticity and stream function at an imaginary column of points just outside the boundary. These values are eliminated by solving Equation (101) for $\omega_{M+1,j}$ and similarly for $\psi_{M+1,j}$.

2.4 ADAPTIVE-GRID GENERATION

When partial differential equations are solved using a fixed grid, the grid points are distributed before the solution is known. Therefore, the grid may not be best suited for the physical problem because of the possibility that large solution variations could appear somewhere on a scale that is too small for the prescribed spacing of points. The basic idea of the adaptive grid used in this study is to have points move from regions of relatively small solution gradients to regions of large gradients as the physical solution evolves. In this approach, there is no formal increase in global accuracy in the limit of infinitesimal spacing, but it is possible to improve the approximation locally as significant gradients are better resolved (Kim & Thompson, 1988). This approach has not only the advantage of not increasing computational time and storage during the solution, but also the undesirable possibility of decreasing the number of points in other regions of possible significant gradients. In addition, the grid could become too skewed. In this report only one-dimensional adaptation will be described in the y-direction. However, a direct extension to multiple dimensions can be made in a robust, straightforward manner. (See Shen & Reed 1990a-b.)

Adaptive redistribution of points traces its roots to the concept of equidistribution. In one dimension, equidistribution occurs when the spacing between points is inversely proportional to a weight function. The mapping of a uniform distribution in η into a nonuniform distribution in s, where s is the arc length along a given curve, is determined by the differential statement,

$$wds = cd\eta \qquad (109)$$

where c is the constant of proportionality and w is the weight function. The desired spacing is achieved because $d\eta$ is viewed as a constant, therefore, the physical mesh increment ds is small when w is large, and vice versa.

2.4.1 ADAPTATION OF THE BOUNDARIES

The grid points on the upstream and downstream boundaries were moved adaptively based on a faction method by Eiseman (1987). The form of the weight function used to move the grid points on these boundaries is given by the linear combination

$$w = 1 + c_1 M_1 + c_2 M_2 + \ldots + c_m M_m, \tag{110}$$

where the nonnegative functions M_k are the magnitudes of quantities which attract points when they are large and have nonnegative coefficients c_k to indicate the level of importance attached to them. Smoothness of the grid is provided by the choice of unity for the first term which guarantees that the weight function is never zero. When w is a function of s, a direct integration of (109) leads to the transformation

$$(\eta - \eta_{min})/(\eta_{max} - \eta_{min}) = F(s)/F(s_{max}) \tag{111}$$

where

$$F(s) = \int_{S_{min}}^{S} w\,ds \tag{112}$$

With the general linear weight of Equation (110), the integral of (111) becomes

$$F(s) = H_0(s) + \sum_{k=1}^{m} C_k H_k(s) \tag{113}$$

where

$$H_0(s) = s - s_{min}, \quad H_k(s) = \int_{S_{min}}^{S} M_k\,dx \tag{114}$$

Upon evaluation at $s = s_{max}$, Equations (113) and (114) become a relationship between total amounts with the total length,

$$L = H_0(s_{max}) - s_{max} - s_{min} \tag{115}$$

and the total amount of each quantity

$$I_k = H_k(s_{max}) \tag{116}$$

The application of Equation (111) requires a curve given as a function of a parameter s and then a new parameter η which is also expressed as a function of s. In terms of mapping, the relationships become the map from an interval of values of s to the curve and the map from the same interval to the interval for η. The latter map is backwards with respect to the straight composition of maps, which is from η to s and then to the curve. Therefore, the map of (111) is called the backward global integral statement (Eiseman, 1987). A consequence of the backwardness is the need to invert the transformation in order to apply it. The inversion is accomplished by interpolating previous grid points using cubic-spline interpolation. The total weight integral is given by

$$F(s_{max}) = L + c_1 I_1 + \ldots c_m I_m \tag{117}$$

Since each term is positive and represents a part of the total weight, a division by the total weight results in the factional decomposition,

$$1 = f_0 + f_1 + \ldots + f_m \tag{118}$$

where
$$f_0 = L/F(s_{max}) \tag{119}$$

is the fractional contribution from the total length and

$$f_k = c_k I_k / F(s_{max}) \tag{120}$$

is the factional contribution from the total amount of the kth quantity. The strategy is to specify the fraction of (120) and then solve for the resultant c_k. Equations (119) and (120) give the weighting coefficients,

$$c_k = L f_k / [(1 - f_1 - \ldots - f_m) I_k] \tag{121}$$

When these coefficients are used in the integral F(s) of (113), the backward global integral statement of (111) becomes

$$(\eta - \eta_{min})/(\eta_{max} - \eta_{min}) = \sum_{k=0}^{m} f_k H_k(s)/H_k(s_{max}) \tag{122}$$

This study only considered m = 1, for which Equation (122) becomes

$$\eta(s) = \eta_{min} + \left(\eta_{max} - \eta_{min}\right)\left[\left(1 - f_1\right)H_0(s)/H_0(s_{max}) + f_1 H_1(s)/H_1(s_{max})\right] \tag{123}$$

where

$$H_1(s) = \int_{S_{min}}^{S_{max}} M_1 dx \qquad (124)$$

2.4.2 ADAPTATION OF INTERIOR GRID POINTS

Based on the grid distribution along the upstream and downstream boundaries obtained from the one-dimensional adaptation described in Section 2.4.1, the interior grid points in the y-direction are moved adaptively according to the control-function approach. This approach is developed by noting the correspondence between Equation (109) and the one-dimensional form of the elliptic grid-generation system (Kim & Thompson, 1988). The one-dimensional form of this system is

$$y_{\eta\eta} + Qy_\eta = 0 \qquad (125)$$

where Q is the control function which provides some measure of control over the interior grid spacing. Differentiation of Equation (109) with respect to η and setting $y = s$ yields

$$wy_{\eta\eta} + w_\eta y_\eta = 0 \qquad (126)$$

Then, from Equations (125) and (126)

$$y_{\eta\eta}/y_\eta = -Q = -w_\eta/w \qquad (127)$$

Thus, the control function is given by

$$Q = w_\eta/w \qquad (128)$$

The direct extension of the above derivation into two dimensions is as follows: In two dimensions the elliptic system of equations is (see Thomas & Middlecoff, 1980)

$$\alpha x_{\xi\xi} - 2\beta x_{\xi\eta} + \gamma x_{\eta\eta} = -J^2(Px_\xi + Qx_\eta) \qquad (129)$$

$$\alpha y_{\xi\xi} - 2\beta y_{\xi\eta} + \gamma y_{\eta\eta} = -J^2(Py_\xi + Qy_\eta) \qquad (130)$$

where

$$P = (w_1)_\xi/w_1 - \beta/\alpha \, (w_1)_\eta/w_1 \qquad (131)$$

$$Q = (w_2)_\eta/w_2 - \beta/\gamma \, (w_2)_\xi/w_2 \qquad (132)$$

with α, β, γ, and J defined in Equations (28) and (33) through (35). P is also a *control function*. Since the grid points will be moved in the y-direction, only Equation (130) needs to be solved. This was done by successive line overrelation (SLOR) iteration in the computation domain to generate the grid in the physical domain. The weight functions, w_1, and w_2, are based on the gradient of the u-component of velocity according to Anderson (1987).

$$w_1 = 1 + A(\partial u/\partial \xi)^2 \tag{133}$$
$$w_2 = 1 + B(\partial u/\partial \eta)^2 \tag{134}$$

where A and B are constants which are adjusted to alter the adaptivity in the mesh. The unity term is added to prevent excessive mesh stretching where the values of the gradients vanish.

The control function adaptive approach has the advantage of being based on the same elliptic generation equations that are commonly used in grid generation codes. Two separate weight functions could be a definite advantage, with the possibility of using the velocity gradient in one direction and the pressure gradient in the other.

2.5 ALGORITHM

A summary of the algorithm which advances Equations (29) through (32) from (n) to the (n+1) time level is as follows:

(i)   Obtain boundary values for ψ^{n+1}, ω^{n+1} or their derivatives. These values are known except for ω^{n+1} at the wall.

(ii)   Solve (40a) and (40b) to obtain ω^{n+1}.

(iii)   Solve for ψ^{n+1} using the iterative scheme given by (61a) and (61b).

(iv)   Compute u^{n+1} and v^{n+1} from ψ^{n+1} using three-point central differencing.

(v)   Calculate new values for ω^{n+1} at the wall using (93).

(vi)   Return to Step (ii) and repeat this procedure until the values of ω^{n+1} at the wall computed in Step (v) converge.

The above algorithm requires convergence criteria for Steps (iii) and (vi). The wall vorticity was used as the test quantity in both criteria. After each application of Equations (61a) and (61b) in Step (iii), values of vorticity at the wall were computed by Equation (93). The iteration was stopped when

$$\max \left| (\omega^{n+1})^{q+1} - (\omega^{n+1})^q \right|_{wall} / \max \left| (\omega^{n+1})^{q+1} \right|_{wall} \leq \varepsilon_1 \tag{135}$$

where q is the iteration index in the procedure for solving the stream-function equation. In Step (iv), a similar criterion was used for the iteration over the time step. The iteration is stopped when

$$\max \left| (\omega^{n+1})^{k+1} - (\omega^{n+1})^{k+1} \right|_{wall} / \max \left| (\omega^{n+1})^{k+1} \right|_{wall} \leq \varepsilon_2 \tag{136}$$

where k is the iteration index for the iteration over the time step. The advantage of using vorticity at the wall in the above convergence criteria is that ε_1 and ε_2 are related to one another. In order for the time-step iteration to converge, ε_1 should be less than ε_2. The present calculations were made with $\varepsilon_1 = 1/2\varepsilon_2$ in accordance with Briley (1971). A solution was accepted as the steady-state solution when the following condition was satisfied:

$$\max \left| \omega^{n+1} - \omega^n \right|_{i,j} / \max \left| \omega^{n+1} \right|_{i,j} \leq \varepsilon_3 \tag{137}$$

3 RESULTS

3.1 STEADY HOWARTH RETARDED FLOW

In this case, at the upstream boundary, the vorticity and stream function are prescribed from the boundary-layer theory of Howarth (1938) for a linear retarded freestream velocity given by

$$\overline{u}_e(\overline{x}) = b_0 - b_1 \overline{x} \tag{138}$$

where b_0 has the units of feet/seconds and b_1 of 1/seconds. Following the procedure of Briley (1971), the separation bubble was produced by retarding the freestream in accordance with Equation (138) from the upstream boundary to a point slightly downstream of the expected separation point. Thereafter, downstream, a constant freestream velocity is prescribed. This reverses the growth of the separated region and eventually causes reattachment.

The governing equations and boundary condition from above were made dimensionless

in accordance with the nomenclature of Howarth (1938).

$$x = b_1 \bar{x}/b_0, \; y = b_1 \bar{y}/b_0$$

$$u = \bar{u}/b_0, \; v = \bar{v}/b_0$$

$$\omega = \bar{\omega}\upsilon^{1/2}/b_0 b_1^{1/2} \tag{139}$$

$$\psi = \bar{\psi} b_1^{1/2}/b_0 \upsilon^{1/2}$$

$$t = \bar{t} b_1$$

Substituting Equation (139) into Equations (12) through (15) and then transforming them into the computational plane by Equations (23) through (27), the nondimensional form of the governing equations are:

Vorticity-Transport Equation

$$\omega_t + \omega_\xi\left[y_\eta(u-x_t) - x_\eta(v-y_t)\right]/J + \omega_\eta\left[-y_\xi(u-x_t) + x_\xi(v-y_t)\right]/J =$$
$$\left(\tau\omega_\xi + \sigma\omega_\eta + \alpha\omega_{\xi\xi} - 2\beta\omega_{\xi\eta} + \gamma\omega_{\eta\eta}\right)/[ReJ^2] \tag{140}$$

Stream-Function Equation

$$\alpha\psi_{\xi\xi} - 2\beta\psi_{\xi\eta} + \gamma\psi_{\eta\eta} + \tau\psi_\xi + \sigma\psi_\eta = J^2 Re\omega \tag{141}$$

Velocity-Component Equations

$$u = (-x_\eta\psi_\xi + x_\xi\psi_\eta)/[\sqrt{Re}\, J] \tag{142}$$
$$v = (-y_\eta\psi_\xi + y_\xi\psi_\eta)/[\sqrt{Re}\, J] \tag{143}$$

where the nondimensional Reynolds number is defined by

$$Re = b_0^2/[b_1\upsilon] \tag{144}$$

and the nondimensional form of Equation (138) is

$$u_e(x) = 1 - x \tag{145}$$

Calculations are presented for two freestream velocity distributions representing two different Howarth retarded flows; that is, two different constant downstream velocities are specified for the problem

$$u_e(x) = 1-x \qquad x_1 \le x \le x_{end}$$
$$u_e(x) = 1-x_{end} \qquad x_{end} \le x \le x_2 \tag{146}$$

Initial conditions for u, v, ω and ψ were obtained from the Blasius similarity solution of the

boundary-layer equations for flow past a flat plate parallel to a uniform freestream. Values of the convergence criteria discussed in Section 2.5 are $\varepsilon_1 = 5 \times 10^{-4}$ and $\varepsilon_3 = 1 \times 10^{-7}$.

The nondimensional form of the wall shearing stress is

$$\tau\big|_{wall} = (\sqrt{Re}\ J)^{-1}\ (x_\xi u_\eta)\big|_{wall} \tag{147}$$

In Figures 2 and 3, distributions of wall shearing stress along with the freestream velocity distribution are given for values of x_{end} equal to 0.16296 (solution 1) and 0.20058 (solution 2). Solution 1 (Figure 2) did not separate, whereas solution 2 (Figure 3) produced a separation bubble which appears as negative wall shearing stress.

Figure 4 shows a vorticity profile downstream of the separation bubble at x = 0.40122. Briley (1971) points out that the presence of this additional inflection point in the vorticity profile indicates that the diffusion has not had a sufficient distance over which to smooth the new vorticity being generated at the wall with the vorticity being convected and diffused from further upstream.

To validate the downstream boundary conditions, the u-component of velocity at the downstream boundary was compared to the Blasius profile. This comparison is shown in Figure 5 for the solution near separation and in Figure 6 for the solution which contains the separation bubble. Moreover, when the domain is lengthened in the downstream direction, the solution within the domain is unaffected. All the above results are in good agreement with Briley's.

In solution 2, separation occurred without any evidence of the singular behavior found in solutions to the boundary-layer equations when the external velocity distribution is prescribed. As already discussed, this singular behavior did not occur because the complete Navier-Stokes equations were solved which include the elliptic terms associated with upstream influences that are are not included in the parabolic boundary-layer equations. Because the Navier-Stokes equations are elliptic in the spatial variables, their solutions satisfy all boundary conditions simultaneously. Therefore, a perturbation in a boundary condition, such as freestream velocity downstream of a given point, will affect the solution upstream of that point.

3.2 UNSTEADY HOWARTH RETARDED FLOW

We next considered the case of oscillations about an established steady Howarth retarded flow. The wall shear-stress distribution is shown in Figure 7 where the freestream velocity is given by

$$u_e(x) = 1 - (1 - 0.1\cos(2\pi t))x \qquad x_1 + 1 \le x \le x_{end} \qquad (148a)$$

$$u_e(x) = 1 - (1 - 0.1\cos(2\pi t))x_{end} \qquad x_{end} < x < x_2 \qquad (148b)$$

and is denoted by a solid line. The initial conditions are obtained by the steady-state solution, t=0, where the freestream velocity distribution is denoted by a line of asterisks. Five complete cycles were required for convergence. Figure 8 displays the velocity profiles, the "separation" line, the edge of the region of reversed flow and the boundary-layer thickness for a Reynolds number of 20,833.

3.3 UNSTEADY 2-D AIRFOIL FLOW

This work includes the application of this technique to the ASM-LRN-010 and Wortmann FX 63-137 airfoil sections at 50,000-500,000 chord Reynolds number. Inviscid surface pressure distributions for pitching and plunging airfoils (as computed from the vortex-lattice code) are applied as outer-flow boundary conditions in unsteady calculations as described above. An unsteady boundary-layer solution is applied as the upstream condition.

Figure 9 shows the contour of the Wortmann airfoil. For a chord Reynolds number of 125,000 and at an angle of attack of -10 degrees, Figure 10 shows the inviscid, panel-method prediction of both upper and lower surface C_p. Also shown are the resulting Navier-Stokes calculations of surface C_p. Here the viscous pressure coefficients were calculated by evaluating the x-momentum equation at the wall, with the results of

$$\frac{\partial C_p}{\partial x} = \frac{2}{\sqrt{Re}} \frac{\partial \omega}{\partial y} \bigg|_{wall} \qquad (149)$$

In this case, no separation is observed, as seen from shear stress calculations in Figure 11.

Figures 12-13 show similar results for a chord Reynolds number of 250,000.

For a chord Reynolds number of 125,000 and at an angle of attack of 0 degrees, the boundary layer on the upper surface separates and the Navier-Stokes calculation for C_p differs

from the inviscid calculation (see Figures 14-15). These results agree well with the experiments of Wu & Covert 1989 (see their Figure 3), except for the fact that our calculation is laminar and does not include transition, and therefore our bubble reattaches further downstream. Our force predictions are therefore more conservative. Figure 16 then shows the extent of the separated region relative to the boundary layer.

Further detailed results, including the prediction of temporal separation development and whether gusty off-design conditions are fatal to the vehicle, are found in Reed & Toppel (1990). Steady conditions include the Wortmann airfoil at -10°, -4°, 0°, and 4° incidence. Gusting conditions include two types: 1) oscillatory pitching and plunging and 2) ramped to an incidence angle, held until steady-state is achieved, released, and held until steady-state is achieved. The ramping function is one-half of the oscillatory cycle.

The oscillation is described by the equation

$$\alpha° = -10° + 14° \sin (2 k t)$$

Here k is the reduced frequency

$$k = \omega c / (2 U_\infty)$$

ω is the dimensional frequency of the oscillation, c is the chord, and U_∞ is the freestream speed. Values of k studied include 0.15, 2.0, and 6.4; these were the values considered by Wu & Covert (1989). Chord Reynolds numbers considered include 125,000 and 250,000.

Figure 17 shows inviscid C_p predictions for the airfoil pitching from -10° to 0° at a reduced frequency of 6.4. (Results for -10°, -4°, and -2° are shown.) Unsteady, separation characteristics are then predicted based on the upper-surface C_p values.

4 REFERENCES

Anderson, D.A., 1987. "Equidistribution Schemes, Poisson Generators, and Adaptive Grids." *Applied Mathematics and Computation*, 24, 211.

Anderson, D.A., Tannehill, J.C., and Pletcher, R.H., 1984. *Computational Fluid Mechanics and Heat Transfer*. New York: Hemisphere Publishing Corporation.

Briley, W.R., 1972. "A Numerical Study of Laminar Separation Bubbles Using the Navier-Stokes Equations." *Journal of Fluid Mechanics*, 47, 713.

Crouch, J.D. and Saric, W.S., 1986. "Oscillating Hot-Wire Measurements Above an FX63-137 Airfoil." *AIAA 86-0012*.

Eiseman, P.R., 1987. "Adaptive Grid Generation." *Computer Methods in Applied Mechanics and Engineering*, 64, 321.

Frankel, S.P., 1950. "Convergence Rates of Iterative Treatments of Partial Differential Equations." *Math Tables and Other Aids to Computation*, 4, 65.

Geibler, W., Carr, L.W. and Cebeci, L.W., 1988. "Viscous/Inviscid Interaction Procedure for High-Amplitude Oscillating Airfoils." *ICAS-88-5.5.1*, 766.

Henk, R.W., Reynolds, W.C. and Reed, H.L., 1990. "Unsteady, Three-Dimensional Separation Experiments." in preparation.

Howarth, L., 1938. "On the Solution of the Laminar Boundary Layer Equations." *Proceedings of the Royal Society of London*, 164, 547.

Kim, H.J. and Thompson, J., 1988. "Three-Dimensional Adaptive Grid Generation on a Composite Block Grid." *AIAA-88-0311*.

Moore, F.K., 1957. "On the Separation of the Unsteady Laminar Boundary Layer." in Boundary Layer Research, Proceedings of a Symposium of the International Union of Theoretical and Applied Mechanics, editor H.Görtler, Freiburg, 296.

Mueller, T.J. (editor), 1989. *Low Reynolds Number Aerodynamics*, Proceedings of the Conference, Notre Dame, Springer-Verlag Lecture Notes in Engineering, 54.

O'Meara, M.M. and Mueller, T.J., 1987. "Laminar Separation Bubble Characteristics on Airfoil at Low Reynolds Numbers." *AIAA Journal*, 25, 1033.

Panton, R.L., 1984. *Incompressible Flow*. New York: John Wiley & Sons, Inc.

Peaceman, D.W. and Rachford, H.H., Jr., 1955. "The Numerical Solution of Parabolic and Elliptic Differential Equations." *Journal of the Society for Industrial and Applied Mathematics*, 3, 28.

Pfenninger, W., Vemuru, C.S., Mangalam, S.M. and Evangelista, R., 1988. "Design of Low Reynolds Number Airfoils-11." *AIAA-88-3766*.

Reed, H.L., and Toppel, B.A., 1990. "Low Reynolds Number Airfoils Under Gusting Conditions." in preparation.

Roache, P.J., 1972. *Computational Fluid Dynamics*. Hermosa, Albuquerque, New Mexico.

Roberts, W.B., 1980. "Calculations of Laminar Separation Bubbles and Their Effect on Airfoil Performance." *AIAA Journal*, 18, 25.

Rott, N., 1956. "Unsteady Viscous Flow in the Vicinity of a Stagnation Point." *Quarterly Appl. Maths*, 13, 444.

Sears, W.R., 1956. "Some Recent Developments in Airfoil Theory." *Journal of Aeronautical Science*, 23, 490.

Shen, C.-Y., and Reed, H.L., 1990a. "Shepard's Interpolation for Solution-Adaptive Methods." submitted to *Journal of Computational Physics.*

Shen, C.-Y., and Reed, H.L., 1990b. "Solution-Adaptive Methods for Incompressible Navier-Stokes Equations." in preparation.

Shen, C.-Y., and Reed, H.L., 1990c. "Three-Dimensional Separation at Low Reynolds Numbers." in preparation.

Thomas, L.H., 1949. "Elliptic Problems in Linear Difference Equations Over a Network." *Watson Scientific Computations Laboratory Report*, New York: Columbia University.

Thomas, P.D. and Middlecoff, J.F., 1980. "Direct Control of the Grid Point Distribution in Meshes Generated by Elliptic Equations." *AIAA Journal*, 18, 652.

Wo, A.M., and Covert, E.E., 1989. "Unsteady Aerodynamics of Wortmann FX63-137 Airfoil at Low Reynolds Numbers." in Low Reynolds Number Aerodynamics (see Mueller 1989), p. 206.
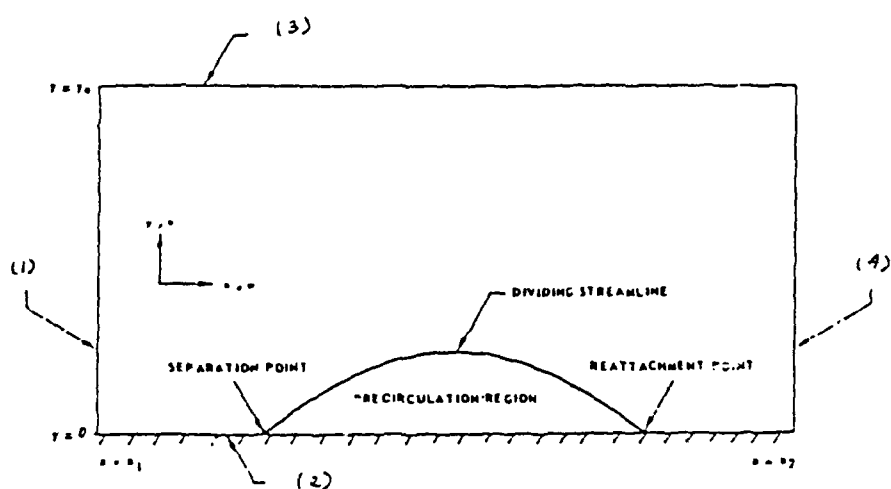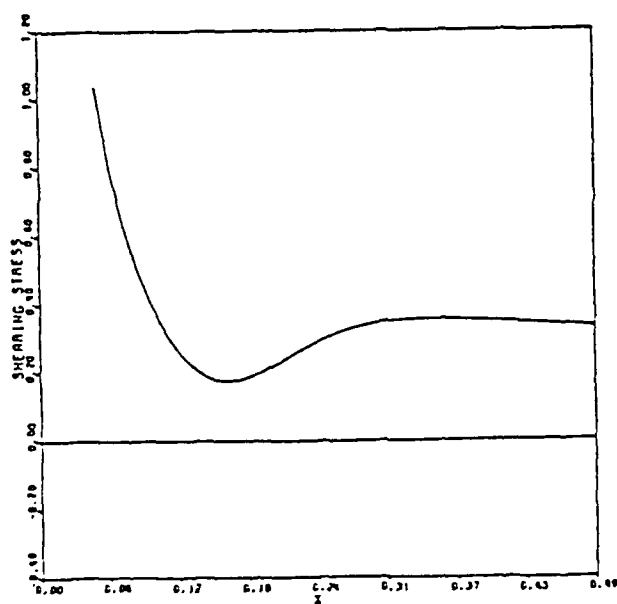
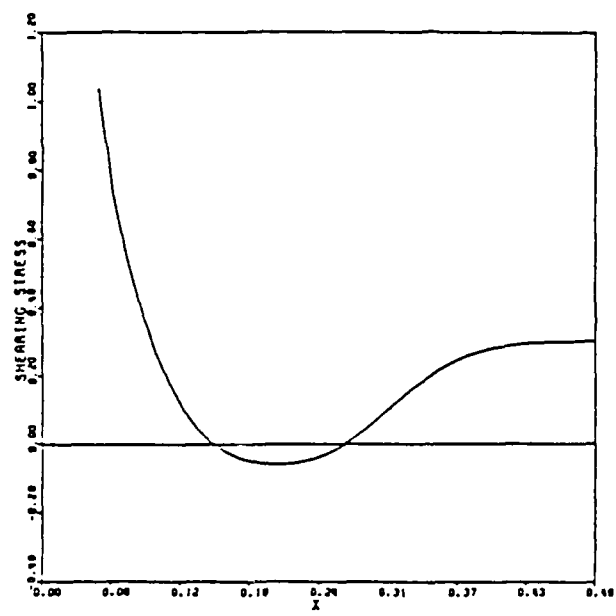Figure 1. Schematic of solution domain for separation bubble (Briley [4])

Figure 2. Wall shearing stress for $x_{end} = 0.16296$

$X_1 = .0501$
$X_2 = .489$
$\Delta X = .01254$
$\Delta y = .00125$
$\Delta l = .0075$
$\rho = 10$

Figure 3. Wall shearing stress for $x_{end} = 0.20058$

$$ E\mathcal{TI} = \frac{1}{2}\sqrt{\frac{Re}{X}} , \quad Re = 20833 $$
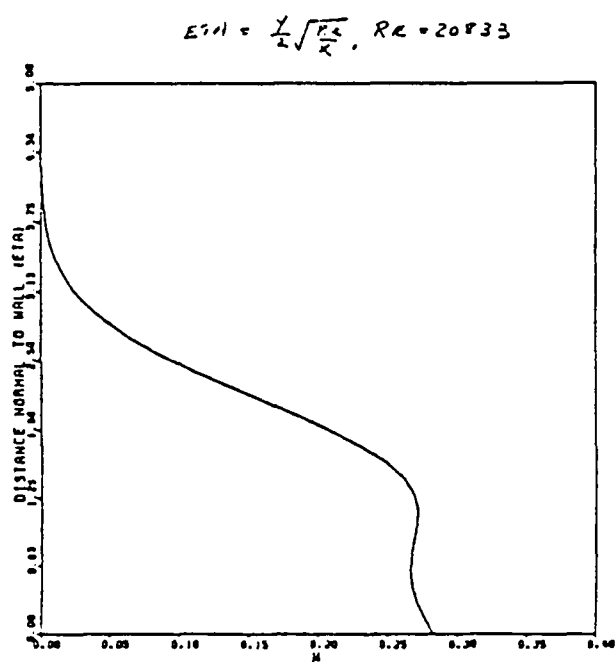
Figure 4. Vorticity profile at x = 0.40122

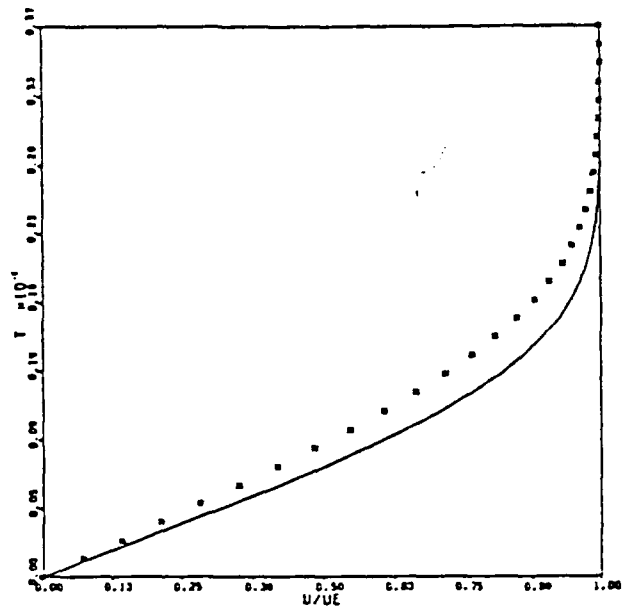Figure 5. Comparison of velocity profile at downstream boundary with Blasius profile for solution near separation
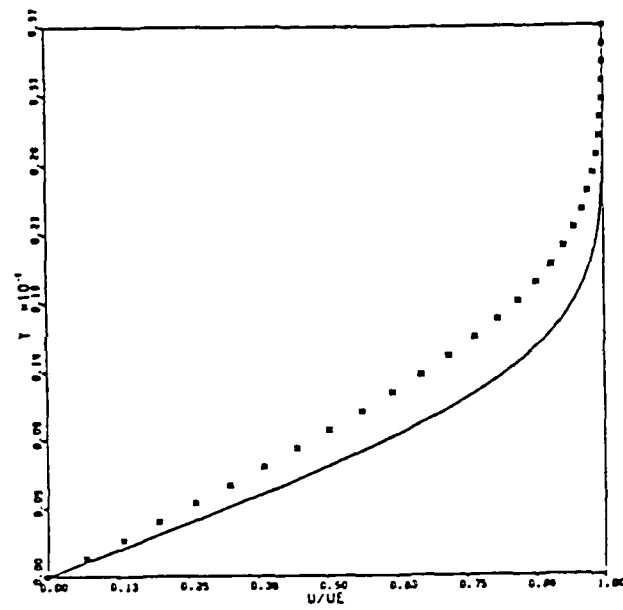
Figure 6. Comparison of velocity profile at downstream boundary with Blasius profile for solution with separation bubble
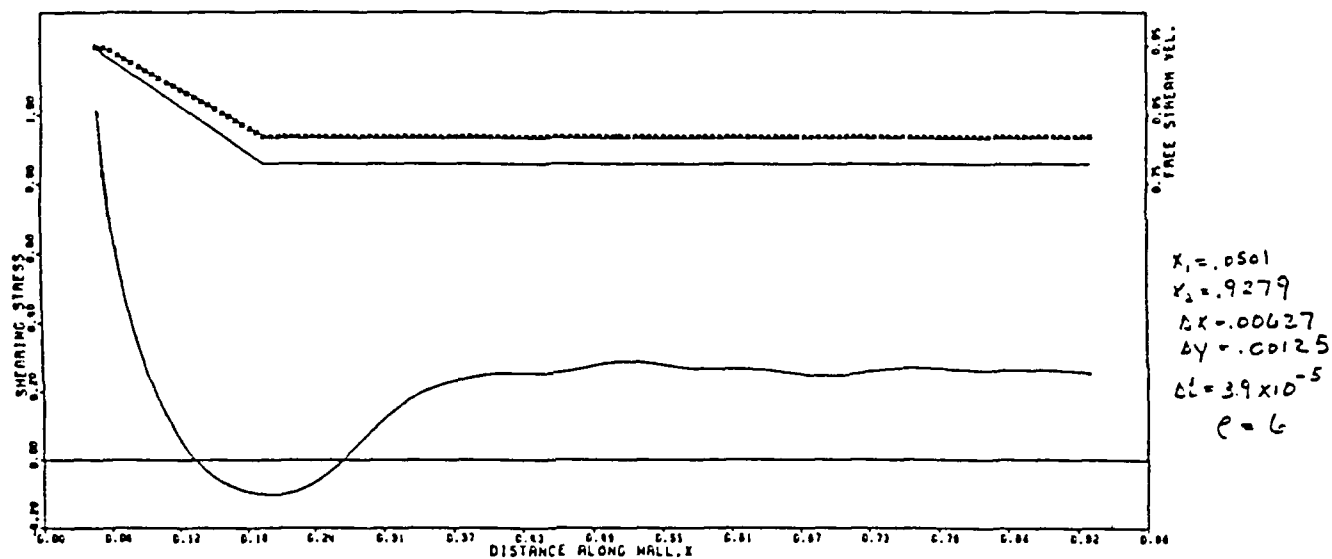
Figure 7. Wall shearing stress for t=4.5
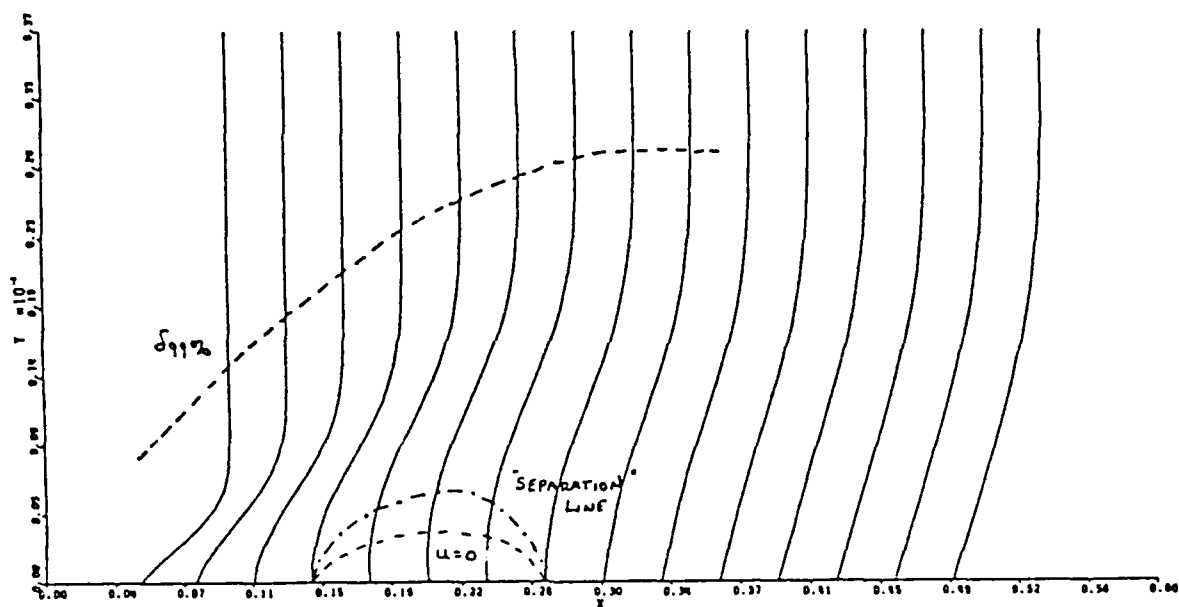
Figure 8. Velocity profiles with "separation" line, edge of reversed flow region, and boundary layer thickness indicated
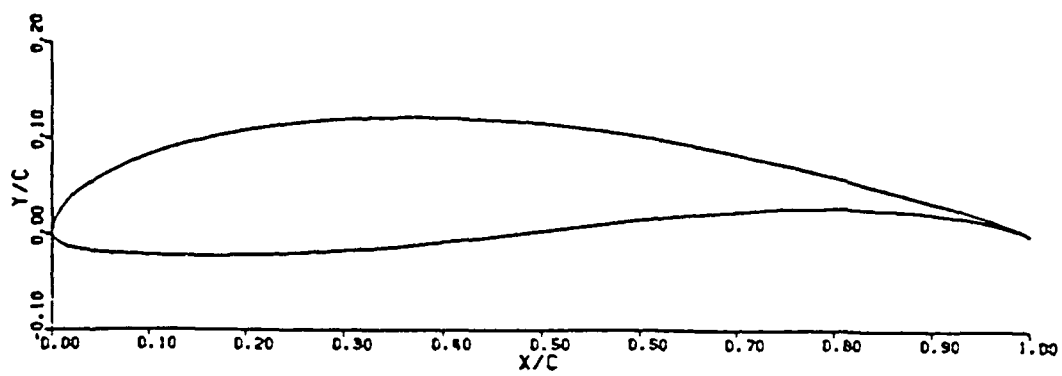
Figure 9. Wortmann airfoil contour
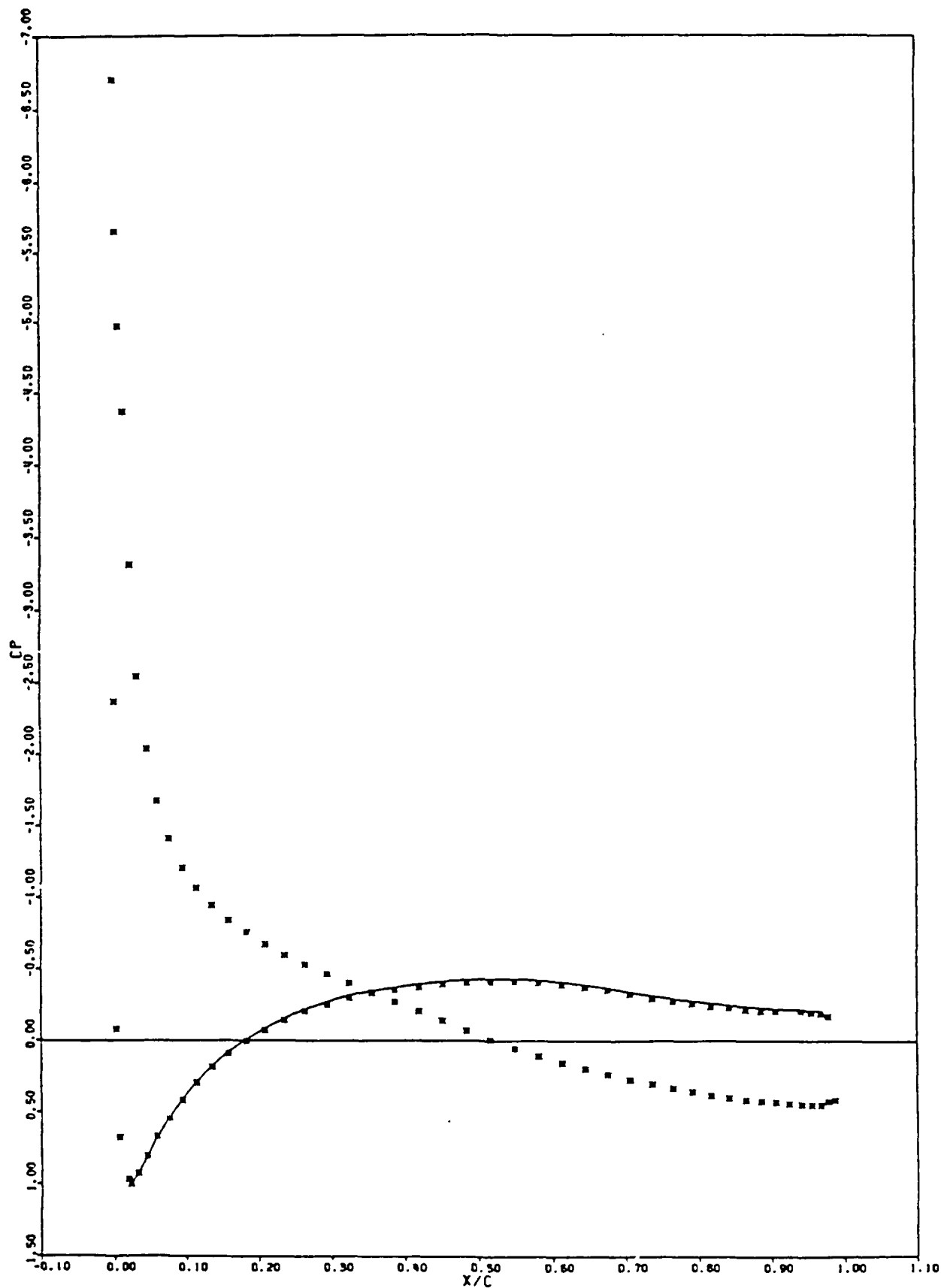
Figure 10. C_p distributions for Wortmann airfoil at -10 degrees incidence: Symbol - Inviscid, panel-method calculation, Solid line - Boundary-layer and Navier-Stokes calculation on the upper surface. Chord Reynolds number is 125,000.
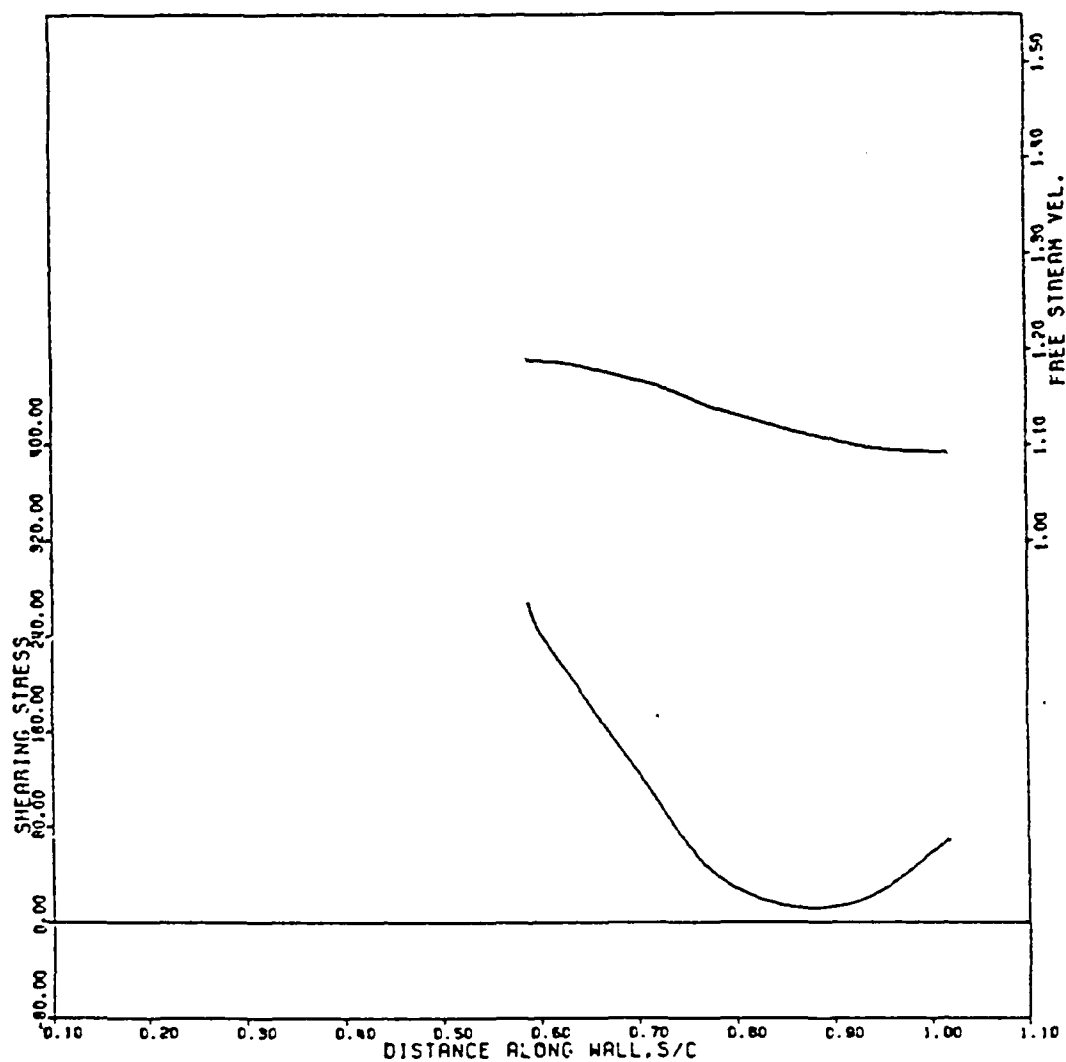
Figure 11. Freestream velocity (top curve) and shear stress (bottom curve) distributions in region of Navier-Stokes calculation on upper surface of Wortmann airfoil at -10 degrees incidence. Chord Reynolds number is 125,000.
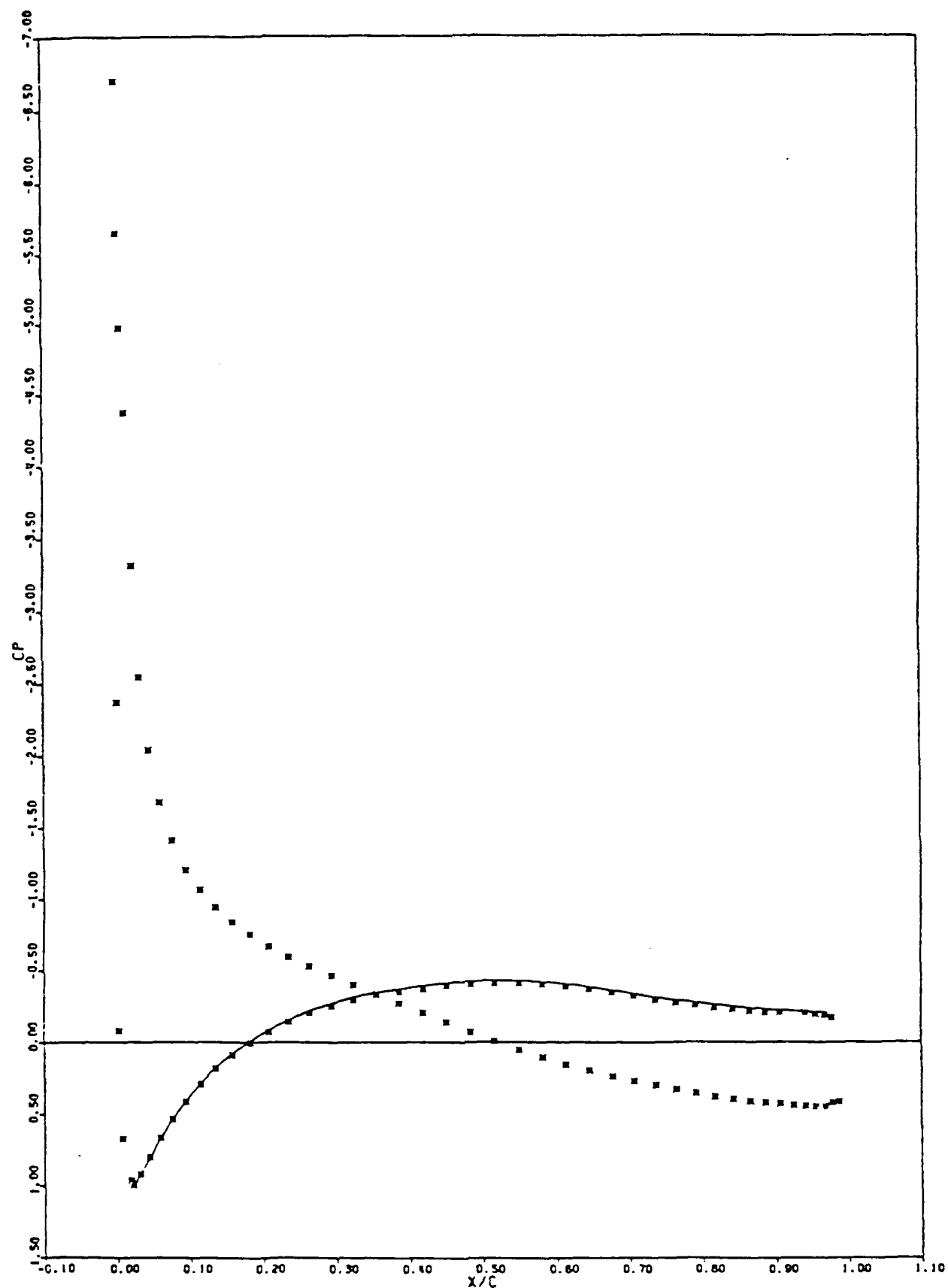
Figure 12. C_p distributions for Wortmann airfoil at -10 degrees incidence: Symbol - Inviscid, panel method calculation, Solid line - Boundary-layer and Navier-Stokes calculation on the upper surface. Chord Reynolds number is 250,000.
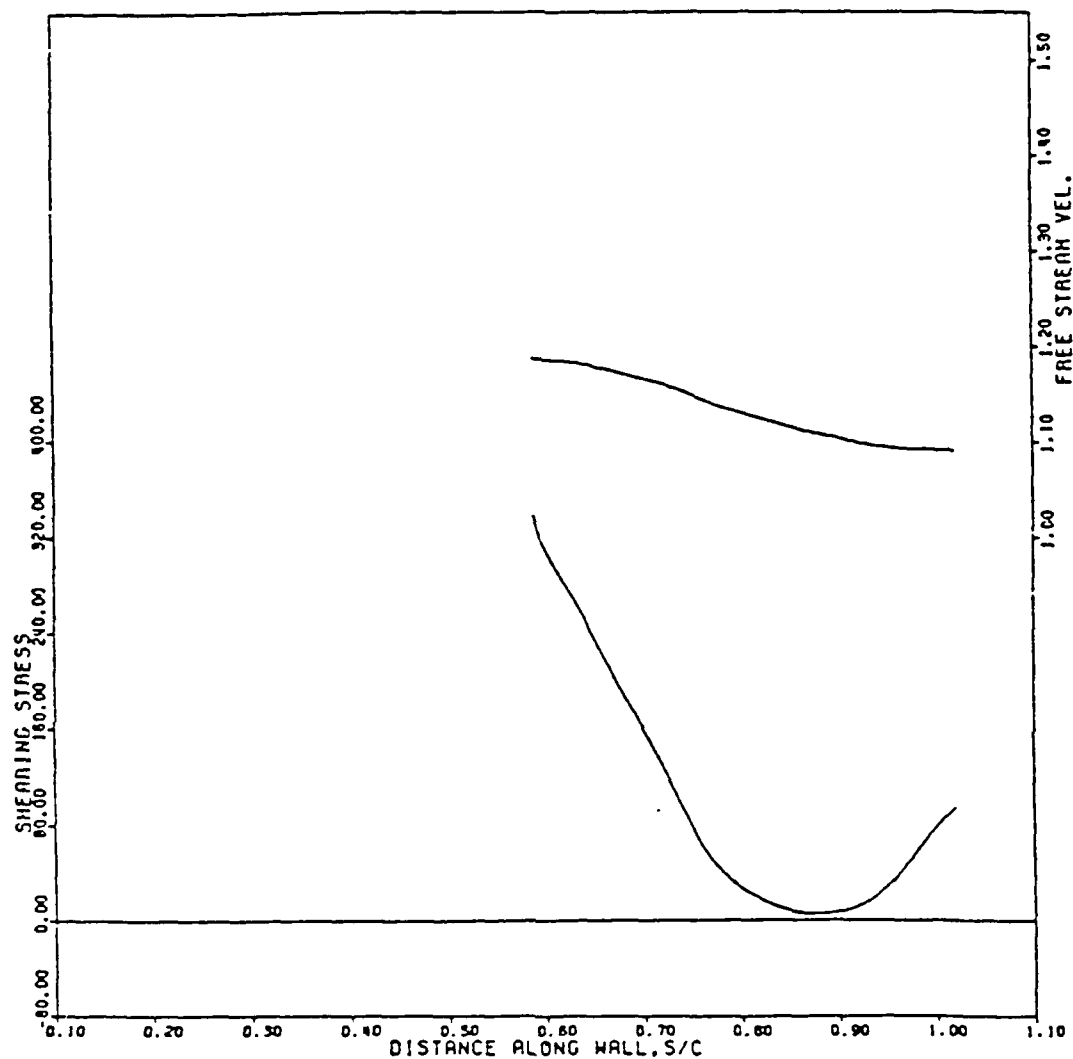
Figure 13. Freestream velocity (top curve) and shear stress (bottom curve) distributions in region of Navier-Stokes calculation on upper surface of Wortmann airfoil at -10 degrees incidence. Chord Reynolds number is 250,000.
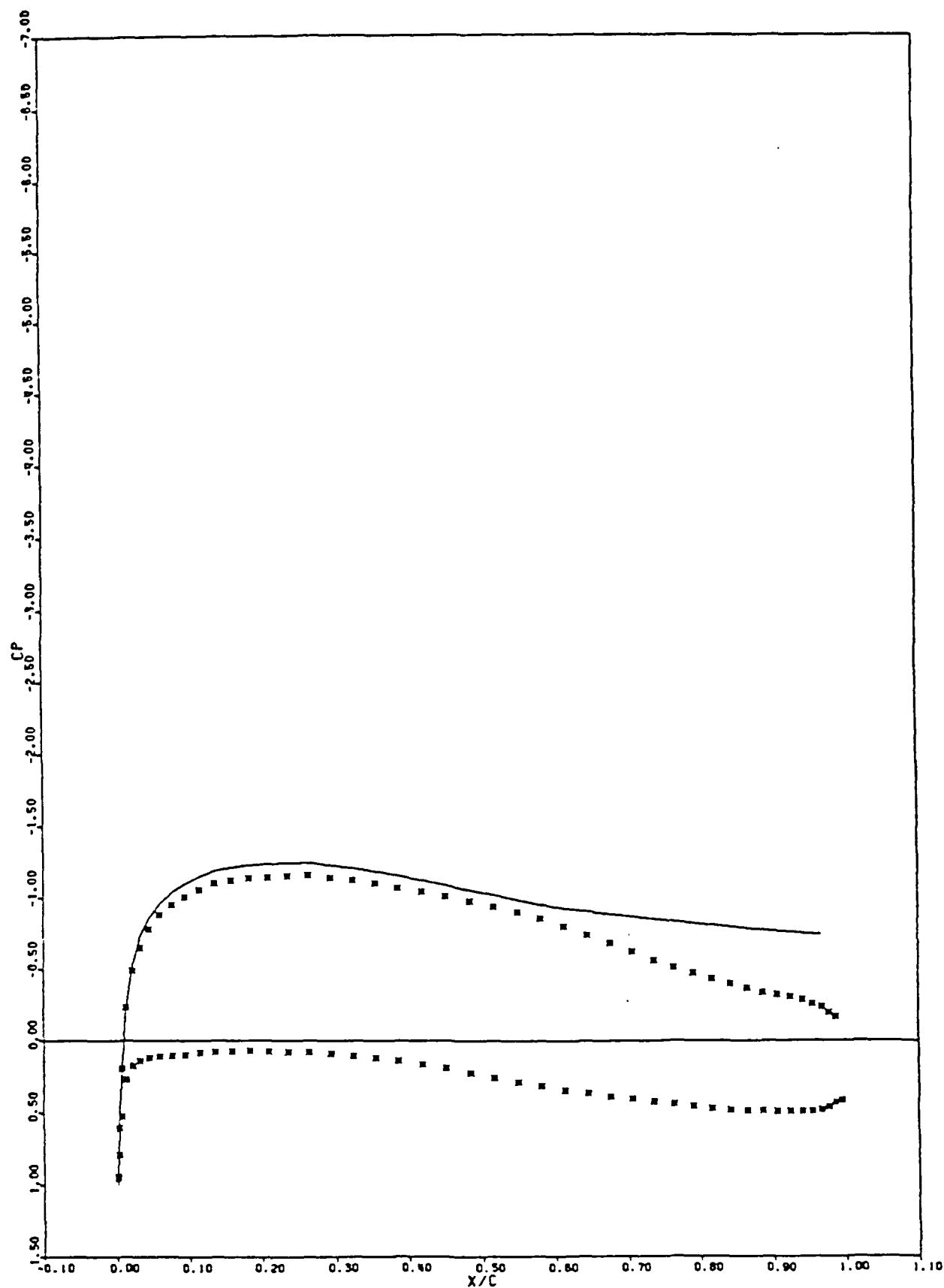
Figure 14. C_p distributions for Wortmann airfoil at 0 degrees incidence: Symbol - Inviscid, panel-method calculation, Solid line - Boundary-layer and Navier-Stokes calculation on the upper surface. Chord Reynolds number is 125,000.
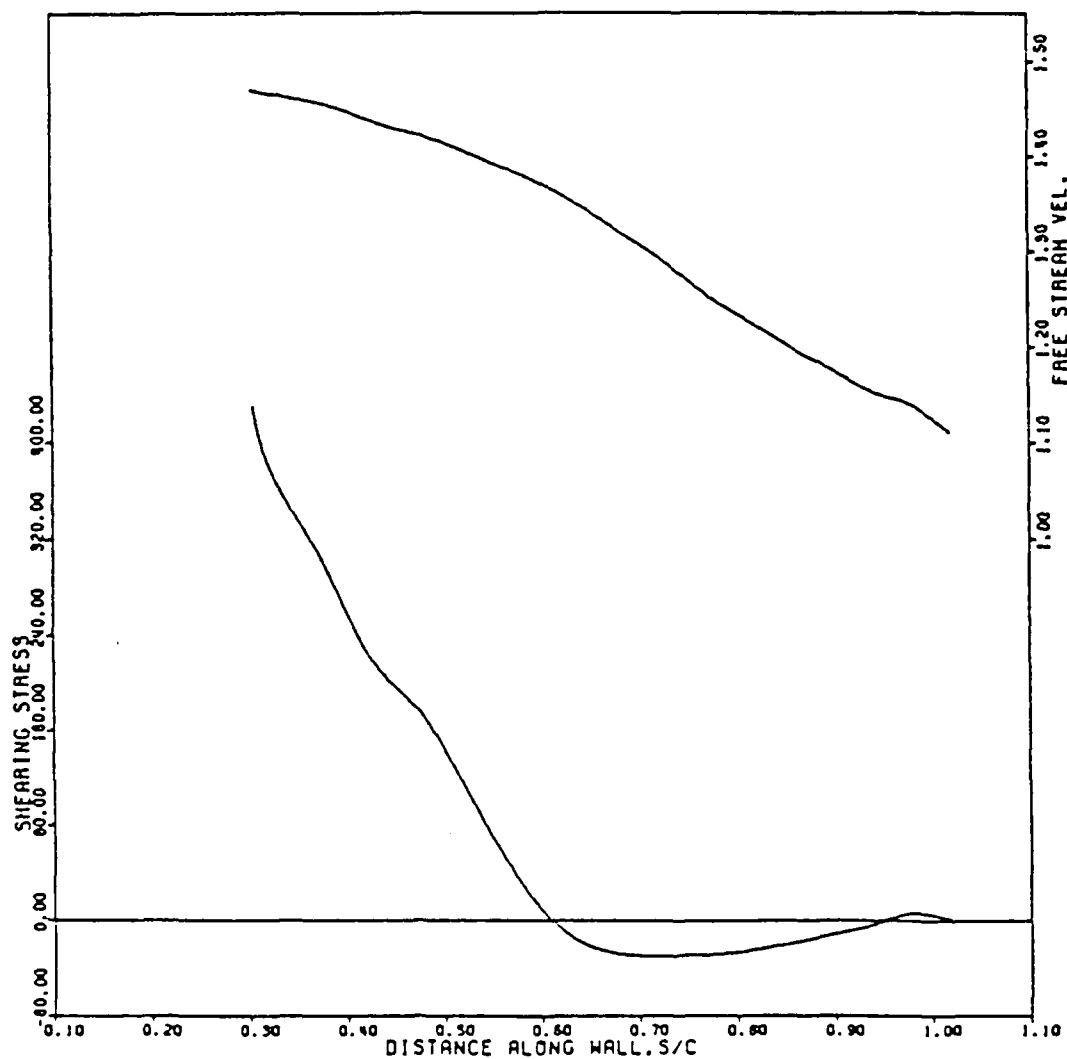
Figure 15. Freestream velocity (top curve) and shear stress (bottom curve) distributions in region of Navier-Stokes calculation on upper surface of Wortmann airfoil at 0 degrees incidence. Chord Reynolds number is 125,000.
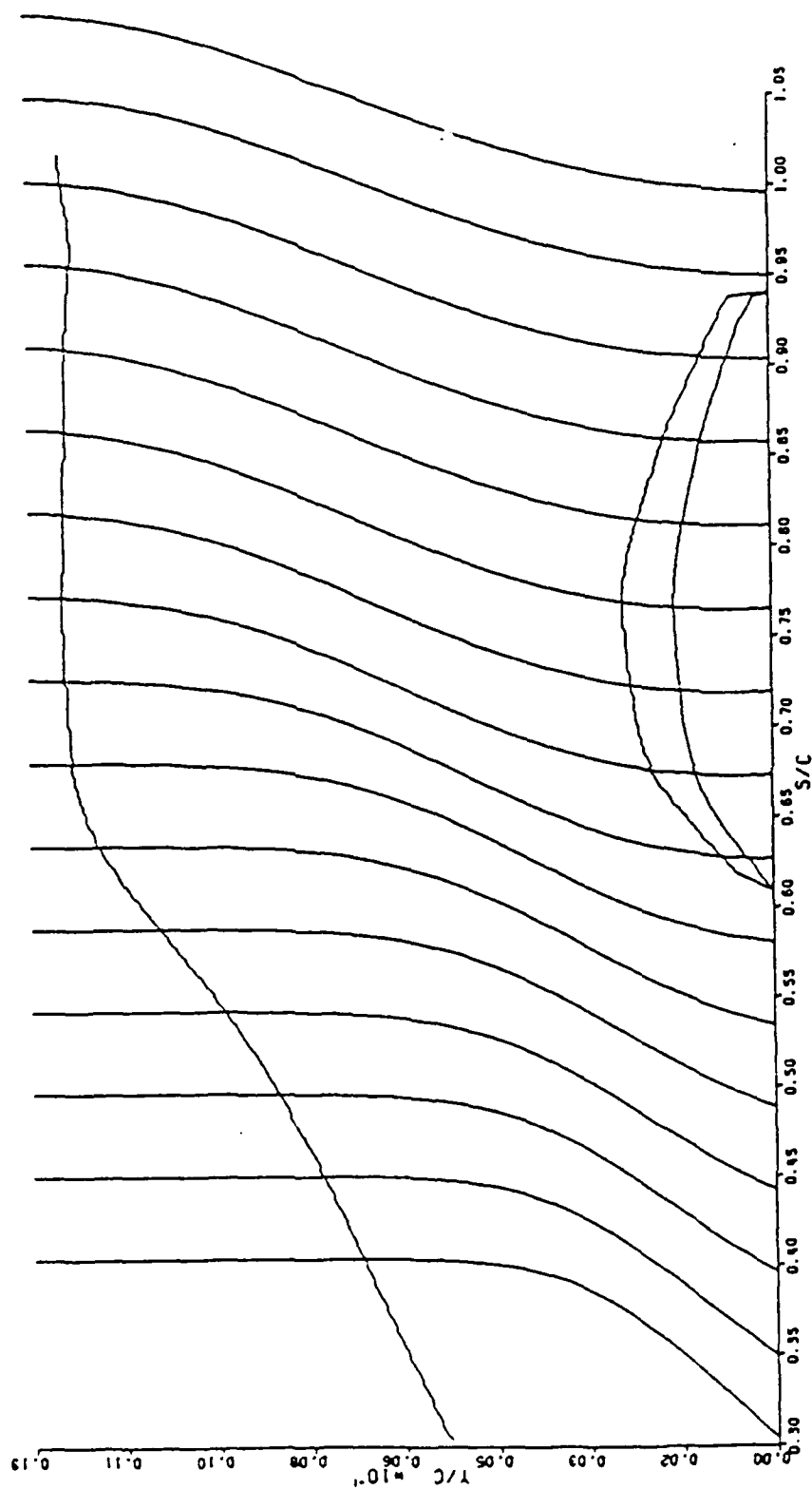
Figure 16. Separated region on upper surface of Wortmann airfoil at 0 degrees incidence. Chord Reynolds number is 125,000.
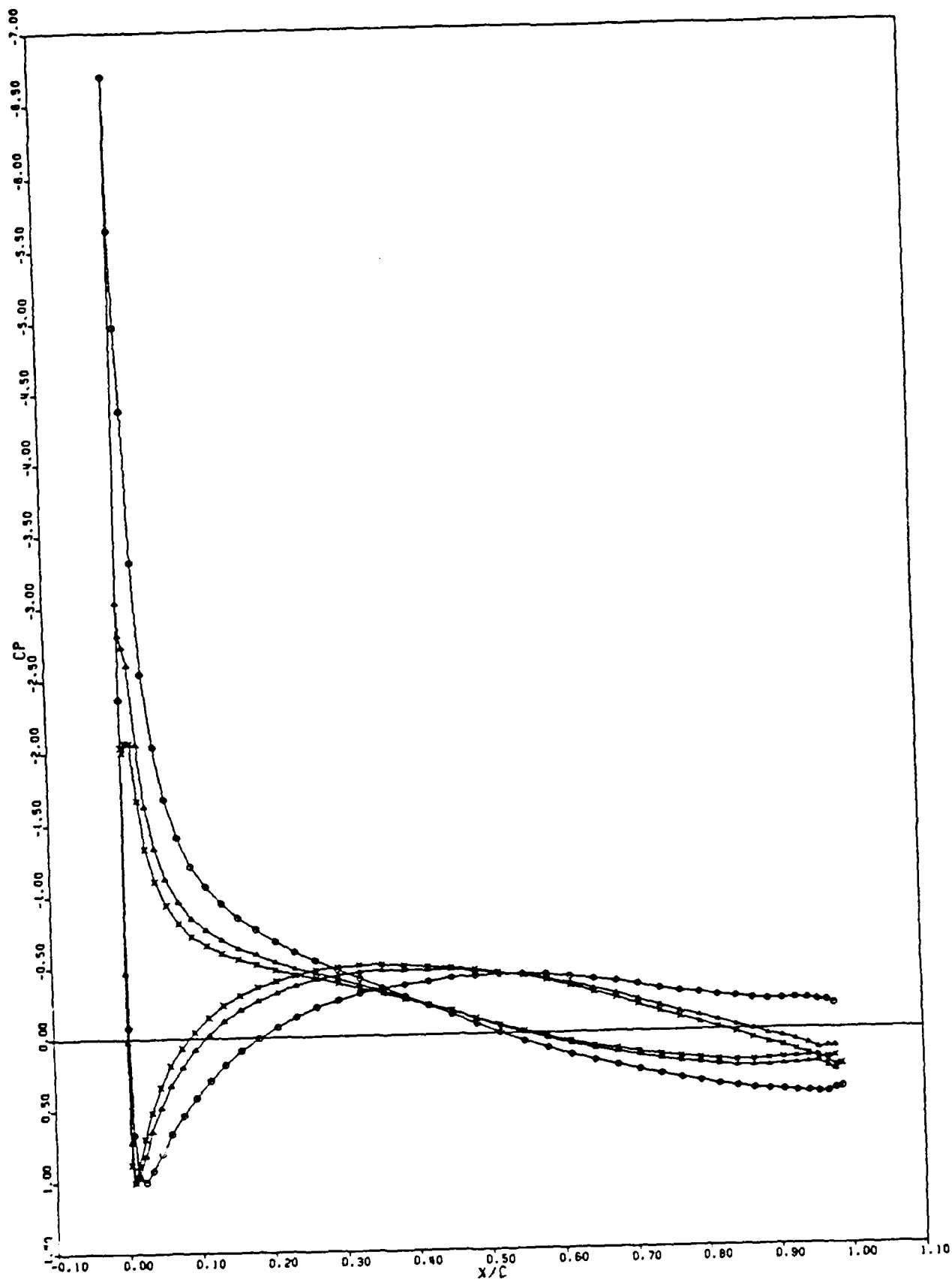
Figure 17. Inviscid C_p predictions for the Wortmann airfoil pitching from -10° to 0° at a reduced frequency of 6.4. Results for -10°, -4°, and -2° are shown.

PART 5. COMPLETED UNSTEADY 3 - D COMPUTATIONAL WORK

Other work completed includes the formulation and demonstration of novel adaptive-grid procedures for *incompressible* flows for both 2-D and 3-D geometries at these Reynolds numbers (Shen & Reed 1990a-b), as well as 3-D results for 2-D base flows experiencing unsteady 3-D freestream pressure gradients (Shen & Reed 1990c). The geometry here includes a flat plate with unsteady 2-D and 3-D suction distributions applied on the outer boundary. The companion experimental results can be found in Henk, Reynolds, & Reed (1990) and were described in Part 3.

The extension to three dimensions of the above discussion in Part 4 is straightforward, but much more lengthy, and is not presented here. We do describe some of the numerical work developed in the context of simulating 3-D unsteady, *incompressible* flows and demonstrated on the well-known problem of driven-cavity flow. The idea of using Shepard's method for interpolation in solution-adaptive procedures is described below, while the adaptive-grid procedures developed as part of this effort are left to be found in Shen & Reed (1990b).

1. Introduction

In the past decade, solution-adaptive methods have proven to be very powerful tools in problems in computational fluid dynamics where large gradients exist. Compared to grid refinement, the moving-grid approach has been commonly used because of its easy implementation, especially for 3-D flows. Saltzman and Brackbill [1] addressed the difficulties of multidimensional adaptive-grid-generation through the variational approach. Subsequently, most methods have dealt with how to move the grid efficiently and how to choose the parameters to be specified in the adaptive-grid-generation (e.g., Nakahashi and Deiwert [2]). Several good reviews on adaptive-grid methods are given by Anderson [3], Thompson [4], and Eiseman [5].

During the solution-adaption procedure, the (intermediate) solutions obtained from a PDE solver (e.g., a Navier-Stokes solver) must interact with the grid obtained from an adaptive-grid generator. The interaction occurs either through grid-speed terms in the PDE solver or simply by transferring the solution data from one computational grid to another, namely, remapping [5] (or rezoning). The advantage of the grid-speed approach is that one is able to get better resolution in time, particularly, for the implicit schemes. But, since the grid-point locations are not known *a priori*, the grid-speed approach suffers from the difficulty to control coordinate singularity [5]. For example, if local grid speeds are too large or move too rapidly during the solution procedure, the result could be an overlapping or highly skewed grid. In contrast to the grid-speed approach, the remapping procedure is commonly used because of its simplicity, efficiency, and numerical stability [5], especially when steady-state solutions are the prime interest. The main purpose of this paper is to consider how to apply the remapping step to solution-adaptive methods.

Recently, Mastin [6] presented some interpolation schemes to transfer solution data from one computational grid to another. One of his suggestions is to first use a point-search algorithm to find a grid point sufficiently close to Q, the point for which interpolated solution values are desired, and then to determine a cell C which contains Q using a cell-search algorithm. Thus one

can compute the value at Q using bilinear (2-D) or trilinear (3-D) interpolation since the solution values at the vertices of C are known. But this algorithm suffers from two difficulties. First, bilinear (2-D) and trilinear (3-D) interpolation can not always be applied to arbitrary quadrilateral and hexahedral cells, respectively. Although Seldner and Westerman [7] have already given a generalization of how to apply bilinear interpolation to arbitrary convex quadrilateral cells, there is no corresponding generalization of trilinear interpolation yet (to the authors' knowledge). Secondly, the cell-search algorithm may fail to locate the point Q within a cell C in general 3-D curvilinear coordinates if the faces of the cell are not planar. This is also pointed out by Mastin himself. Generally, this is a common case in solution-adaptive methods. Furthermore, the interpolant obtained from bilinear or trilinear interpolation is only a continuous function across the interfaces between cells. From the computational point of view, not only a continuous function, but rather a continuous, smooth function across the interfaces between cells would be preferred.

Because of the importance of the remapping step in solution-adaptive methods, an interpolation scheme is needed which is *robust*, *highly accurate* (at least a continuous, smooth function across the interfaces between cells), *efficient* (or at a reasonable computational cost), and *easy to implement*. Among different interpolation methods, the modified Shepard's interpolation [8-13] is possibly the best candidate for solution-adaptive methods for the following reasons. First, it is designed for scattered data (it will be shown how to apply it to a well-structured grid later) so it is robust even when the faces of the cell are not planar. Secondly, the modified Shepard's method used in this paper has quadratic precision [12], which is more accurate than the bilinear and trilinear interpolation for 2-D and 3-D, respectively. It also satisfies the requirement that the resulting interpolant is a continuous smooth function across the interfaces between cells. Next, it is a local interpolation method which makes it efficient, with the level depending on how many points are involved in the calculation. Lastly, it is easy to implement for both 2-D and 3-D.

In the following sections, the control-function approach is reviewed first. Then the original Shepard's method and some of its properties will be described. Following this, the modified

Shepard's method as given by Franke and Nielson [12] is presented. In the same section, we show how to apply this technique to a well-structured grid. For completeness, Mastin's algorithm is also included. Finally, numerical results of 2-D and 3-D driven cavity flow are presented. Here, we couple the modified Shepard's method with the control-function approach.

2.   Adaptive-Grid Scheme

Grid-generation codes based on the elliptic grid-generation equations are commonly used in computational fluid dynamics. Since the control-function approach is also based on these equations, it is natural to consider it among different adaption strategies [14,15]. Additionally, it is easy to add the control adaptive functions (used in the control-function approach) to those already evaluated from the elliptic grid-generation codes in which the geometry is considered [14].

The basic idea of the control-function approach is easily explained by considering its one-dimensional version---*equidistribution*. In order to reduce error the principle of equidistribution is to move the grid such that the product of the spacing and a weight function is *constant* over the points:

$$w \, \Delta x = \text{constant} \qquad (2.1)$$

where w is the weight function. If $x(\xi)$ is defined as a point distribution function and ξ varies by a unit increment between points, eq. (2.2) can be written as

$$w \, x_\xi = \text{constant} \qquad (2.2)$$

Differentiating eq. (2.1) with respect to ξ, one has

$$(w \, x_\xi)_\xi = 0 \qquad (2.3)$$

or

$$x_{\xi\xi} + P\, x_\xi = 0 \tag{2.4}$$

where

$$P = \frac{w_\xi}{w} \tag{2.5}$$

Eq. (2.4) is nothing more than the one-dimensional form of the elliptic grid-generation system [16],

$$\sum_i \sum_j g^{ij}\, \tilde{r}_{\xi^i \xi^j} + \sum_k P_k\, g^{kk}\, \tilde{r}_{\xi^k} = 0 \tag{2.6}$$

often used in grid-generation codes with the control function given as eq. (2.5). Here, the elements of the controvariant metric tensor, g^{ij}, are

$$g^{ij} = \nabla\xi^i \cdot \nabla\xi^j \tag{2.7}$$

It is more convenient to compute g^{ij} through g_{ij}. That is

$$g^{ij} = \frac{1}{g}\,(\, g_{mk}\, g_{nl} - g_{ml}\, g_{nk}\,) \tag{2.8}$$

$$(i,m,n)\ \text{cyclic}, \qquad (j,k,l)\ \text{cyclic}$$

where g_{ij}, the elements of the covariant metric tensor, are

$$g_{ij} = \tilde{r}_{\xi^i} \cdot \tilde{r}_{\xi^j} \tag{2.9}$$

The quantity g is the square of the Jacobian given as

$$g = \det |\, g_{ij}\, | = \left[\, \tilde{r}_{\xi^1} \cdot (\,\tilde{r}_{\xi^2} \times \tilde{r}_{\xi^3}\,)\, \right]^2 \tag{2.10}$$

In these relations, $\tilde{r} = x\,\hat{i} + y\,\hat{j} + z\,\hat{k}$ and ξ^i (i = 1,2,3) are the Cartesian position vector of a grid point and the curvilinear coordinates, respectively. The control functions, P_k, are used to control the spacing and orientation of the grid lines in the domain.

By examining eq. (2.5) and (2.6) it is easy to extend the control functions to 3-D as

$$P_k = \frac{w_{\xi^k}}{w} \tag{2.11}$$

Anderson and Steinbrenner [17,18] applied this approach to 2-D cases, then Kim and Thompson [15] applied it to 3-D cases. Both were successful. Eiseman [5] gave a complete generalization of eq. (2.11) as follows:

$$P_i = \sum_j \frac{g^{ij}(w_i)_{\xi^j}}{g^{ii} w_i} \tag{2.12}$$

Note that eq. (2.12) involves two and three weight functions for 2-D and 3-D, respectively. Using different weight functions in applications makes the method more flexible. For example, one can use gradients of different velocity components as weight functions in different directions as demonstrated in our driven-cavity-flow results in section 6.

3. Shepard's Method

Shepard [8] developed a technique for interpolating 2-D scattered data and applied it to the fitting of geographic and demographic data. Most of the basic properties of Shepard's method can be understood readily through the discussion of the 2-D case. Also there is a straightforward extension from 2-D to 3-D for this particular method. Thus, only 2-D interpolation is given in this section.

Let f be a function with values f_k at nodes (x_k, y_k) for $k = 1,...,N$, and define

$$F(x,y) = \sum_{k=1}^{N} W_k(x,y)\, Q_k(x,y) \,/\, \sum_{k=1}^{N} W_k(x,y) \tag{3.1}$$

where F is a smooth bivariate interpolant with the property that $F(x_k, y_k) = f_k$, $k = 1,...,N$. If $W_k = 1 / d_k^{\mu}$ and $Q_k(x,y) = f_k$, then eq. (3.1) can be written as

$$F(x,y) = \begin{cases} f_k , & (x,y) = (x_k,y_k) \text{ for some } k. \\[1em] \left(\displaystyle\sum_{k=1}^{N} f_k / d_k^\mu \right) \Big/ \left(\displaystyle\sum_{k=1}^{N} 1 / d_k^\mu \right) , & \text{otherwise.} \end{cases} \qquad (3.2)$$

where $\mu > 0$, and $d_k = \left[(x - x_k)^2 + (y - y_k)^2 \right]^{1/2}$. It is easy to see from eq. (3.2) that closer points have a larger contribution to the interpolant F. Note that eq. (3.2) has exactly the same form as that found in Shepard [8].

Here, we will briefly describe some of the properties of Shepard's formula. More details may be found from references [9,10,11]. Eq. (3.2) may be rewritten in cardinal form as

$$F(x,y) = \sum_{k=1}^{N} f_k \, \overline{W}_k(x,y) \qquad (3.3)$$

where

$$\overline{W}_k(x,y) = \begin{cases} \delta_{kj} , & (x,y) = (x_j,y_j) \text{ for some } j. \\[1em] \left(1 / d_k^\mu \right) \Big/ \left(\displaystyle\sum_{j=1}^{N} 1 / d_j^\mu \right) , & \text{otherwise.} \end{cases} \qquad (3.4)$$

Multiplying eq. (3.4) by $\displaystyle\prod_{j=1}^{N} d_j^\mu$, $\overline{W}_k(x,y)$ becomes

$$\overline{W}_k(x,y) = \prod_{\substack{j=1 \\ j \neq k}}^{N} d_j^\mu \Big/ \sum_{i=1}^{N} \prod_{\substack{j=1 \\ j \neq i}}^{N} d_j^\mu \qquad (3.5)$$

$\overline{W}_k(x,y)$ is a *continuous* function in the domain. This follows from the fact that the denominator of eq. (3.5) never vanishes if the (x_k,y_k) are distinct.

It is clear that except for the points (x_k,y_k), the interpolant F constructed by Shepard's method is *analytic* everywhere in the domain. Its shape depends on the values of μ. For $0 \leq \mu \leq 1$, Shepard's interpolant is not a smooth function, for it has cusps or corners at the point (x_k,y_k). For $\mu > 1$, the partial derivatives of F at each point (x_k,y_k) are zero which produces a flat spot at the point (x_k,y_k). Shepard [8] suggested $\mu = 2$. There are other interesting properties of Shepard's formula, a few of which are listed below:

a.   It satisfies the maximum principle, i.e.,

$$\min_{1 \leq k \leq N} f_k \leq F(x,y) \leq \max_{1 \leq k \leq N} f_k \tag{3.6}$$

b.   F is also a constant function if the values of f are constant, i.e., if $f_k = C$, $k = 1,...,N$, then $F = C$.

c.   F is a convex combination of f_k; this is based on the fact that $\displaystyle\sum_{k=1}^{N} \overline{W}_k(x,y) = 1$ and $\overline{W}_k(x,y) \geq 0$ for all k.

d.   Whenever the minimum of d_k or the distance between (x,y) and (x_k,y_k) becomes large enough, F approaches the average of the values of f_k, i.e.,

$$\lim_{\min_k d_k \to \infty} F(x,y) = \frac{1}{N} \sum_{k=1}^{N} f_k \tag{3.7}$$

Several defects of Shepard's method (eq. (3.2)) have been pointed out, even by Shepard [8] himself. First, since it is a global method, the amount of work needed to evaluate F at a particular point becomes tremendous if the data set is large. This is true for most fluid-flow problems.

Secondly, the weight functions are only based on the distance of points from (x,y) and do not consider the effect of their direction. Finally, the flat spots at the data points make the method less attractive. In order to avoid those defects, several modifications have been suggested including by Shepard himself [8-10,12,13]. One of the modifications of Shepard's method given by Franke and Nielson [12] will be discussed in detail in section 4.1. Our proposed modification for a well-structured grid is given in section 4.2.

4. A Modified Shepard's Method

4.1 Franke and Nielson's modification.

In Franke and Nielson's paper [12], Shepard's method becomes a special case of an *inverse, distance-weighted, least-squares* interpolant. Again, the interpolant F is eq. (3.1), conveniently rewritten here as

$$F(x,y) = \sum_{k=1}^{N} \overline{W}_k(x,y) \, Q_k(x,y) \tag{4.1}$$

where

$$\overline{W}_k(x,y) = W_k(x,y) \, / \sum_{k=1}^{N} W_k(x,y) \tag{4.1'}$$

$Q_k(x,y)$ is called the nodal function [12] since it is associated with the node (x_k,y_k), $k = 1,...,N$, respectively. We note that $Q_k(x,y)$ approximates f at (x_k,y_k) locally. In general, $Q_k(x,y)$ can be any function that satisfies

$$Q_k(x_k,y_k) = f_k \, , \qquad k = 1,..., N \tag{4.2}$$

In this study, $Q_k(x,y)$ is a bivariate quadratic function, specifically. the weighted least-squares fit at the node (x_k,y_k).

Certain properties are required for $\overline{W}_k(x,y)$ so that the interpolant F will maintain the local shape characteristics of the nodal functions. First, the weight function $\overline{W}_k(x,y)$ must satisfy

$$\overline{W}_k(x_j,y_j) = \delta_{kj} , \qquad k,j = 1,...,N \qquad (4.3)$$

Next, in order to preserve

$$\frac{\partial F}{\partial x}(x_k,y_k) = \frac{\partial Q_k}{\partial x}(x_k,y_k) \qquad (4.4)$$

and

$$\frac{\partial F}{\partial y}(x_k,y_k) = \frac{\partial Q_k}{\partial y}(x_k,y_k) , \qquad k = 1,...,N \qquad (4.5)$$

the first derivatives of $\overline{W}_k(x,y)$ must be zero, i.e.,

$$\frac{\partial \overline{W}_k}{\partial x}(x_j,y_j) = \frac{\partial \overline{W}_k}{\partial y}(x_j,y_j) = 0 \qquad (4.6)$$

It is easy to see this, since

$$\frac{\partial F}{\partial x}(x_k,y_k) = \sum_{j=1}^{N} \left[\frac{\partial \overline{W}_j}{\partial x}(x_k,y_k) Q_j(x_k,y_k) + \overline{W}_j(x_k,y_k) \frac{\partial Q_j}{\partial x}(x_k,y_k) \right]$$

$$= \frac{\partial Q_k}{\partial x}(x_k,y_k) \qquad (4.7)$$

and similarly for eq. (4.5). Moreover, the function Q_k will be identical to f as long as f is a quadratic function, i.e., $Q_k(x,y) = f(x,y)$, $k = 1,...,N$. It follows from eq. (4.1) that

$$F(x,y) = f(x,y) \sum_{k=1}^{N} \overline{W}_k(x,y) \qquad (4.8)$$

whenever f is a quadratic function. The last equation shows that one more requirement of $\overline{W}_k(x,y)$ is needed in order for interpolant F to be of quadratic precision. That is

$$\sum_{k=1}^{N} \overline{W}_k(x,y) \equiv 1 \qquad (4.9)$$

The weight function to be used, as suggested by Franke and Little (reference 19, page 112) is

$$W_k(x,y) = \left[\frac{(R_w - d_k)_+}{R_w \, d_k} \right]^2 \qquad \text{for}$$

$$(R_w - d_k)_+ = \begin{cases} R_w - d_k & \text{if } d_k < R_w \ , \\ 0 & \text{if } d_k \geq R_w \end{cases} \qquad (4.10)$$

where R_w is a radius of influence about node (x_k, y_k), and $d_k(x,y)$ is the distance between (x,y) and (x_k, y_k) in Euclidean space. Since Q_k is a bivariate quadratic function that satisfies eq. (4.2), it is defined [12,13] by

$$Q_k(x,y) = \bar{c}_{k1}(x - x_k)^2 + \bar{c}_{k2}(x - x_k)(y - y_k) + \bar{c}_{k3}(y - y_k)^2$$

$$+ \bar{c}_{k4}(x - x_k) + \bar{c}_{k5}(y - y_k) + f_k \qquad (4.11)$$

with the coefficients satisfying the following expression in the weighted least-squares sense [12,13].

$$\sum_{i=1}^{N} W_i(x_k, y_k) \left[\bar{c}_{k1}(x_i - x_k)^2 + \ldots + \bar{c}_{k5}(y_i - y_k) + f_k - f_i \right]^2 \qquad \text{for}$$

$$W_i(x,y) = \left[\frac{(R_q - d_i)_+}{R_q \, d_i} \right]^2 \qquad (4.12)$$

where R_q is a radius of influence about node (x_i, y_i) and $d_k(x_i, y_i)$ is the distance between (x_i, y_i) and (x_k, y_k) in Euclidean space. It is obvious that Q_k is a *local* approximation to f because non-zero contributions to the least-squares fit only come from the nodes whose radii of influence include (x_k, y_k). Similarly, $\overline{W}_k$, used in eq. (4.1), is locally defined. Thus, F is a *local* interpolant.

The only problem left is how to choose the radii of influence, both R_w and R_q. Franke and Nielson [12] used fixed, uniform radii for their work. In contrast to that, Renka [13] chose R_w and R_q just large enough to include the N_w and N_q nodes, respectively, for fixed values of N_w and N_q. Here, N_w and N_q are the numbers of points used to calculate R_w and R_q, respectively. But both methods were designed for scattered data, so a good way to search the nearest points in order to implement the methods is needed; e.g., Renka [13] used the cell method.

4.2   Proposed simplified modification for a well-structured grid.

Since the adaptive-grid scheme used this study work is a finite-difference method, the topology of the grid structure is regular, actually being uniform in logical space (see Fig. 1). Thus it is natural to include the neighboring points from the grid structure (see Fig. 1) for the finite-difference method. In order to make the implementation of Shepard's ideas easy, the fixed values of ISP_q and ISP_w is used. Here, ISP_q and ISP_w are the grid numbers to be included along each grid line when calculating the R_q and R_w, respectively. For example, $ISP_q = 3$ in the 2-D case corresponds to $N_q = 8$th Renka's work. Actually, numerical experiments show that the results are best if the structure of the neighboring points used in the modified Shepard's method is the same as that of the finite-difference scheme used. (The stencil of the finite-difference scheme used in this study is a nine-point 'star'.) For example, the results of numerical experiments show that $ISP_q = 3$ is best. (See Table I in Section 6).

The algorithm of the simplification of the modified Shepard's method proposed here is summarized below.

1.   Select ISP_q in order to define

$$W_i = \left[\frac{\left(R_q - d_i \right)_+}{R_q \, d_i} \right]^2 \qquad \text{used in (4.12)}$$

The default value of ISP_q is 3.

2.   For k = 1,...,N solve the weighted least-squares problem:

$$\min_{\bar{c}_{kj},\, j\,=\,1,...,5} \sum_{i\,=\,1}^{N} W_i\,(x_k, y_k)\left[\,\bar{c}_{k1}(x_i - x_k)^2 + ... + \bar{c}_{k5}(y_i - y_k) + f_k - f_i\,\right]^2$$

to yield $\bar{c}_{kj}$, j = 1,...,5.

3.   Search for the nearest point (x_k, y_k) of point Q. Here, (x_k, y_k) is the coordinate of point P in the old grid, and (x,y) is the coordinate of point Q in the new grid (see Fig. 1). The search algorithm used here is the point-search algorithm described in section 5.1.

4.   Select ISP_w in order to define

$$W_k = \left[\frac{\left(R_w - d_k\right)_+}{R_w\, d_k}\right]^2 \qquad \text{used in (4.1)}$$

The default value of ISP_w is 3.

5.   Define

$$Q_k(x,y) = \bar{c}_{k1}(x - x_k)^2 + \bar{c}_{k2}(x - x_k)(y - y_k) + \bar{c}_{k3}(y - y_k)^2 + \bar{c}_{k4}(x - x_k) + \bar{c}_{k5}(y - y_k) + f_k$$

and compute

$$F(x,y) = \sum_{k\,=\,1}^{N} W_k(x,y)\, Q_k(x,y) \;/\; \sum_{k\,=\,1}^{N} W_k(x,y)$$

5. Mastin's Algorithm

5.1 *Search algorithm.*

As described in the previous section, an efficient point-search algorithm is required for the proposed modification. Recently, Mastin [6] presented interpolation schemes for solution-adaptive methods and related problems. He gave two search algorithms in his work, namely, the *point-*

search algorithm and the *cell*-search algorithm (to be described later) the former of which has been adopted in this study.

Suppose an interpolated solution value is desired at point Q. One of Mastin's schemes uses a point-search algorithm to find a grid point sufficiently close to Q, and then determines a cell C which contains Q by using a cell-search algorithm. Following Mastin [6], the algorithms are given as follows.

a.   Point-search algorithm: to locate a grid point sufficiently close to Q.

Assume P is a starting point (see Fig. 2). First, both the distance from P to Q and the distance from Q to R, where R is a neighbor of P, are computed and compared with each other. P is replaced by R whenever R is found to be closer to Q than P is. Then, the procedure is repeated until P is closer to Q than any of its four (2-D) or six (3-D) neighbors are.

b.   Cell-search algorithm: to determine a grid cell which contains Q.

Starting from a cell C (see Fig. 3), the first step is to decide on which side of L that Q lies. This is determined simply by computing a signed area A (will be defined later). For example, based on the signed area A calculation, Q is determined to be on the opposite side of the cell C (see Fig. 3). Then, the cell C is replaced by the cell D in the search. If there is no sign change in A, then the algorithm is repeated. Once the sign of A changes, the match direction is switched to an adjacent side; e.g., from line L_1 to L_2 as illustrated in Fig. 4. The algorithm is continued until a cell is found which contains Q.

The signed area A depends on the orientation of the points (see Fig. 5) which is defined by:

$$A = x_1(y_2 - y_3) + x_2(y_3 - y_1) + x_3(y_1 - y_2) \tag{5.1}$$

For 3-D grids (see Fig. 6), eq. (5.1) is replaced by

$$A = \bar{v}_1 \cdot \bar{v}_2 \times \bar{v}_3 \qquad\qquad (5.2)$$

It is easy to see from eq. (5.2) that the 3-D search algorithm will fail to locate the cell which contains the point Q if the cell faces are not *planar*, as in a general 3-D curvilinear grid and this happens to be a common case for the solution-adaptive method.

5.2   Interpolation scheme.

To verify the modification proposed here, another interpolation method against which to compare is needed. After determining the cell C which contains Q, Mastin computed the value at Q using bilinear (2-D) or trilinear (3-D) interpolation since the solution values at the vertices of C are known. But bilinear (or trilinear) interpolation is no more than the area-weighting method [7] and, in general, cannot be applied to arbitrary cells. Seldner and Westermann [7] give a generalization of bilinear interpolation to arbitrary, convex, four-point cells. This explicit formula (see Appendix) is used in this study to compare to the proposed simplification of the modified Shepard's method for the 2-D case. Since there is no corresponding generalization for the 3-D case as yet, no comparison is made for the 3-D case.

6.   Numerical Results

It has been recognized that the numerical simulation of incompressible Navier-Stokes equations becomes increasingly more difficult as the Reynolds number (Re) increases. The major difficulty arises due to the large gradients associated with high Re flows. In order to resolve these gradients one a very fine uniform grid is often used, thereby increasing the computational time. Otherwise problems, of numerical instability [20] or inconsistency (i.e. the solution converges but converges to the wrong solution) [21] would be encountered. An alternative to this approach is to automatically place more grid points in regions with large gradients and less grid points where the solution is smooth. This is exactly what the solution-adaptive method does.

Driven cavity flow has become a standard test case for incompressible Navier-Stokes equations in the past two decades. For example, Ghia et al. [22] used a multi-grid coupled with a strongly implicit procedure (SIP) to solve 2-D driven cavity flow up to Re = 10,000 on a 257 × 257 grid. Schreiber and Keller [23] also solved the same problem up to Re = 10,000 on a 180 × 180 grid using Newton iteration coupled with continuation method. Both used uniform grid. Here, the solution-adaptive method with Shepard's interpolation is used to obtain a solution yielding comparable results while using fewer grid points.

In this section, the problem formulation and solution algorithm for the 2-D case are described briefly. Results obtained from 2-D driven cavity flow with Re = 5,000 on a 81 × 81 grid are shown. Finally, some results for 3-D driven-cavity flow are given to demonstrate the ease with which Shepard's interpolation can be applied to 3-D flows.

6.1 Problem formulation and solution algorithm.

The Navier-Stokes equations in terms of curvilinear coordinates for 2-D flow in a square cavity (see Fig. 7) can be written as:

$$
\omega_t + \frac{y_\eta(u-x_t) - x_\eta(v-y_t)}{J}\omega_\xi + \frac{-y_\xi(u-x_t) + x_\xi(v-y_t)}{J}\omega_\eta
$$

$$
= \frac{1}{Re}\frac{1}{J^2}\left(\alpha\omega_{\xi\xi} - 2\beta\omega_{\xi\eta} + \gamma\omega_{\eta\eta} + \sigma\omega_\eta + \tau\omega_\xi\right)
\tag{6.1}
$$

$$
\frac{1}{J^2}\left(\alpha_{\psi\xi\xi} - 2\beta\psi_{\xi\eta} + \gamma\psi_{\eta\eta} + \sigma\psi_\eta + \tau_{\psi\xi}\right) = -\omega
\tag{6.2}
$$

where $u = \psi_y$, $v = -\psi_x$, and $\omega = v_x - u_y$. Here, (x, y) and (ξ,η) are coordinates of the physical and logical spaces, respectively. J is the Jacobian of the transformation from physical space to logical space. x_t and y_t are the grid speed terms. x_ξ, y_ξ, x_η, y_η, α, β, γ, σ and τ are metric terms.

The boundary conditions are given by

$$
\begin{aligned}
u = v = 0 \quad &, \quad \text{when } x = 0 \text{ or } 1, \\
u = v = 0 \quad &, \quad \text{when } y = 0, \\
u = 1, v = 0 \quad &, \quad \text{when } y = 1.
\end{aligned}
\tag{6.3}
$$

Eqs. (6.1) and (6.2) were discretized by applying a three-point central difference to spatial derivatives in ω and ψ and a first-order backward difference to time derivatives in ω. In order to ensure second-order accuracy of the converged solutions, Briley's formula [24] was used for vorticity boundary conditions at the wall. The resulting nonlinear system of algebraic equations was solved by the modified strongly implicit procedure (MSI) which originated from Stone [25] and was subsequently extended to a nine-point finite difference scheme by Schneider and Zedan [26]. Since steady-state solutions are of principal interest, adaptation has to be done only occasionally during the solution procedure. Here the solution-adaptive method coupled with a continuation method is used.

The solution algorithm [27] is outlined as follows:

1. Specify the initial value of Re.

2. Solve eqs. (6.1-3) on a grid system using one-by-one iteration, i.e., one iteration for the stream-function equation followed by another iteration for vorticity equation.

3. Calculate the weight functions (will be given later) based on the convergent (or reasonable intermediate) solutions of step 2.

4. Generate a new grid by solving the corresponding 2-D version of the grid equations (2.6) and (2.12).

5. Map values of ω, ψ, u, and v from the old grid to the new grid.

6. Increase the value of Re.

7. Repeat steps 2 through 6 until the solution converges for the desired Re number.

Note that the initial grid used can be either a uniform grid or a nonuniform grid based on previous knowledge flow.

6.2   *Results of 2-D driven cavity flow with Re = 5,000.*

Since the principal interest here is the steady-state solution, the grid speed terms in eq. (6.1) are set to zero for the obvious reason already mentioned in the Introduction. The solution procedure starts from Re = 400 on a 81 × 81 uniform grid then Re = is increased to 1000, 2000, 3200, and 5000. Solution data for the intermediate solutions during the adaptions since (Ghia et

al. [22]). The convergence criteria for both the Navier-Stokes solver and the grid-generation solver is defined as

$$TOL = \max_{i,j} \frac{\left|(\varphi_s)_{ij}^{k+1} - (\varphi_s)_{ij}^{k}\right|}{\left|(\varphi_s)_{ij}^{k+1}\right|_{max}} < \varepsilon \tag{6.4}$$

where k is the iteration number. φ_s represents ω and ψ for the Navier-Stokes solver and x and y for the grid-generation solver. Here ε is set to 10^{-5} for grid-generation solver, and 10^{-4} for the intermediate solutions of the Navier-Stokes solver. The value of ε for the final converged solutions 10^{-5}.

Numerical experiments show that changes of the solutions in the central-core region tend to be slow if Δt is applied uniformly over the whole domain. The remedy is to apply a false-transient method to the vorticity equation (i.e., vary Δt based on the calculation of the local velocity [28] over the whole domain). As the step size of the grid becomes smaller and smaller, the advantage of the false-transient method diminishes rapidly. (A similar observation was obtained by Benjamin and Denny [29] where the local Δt calculation was based on a Neumann stability analysis.) No improvement is found for convergence after the adaption based on solutions of Re = 3200, so that $\Delta t = 2 \times 10^{-3}$ is applied uniformly to the whole domain in the rest of the calculation. Because one by one iteration is used in this study, the boundary values of vorticity at the walls have to be damped as follows:

$$(\omega_B)^{k+1} = \lambda(\omega_B)^{k+1} + (1-\lambda)(\omega_B)^{k} \tag{6.5}$$

with $\lambda = 0.15$ [29].

During the adaption the choice of the weight functions is the key to the success of solution-adaptive methods which is also a problem dependent. In order to follow the flow the weight functions used in this study involved velocity gradient along each coordinate line, that is,

$$\widetilde{W}_1 = \left(1 + C_1 \frac{u_\xi^2 + v_\xi^2}{x_\xi^2 + y_\xi^2} \right)^{1/2}$$

(6.6)

$$\widetilde{W}_2 = \left(1 + C_2 \frac{u_\eta^2 + v_\eta^2}{x_\eta^2 + y_\eta^2} \right)^{1/2}$$

(6.7)

where C_1 and C_2 are adaptive constants [27] used to adjust the density of the grid. Since large gradients are known *a priori* to exist near the walls, in this study a stretching function is incorporated into the weight functions. The stretching function [30] is

$$\gamma(s) = \frac{1}{2} + \frac{1}{2} \frac{\ln\left[(\beta + 2s - 1)/(\beta - 2s + 1)\right]}{\ln\left[(\beta + 1)/(\beta - 1)\right]}$$

(6.8)

where s can be either x or y.

Finally, the weight functions become

$$W_1 = \theta\widetilde{W}_1 + (1 - \theta)(1 + C_3\gamma_x^2)^{1/2}$$

(6.9)

$$W_2 = \theta\widetilde{W}_2 + (1 - \theta)(1 + C_4\gamma_y^2)^{1/2}$$

(6.10)

Fig. 8 shows that a good choice for θ and β are 0.5 and 1.054 respectively. The grid follows not only the flow but also places more points near the walls and corners which is also important in order to resolve the secondary vortex.

In order to ensure that the numerical accuracy of the interpolation method described in section 4.2 is at least one order higher than generalized bilinear interpolation (see the Appendix), a test was performed. The solutions based on the grid from the second adaption were used to generate a new grid and then mapped onto this new grid. Since there are no analytic solutions available for comparison, the data on the new grid was then remapped onto the previous grid and

the results compared with the original data from this grid. The Euclidean norm was used to calculate the error; that is,

[(original data - data obtained after two mappings)^2/(number of grid points)]$^{1/2}$

The results of Table I confirm that the modified Shepard's interpolation is at least one order of accuracy higher than the generalized bilinear interpolation. The errors in stream function are small for both interpolation schemes. This due to the fact that the strem-function profile is smooth and can be fit very well by either method.

The results for $ISP_q = ISP_w = 3$ are the best. The possible explanation is that the stencil of the finite-difference method used in this study is a nine-point 'star' (results from cross-derivative terms) which has the same structure as the proposed modified interpolation with $ISP_q = ISP_w = 3$. Note that the error in u remains the same for the different values of ISP_q and ISP_w used. Here the largest contribution to the errors is from the two uppoer corners and this dominates the calculation of the Eucidean norm.

Acknowledgement

Appendix   Generalization of Bilinear Interpolation for Arbitrary Convex Four-point Cells [15].

Let G be a convex quadrangle (see Fig. A) with the corners (x_i, y_i), i = 1,...,4, and I^2 be a unit square, i.e., $I^2 = [0,1] \times [0,1]$,

In order to assign values $\xi, \eta \in [0,1]$ to every point $(x,y) \in G$, a function T is needed for which

$$T : G \to I^2 , \qquad (x,y) \to T(x,y) = (\xi, \eta)$$

For all linear functions

$$f : \mathfrak{R}^2 \to \mathfrak{R}^2 \quad \text{with} \quad f(x,y) = a\,x + b\,y + c \qquad (a, b, c \in \mathfrak{R}) \tag{1}$$

the following property must hold:

$$f(x,y) = (1 - \xi)(1 - \eta)\, f(x_1, y_1) + \xi(1 - \eta)\, f(x_2, y_2) + \xi \eta\, f(x_3, y_3)$$
$$+ (1 - \xi)\eta\, f(x_4, y_4) \qquad \text{for all } (x,y) \in G \tag{2}$$

With $a, b, c \in \mathfrak{R}$ arbitrary, eq. (2) assures exact approximation of every *linear* function. Here,

$$\eta = \begin{cases} \dfrac{-p + (p^2 + q)^{1/2}}{\left(x_3^s - 1\right)} & \text{for } x_3^s \neq 1. \\[4mm] \dfrac{y^s}{1 + x^s(y_3^s - 1)} & \text{for } x_3^s = 1. \end{cases} \tag{3}$$

and

$$\xi = \frac{x^s}{1 + \eta\,(x_3^s - 1)}$$

with

$$p = \frac{1}{2}\left[\, 1 + x^s(y_3^s - 1) - y^s(x_3^s - 1)\,\right] \quad \text{and} \quad q = y^s(x_3^s - 1)$$

where

$$\begin{pmatrix} x^s \\ y^s \end{pmatrix} = A \begin{pmatrix} x - x_1 \\ y - y_1 \end{pmatrix}, \qquad \begin{pmatrix} x_3^s \\ y_3^s \end{pmatrix} = A \begin{pmatrix} x_3 - x_1 \\ y_3 - y_1 \end{pmatrix}$$

$$A = \begin{pmatrix} x_2 - x_1 & x_4 - x_1 \\ y_2 - y_1 & y_4 - y_1 \end{pmatrix}^{-1}$$

Note that the area-weighting method is included as a special case if G^s is already the unit square, i.e., if $x_3^s = 1$, and $y_3^s = 1$, then $\xi = x^s$, $\eta = y^s$ is implied.

References

1. Saltzman, J. and Brackbill, J. (1982) "Application and Generalizations of Variational Methods for Generating Adaptive Meshes," in Numerical Grid Generation, ed. Thompson, J.F., 865-884, North-Holland, Amsterdam.

2. Nakahashi, K. and Deiwert, G.S. (1986) "Three-Dimensional Adaptive Grid Method," *AIAA J.*, **24, No. 6,** p. 948-954.

3. Anderson, D.A. (1983) "Adaptive Grid Methods for Partial Differential Equations," in Advances in Grid Generation, eds. Ghia, K.N. and Ghia, U., ASME-FED, ASME, New York.

4. Thompson, J.F. (1985) "A Survey of Dynamically Adaptive Grids in the Numerical Solution of Partial Differential Equations," Appli. Numerical Mathematics 1, 3-27.

5. Eiseman, P.R. (1987) "Adaptive Grid Generation," *Computer Methods in Applied Mechanics and Engineering*, **64**, p. 321-376.

6. Mastin, C.W. (1988) "Fast Interpolation Schemes for Moving Grids," in Numerical Grid Generation in Computational Fluid Mechanics '88, eds. Sengupta, S., Hauser, J., Eiseman, P.R., Thompson, J.F., 63-73, Pineridge Press Limited, U.K.

7. Seldner, D. and Westermann, T. (1988) "Algorithms for Interpolation and Localization in Irregular 2D Meshes," *J. Computational Physics*, **79**, p. 1-11.

8. Shepard, D. (1968) "A Two Dimensional Interpolation Function for Irregularly Spaced Data," *Proceedings 23rd National Conference of ACM*, p. 517-523.

9. Gordon, W.J. and Wixom, J.A. (1978) "Shepard's Method of Metric Interpolation to Bivariate and Multivariate Interpolation," *Mathematics of Computation*, **32, No. 141**, p. 253-264.

10. Barnhill, R.E., Dube, R.P., and Little, F.F. (1983) "Properties of Shepard's Surfaces," *Rocky Mountain J. of Mathematics*, **13, No.2**, p. 365-382.

11. Schumaker, L.L. (1976) "Fitting Surfaces to Scattered Data," Approximation Theory 2, eds. Lorentz, G.G., Chui, C.K., and Schumaker, L.L., p. 203-268, Academic Press, New York.

12. Franke, R. and Nielson, C. (1980) "Smooth Interpolation of Large Sets of Scattered Data," *Int'l J. for Numerical Methods in Engineering*, **15**, p. 1691-1704.

13. Renka, R.J. (1988) "Multivariate Interpolation of Large Sets of Scattered Data," *ACM Transactions on Mathematical Software*, **14, No.2**, p. 139-148.

14. Thompson, J.F. (1988) "Some Current Trends in Numerical Grid Generation," in Numerical Grid Generation in Computational Fluid Mechanics '88, eds. Sengupta, S., Hauser, J., Eiseman, P.R., and Thompson, J.F., p. 87-100, Pineridge Press Limited, U.K.

15. Kim, H.J. and Thompson, J.F. (1988) "Three Dimensional Adaptive Grid Generation on a Composite Block Grid," AIAA-88-0311.

16. Thompson, J.F., Warsi, Z.U.A., and Mastin, C.W. 1985 "Numerical Grid Generation:" Foundations and Applications, Chapter 6, North-Holland.

17. Anderson, D.A. and Steinbrenner, J. (1986) "Generating Adaptive Grid with a Conventional Grid Scheme," AIAA-86-0427.

18. Anderson, D.A. (1987) "Equidistribution Schemes, Poisson Generators, and Adaptive Grids," *Applied Mathematics and Computation*, **24**, p. 211-227.

19. Barnhill, R.E. (1977) "Representation and Approximation of Surfaces", in Mathematical Software, **3**, ed. Rice, J.R., p. 69-120, Academic Press, New York.

20. Roache, P.J. (1976) "Computational Fluid Dynamics," (Hermosa Publishers, Albuquerque.

21. Schreiber, R. and Keller, H.B. (1983) "??????????????????," *J. Comput. Phys.*, **49**, p. 165-172.

22. Ghia, U., Ghia, K.N., and Shin, C.T. (1982) "??????????????????," *J. Comput. Phys.*, **48**, p. 387-411.

23. Schreiber, R. and Keller, H.B. (1983) "???????????????????," *J. Comput. Phys.*, **49**, p. 310-333.

24. Briley, W.R. (1971) "A Numerical Study of Laminar Separation Bubbles using the Navier-Stokes Equations," *J. Fluid Mech.*, **47**, **Part 4**, p. 713-736.

25. Stone, H.L. (1968) "Iterative Solution of Implicit Approximations of Multi-Dimensional Partial Differential Equations," *SIAM J. Numer. Anal.*, **5**, **No. 3**, p. 530-558.

26. Schneider, G.E. and Zedan, M. (1981) "A Modified Strongly Implicit Procedure for the Numerical Solution of Field Problems," *Numerical Heat Transfer*, **4**, p. 1-19.

27. Shen, C.Y. and Reed, H.L., in preparation.

28. Chen, K.H., private communication.

29. Benjamin, A.S. and Denny, V.E. (1979) "??????????????????," *J. Comput. Phys.*, **33**, p. 340-358.

30. Anderson, D.A., Tannehill, J.C., and Pletcher, R.H. (1984) "Computational Fluid Mechanics and Heat Transfer," Hemisphere Publishing Corporation, McGraw-Hill Book Company, p. 247-250.
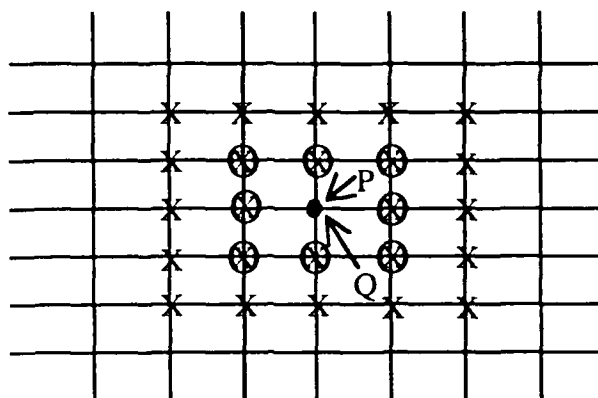
Fig. 1 Grid structure of solution-adaptive methods in logical space for 2-D case.

$$\times \ : \ \mathrm{ISP_q} = 5 \ (\mathrm{N_q} = 24)$$
$$\mathrm{O} \ : \ \mathrm{ISP_w} = 3 \ (\mathrm{N_w} = 9)$$
$$\mathrm{Q} \ : \ (x,y)$$
$$\mathrm{P} \ : \ (x_k,y_k)$$

Fig. 2 Move from P to R.

Fig. 3 Move from C to D.

Fig. 4 Switch from L_1 to L_2.

Fig. 5 Relation between the position of Q and the sign of A.

P_1: (x_1, y_1), P_2: (x_2, y_2), Q: (x_3, y_3)

Fig. 6 Move from C to D.

Fig. 7 Driven cavity.

Fig. A Transformation from G to G^s.

PART 6. RESUME OF H. L. REED

HELEN LOUISE REED

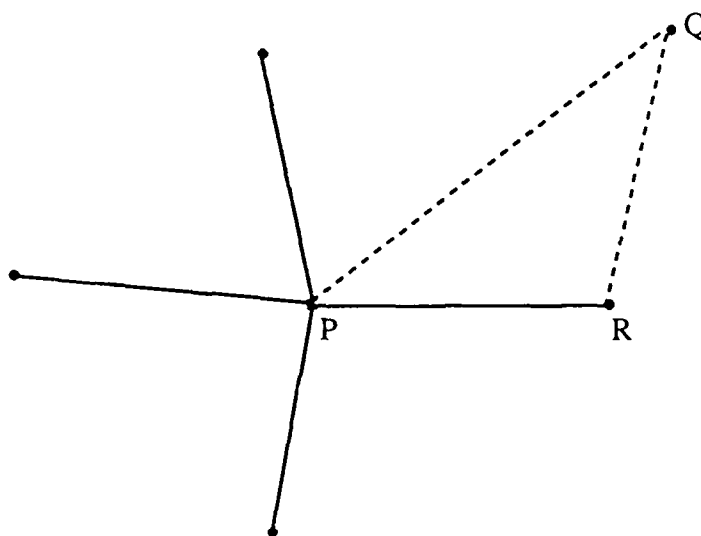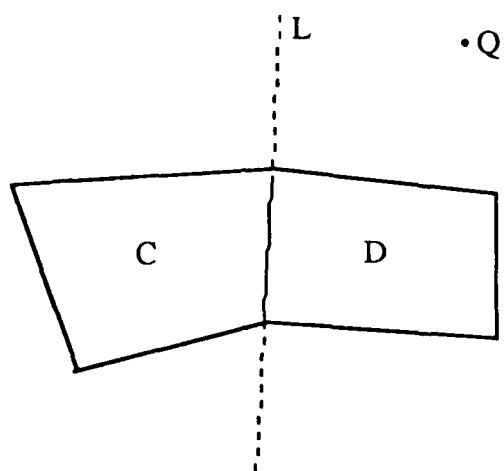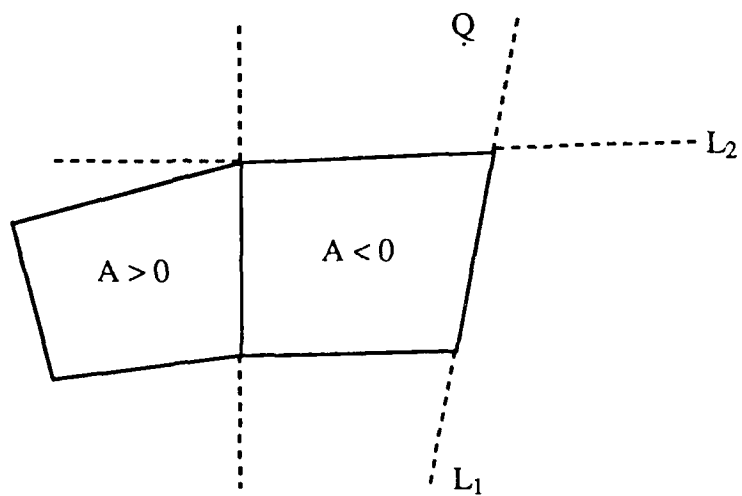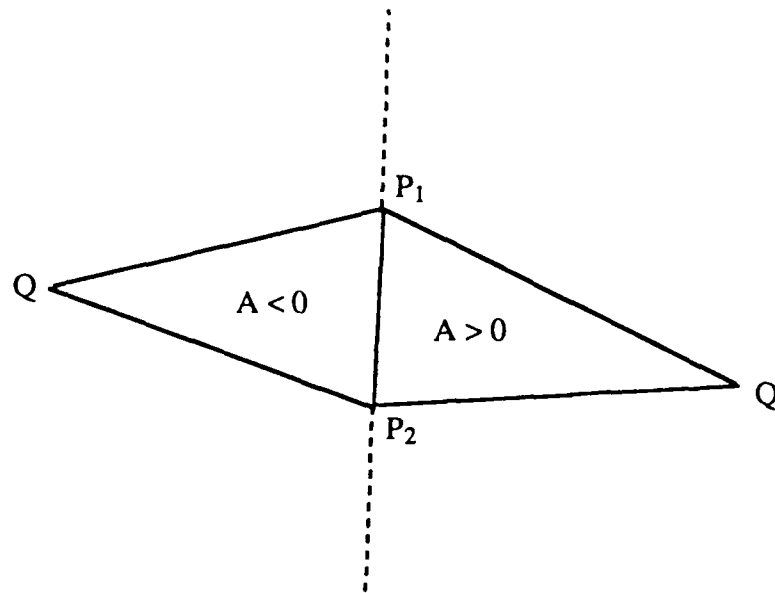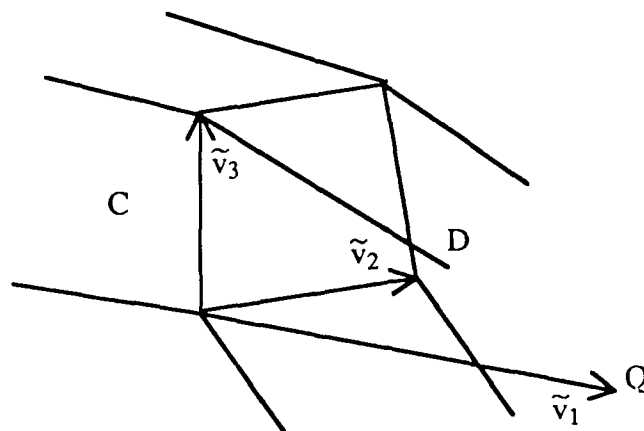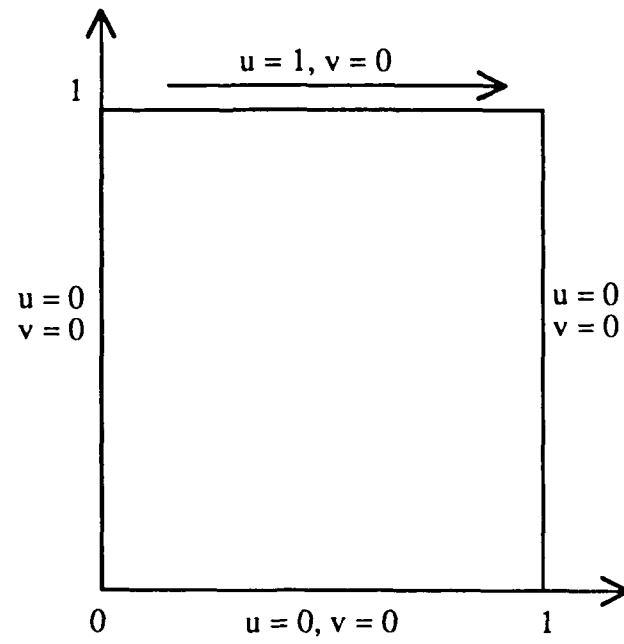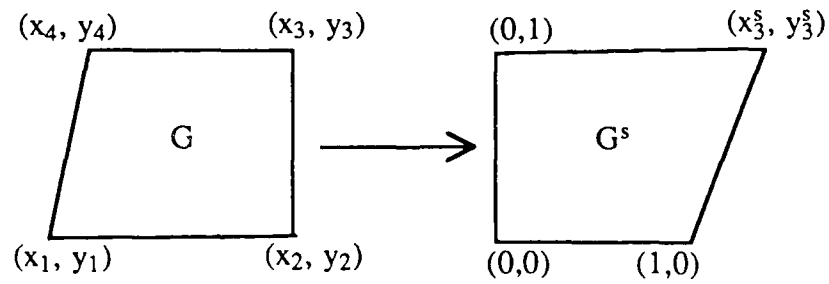Associate Professor, Mechanical and Aerospace Engineering
Arizona State University
Tempe, Arizona 85287-6106
602-965-2823

A. PERSONAL DATA

Date of Birth: October 3, 1956, Havre DeGrace, Maryland, USA
Social Security Number: 215-68-5475
Home: 8425 S. JenTilly Lane, Tempe, Arizona 85284-2425

B. EDUCATION

A.B., Mathematics, Goucher College, May 1977.
   Graduated with general honors and honors in mathematics, GPA 3.98/4.0.
   Graduated in three years via special honors program.
   Thesis: *Limit Cycles of Autonomous Systems of Differential Equations.*
   Advisor: Dr. Dorothy Bernstein.

M.S., Engineering Mechanics, Virginia Polytechnic Institute & State Univ., June 1980.
   GPA 4.0/4.0.
   Thesis: *Closed-Form Solutions for Subsonic Flows over Plates with Porous Strips.*
   Advisor: Dr. Ali Nayfeh.

Ph.D., Engineering Mechanics, Virginia Polytechnic Institute & State Univ., Dec. 1981.
   GPA 4.0/4.0.
   Thesis: *The Tollmien-Schlichting Instability of Laminar Viscous Flows.*
   Advisor: Dr. Ali Nayfeh.

C. EXPERIENCE

August 1985 - present, Associate Professor (Tenure awarded April 1988), Arizona State University.
   Department - Mechanical and Aerospace Engineering.
   Duties - teach fluid mechanics and aerodynamics; research in boundary-layer separation, stability and transition, and laminar flow control; student advisement.

September 1982 - August 1985, Assistant Professor, Stanford University.
   Department - Mechanical Engineering.
   Duties - teach gas dynamics, undergraduate fluid mechanics, mathematics, hydrodynamic stability; research in boundary-layer separation, stability and transition, and laminar flow control; student advisement.

January 1982 - August 1982, Assistant Professor, Virginia Polytechnic Institute & State University.
   Department - Engineering Science and Mechanics.
   Duties - teach undergraduate fluid mechanics; research in boundary-layer transition and laminar flow control, specifically the use of suction in controlling the Tollmien-Schlichting instability; student advisement.

June 1979 - December 1981, Aerospace Technologist (NASA/Langley Research Center) on graduate leave without pay to study for Master's and Ph.D. degrees in Engineering Mechanics at Virginia Polytechnic Institute and State University. Position (June 1979-August 1981): Graduate Research Assistant; position (September 1981-December 1981): Graduate Research Associate.

September 1978 - June 1979, Aerospace Technologist (NASA/Langley Research Center) on graduate leave with pay to study for Master's degree in Engineering Mechanics at Virginia Polytechnic Institute and State University.

June 1977 - September 1978, Aerospace Technologist, NASA/Langley Research Center.
Division - Aeronautical Systems Division.
Chief - A. Nagel
Principal Supervisor - Dr. Werner Pfenninger, Chief Scientist.
Duties - design of supercritical laminar flow control (LFC) airfoils; investigation of induced drag associated with a modular system of aircraft; supervise co-op students also assigned to these projects.

Summer 1976, Mathematics Aid, NASA/Langley Research Center.
Division - Subsonic Transonic Aerodynamics Division.
Branch - Dynamic Stability.
Principal Supervisor - Claude Patterson.
Duties - support experimental research investigating the effect of wing-tip vortices of large aircraft on small following aircraft and the attenuation of such vortices.

OTHER EXPERIENCE

July 1984 - August 1984, NASA/Langley Research Center, Hampton, VA
Office - Aircraft Energy Efficiency Office (ACEE)
Supervisor - Mr. D.V. Maddalon
Duties - Consult on and develop computer code to predict effects of disturbance-wave interactions in support of variable-sweep, laminar-flow control flight tests (JETSTAR).

July 1983 - August 1983, Summer University Faculty, Sandia National Laboratories, Albuquerque, NM
Division - Applied Mathematics Division
Supervisor - Dr. M.R. Scott
Duties - Work on problems of boundary-layer stability and disturbance interactions.

D. CONSULTING

D.1 Past

September 1981 - December 1981, International Consultants in Science and Technology, Inc. Developed a computer code for Westinghouse Electric and Naval Underwater Sea Center, optimizing suction strip configuration on axisymmetric bodies using linear triple-deck theory; supervise two computer science students.

D.2 Current

ICASE, NASA/Langley Research Center

Pratt and Whitney. Develop compressible, axisymmetric stability code for inlet design.

E. PROFESSIONAL ACTIVITIES

E.1 Scientific and Professional Societies

Member, American Academy of Mechanics
Member, American Institute of Aeronautics and Astronautics (AIAA)
Member, American Physical Society (APS)
Member, American Society for Engineering Education (ASEE)
Associate Member, American Society of Mechanical Engineers (ASME)
Member, International Association for Computational Mechanics (IACM)
Member, Mathematical Association of America (MAA)
Member, Sigma Xi
Member, Society for Industrial and Applied Mathematics (SIAM)

E.2 Service to the Profession

National

1. Associate Editor, *Annual Review of Fluid Mechanics*, 1986-Present. With the work divided equally among Milton Van Dyke, John Lumley and myself, we are responsible for complete selection, refereeing, and editorial correction of all articles in each yearly volume.

2. Technical Chairperson, *AIAA 19th Fluid, Plasma Dynamics, and Lasers Conference*, Honolulu, June 1987.

3. Co-Chairperson, with Dan Jankowski, *44th Annual American Physical Society/Division of Fluid Dynamics Meeting*, Scottsdale, November 1991.

4. Originator of *Annual Picture Gallery of Fluid Motions* at annual meetings of the *American Physical Society*, November, 1983, Houston. Responsibility for the gallery at *American Physical Society* meeting at Brown University, November 1984; Eugene, November 1987; Buffalo, November 1988; Palo Alto, November 1989.

5. Member of *U.S. National Transition Study Group* under the direction of Eli Reshotko, 1984-Present.

6. Member of *AIAA Technical Committee on Fluid Dynamics*, 1984-1989. APS/AIAA and ASME-AMD/AIAA Liaison. Prepared *Aerospace Audit* article for Fluid Dynamics, *Aerospace America*, December 1988 (did not appear because of difficulties between Technical Committee and editors).

7. Member of *Fluid Mechanics Technical Committee* of the *Applied Mechanics Division of the ASME*, 1984-Present.

8. Member of Steering Committee for *National Fluid Dynamics Congress*, June 1988-Present.

9. University Representative of *National Science Foundation Workshop on Engineering Fluid Mechanics-Future Directions in Fluid Mechanics.* Group Leader and Coordinator of final document for Unsteady Flow Panel, Savannah, September 17-20, 1986.

10. Chairperson of *ASME Junior Awards Committee* 1989-Present. Vice-Chairperson 1987-1988.

11. Member of Scientific Committee of 1992-3 IUTAM Symposium on *Nonlinear Stability of Nonparallel Flows*, January 1990-Present.

12. Organizer of *Transition Simulation Olympics* to be held at *National Fluid Dynamics Congress*, Summer 1992.

13. Co-Organizer with Dr. Daniel Reda (Sandia National Laboratories) of *Symposium on Experimental and Theoretical/Numerical Studies of Boundary-Layer Stability and Transition*, to be held at the *First Joint ASME/JSME Fluids Engineering Conference*, Portland, June 23-26, 1991.

14. Organizer of sessions on *Numerical Methods in Transition Simulation* for *1st U.S. National Congress on Computational Mechanics*, Chicago, July 21-24, 1991.

15. Judge for AIAA Student Paper Competition, Reno, January 1987.

16. Chaired workshop on "Transition Prediction Models, Code Development, and Verification" at *NASA/Lewis Symposium on Transition in Turbines*, Cleveland, May 15-16, 1984.

17. Chaired Fluid Mechanics session at *21st Annual Meeting of the Society of Engineering Science, Inc.*, Virginia Polytechnic Institute and State University, October 15-17, 1984.

18. Chaired session at the *Fall 1985 Meeting of the Society for Industrial and Applied Mathematics*, Arizona State University, October 1985.

19. Puzzlemaker on "Three-Dimensional Basic States" for *International Workshop on Stability and Transition in Bounded Shear Flows*, Tucson, November 22-23, 1985.

20. Chaired Fluid Dynamics session at *AIAA 1986 Aerospace Sciences Meeting*, Reno, January 6-9, 1986.

21. Chaired Fluid Dynamics session at *AIAA/ASME Joint Fluid Mechanics/Plasma Dynamics and Lasers Conference*, Atlanta, May 12-14, 1986.

22. Chaired Boundary Layer Stability session at *39th Annual Meeting of the American Physical Society/Division of Fluid Dynamics*, Columbus, November 23-25, 1986.

23. Moderated *National Science Foundation Workshop on Engineering Fluid Mechanics-Future Directions in Fluid Mechanics, Winter Annual Meeting of ASME*, Anaheim, December 7-12, 1986.

24. Chaired Fluid Dynamics session at *AIAA 19th Fluid Dynamics, Plasma Dynamics, and Lasers Conference*, Honolulu, June 8-10, 1987.

25. Organized Stability and Transition session for *National Fluid Dynamics Conference,* Cincinnati, June 1988.

26. Chaired Fluid Dynamics session at *AIAA 1989 Aerospace Sciences Meeting,* Reno, January 1989.

27. Chaired Computational Fluid Dynamics session at *3rd IUTAM Symposium on Laminar-Turbulent Transition,* Toulouse, September 1989.

28. Chaired Boundary Layer Receptivity session at *42th Annual Meeting of the American Physical Society/Division of Fluid Dynamics,* Palo Alto, November 1989.

29. Chaired Boundary-Layer Stability session at *3rd International Congress of Fluid Mechanics,* Cairo, January 1990.

30. Chaired Theoretical Fluid Mechanics session at *Eleventh U.S. National Congress of Applied Mechanics,* Tucson, May 1990.

31. Chaired Stability and Transition session at *AIAA 21st Fluid Dynamics, Plasmadynamics and Lasers Conference,* Seattle, June 18-20, 1990.

32. Referee journal articles for *Physics of Fluids, Journal of Fluid Mechanics, Journal of Fluids Engineering, AIAA Journal,* and *Fluid Dynamics Research (The Japan Society of Fluid Mechanics)* and proposals for the National Science Foundation.

Local

1. Chairperson, *2nd Arizona Fluid Mechanics Conference,* Arizona State University, April 4-5, 1986.

2. Chaired session at *3rd Arizona Fluid Mechanics Conference,* University of Arizona, February 20-21, 1987.

3. Chaired session at *5th Arizona Fluid Mechanics Conference,* University of Arizona, February 17-18, 1989.

E.3 Honors and Recognitions

Phi Kappa Phi
Phi Beta Kappa
Merit Scholarship from the State of Maryland, 1974
Recipient of a NASA fellowship, 1976
Outstanding Summer Employee Award from NASA/Langley Research Center, 1976
Torrey Award for Excellence in Mathematics, Goucher College, 1977
Outstanding Achievement Award from NASA/Langley Research Center, 1978
Listed in *Who's Who in American Colleges and Universities*
Cunningham Fellowship Award from Virginia Polytechnic Institute & State University, 1981
Presidential Young Investigator Award, National Science Foundation, 1984
Winner *4th Annual Picture Gallery of Fluid Motions* at the *39th Annual Meeting of the American Physical Society/Division of Fluid Dynamics,* Columbus, November 1986.
American Academy of Mechanics, 1988
AIAA Excellence in Teaching Award, Arizona State University, Fall 1988
Professor of the Year, Pi Tau Sigma, Arizona State University, 1988-1989

E.4 Current Fields of Interest

Separated and Transitional Flows, Unsteady Flows, Hypersonics, Supersonics, Hydrodynamic Stability, Laminar Flow Control, Three-Dimensional Boundary Layers, Aerodynamics, Computational Fluid Mechanics, Perturbation Methods.

F. TEACHING

F.1 Arizona State University

Awards

AIAA Excellence in Teaching Award, Arizona State University, Fall 1988
Professor of the Year, Pi Tau Sigma, Arizona State University, 1988-1989

Post Doctoral Associates Supervised

H. Haj-Hariri, "Spatial Simulation of Transition," completed Spring 1988.

P. Balakumar, "Stability of Three-Dimensional Supersonic Boundary Layers," completed Spring 1989.

E. Tuliszka-Sznitko, "High-Frequency Breakdown of Three-Dimensional Boundary Layers," completed Spring 1990.

Ph.D. Students Supervised

C.Y. Shen, "Numerical Simulation of Three-Dimensional Unsteady Separation at Low Reynolds Numbers," expected Summer 1990.

G. Stuckert, "Stability of Hypersonic Boundary-Layer Flows," expected Summer 1990.

R.S. Lin, "The Crossflow Instability in Swept-Wing Flows," expected Spring 1991.

T. Buter, "Receptivity of Boundary-Layer Flows to Freestream Vorticity," expected Spring 1992.

N. Lin, "Receptivity of Boundary-Layer Flows to Freestream Acoustic Disturbances," expected Spring 1992.

C. Lu, "The Effect of Initial Conditions and Active Control on Transition in a Flat-Plate Boundary Layer," expected Spring 1992.

MS Students Supervised

G. Stuckert, "Hypersonic Viscous Flow over Two-Dimensional and Axisymmetric Bodies," completed Spring 1987.

N. Lin, "Receptivity of the Boundary Layer on a Semi-Infinite Flat Plate with an Elliptic Leading Edge," completed Fall 1989.

R. Holz, "The No Tail Rotor," McDonnell-Douglas Fellow, expected Summer 1990.

B. Toppel, "Numerical Simulation of Two-Dimensional Unsteady Separation at Low Reynolds Numbers," expected Summer 1990.

T. Haynes, "Stability of Three-Dimensional Supersonic Boundary Layers," expected Spring 1991.

T. Trekas, "Attachment-Line Instabilities in High-Speed Flows," Garrett Fellow, expected Spring 1991.

Senior Projects Supervised

T. Haynes, "Stability of Boundary-Layer Flows," completed Fall 1988.

P. Flynn, "AERO DESIGN '89: SAE International Remotely Controlled Cargo Aircraft Competition," completed Spring 1989, *Prize-winner at the competition in Missouri.*

G. Loring, "Secondary Instabilities in Three-Dimensional Boundary Layers," completed Summer 1989.

T. Taylor, "Stability of High-Speed Flows," completed Summer 1989.

H. Phouybanhdyt, "Formula SAE Competition: Development of a Small Formula-Style Racing Car," completed Spring 1990.

T. Wolcott, "Formula SAE Competition: Development of a Small Formula-Style Racing Car," completed Spring 1990.

Ph.D. Reading Committees

G. Abdy, I. DeSilva, M. Mousseux

MS Reading Committees

J. Hoos, S. Kersey, T. Kincheloe, M. Mousseux, P. Pupator, T. Vincent, D. Wang

Staff Supervised

Ms. Jane Hawthorne, Administrative Assistant I, Jun 86-Sept 87
Dr. P. Balakumar, Visiting Faculty Associate, Jan 87-Jun 89
Dr. H. Haj-Hariri, Visiting Faculty Associate, Feb 87-Jun 88
Ms. Sue Johnson, Office Assistant, Feb 87-Apr 88
Mr. David Alvarez, Computer Assistant, Sept 87-Jan 88
Ms. Myrna Pena, Administrative Assistant II, Nov 87-Feb 90
Ms. Tracy Jensen, Office Assistant, Apr 88-Pres
Dr. E. Tuliszka-Sznitko, Visiting Faculty Associate, Jan 90-Apr 90
Ms. Christine Petiford, Administrative Assistant II, Apr 90-Pres
Ms. Media Petraglia, Office Assistant, Apr 90-Pres

Committees (Arizona State University)

University:

Faculty Women's Association Executive Board (1989-1990)

College of Engineering and Applied Sciences:

Affirmative Action (1985-1990)
1988-89 Active member of 7 Search Committees for Computer Science
and 2 Search Committees for Industrial Engineering
1989-90 Active member of 1 Search Committee for Agribusiness

Mechanical and Aerospace Enginee.ing:

Ph.D. Qualifying Examination in Mathematics (1985-1986)
Aerospace Curriculum Committee (1985-1987)
Undergraduate Affairs Committee (1985-1987)
Ph.D. Qualifying Examination in Fluid Mechanics (1986-1987, 1988-1989)
Department-Chair Search Committee (1987-1988)
Seminar Committee (1988-1989)
Development Committee Chair (1988-1990)
Heat-Transfer Search Committee (1988-1989)
Faculty Lounge Committee (1988-1989)
Aerospace Center of Excellence Committee (1988-1989)

Service

Recruited Dr. Valana Wells, Assistant Professor in Aerospace Engineering
Developed junior-level course, Aerodynamics I
Coordinated 3 junior/senior-level courses, Aerodynamics I, Gasdynamics, Aerodynamics II
for Aerospace Accreditation (1988)

F.2 Stanford University

Ph.D. Students Supervised

B. Singer, "Numerical Simulation of Transition to Turbulence in a Channel," completed Spring 1987.

R. Henk, "Fundamental Studies of Three-Dimensional Unsteady Separation at Low Reynolds Numbers," completed Spring 1990.

Ph.D. Reading Committees

B. Afshari, T. Cheung, R. Strawn, V. Wells

Committees

University:

> Academic Council
> Freshman Advisor (1983-1985)

College of Engineering:

> Undergraduate Council (1983-1985)
> Women in Science and Engineering (WISE) Advisor (1984-85)

Mechanical Engineering:

> Undergraduate Advising Committee (1982-1983)
> Graduate Admissions Committee (1983-1985)

F.3 Virginia Polytechnic Institute and State University

Ph.D. Committee: J.R. Dagenhart
Staff Supervised: R. Eskelund, B. Wong (two computer science students)

G. SCHOLARLY AND CREATIVE CONTRIBUTIONS

G.1 Publications

Refereed

1. "Flow over Plates with Suction through Porous Strips," A.H. Nayfeh, H.L. Reed, and S.A. Ragab, *AIAA Journal*, Volume 20, Number 5, Page 587, May 1982.

2. "Stability of Flow over Axisymmetric Bodies with Porous Suction Strips," A.H. Nayfeh and H.L. Reed, *Physics of Fluids*, Volume 28, Number 10, Page 2990, October 1985.

3. "Numerical-Perturbation Technique for Stability of Flat-Plate Boundary Layers with Suction," H.L. Reed and A.H. Nayfeh, *AIAA Journal*, Volume 24, Number 2, Page 208, February 1986.

4. "Effect of Suction and Weak Mass Injection on Boundary-Layer Transition," W.S. Saric and H.L. Reed, *AIAA Journal*, Volume 24, Number 3, Page 383, March 1986.

5. "Flow over Bodies with Suction through Porous Strips," A.H. Nayfeh, H.L. Reed, and S.A. Ragab, *Physics of Fluids*, Volume 29, Number 7, Page 2042, July 1986.

6. "Wave Interactions in Swept-Wing Flows," H.L. Reed, *Physics of Fluids*, Volume 30, Number 11, Page 3419, November 1987.

7. "Stability of Three-Dimensional Boundary Layers," H.L. Reed and W.S. Saric, *Annual Review of Fluid Mechanics*, Volume 21, Page 235, January 1989.

8. "Numerical Simulations of Transition in Oscillatory Plane Channel Flow," B.A. Singer, J.H. Ferziger, and H.L. Reed, *Journal of Fluid Mechanics*, Volume 208, Page 45, 1989.

9. "The Effects of Streamwise Vortices on Transition in the Plane Channel," B.A. Singer, H.L. Reed and J.H. Ferziger, *Physics of Fluids A,* Volume 1, Number 12, Page 1960, December 1989.

10. "Compressible Boundary-Layer Stability Theory," H.L. Reed and P. Balakumar, in press *Physics of Fluids A,* July 1990.

11. "An Application of Geometric Deformations Using Triparametric Volumes to Approximate Fluid Flow," S. Kersey, M. Henderson, H.L. Reed, and R. Barnhill, accepted *Computers and Fluids.*

12. "Stability of Three-Dimensional Supersonic Boundary Layers," P. Balakumar and H.L. Reed, accepted *Physics of Fluids A.*

Books Edited

1. *Annual Review of Fluid Mechanics* (edited by M. VanDyke, J. Lumley, and H. Reed), Volume 19, 1987.

2. *Annual Review of Fluid Mechanics* (edited by M. VanDyke, J. Lumley, and H. Reed), Volume 20, 1988.

3. *Annual Review of Fluid Mechanics* (edited by M. VanDyke, J. Lumley, and H. Reed), Volume 21, 1989.

4. *Annual Review of Fluid Mechanics* (edited by M. VanDyke, J. Lumley, and H. Reed), Volume 22, 1990.

Reviewed Papers

Invited

1. "Stability and Transition of Three-Dimensional Flows," H.L. Reed and W.S. Saric, *Invited Paper,* in *Proceedings of the Tenth U.S. National Congress of Applied Mechanics,* ASME, New York, 1987.

2. "Stability of Three-Dimensional Boundary Layers," H.L. Reed, *Invited Paper, SAE 871857, AEROTECH '87 (Aerospace Technology Conference and Exposition),* Long Beach, October 5-8, 1987.

3. "Stability and Transition of Three-Dimensional Boundary Layers," W.S. Saric and H.L. Reed, *Invited Paper,* AGARD Conference Number 438, *Fluid Dynamics of Three-Dimensional Turbulent Shear Flows and Transition,* Cesme, Turkey, October 1988.

4. "Supersonic/Hypersonic Laminar/Turbulent Transition," H.L. Reed, G.K. Stuckert, and P. Balakumar, *Invited Paper,* in *Developments in Mechanics,* Volume 15, *Proceedings of the 21st Midwestern Mechanics Conference,* August 13-16, 1989.

5. "Boundary-Layer Receptivity: Navier-Stokes Computations," H.L. Reed, N. Lin, and W.S. Saric, *Invited Paper,* in *Proceedings of the Eleventh U.S. National Congress of Applied Mechanics,* ASME, New York, 1990.

6. "Navier-Stokes Simulations of Boundary-Layer Receptivity," H.L. Reed, *Keynote Speaker, 22nd Turbulence Symposium*, National Aerospace Laboratory, Tokyo, July 25-27, 1990.

Other

1. "Design Considerations of Advanced Supercritical Low Drag Suction Airfoils," W. Pfenninger, H.L. Reed, and J.R. Dagenhart, *Viscous Flow Drag Reduction, AIAA Progress in Astronautics and Aeronautics Series*, Volume 72, 1980.

2. "Flow over Plates with Suction through Porous Strips," A.H. Nayfeh, H.L. Reed, and S.A. Ragab, *AIAA Paper 80-1416*.

3. "Stability of Flow over Plates with Porous Suction Strips," H.L. Reed and A.H. Nayfeh, *AIAA Paper 81-1280*.

4. "Stability of Compressible Three-Dimensional Boundary Layer Flows," H.L. Reed and A.H. Nayfeh, *AIAA Paper 82-1009*.

5. "Stability of Flow over Axisymmetric Bodies with Porous Suction Strips," A.H. Nayfeh and H.L. Reed, *AIAA Paper 82-1025*.

6. "Effect of Suction and Weak Mass Injection on Boundary-Layer Transition," W.S. Saric and H.L. Reed, *AIAA Paper 83-0043*.

7. "Wave Interactions in Swept-Wing Flows," H.L. Reed, *AIAA Paper 84-1678*.

8. "An Analysis of Wave Interactions in Swept-Wing Flows," H.L. Reed, *2nd IUTAM Symposium on Laminar-Turbulent Transition*, ed. V.V. Kozlov and V. Ya Levchenko. Springer-Verlag, New York, 1985.

9. "Disturbance-Wave Interactions in Flows with Crossflow," H.L. Reed, *AIAA Paper 85-0494*.

10. "Investigation of the Effects of Initial Disturbances on Plane-Channel Transition," B.A. Singer, H.L. Reed, and J.H. Ferziger, *AIAA Paper 86-0433*.

11. "An Analysis of Unsteady, Two-Dimensional Separation Bubbles," H.L. Reed and L.K. Pauley, in *Proceedings of the Royal Aeronautical Society Conference on Aerodynamics at Low Reynolds Numbers*, London, October 15-18, 1986.

12. "Effect of Streamwise Vortices on Transition in Plane Channel Flow," B.A. Singer, H.L. Reed and J.H. Ferziger, *AIAA Paper 87-0048*.

13. "Numerical Simulation of Transition in a Decelerating Boundary Layer," K.S. Yang, P.R. Spalart, H.L. Reed, and J.H. Ferziger, *IUTAM Symposium on Turbulence Management and Relaminarization*, ed. R. Narasimha and H. Liepmann, Springer-Verlag, New York, 1987.

14. "Three-Dimensional Stability of Boundary Layers," W.S. Saric and H.L. Reed, in *Perspectives in Turbulence Studies*, ed. H.U. Meier and P. Bradshaw, Springer-Verlag, New York, 1987.

15. "Local Intermodal Energy Transfer of Secondary Instabilities in the Plane Channel," B.A. Singer, P.R. Spalart, J.H. Ferziger, and H.L. Reed, *AIAA Paper 87-1202*.

16. "Unsteady Separation at Low Reynolds Numbers," H.L. Reed, *ASME Forum on Unsteady Separation*, Cincinnati, June 1987.

17. "Experiments on an Unsteady, Three-Dimensional Separation," R.W. Henk, W.C. Reynolds, and H.L. Reed, in *Proceedings of the Second AFOSR Workshop on Unsteady Separated Flows*, USAF, Colorado, July 28-29, 1987.

18. "Numerical Simulations of Transition with an Oscillating Mean Flow," B.A. Singer, J.H. Ferziger, and H.L. Reed, *AIAA Paper 88-0406*.

19. "A Method to Determine the Performance of Low-Reynolds-Number Airfoils Under Off-Design Unsteady Freestream Conditions," H.L. Reed and B.A. Toppel, *Low Reynolds Number Aerodynamics Conference*, Notre Dame, June 5-7, 1989; in *Lecture Notes in Engineering*, Springer-Verlag, New York, 1989.

20. "Stability of High-Speed Chemically Reacting and Three-Dimensional Boundary Layers," H.L. Reed, G.K. Stuckert, and P. Balakumar, *3rd IUTAM Symposium on Laminar-Turbulent Transition*, Toulouse, ed. R. Michel and D. Arnal, Springer-Verlag, New York, to be published, 1990.

21. "Boundary Layer Receptivity: Computations," N. Lin, H.L. Reed, and W.S. Saric, *Third International Congress of Fluid Mechanics*, Cairo, January 1990.

22. "Experiments on an Unsteady, Three-Dimensional Separation," R.W. Henk, W.C. Reynolds, and H.L. Reed, *Workshop on the Physics of Forced Unsteady Separation*, NASA/Ames Research Center, April 1990.

23. "Stability Limits of Supersonic Three-Dimensional Boundary Layers," H.L. Reed, T. Haynes, and P. Balakumar, *AIAA Paper 90-1528*.

24. "Stability of Chemically Reacting, Hypersonic, Viscous Flows," G.K. Stuckert and H.L. Reed, *AIAA Paper 90-1529*.

25. "Multiple-Jet Circulation Control Airfoils with Large Coanda Surfaces," R.G. Holz, A.A. Hassan, and H.L. Reed, submitted to *1991 AIAA Aerospace Sciences Meeting*, Reno, January 1991.

Other

1. "Design Considerations of Transonic LFC Airfoils with Practically Full Chord Laminar Flow," W. Pfenninger and H.L. Reed, in *Langley Research Center Basic Research Review*, April 1978.

2. "The Stability of Boundary Layers with Porous Suction Strips: Experiment and Theory," G.A. Reynolds, W.S. Saric, H.L. Reed, and A.H. Nayfeh, in *Proceedings ACEE Project Oral Status Review*, Dryden Flight Research Center, September 1981.

3. "Report of Computational Group," H.L. Reed, in *Transition in Turbines, NASA CP 2386*, NASA/Lewis Research Center, May 1984.

4. "Gallery of Fluid Motions," H.L. Reed, *Physics of Fluids*, Volume 28, Number 9, Page 2631, September 1985.

5. "Gallery of Fluid Motions," H.L. Reed, *Physics of Fluids*, Volume 29, Number 9, Page 2769, September 1986.

6. "Fluids Engineering Workshop Unsteady-Flow Subgroup Final Report," H.L. Reed et al. (Prepared and edited: H.L. Reed), *National Science Foundation Workshop on Engineering Fluid Mechanics-Future Directions in Fluid Mechanics*, Savannah (September 1986), December 1986.

7. "Gallery of Fluid Motions," H.L. Reed, *Physics of Fluids*, Volume 30, Number 9, Page 2597, September 1987.

8. "Gallery of Fluid Motions," H.L. Reed, *Physics of Fluids*, Volume 31, Number 9, Page 2383, September 1988.

9. "Gallery of Fluid Motions," H.L. Reed, *Physics of Fluids* A, Volume 1, Number 9, Page 1439, September 1989.

10. "Receptivity of the Boundary Layer on a Semi-Infinite Flat Plate with an Elliptic Leading Edge," N. Lin, H.L. Reed, and W.S. Saric, Arizona State University, *ASU CR-R 90006*, September 1989.

11. "Gallery of Fluid Motions," H.L. Reed, *Physics of Fluids* A, Volume 2, Number 9, September 1990.

Publications Submitted

1. "A Shear-Adaptive Solution of the Spatial Stability of Flat-Plate Boundary Layers with Natural Outflow Conditions," H. Haj-Hariri and H.L. Reed, in preparation.

2. "Shepard's Interpolation for Solution-Adaptive Methods," C.-Y. Shen and H.L. Reed, in preparation.

3. "Spatial Simulation of Boundary-Layer Transition," H.L. Reed, *Invited paper*, in preparation for *Applied Mechanics Review*.

G.2 Presentations by H. Reed

Conference Presentations

1. "Stability of Flow over Plates with Porous Suction Strips," H.L. Reed and A.H. Nayfeh, *AIAA 14th Fluid and Plasma Dynamics Conference*, Palo Alto, *AIAA Paper 81-1280*, June 23-25, 1981.

2. "Stability of Compressible Three-Dimensional Boundary-Layer Flows," H.L. Reed and A.H. Nayfeh, *AIAA/ASME Conference*, St. Louis, *AIAA Paper 82-1009*, June 7-11, 1982.

3. "Stability of Flow over Axisymmetric Bodies with Porous Suction Strips," A.H. Nayfeh and H.L. Reed, *AIAA/ASME 3rd Joint Thermophysics, Fluids, Plasma and Heat Transfer Conference*, St. Louis, *AIAA Paper 82-1025*, June 7-11, 1982.

4. "Experiments on the Stability of the Flat-Plate Boundary Layer with Suction," G.A. Reynolds and W.S. Saric, *AIAA/ASME 3rd Joint Thermophysics, Fluids, Plasma and Heat Transfer Conference*, St. Louis, Missouri, *AIAA Paper 82-1026*, June 7-11, 1982.

5. "Boundary Layer Stability - Recent Developments," H.L. Reed, Seminar in Fluid Mechanics, Stanford, November 2, 1982.

6. "Nonparallel Stability of Compressible Three-Dimensional Boundary-Layer Flows," H.L. Reed and A.H. Nayfeh, *35th Meeting of the American Physical Society, Division of Fluid Dynamics*, Rutgers, *Bulletin American Physical Society*, Volume 27, Number 9, Page 1188, November 21-23, 1982.

7. "Plans for Transition Research," H.L. Reed, *1983 Meeting of the Stanford Thermosciences Affiliates*, Stanford, January 24, 1983.

8. "Wave Interactions in Swept-Wing Flows," H.L. Reed, NASA/Langley Research Center, June 13, 1984.

9. "Wave Interactions in Swept-Wing Flows," H.L. Reed, *AIAA 17th Fluid Dynamics, Plasma Dynamics and Lasers Conference*, Snowmass, *AIAA Paper 84-1678*, June 25-27, 1984.

10. "Wave Interactions in Swept-Wing Flows," H.L. Reed, *2nd IUTAM Symposium on Laminar-Turbulent Transition*, Novosibirsk, USSR, July 9-13, 1984.

11. "Crossflow/Tollmien-Schlichting Interactions in Swept-Wing Flows," H.L. Reed, *37th Meeting of the American Physical Society, Division of Fluid Dynamics*, Providence, *Bulletin American Physical Society*, Volume 29, Number 9, Page 1554, November 18-20, 1984.

12. "Disturbance-Wave Interactions in Flows with Crossflow," H.L. Reed, *AIAA 23rd Aerospace Sciences Meeting*, Reno, *AIAA Paper 85-0494*, January 14-17, 1985.

13. "Disputed Results in Compressible Boundary-Layer Stability Theory," H.L. Reed, *38th Meeting of the American Physical Society, Division of Fluid Dynamics*, Tucson, *Bulletin American Physical Society*, Volume 30, Number 10, Page 1709, November 24-26, 1985.

14. "Effect of Streamwise Vorticity on Plane-Channel Transition," B.A. Singer, H.L. Reed, and J.H. Ferziger, *2nd Annual Arizona Fluid Mechanics Meeting*, Arizona State University, April 4-5, 1986.

15. "An Analysis of Unsteady, Two-Dimensional Separation Bubbles," H.L. Reed and L.K. Pauley, *Royal Aeronautical Society Conference on Aerodynamics at Low Reynolds Numbers*, London, October 15-18, 1986.

16. "The Future of Unsteady-Flow Research," H.L. Reed et al., *National Science Foundation Workshop on Engineering Fluid Mechanics-Future Directions in Fluid Mechanics, Winter Annual Meeting of ASME*, Anaheim, December 7-12, 1986.

17. "Numerical Simulation of Transition in a Decelerating Boundary Layer", K.S. Yang, P.R. Spalart, H.L. Reed, and J.H. Ferziger, *IUTAM Symposium on Turbulence Management and Relaminarization*, Bangalore, India, January 19-23, 1987.

18. "Effect of Streamwise Vorticity on Plane-Channel Transition," B.A. Singer, H.L. Reed, and J.H. Ferziger, *3rd Arizona Fluid Mechanics Conference*, University of Arizona, February 20-21, 1987.

19. "Numerical Simulation of Transition in a Decelerating Boundary Layer", K.S. Yang, P.R. Spalart, H.L. Reed, and J.H. Ferziger, *3rd Arizona Fluid Mechanics Conference*, University of Arizona, February 20-21, 1987.

20. "Unsteady Separation at Low Reynolds Numbers," H.L. Reed, *ASME Forum on Unsteady Separation*, Cincinnati, June 1987.

21. "A Method to Determine the Performance of Low-Reynolds-Number Airfoils Under Off-Design Unsteady Freestream Conditions," H.L. Reed and B.A. Toppel, *Low Reynolds Number Aerodynamics Conference*, Notre Dame, June 5-7, 1989; in *Lecture Notes in Engineering*, Springer-Verlag, New York, 1989.

22. "Stability of High-Speed Chemically Reacting and Three-Dimensional Boundary Layers," H.L. Reed, G.K. Stuckert, and P. Balakumar, *3rd IUTAM Symposium on Laminar-Turbulent Transition*, Toulouse, ed. R. Michel and D. Arnal, Springer-Verlag, New York, to be published, 1990.

23. "Stability of High-Speed Chemically Reacting and Three-Dimensional Boundary Layers," H.L. Reed, ICASE, NASA/Langley Research Center, October 31, 1989.

24. "Receptivity of the Boundary Layer on a Semi-Infinite Flat Plate with an Elliptic Leading Edge," H.L. Reed, ICASE, NASA/Langley Research Center, October 31, 1989.

25. "Boundary Layer Receptivity: Computations," N. Lin, H.L. Reed, and W.S. Saric, *Third International Congress of Fluid Mechanics*, Cairo, January 1990.

26. "Stability Limits of Supersonic Three-Dimensional Boundary Layers," H.L. Reed, T. Haynes, and P. Balakumar, *AIAA 21st Fluid Dynamics, Plasmadynamics and Lasers Conference, AIAA Paper 90-1528*, Seattle, June 18-20, 1990.

Invited Seminars By H. Reed

1. "An Analysis of Instabilities in Laminar Viscous Flows," H.L. Reed, *Invited Seminar* in Applied Mathematics, Sandia National Laboratories, Albuquerque, August 3, 1983.

2. "The Effect of Suction and Blowing on Boundary Layer Transition," W.S. Saric and H.L. Reed, *Invited*, Applied Mechanics Seminar, University of Southern California, February 8, 1984.

3. "The Effect of Suction and Blowing on Boundary Layer Transition," W.S. Saric and H.L. Reed, *Invited*, Fluid Mechanics Seminar, California Institute of Technology,April 25, 1984.

4. "Wave Interactions in Swept-Wing Flows," H.L. Reed, *Invited Paper, 21st Annual Meeting of the Society of Engineering Science, Inc.*, Virginia Polytechnic Institute and State University, Blacksburg, Virginia, October 15-17, 1984.

5. "Disturbance-Wave Interactions in Flows with Crossflow," H.L. Reed, *Invited*, Fluid Mechanics Seminar, University of California at Berkeley, February 28, 1985.

6. "Stability and Transition of Three-Dimensional Flows," H.L. Reed and W.S. Saric, *Invited Talk, 10th U.S. National Congress of Applied Mechanics*, Austin, Texas, June 16-20, 1986.

7. "Computational Simulation of Transition," H.L. Reed, *Invited Talk, ICASE Meeting of Stability Theory*, NASA/Langley Research Center, November 21, 1986.

8. "Nonequilibrium-Chemistry Considerations in Hypersonic Boundary-Layer Stability," H.L. Reed, *Invited Talk, ICASE Meeting of Stability and Transition of High Mach Number Shear Layers*, NASA/Langley Research Center, March 20, 1987.

9. "Stability and Transition of Three-Dimensional Flows," H.L. Reed and W.S. Saric, *Invited Seminar*, Princeton University, April 21, 1987.

10. "Transition at Hypersonic Speeds," H.L. Reed, *Invited Talk*, General Dynamics, Fort Worth, May 27, 1987.

11. "Transitional and Unsteady Flows," H.L. Reed, *Invited Talk*, General Electric, Ohio, July 29, 1987.

12. "Stability of Three-Dimensional Boundary Layers," H.L. Reed, *Invited Talk, SAE 871857, AEROTECH '87 (Aerospace Technology Conference and Exposition)*, SAE, Long Beach, October 5-8, 1987.

13. "Three-Dimensional Boundary-Layer Stability," H.L. Reed, *Invited Lecture*, University of Oregon, Eugene, November 6, 1987.

14. "Stability and Transition of Compressible Boundary Layers," H.L. Reed, *Invited Talk*, McDonnell Aircraft Company, St. Louis, November 12, 1987.

15. "Three-Dimensional Boundary-Layer Stability," H.L. Reed, *Invited Talk*, Naval Post Graduate School, Monterey, February 18, 1988.

16. "Computational Simulation of Three-Dimensional Boundary-Layer Flows," H.L. Reed, *Invited Lecture*, Tohoku University, Sendai, Japan, April 1988.

17. "Computational Simulation of Three-Dimensional Boundary-Layer Flows," H.L. Reed, *Invited Lecture*, Hokkaido University, Sapporo, Japan, April 1988.

18. "Stability and Transition of Compressible Boundary Layers," H.L. Reed, *Invited Talk*, McDonnell Aircraft Company St. Louis, May 26, 1988.

19. "Energy-Efficient Aircraft," H.L. Reed, *Invited Talk*, Society of Women Engineers, Notre Dame, Indiana, November 9, 1988.

20. "Three-Dimensional Boundary-Layer Stability," H.L. Reed, *Invited Talk*, IBM Lecture Series, Notre Dame, Indiana, November 9, 1988.

21. "Three-Dimensional Boundary-Layer Stability," H.L. Reed, *Invited Lecture*, University of Western Ontario, London, Canada, November 23, 1988.

22. "Spatial Simulation of Three-Dimensional Boundary-Layer Transition" and "Supersonic/Hypersonic Stability," H.L. Reed, *Invited Presentation*, NASA/Langley Research Center, January 30, 1989.

23. "Three-Dimensional Boundary-Layer Stability," H.L. Reed, *Invited Seminar*, University of Houston, March 2, 1989.

24. "Supersonic/Hypersonic Stability and Transition," H.L. Reed, *Invited Presentation*, General Dynamics, Fort Worth, March 17, 1989.

25. "Supersonic/Hypersonic Laminar/Turbulent Transition," H.L. Reed, G.K. Stuckert, and P. Balakumar, *Invited Paper, 21st Midwestern Mechanics Conference*, Michigan Technological University, August 13-16, 1989.

26. "Stability of High-Speed Chemically Reacting and Three-Dimensional Boundary Layers," H.L. Reed, *Invited Seminar*, University of Virginia, October 26, 1989.

27. "Boundary-Layer Receptivity," H.L. Reed, *Invited Seminar*, Michigan Technological University, February 9, 1990.

28. "Transition in High-Speed Flows," H.L. Reed, *Invited Presentation*, H.L. Reed, General Dynamics, Fort Worth, April 9, 1990.

29. "Boundary-Layer Receptivity: Navier-Stokes Computations," N. Lin, H.L. Reed, and W.S. Saric, *Invited Paper*, in *Proceedings of the Eleventh U.S. National Congress of Applied Mechanics*, Tucson, ASME, New York, May 1990.

30. "Navier-Stokes Simulations of Boundary-Layer Receptivity," H.L. Reed, *Keynote Speaker, 22nd Turbulence Symposium*, National Aerospace Laboratory, Tokyo, July 25-27, 1990.